Numerical Simulations of wind-driven Protoplanetary Nebula

—— **Igor Novikov** ——

Center for Astrophysics and Planetary Science
—— University of Kent ——

Submitted to the University of Kent in partial fulfilment of the requirements of the degree of PhD.

Principal Supervisor: Professor of Astronomy Michael D. Smith

—— July 2019 ——

Dedicated to Alexander and Julia

Acknowledgements

I wish to thank my supervisor, Prof. Michael D. Smith for allowing me and my friends to take this course. Working with Prof. Smith has turned physics from memorising lecture notes into a self evolving world of discovery and progress.

I am very grateful to the entire community of staff and students at the School of Physical Sciences, UKC. PhD staff: Tim Kinnear and Justin Donohoe for their help with the first steps in code setup.

Fellow PhD students: Greg Smith and James New.

Special Thanks to the first friend I met at University, Mubashar Iqbal. Mubashar has always helped me out and supported me throughout all these years. Thank you for all those FIFA football simulator hours and Magic the Gathering card games.

I must also mention my housemate and fellow Starfleet officer and Jedi Dr. James New for guarding the United Federation of Planets and using the Force for good and above all for encouraging me to start writing this Thesis.

Thank you to Gregory Smith for helping me with outreach at schools and giving me lift to work. I would also like to congratulate him on submitting his Thesis recently.

I would also like to say thank you to my Grandparents Igor Novikov and Eleonora Kotok. I am very grateful to them for mental and financial help. Without their support I wouldn't be able to make so many friends and learn so many new things that will help me in the future.

I must say thank you to my wife Julia and son Alexander for letting me go abroad to finish this work I set out to do a long time ago.

Summary

To understand how the circumstellar environments of post-AGB stars develop into planetary nebulae, we initiate a systematic study of 2D axisymmetric hydrodynamic simulations of protoplanetary nebula (pPN) with a modified ZEUS code. We constrain molecular dissociative fractions and timescales of fast H_2 and H winds and the pPN lifetime with wind densities $\sim 10^5 \mathrm{cm}^{-3}$ and shock speeds of $80 \sim 200\,\mathrm{km\,s}^{-1}$. The aim of this work is to compare the structure of prolate ellipsoidal winds into a stationary ambient medium where both media can be either atomic or molecular. We specifically model the early twin-shock phase which generates a decelerating shell leading to multiple hydrodynamic and emission stages.

A deformed and turbulent advancing shell thickens with time when an atomic wind expands into an atomic medium. This contrasts with cases of molecular outflows where a shell region fragments into a multitude of radial cometary-shaped protrusions 'bullets' with weak shocks as the main source of gas excitation due to molecular cooling and chemistry. This rough surface implies that weak shocks are prominent in the excitation of the gas despite the fast speed of advance. This may explain why low excitation molecular hydrogen is found towards the front of elliptical pPN.

We identify a variety of stages associated with thermal excitation of molecular emission and generate the atomic optical analogues of the H_2 near-infrared models with strong [Fe II] $1.64\,\mu$m and [Si II] $6716\,\lambda$ forbidden lines, the [O I] $6300\,\lambda$ airglow line, and Hα $6563\,\lambda$ emission. We find that the atomic wind-ambient simulation leads to considerably higher excitation, stronger peak and integrated atomic emission as the pPN expands. The weaker emission when one component is molecular is due to the shell fragmentation into fingers so that shock surface area is increased and oblique shocks are prevalent. Position-velocity diagrams indicate that the atomic-wind model may be most easy to distinguish with more emission at higher radial velocities. However, the comparison with post-AGB winds and shells remains limited due to the high obscuration and apparent multitude of configurations that are observed.

Contents

List of Tables

List of Figures

List of Symbols

A_w	Jet Surface Area
a_x	Acceleration
Be	Beryllium
C	Carbon
C	Courant Number
c	Speed of Sound ($2.998 \times 10^8\, m\, s^{-1}$)
E	Energy
e	Internal Energy Density
F	Acting Force
f	Molecular Graction
$\hbar$	Reduced Planck Constant ($1.054571 \times 10^{-34}\, J\, s$)
H_2	Molecular Hydrogen
He	Helium
$L_\odot$	Solar Luminosity ($3.827 \times 10^{26}\, W$)
$M_\odot$	Solar Mass ($1.989 \times 10^{30}\, kg$)
$\dot{M}$	Mass Loss
U_{int}	Internal Energy
M	Mach Number
m	Mass Element
P_e	Degeneracy Pressure
pc	Parsec ($3.086 \times 10^{16}\, m$)
r	Diatomic Bond Length
T_c	Stellar Core Temperature
t_{cpu}	Computational Run-Time
t_{lim}	Timescale for PPN Outflow
U	Velocity of Working Surface
u	Radial Velocity
V_w	Wind velocity
v	Velocity
α	Bowshock Angle
γ	Specific Heat Ratio
η	Density Ratio
θ	Orifice Angle
κ	Pressure Ratio
Λ	Cooling Term
μ	Reduced Mean Mass
ν	Vibrational Quantum Number
ρ	Density

Abbreviations

AGB	Asymptotoc Giant Branch
CE	Central Star
CFW	Collimated Fast Wind
CNO	Carbon Nitrogen Oxygen
CSE	Circumstellar Envelope
CSPN	Central Stars of Planetary Nebula
DUPLEX	Dust-Prominent Longitudinally Extended
EUV	Extreme Ultra Violet Radiation
HB	Horizontal Branch
LAGB	Late Asymptotic Giant Branch
MLR	Mass Loss Rate
MS	Main Sequence
npPN	Nascent Protoplanetary Nebula
P-AGB	Canonical Post-AGB
PE-AGB	Post-early AGB
PN	Planetary Nebula
pPN	Protoplanetary Nebula
RGB	Red Giant Branch
RSG	Red Supergiant
SED	Spectral Energy Distribution
SOLE	Star-Obvious Low-Level Elongated
TP	Thermal Pulse
TP-AGB	Thermal Pulse AGB
WD	White Dwarf

Publications

Novikov, Igor D. and Smith, Michael D. Numerical simulations of wind-driven protoplanetary nebulae - I. near-infrared emission

Monthly Notices of the Royal Astronomical Society, October 2018, Volume 480, Issue 1, p.75-95, DOI: 10.1093/mnras/sty1842

Novikov, Igor D. and Smith, Michael D. Numerical simulations of wind-driven protoplanetary nebulae - II. signatures of atomic emission

Monthly Notices of the Royal Astronomical Society, November 2019, Volume 489, Issue 3, p. 3710–3724, DOI: 10.1093/mnras/stz2377

Chapter 1

Post-AGB Stars and Winds

1.1 Introduction

Proto-planetary nebulae (pPNe) are transient objects between the late asymptotic giant branch (LAGB) phase and the planetary nebula (PN) phase in the evolution of low-to intermediate-mass stars $\sim 0.8 - 8\,M_{\odot}$ Mishra et al. (2016). In the lifetime of $\sim 10^3$ years Sahai et al. (2012), pPNe transforms into PNe where the central stars evolve to hot white dwarfs and photoionize their envelopes. In the literature, the term preplanetary (or proto-planetary) nebulae has been interchangeably used with the term post-AGB objects.

This transient stage is described by a sharp decrease in wind mass-loss rate from $\sim 10^{-4}\,M_{\odot}\,yr^{-1}$ at the end of the asymptotic giant branch (AGB), to $\sim 10^{-7}\,M_{\odot}\,yr^{-1}$ in the post-AGB phase, which leads to detached circumstellar envelope (CSE) of gas and dust, slowly expanding away from the star Gledhill & Yates (2003). Despite the spherical halo formed by radiatively driven wind at previous AGB stage, the morphological nebular features show asymmetries Sahai et al. (2007) in the star's surrounding envelope throughout the post-AGB and early PN stages such as bipolar and, or multipolar lobes. This is believed to be a cause of injection of collimated fast winds or jets (CFW) during this rapid transient stage that shocks and shapes the surrounding envelope of gas and dust in the nebula. To set the scene of post-AGB stars and the surrounding circumstellar envelopes the survey of ~ 50 young objects that had just begun the transition to the pPN phase labeled in literature as nascent pPN or (npPN) has been carried out by Sahai et al. (2007) deducing a morphological classification and derivation of post-AGB and AGB mass-loss time-scales along with ejected envelope masses resulting in CSE. The main structural components classified by the survey present in npPNs in order of

morphological importance are the lobes, the waist, and the halo. The waist is a dark obscuring band of optically thick cocoon of dust concentration in equatorial plane that separates the optically thin bipolar or multipolar lobes. These lobes are also known as searchlight-beams that appear to emanate from the center and can be seen illuminating the outer AGB halo. A Hubble Space Telescope (HST) survey by Sahai et al. (2007) suggests that the dusty waist may be due to (i) an opaque dust torus that blocks light that arises or is scattered from a central region, or (ii) a disk that prevents light from the central star to emerge in directions near the equatorial plane. The lobes are formed by a highly collimated fast wind of debated origin that carves out a cavity in the previously ejected AGB halo deposited by slow, dense, spherically symmetrical, radiatively driven outflow. Nascent pPNs have a prominent heavily reddened photosphere in the near infrared region suggesting a gradual dispersion of the circumstellar envelope enabling the light from the photosphere to emerge. A more evolved pPN generates approximately equal amount of flux from the circumstellar dust and the photosphere Mennessier & Omont (1990). In this nebular set up, the fast, collimated post-AGB wind evolves with velocities of several 100 km s^{-1} emanating from the stellar core Bujarrabal et al. (2001). The cause of the driving mechanism of CFW is unclear and is discussed in section 2.4. The interaction of CFW with the dense core and the surrounding, previously ejected AGB wind halo is believed to lead to asymmetries in the remnant, resulting in a vast array of morphologies present in planetary nebulas. Direct evidence from high angular resolution radio observations for CFWs during the pre-PN phase has come from sensitive molecular-line observations which reveal the presence of very fast (few 100 km s^{-1}) molecular outflows in pPNs Cernicharo et al. (1989) and a few very late AGB stars, with huge momentum excesses showing that these winds cannot be radiatively driven (e.g., Bujarrabal et al. 2001; Sahai et al. 2006). The collimated fast wind is likely to be episodic, and either change it's directionality (i.e., wobbling of axis or precession) or have multiple components operating in different directions (quasi)simultaneously Sahai et al. (2011). A good example of the above variations is described in a hydrodynamical and emission model of well known and studied young nebula CRL 618. This object has been numerically investigated in a paper by Lee et al. (2009) describing 3D hydrodynamical simulations fitted with cooling functions by Suttner et al. (1997) coupled together with molecular chemistry by Smith & Rosen (2003) that calculates the fraction of molecular hydrogen and atomic hydrogen to produce intensity maps for comparison with observations. In their models, the typical velocities and mass outflow rates for the cool 10 K slow $10 \sim 20$ km s^{-1} molecular AGB wind and fast molecular $\sim 10^3$ km s^{-1} CFW are assumed to be $\sim 10^{-5}\,M_\odot\,yr^{-1}$ and $\sim 10^{-7}\,M_\odot\,yr^{-1}$ respectively, similar to observational values of the optical lines and CO outflows by Riera et al. (2014).

1.2 Thesis Overview

The research in this work develops a morphological nascent pPN model based on the observational surveys by Sahai et al. (2007) with hydrodynamical wind parameters based on CRL 618 in Lee et al. (2009). The resultant model features a collimated fast wind injected into the npPN environment surrounded by the AGB halo in order to undergo an early/late expansion shock phase due to density gradient of wind/ambient interface. Additional molecular cooling, atomic recombination terms and molecular chemistry by Smith & Rosen (2003) is included to create shock-induced emission in the optical and near-infrared part of the spectrum along with position-velocity (PV) diagrams for comparison with pPN observations. The primary aim of this thesis is to investigate the interaction of the atomic/molecular medium with young pPN stellar wind models to understand the transition of H_2 molecules from the cold AGB envelope phase to subsequent molecular presence in hot, ionised PNe medium.

The thesis begins with the introduction to different types of stellar winds and is followed by a description of the star's evolutionary track starting with main sequence (MS) stage up to and during post-AGB in chapter 1. This section of thesis highlights the key features of pPN environment and establishes main goals to be answered by generating high-resolution hydrodynamical models and subsequent near-infrared & optical synthetic maps used for detailed analysis of kinematic and chemical evolution. Chapter 2 is dedicated to theory of shock-excited emission that explains the origin of near-infrared J-shock emission present in PPN environment, followed by generalised interacting stellar winds model (GISW) that highlights the need for non-radiatively driven wind launching mechanism required to drive the collimated fast PPN wind. This chapter also focuses on recently proposed theoretical wind drivers as well as observational PPN statistics including morphology and galactic distribution. Chapter 3 defines main macroscopic computational parameters and code configuration of 2D axisymmetric computational grid set up in ZEUS code. Chapter 4 describes K-band and optical integration routines implemented in ZEUS. The following chapters 5 and 6 presents hydrodynamical and line emission results respectively, conducted with numerical simulations of wind-driven proto-Planetary nebula. The synthetic maps are generated using cylindrical symmetry with line of sight as a user variable enabling results evaluation in 3D. The next chapter 7, is dedicated to discussion of results with comparison to other numerical PPN studies and observational surveys, followed by chapter 8, where main conclusions are derived and future potential work is discussed.

In our results we find that the molecular interacting shell region fragments into a multitude of cometary knot-shaped (CK) protrusions with weak shocks as the main source of H_2 gas excitation despite the

fast speed of advance $80 \sim 200\,\mathrm{km\,s^{-1}}$ of $10^{-4}\,\mathrm{M_\odot\,yr^{-1}}$ mass outflow originated from $\sim 10^5\,\mathrm{cm^{-3}}$ wind densities. This is a possible explanation of how low excitation molecular hydrogen is found towards the front of elliptical pPN and PN. We find that the atomic H wind-ambient simulation leads to considerably higher gas excitation, stronger peak and integrated atomic emission as the pPN expands. Further away from the star, flow instabilities (e.g. Rayleigh-Taylor) have time to fragment the outward moving arcs and shells to produce numerous small-scale cloud-like sub-structures. The weaker emission when one component is molecular (either wind or ambient) is due to the shell fragmentation into cometary knots (CKs) increased shock surface area with oblique shocks prevalence. We also conclude that the unstable interface can be produced, not only by wind-wind models, but also by wind-uniform ISM interaction with formation of molecular clumps and filaments.

1.3 History and Types of Stellar Mass Loss

This section starts off with driving physics and history of discovery of different types of stellar mass loss due to wind ejection. Subsequently, this introduction gradually leads to the description of interacting winds shaping the resultant proto-Panetary nebula, where a collimated fast wind (CFW) $\sim 100\,\mathrm{kms^{-1}}$ catches up with slowly coasting $\sim 10\,\mathrm{kms^{-1}}$ wind ejected during the previous AGB mass loss epoch Kwok (1982). The characteristics that define pPN morphology and kinematics are briefly discussed in this section and referred to later chapters that explain these features in more detail.

1.3.1 Stellar Outflow Driving Mechanisms

A stellar wind consists of particles emitted from the stellar atmosphere with a sufficiently large velocity $\mathrm{v_{go}}$ to escape the star's gravitational attraction.

$$\mathrm{v_{go}} = (2\mathrm{GM_*/R_*})^{1/2} = 620\ \mathrm{kms^{-1}}(M_*/M_\odot)^{1/2}(R_*/R_\odot)^{-1/2} \tag{1.1}$$

In order to overcome the star's gravitational pull, a form of wind-driving, non-gravitational force must be present. The origin of this driving force varies with the physical nature of the wind. It can be driven by gas pressure, radiation pressure or magnetic pressure, or a combination of the above. Observed stellar winds subjected to those forces are categorised into four types:

Type 1. *Winds from main-sequence stars.* The mass loss rate of the Sun is $2 \times 10^{-14}\,\mathrm{M_\odot yr^{-1}}$. This type of wind is hard to observe with spectroscopic techniques due to its high temperature and ionisation state. Winds from solar-type stars are thought to be driven by gas pressure gradients in the corona.

The solar wind can be broken down into two components: slow $400\,\mathrm{kms}^{-1}$ wind emanating from the edges of coronal holes and regions above closed field lines whereas fast $760\,\mathrm{kms}^{-1}$ wind originates from coronal holes Johnstone et al. (2015).

Type 2. *Winds from hot, luminous stars.* Such as Central Stars of Planetary Nebula (CSPN) with $T_{\mathrm{eff}} > 15,000$ K and $L > 3,000\,L_{\odot}$ and mass loss rate that decreases in time from 10^{-7} to $10^{-9}M_{\odot}\mathrm{yr}^{-1}$ at the same time, the fast wind increases in speed from 200 to 2000 kms^{-1} in a manner that conserves wind ram pressure Huarte-Espinosa et al. (2012). Their winds are very fast, with $u_{\infty} \gg v_{\mathrm{go}}$ driven by radiation pressure. Wolf-Rayet stars also fall into this category. WR stars are hot, luminous stars with extended envelopes and mass loss rates of $10^{-5}M_{\odot}\mathrm{yr}^{-1}$ and wind terminal velocities of $u_{\infty} \sim 2500\,\mathrm{kms}^{-1}$ are among the largest observed for any type of star Ryden (2016).

Type 3. *Winds from cool, luminous stars.* Stars with $T_{\mathrm{eff}} < 6,000$ K and $L > 100\,L_{\odot}$ have a high mass loss rate range of $10^{-8} \sim 10^{-5}M_{\odot}yr^{-1}$. Wind velocity is very low $10 \sim 20\,\mathrm{kms}^{-1}$ which is below the escape velocity of the stellar surface $u_{\infty} \ll v_{\mathrm{go}}$ Hartquist & Williams (1998). The mechanism that drives the wind from cool AGB stars is uncertain, a leading candidate is radiation pressure on dust grains, aided by stellar pulsations in the outer atmosphere. Stars in this category are K and M giants and supergiants. During this phase the star can lose between $50 \sim 70\%$ form stellar wind Wood et al. (2004)

Type 4. *Winds from extremely young stars.* T Tauri stars have mass loss rates between $10^{-9} \sim 10^{-7}M_{\odot}yr^{-1}$. These type of stars have circumstellar disks that might result from accretion. The strength of the wind is correlated with disk luminosity suggesting that the outflow might be powered by the accretion disk Ryden (2016).

The main sequence solar wind contrast with the massive winds of hot stars and evolved cool stars, which are comparatively easy to detect spectroscopically with characteristic P-Cygni line profiles that signify the presence of these strong winds. These profiles consist of blue-shifted absorption and a red-shifted emission component that are formed over the entire wind range and provide the observers with data for wind terminal velocity, ion density and mass-loss rates.

1.3.2 Post-Main Sequence Mass Loss History

The first substantial evidence of mass-loss after main sequence stage is based on observations by Deutsch (1956) of an M-type giant α Her and a G-type star surrounded by a circumstellar envelope ejected by the M star in the AGB phase. The circumstellar absorption lines seen in the spectrum of the

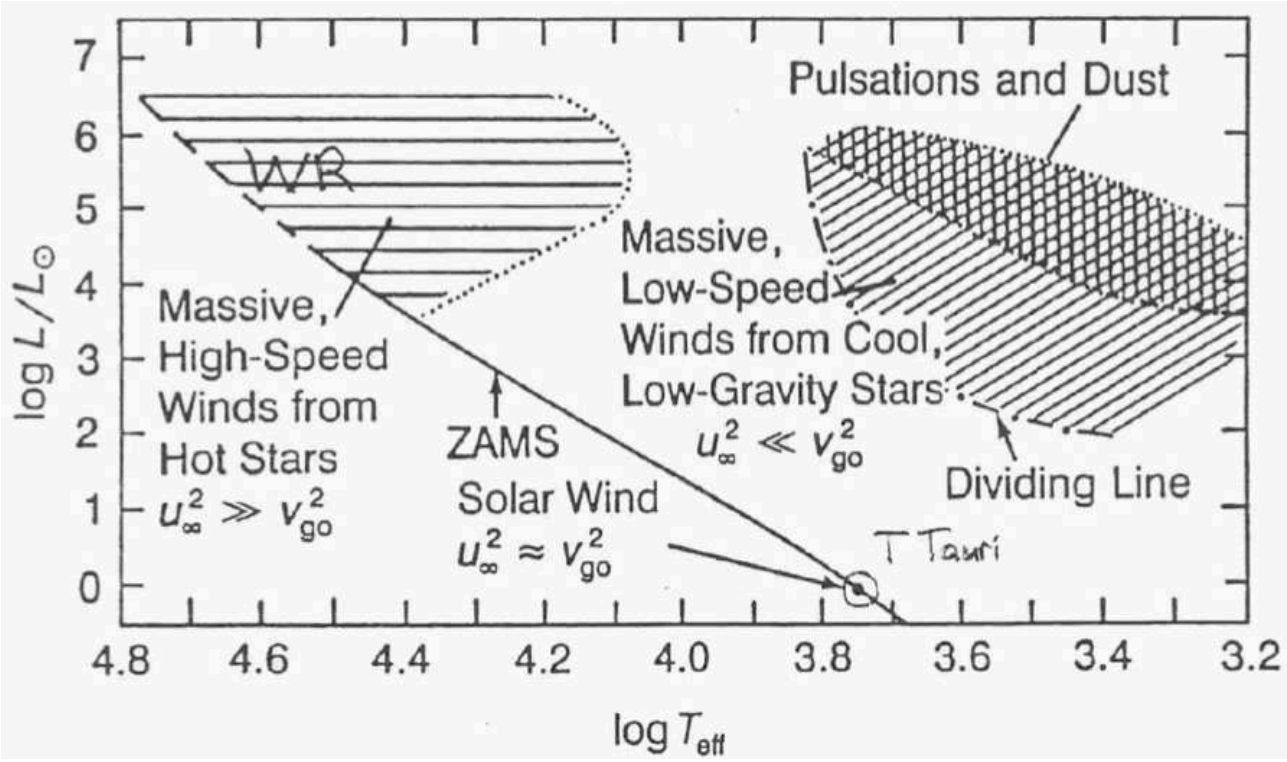

Figure 1.1: A Hertzsprung-Russell diagram (luminosity versus effective temperature) showing the location of stars with high rates of mass loss from stellar winds.

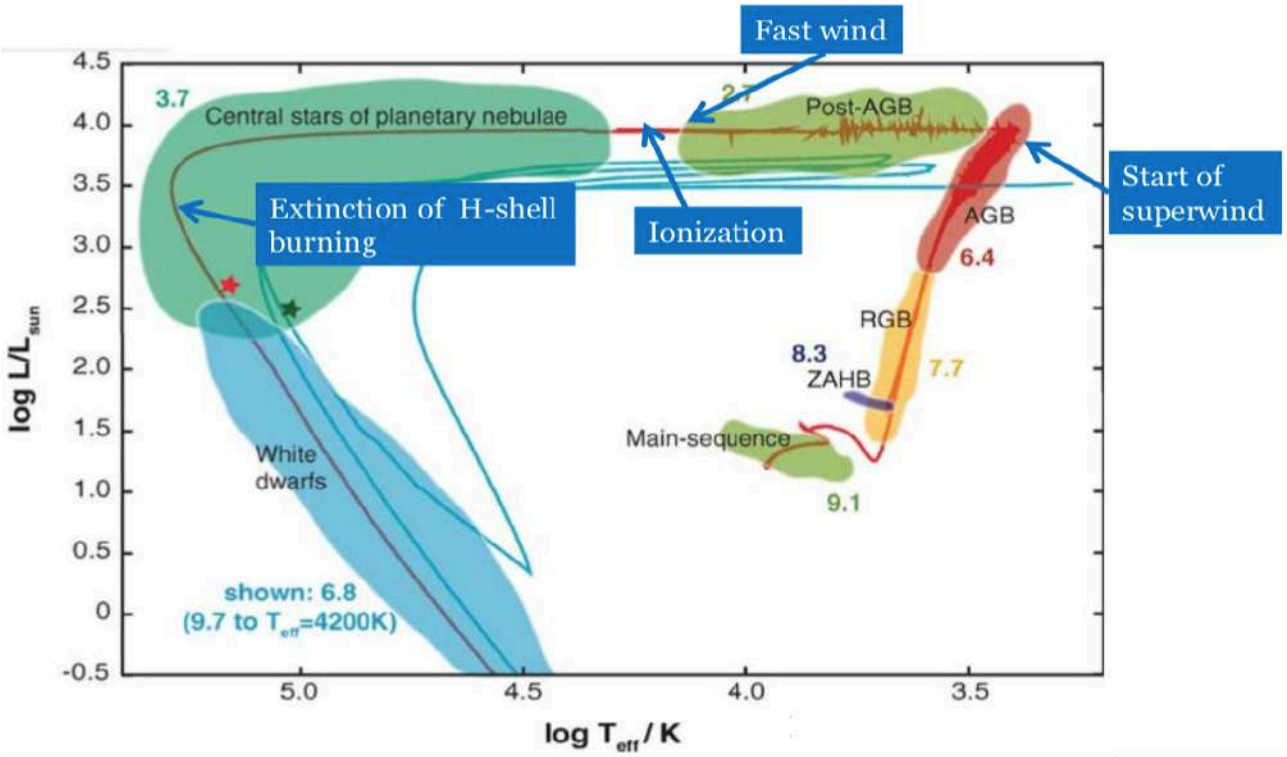

Figure 1.2: The Hertzsprung-Russell Diagram, showing the evolutionary track of 2 $M_\odot$ (red line) covering the main sequence through the white dwarf phase Herwig (2005). The numbers next to the steps correspond to the time that the star passes this step, log in years. As AGB stars dominate the luminosity of the star systems of intermediate age, they are important in studies of extra-galactic systems.

companion G star suggest radius of the envelope of $2 \times 10^5\,\mathrm{R}_\odot$ expanding at $20\,\mathrm{kms}^{-1}$ and estimated wind mass loss rate of $3 \times 10^{-8}\,\mathrm{M}_\odot\mathrm{yr}^{-1}$. In the study of similar systems to Deutsch (1956), the observational data by Dupree & Reimers (1987) from six binary systems consisting of a red supergiant (RSG) and an earlier type companion enabled to determine the mass of the RSG from the orbital motion of the two stars. The rate of mass loss by Lamers & Cassinelli (1999) was estimated from the observation of lines from the wind of the cool star in absorption against the hot companion star. The data by Dupree & Reimers (1987) also served to determine an empirical equation relating mass-loss to stellar mass, luminosity and radius and was formulated by Reimers (1975) and expressed as

$$\dot{M} = 4 \times 10^{-13} \eta L M^{-1} R \qquad \left[\mathrm{M}_\odot\,\mathrm{yr}^{-1}\right] \tag{1.2}$$

This relation ranges from 10^{-8} to 10^{-6} with $\mathrm{M}, \mathrm{L}\,\mathrm{and}\,\mathrm{R}$ in solar units and $1/3 < \eta < 3$ is an empirical correction factor for different types of stars with $\eta = 1$ for red supergiants Lamers & Cassinelli (1999). The Reimers relation assumes the wind energy comes from constant but overall small fraction of the energy output of a star $0.5\dot{\mathrm{M}}\mathrm{v}_{\mathrm{esc}} = 1.3 \times 10^{-9}\eta\mathrm{L}$ in the form of potential energy since $\mathrm{M}_*/\mathrm{R}_* \propto \mathrm{v}_{\mathrm{go}}^2$. Reimers relation has also been used for AGB stars, for which it was not derived. However, there are several implications when applying empirical relation in Equation 1.2 to the AGB phase. AGB mass loss is a time-dependent variable with mass loss rates that increase linearly with the mass of the core. Theoretical studies by (Renzini 1981) suggested that the termination of AGB phase is executed by an increase in mass loss phase themed superwind. Despite the implications, Reimer's law was able to predict the need for acceleration process of mass loss at the AGB throughout which the star ejects most of its mass.

1.3.3 pPN Overwiew

The next stage of stellar mass loss due to wind ejection is the proto-Planetary nebula (pPN) phase. The outflow present in pPN is highly collimated and fast compared to the previous spherical/axisymmetric wind in the AGB phase and it fills the gap separating the region in Figure 1.1 between the low-speed winds (type 3) from cool, low gravity AGB stars and high speed winds (type 2) from hot stars of planetary nebula PN. The central star/nebula ionisation evolution is represented on the Hertzsprung–Russell (HR) diagram in Figure 1.2 where the collimated fast wind (CFW) is present in the post-AGB stellar evolutionary track between the superwind phase and nebula ionisation by the central star of PNe. The wind engine for cool evolved stars and hot stars of PNe is well known and investigated, however due to observed momentum excess at pPN phase that cannot be described by radiation pressure Bujarrabal et al. (2001), the driving mechanism for CFW wind is unknown and the proposed

theoretical models are discussed in section 2.4.

Despite the unknown wind origin, the main resulting pPN feature is evident and presents itself in the form of interaction of collimated fast wind with the previously ejected AGB halo. The resulting interaction of stellar winds from different evolutionary epochs shocks and shapes the resulting cloud leading to axisymmetric like proto-Planetary nebulae. The most famous pPN AFGL 2688 (also known as CRL 2688) and AFGL 618 were first detected in an infrared survey by Ney et al. (1975) tracing regions of dust warmed by starlight $\sim 150\,\mathrm{K}$. However, polarimetry pPN study predates mid-infrared surveys and serves to separate the light scattered by dust in the envelope created by the superwind and the unpolarised light from the central star. Due to scattering of light by dust and the presence of molecular environment developed throughout previous AGB phase that is now subjected to shocks driven by present collimated fast pPN wind, polarimetry studies coupled with optical and infrared bands is used for pPN investigations.

Using the methods described above, the same nebula investigated by Ney is later observed by Sahai et al. (1998) using polarimetry coupled with H_2 near-infrared line imaging results in detection of two pairs of radial "searchlight beams" emerging from the obscured star in the center of the nebula. In the same work, the $2 \rightarrow 1\,\mathrm{S}(1)$ $2.12\,\mu$m K-band emission line was able to resolve the interface between the high velocity collimated wind that produces the cavities in the dusty envelope and the surrounding slow outflow that creates the extended nebula. Further extending our knowledge about pPNe, surveys of multiple pPNe candidates using polarimetry studies coupled with high resolution optical imaging by Hubble Space Telescope (HST) of ~ 27 sources confirmed that axisymmetry found in PN predates the pPN phase suggesting that the source of axisymmetry is created by an equatorially enhanced superwind at the end of AGB Ueta et al. (2000a). The same survey suggested that the equatorial wind strength branches the optical pPN morphology into toroidal and core/elliptical, with corresponding distinct spectral energy distribution (SED) type discussed in section 2.6. Therefore, the morphology of pPN is heavily dependent on the abundance of dust, whereas dust shells themselves preserve the mass loss history and dust grain properties. pPN dust morphologies serve as pristine fossil records of AGB mass loss process due to non-activation of the shaping by hot PNe wind which activates at a later stage of evolution. The pPN fossil circumstellar shells record corresponds directly with time, enabling to determine the onset of different stages of mass loss and the "initial conditions" for the interacting pPN winds models. This was accompished with radiative transfer models by Meixner (2000) illustrated in Figure 1.3. The maximum radius R_{max} indicates when the spherical AGB mass loss began, followed by R_S which corresponds to when the AGB mass loss began to increase in rate

and departured from spherical to axially symmetrical superwind outflow. Finally, the inner radius R_{in} of the "searchlight beams", marks when the AGB mass loss seized which is equal to the dynamical age that has passed since the star left the AGB and entered the proto-Planetary phase. In order to dissect the different parts of the circumstellar envelope of pPN, a range of wavelengths is used starting with the outer colder layers of CSE that are observed in sub-mm and far-infrared (ALMA or Herschel telescopes), while warmer layers of the CSE are observed in the mid-infrared $5 \sim 40\,\mu$m (VISIR/Very Large Telescope (VLT)) Lykou et al. (2018). The layers closer to the star including the stellar photosphere and hot, dusty atmosphere are investigated in the near-infrared range. Due to excitation of ro-vibrational molecular bonds of H_2 by collimated fast wind, the "searchlight beams" are observed in the near-infrared K-band window. The optical emission in the lobes of CFW is a result of 'cavities' excavated in the AGB halo by interaction with a more tenuous post-AGB wind. As presented by optical long-slit spectroscopy and imaging by Sánchez Contreras et al. (2002) of well-studied nebula of CRL 618 which is at the boundary between pPN and young PN, the optical emission results from many recombination and forbidden lines such as H-alpha and [O I], [Fe II]. The resultant molecular/optical line emission caused by collimated fast wind interacting with the AGB remnant/ambient is the main topic of investigation of this work. The synthetic emission maps representing line flux/ratio as well as line profiles and position-velocity diagrams enables us to answer a multitude of questions listed in section 1.6, as well as suggest and motivate selection criteria for new surveys.

To clearly define the nomenclature before moving forward it is important to establish the difference between post-AGB objects and proto-Planetary nebula, due to the fact that they are not the same ensemble. While all pPN develop into PN by definition, it is not the case for all post-AGBs. For instance, if the envelope is removed before the star reaches sufficient enough temperatures to ionise the nebula, the star will go through the post-AGB phase but will not illuminate the non-existent near by nebular gas. As an example, dusty RV Tauri stars are post-AGB objects surrounded by circumstellar disc with no material outside the disk will most likely not form a PN.

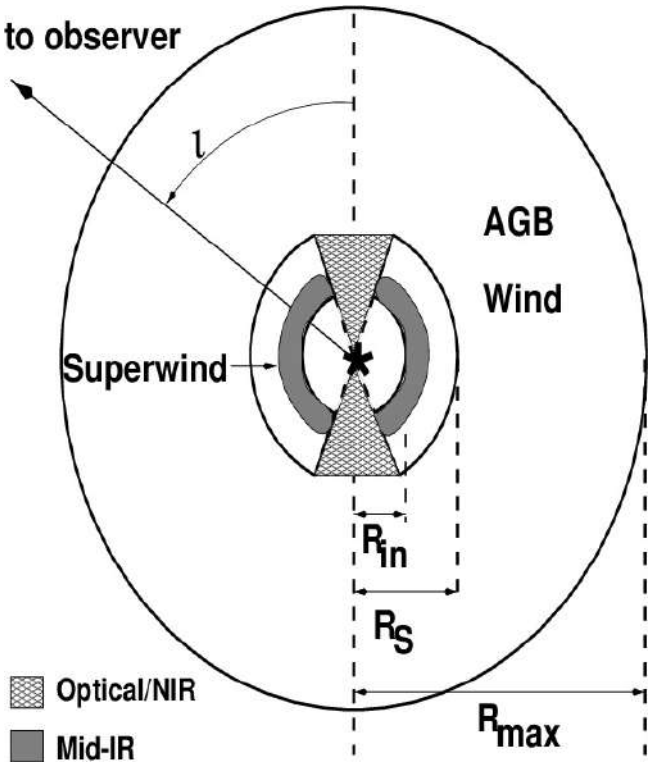

Figure 1.3: Schematic representation of dust shells by Meixner (2000) using radiative transfer models to derive optical depths and morphological PPN structures. R_{max} is the extent of circumstellar AGB envelope, i.e the spherical AGB halo. R_s is the extent of axially symmetric superwind. i.e marking the end of late-AGB phase. R_{in} is the radial extent of axially symmetrical collimated fast wind that emerges in the polar directions and carves out a cavity in the AGB envelope and forms a bipolar nebula.

1.4 Evolution of Low-to Intermediate Mass Stars

This section starts off with an outline of the process of low-to intermediate-mass stellar evolution establishing the conditions that lead to proto-Planetary nebulae being powered by high velocity collimated winds emerging from their central stars.

The life of a star is a multi-phase mechanism, throughout which it undergoes a number of transitions. The star's future evolution is determined by its initial mass. Massive stars with minimum mass range between $8 \sim 10\,M_{\odot}$ undergo carbon fusion resulting in a core-collapse supernova explosion. Very low mass stars of $M_* < 0.8\,M_{\odot}$ do not initiate He burning and subsequently do not ascend the asymptotic giant branch (AGB), they fuse H into He via proton-proton chain and have a main sequence (MS) lifetime longer than the age of the universe. Low-to intermediate mass stars of $0.8 \sim 8\,M_{\odot}$ first classified by Iben & Renzini (1983) and adopted by Kastner (2005) (for pPNe) do enter the AGB and develop a degenerate helium core. Within this mass range the $0.8 \sim 2.5 M_{\odot}$ stars develop electron-degenerate helium core and undergo sudden helium burning (Helium Flash), while intermediate stars of $2.5 \sim 8 M_{\odot}$ evolve more gently. Low-to intermediate mass stars undergo a number of transitions described below which lead to cool, luminous asymptotic giant branch star fuse inner He and outer H

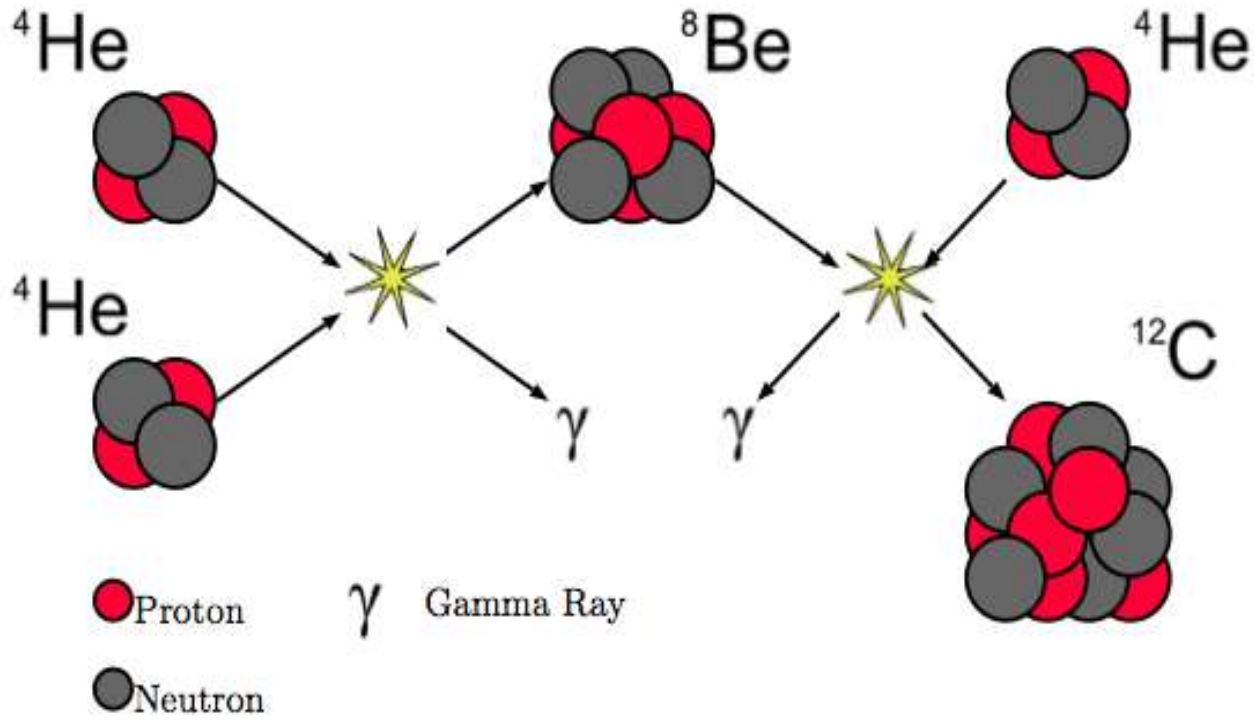

Figure 1.4: Nuclear fusion reaction where three helium-4 nuclei transform into carbon.

shell to subsequently evolve into a pre-Planetary nebula:

Main Sequence and Red Giant Branch

Throughout the main sequence (MS) stage, the star generates energy via the proton-proton and carbon-nitrogen-oxygen (CNO) cycle, resulting in a helium build up in the core, which in turn enables the star to find another source of energy via the triple alpha process where helium nuclei fuse together to form carbon as shown in Figure 1.4.

$$
\begin{aligned}
&{}^{4}_{2}\mathrm{He} + {}^{4}_{2}\mathrm{He} \rightarrow {}^{8}_{4}\mathrm{Be} \\
&{}^{8}_{4}\mathrm{Be} + {}^{4}_{2}\mathrm{He} \rightarrow {}^{12}_{6}\mathrm{C} + 7.367\,\mathrm{MeV}
\end{aligned}
\tag{1.3}
$$

Exhaustion of hydrogen in the core leads to disruption of hydrostatic equilibrium and the core begins to contract. As the core starts to contract, gravitational energy is released. This results in hydrogen in the thin shell around the core being heated enough to undergo fusion. The energy released by this new burst of fusion leads to increase of radiation pressure on the outer layers , as a result, the luminosity of the star is increased by a factor of $10^3 \sim 10^4$ ascending the RGB branch and the outer layers expand to $\sim 10^2\,\mathrm{R}_{\odot}$. The outer layer expansion leads to the fusion energy being spread over

[1]Figures (1.1-1.2 & 3.1, 3.3) are generated with LaTeXdrawing editor http://latexdraw.sourceforge.net

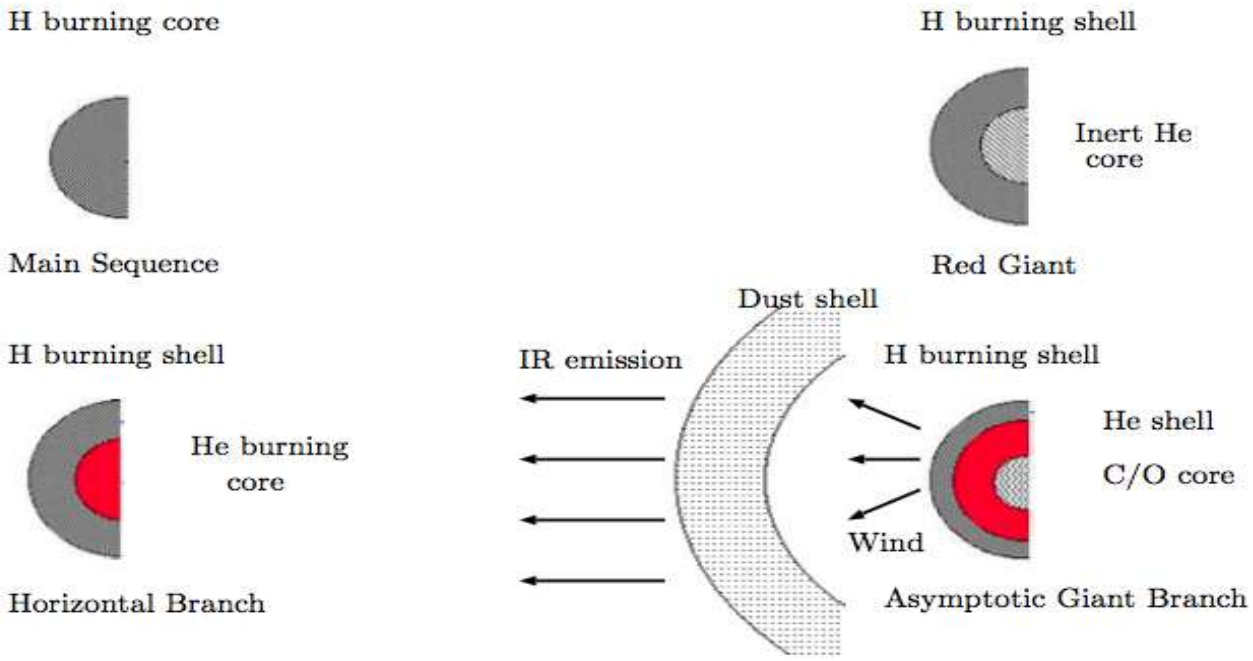

Figure 1.5: Evolution of stellar core for $M_* > 2\,M_\odot$, triple alpha fusion is prior to electron degeneracy, the star experiences a gradual shift to a core helium burning region surrounded by a hydrogen burning shell[1].

a greater surface area lowering the surface temperature, thus the star ascends the Red Giant Branch shown in Figure 1.5 (top right). Starting with the main sequence stage with negligible mass loss rate, the low-to intermediate mass stars will loose mass at every subsequent stage up until the end of planetary nebula phase.

Horizontal Branch phase

Throughout the RGB phase, the core experiences an increase in mass and temperature as the hydrogen shell continues to deposit inert helium in the core. Since no energy is produced in the core, it becomes almost isothermal. For a certain period of RGB evolution, the hydrogen shell advances forward, and the nearly isothermal core increases accordingly accompanied with an increase in core's density that in turn supplies the pressure gradient. There is a limit at which the core's mass can support it's own gravity without undergoing a core collapse. Schönberg & Chandrasekhar (1942) showed that a core of mass between $0.10 \sim 0.15\,M_*$ is at a limit of an isothermal configuration that can balance its own gravity with an additional weight of the hydrogen envelope surrounding it. Upon reaching the Schönberg-Chandrasekhar Limit, the core becomes dense enough and no longer acts as a perfect gas. At such high densities, the electrons exist in high energy states. This quantum mechanical effect is known as electron degeneracy pressure, where the inert helium core is supported by temperature

independent electron degeneracy

$$P_e \propto \rho^{5/3} \qquad \left[\mathrm{gm\,cm^{-1}\,s^{-2}}\right] \tag{1.4}$$

The core is unable to expand and cool and the star experiences a thermal runaway $\mathrm{T_c} \sim 10^8\,\mathrm{K}$ at which point helium can ignite and start to fuse. As a result, the transition to the triple-alpha point of core helium burning is reached explosively with a flash or gradually for heavier stars. This is a local core event known as the Helium Flash shown in Figure 1.6 releasing $\sim 10^{11}\,\mathrm{L_\odot}$ in a few seconds Prialnik (2000), during which surface properties of the star remain unaltered. The output of thermal energy of the helium flash is transmitted into the expansion of the core and electron degeneracy is lifted. This enables the star's core to cool significantly, leading to a drop in energy generation in the hydrogen burning shell. The luminosity decreases as it descends to the horizontal branch (HB), the star shrinks, and the surface temperature rises tracing a horizontal track along the HR diagram. The continuing rise in the star's surface temperature is due to hydrogen fusion in a shell and He-burning triple-alpha reactions in the core shown in Figure 1.5 (bottom left). Stars in the horizontal branch have approximately constant luminosity across a range of temperatures. Triple - alpha is inefficient at producing energy and lasts for about 10^8 yr Karakas (2010) building up abundance of an C/O core but not sufficient enough core temperature to ignite Carbon fusion.

AGB stars and winds

Following helium fusion phase which lasts for a few $\sim 10^6$ years in HB phase, the core becomes He exhausted and turns into carbon and oxygen nuclei, creating an C/O core, encompassed by helium and hydrogen burning shells. The hydrogen shell is deposits helium ash onto the helium shell, presented schematically in Figure 1.5 (bottom right). The outer layer is convective, this allows the core material to dredge up to the surface by convective currents which in turn leads to heavier abundance of carbon and dust grains. The star becomes more luminous than on its first RGB ascent, it expands and cools down becoming an AGB star. AGB phase derives its name as it appears brighter compared to the RGB, i.e it leaves the red side of the HB and looses a large convective envelope and ascends the Giant Branch phase but at higher effective temperature tracing an asymptotic curve in Figure 1.7 relative to previous RGB track. The AGB stars appear as cool $< 3,000\,\mathrm{K}$, luminous $\sim 10^4\mathrm{L_\odot}$ stars on HR diagram with the initial mass range of $0.5 \sim 8\,\mathrm{M_\odot}$ Höfner & Olofsson (2018). This corresponds to characteristical stellar radii of $\sim 10^2\,\mathrm{R_\odot}$, resulting in low surface gravity of $10^{-5} \sim 10^{-4}$ of a sun-like star and subsequent low gas escape velocity Höfner & Olofsson (2018). The double shell (H- and He-) burning phase takes up to ∼1% of the overall intermediate mass star's lifetime. For an even shorter

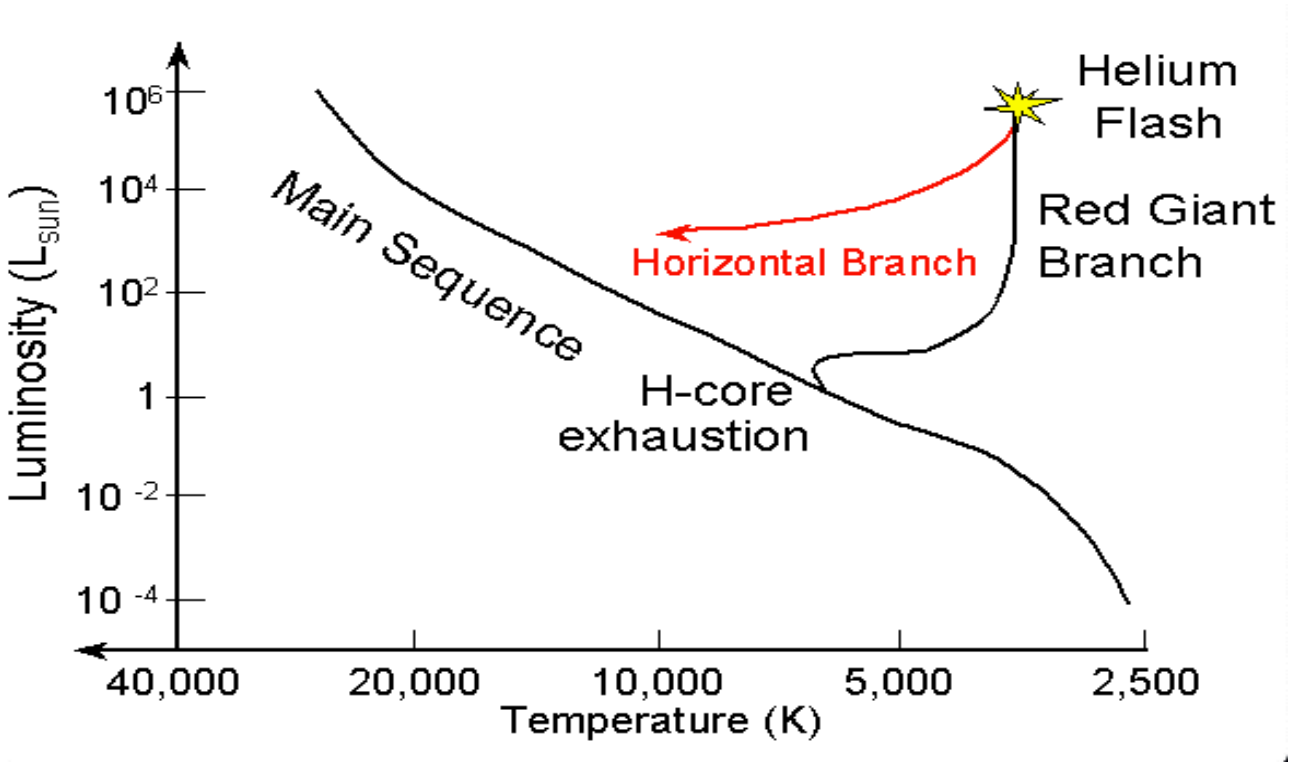

Figure 1.6: The Hertzsprung-Russell Diagram, showing the evolutionary track of $2\,M_\odot$ star. Horizontal branch stars are post-helium-flash, low-mass stars with luminosities of about 50 times that of the Sun and in which there is both core helium burning and shell hydrogen burning. These stars will eventually move back toward the red giant region as their fuel is exhausted.

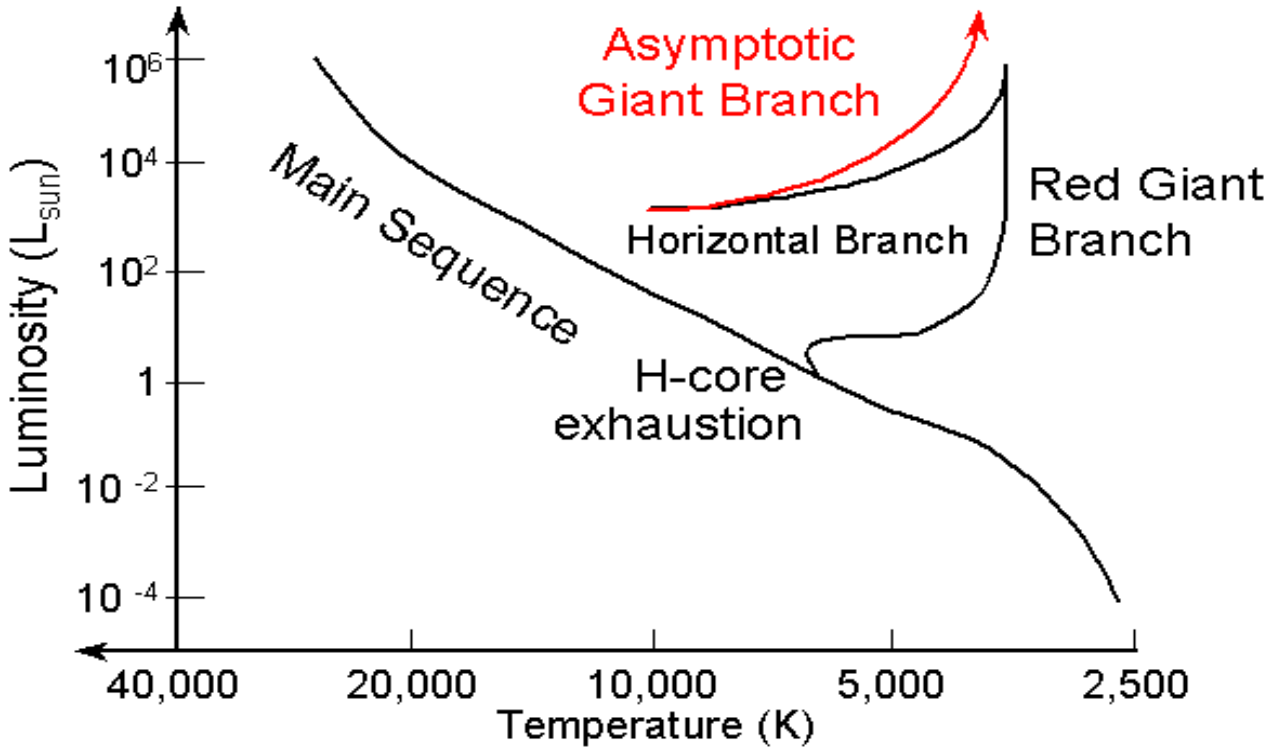

Figure 1.7: The Hertzsprung-Russell Diagram, showing the evolutionary track of $2\,M_\odot$ star. The star climbs the Giant Branch again, but at a higher effective temperature than the Giant Branch, so it ascends with a bluer color, putting it slightly to the left of the original Giant Branch on the H-R Diagram.

fraction of their nuclear AGB life, of order 10^{-3}, the stars experience thermal pulses (TP-AGB phase), during which the temperature and brightness vary significantly on timescales of a few thousand years Salaris et al. (2014). This process is launched by the build up of helium with time that undergoes an explosive event in the He shell called a thermal pulse (TP). This process is barely noticeable on the star's surface but it leads to increase of the C/O core. The core element ratio splits the star's core into 3 chemistry types: O-rich, S-type, C-rich with ($C/O < 1, \sim 1, > 1$). The atomic C to O ratio in the stellar atmosphere of AGB stars sets the molecular and dust content of the CSE formed by the stellar wind Castro-Carrizo et al. (2010). Due to low atmospheric temperatures and relatively high densities, AGB environment enables favourable thermodynamic conditions for molecule formation Kim et al. (2010).

AGB outflow & Superwind

Working back from the PN, Renzini (1981) first proposed a term superwind to account for the observed mass loss characteristics in that phase. By taking the typical mass of PN remnant to be in order of $0.2\,M_\odot$, AGB expansion velocity of $20\,\mathrm{kms}^{-1}$ and nebula radius of ~ 0.1 pc, the resulting mass loss prior to PN is at least several $10^{-5}\,M_\odot\,\mathrm{yr}^{-1}$. With η of the order of unity, Reimers mass loss rate (MLR) Equation 1.2 gives the largest value reached by AGB stars $10^{-6}\,M_\odot\,\mathrm{yr}^{-1}$. Hence the MLR necessary to produce the observed values needs to be at least one order of magnitude larger than predicted by Reimers law. In order to account for PNe envelope mass, the AGB phase must be terminated by a rapid process ejecting most of the residual hydrogen-rich envelope. This "superwind" region in Figure 1.2 marks the location of material ejected during an intense and perhaps axially symmetric mass loss phase that ends a star's life on the AGB known as the late AGB (LAGB) phase. This behaviour along the AGB is in agreement with observations that require the mass loss rate to substantially increase near the termination of the AGB phase.

According to the spherically symmetric 1–D model calculations by Winters et al. (2000); Höfner et al. (2003); Sandin & Höfner (2003); Schirrmacher et al. (2003), these winds are driven by a combination of stellar pulsation, dust formation and radiation pressure on dust grains. Mass loss is known to dominate the evolution on the asymptotic giant branch generating massive stellar winds with mass loss rates up to $10^{-4}\,M_\odot\,\mathrm{yr}^{-1}$ Habing (1996); Le Bertre (1997); Wallerstein & Knapp (1998), which drives them towards the planetary nebula phase. However, the slower evolution of stars with $M_* \leqslant 1\,M_\odot$ means more mass is lost during the red giant branch (RGB) phase than on the AGB. RGB mass loss has been studied much less due to this phase having minor effects on their evolution. However, RGB mass loss is crutial for evolution at later stages as it sets the stellar temperature on the horizontal

branch and dictates the length and path of subsequent evolution along the AGB McDonald & Zijlstra (2015). The AGB wind leads to dust particle formation from dredged up carbon material from the core making it one of the milestones in the study of interstellar clouds and proto-solar systems. AGB stars are surrounded by dust-rich shells of matter produced by their own slow, spherically symmetric AGB stellar wind. During this time in stellar evolution, the thick dust shell blocks the visible light and absorbs the radiation coming from the central star re-emitting it in the far infrared (IR) part of the spectrum Piovan et al. (2003).

Post-AGB stars

The interior pulses lift a layer off the surface of the star ejecting it into the ISM until the envelope becomes stable and the pulses subside. At this phase, the star is at the end of late Asymptotic Giant Branch (LAGB) and the start of the pPN. Thus the dredged-up material is released into the ISM, leading to increase of the relative abundance of carbon in the form of gas or more commonly in form of dust grains. The RGB mass loss phase and core mass reduction due to thermal pulsations determines AGB stars evolutionary track, which branches into canonical Post-AGB (P-AGB), post-early AGB (PE-AGB) and AGB-Manque stars Rosenfield et al. (2012). The time between AGB tip to onset of H ionization lasts about $10^2 \sim 10^4$ yr which is the timescale at which fast-evolving winds shock and shape the resulting pPN nebula before the central star reaches sufficient temperature to start ionising the surrounding nebula. Post-AGB stars follow a horizontal track on the HR diagram towards higher temperature due to core contraction at constant Luminosity provided by H-shell burning:

$$T_\star \propto (L/R^2)^{1/4} \qquad [\mathrm{K}] \tag{1.5}$$

More massive central stars of P-AGB appear hotter and brighter on the HR diagram and consequently undergo faster evolution towards the white dwarf phase along the top track in Figure 1.8. These objects are known as the canonical Post-AGB (P-AGB stars), an end result of the AGB. They are predominantly H burners, have larger thermal pulse cycle (TPC) phase and shorter lifetime. Post-early AGB and AGB-Manque stars have insufficient envelope mass to allow a full AGB phase, undergo slower evolution at lower luminosity compared to H burners Brown et al. (2000).

pPN winds

The circumstellar envelope that has been produced during the AGB phase detaches from the photosphere marking the initiation of the pPN phase. In this stage, a fast collimated wind evolves with velocities of several $100\,\mathrm{km\,s^{-1}}$ emanating from the stellar core Bujarrabal et al. (2001). The cause of

Table 1.1: AGB stars classification, camposition and lifetime by Brown et al. (2000)

Star	M ($M_\odot$)	t (yr)	Shell
P-AGB	$0.8 \sim 8$	$10^3 \sim 10^4$	H burners
PE-AGB & AGB Manque	< 2	$10^4 \sim 10^5$ & $10^6 \sim 10^7$	He burners

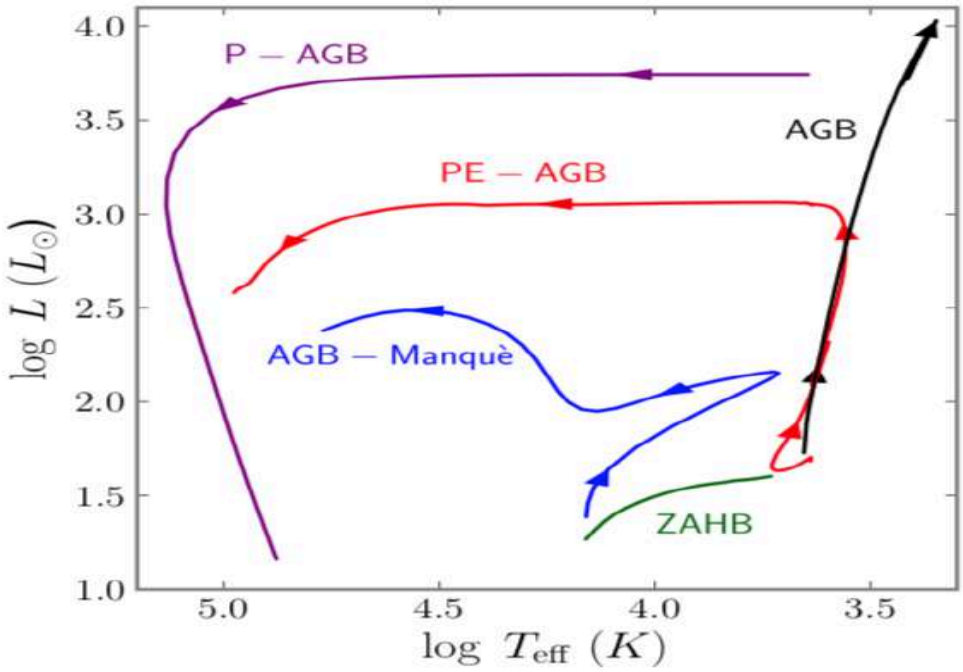

Figure 1.8: Sample stellar evolutionary tracks by Bressan et al. (2012) showing hot HB stars and their progenies' placement on H-R diagram. The P-AGB track is taken from Vassiliadis & Wood (1994) H-burning tracks for a mass of 0.597 $M_\odot$ and Z=0.016.

the driving engine of the CFW is unclear and is discussed in Section 1.3.1. The interaction of fast pPN wind with previous surrounding AGB slow wind halo is believed to cause asymmetries in the remnant, resulting in a vast array of morphologies present in planetary nebulas. Temperatures of central stars of pPNs range between $4,000\,\mathrm{K} \sim 30,000\,\mathrm{K}$ with luminosity of $\sim 10^4\,L_\odot$. The range of pPN spectral types is between late G to early B with low surface gravity and luminosity class I surrounded by an expanding circumstellar envelope (CSE) of molecular gas and cool dust. The post-AGB stage is a very short period in stellar evolution $\sim 10^3$ years Ueta et al. (2000a), making these objects scarce, about ~ 100 pPNe are known Lagadec et al. (2011). Generally, pPNe exhibit a fast bipolar outflow embedded within a slow spherically symmetric wind from the AGB star Bujarrabal et al. (2001) kinematic parameters summarised in Table 1.2.

Like PNe, pPNe are composed of central stars and detached circumstellar envelopes of gas and dust, however, unlike PNe, their central stars are too cool ($T_{\mathrm{eff}} < 10^4\,\mathrm{K}$) to photoionize the envelopes Kwok (1993). Hence, succsessfully used techniques for PNe observations, such as spatial resolution imag-

Table 1.2: Typical pPN/ PN wind conditions

Wind	t_{wind}	U	M outflow	$\dot{M}$	Momentum	P/Lc
	yr	km/s	$M_\odot$	$M_\odot/yr$	g cm/s	erg/s
AGB Superwind	6×10^3	20	0.5	10^{-4}	2×10^{39}	10^{34}
pPN Collimated Fast Wind	$10^2 \sim 10^3$	50	0.5	5×10^{-4}	5×10^{39}	8×10^{35}
PN Slow	10^4	30	0.1	10^{-5}	6×10^{38}	3×10^{33}
PN Fast	10^4	2000	0.0001	10^{-8}	4×10^{37}	1.3×10^{34}

Kinematic parameters for AGB, pPN and PN winds from Bujarrabal et al. (2001). The comparative radius and timescales of PPN and PN is $\sim$ few $\times$ 10^{-1} pc, $\sim$ 10^3 yr and $\sim$ few pc, $\sim$ 10^4 yr respectively. AGB star scales are $R_* \sim$ few10^2 $M_\odot$ with lifetime of $\sim$ 10^6 yr and spherical expansion of U $\sim$ 10 km/s forming circumstellar envelope radius upto $\sim$ 10 pc.

ing of ionised gas lines or free-free radio continium do not reveal the structure of pPNe circumstellar envelopes. Instead, dust-sensitive techniques such as thermal emission at infrared wavelengths or scattering of visible light at optical wavelengths or neutral gas CO or OH mapping in radio is used.

Dust-driven outflow:

AGB stars have a lifetime of $\sim$ 1 Myr with wind velocities of 10 km s^{-1}, hence they form a circumstellar envelope CSE. In the pPN phase the CSE is a low-density spherical halo representing a remnant of the AGB wind. These AGB winds are driven by a combination of stellar pulsation and radiation pressure on dust grains. Grains drag the gas along via friction with radiative momentum of $L/c \sim \dot{M} \times U$, where U is the wind shell velocity. The outflows contain dusty, spherically expanding r^{-2} density profile at slow speeds but very large mass loss rates up to $\sim$ 10^{-4} $M_\odot$ yr^{-1}.

Collimated fast wind:

During the evolutionary transition between the AGB and post-AGB (pAGB) phase the morphology of circumstellar envelope (CSE) undergoes significant changes that require to be driven by a physical agent or agents that brake the spherical symmetry of the radiatively driven, dusty mass-loss phase. Faced with the complexity, organization and frequent presence of point symmetry in the morphologies of their survey PNs, Sahai et al. (1998) proposed that the primary agent for breaking spherical symmetry is a jet or collimated, fast $\sim 10^2$ km s^{-1}, $\dot{M} \sim 5 \times 10^{-6}$ $M_\odot$ yr^{-1} wind (CFW) operating during the early pAGB or late AGB evolutionary phase. The CFWs are likely to be episodic, and either change their directionality (i.e., wobbling of axis or precession) or have multiple components operating in different directions (quasi)simultaneously Sahai et al. (2011).

Planetary Nebula

Further on as the central star ejects its outer layers to form the cold pPN nebula, the core of the star is left behind. This is a relatively short ($\sim 10^4$ yr) phase of stellar evolution between the asymptotic giant branch and white dwarf stages (WD). At the end of post-AGB period the faint pPN reflection nebula becomes a bright emission nebula (PN) due to a strong ionising ultraviolet flux from the hot $10^4 \sim 10^5$ K central star. PN masses range from $0.1 \sim 1M_{\odot}$ with gas density of $\sim 10^3\,cm^{-3}$ and spatial extent of roughly 3 pc across. Back in the pPN phase, the radiation is not sufficient to dissociate the molecules, it is mainly shock waves that generate the near-IR emission. As stated by Davis et al. (2005), the pPN stage should generate more molecular emission relative to its successor the PN, since there is no extreme UV (EUV) to destroy the molecules. Upon reaching the PN stage, EUV generates the HII region and the subsequent emission nebula. The remnants of the electron-degenerate C/O cores developed by AGB progenitors represent the central stars of PNe with most of their hydrogen shell lost due to mass loss throughout the AGB phase. The energy produced is maintained with hydrogen shell burning with constant luminosity output during low to high temperature range across the H-R diagram. Eventually, the entire hydrogen envelope is utilised by a combination of nuclear burning and mass loss traced in Figure 1.2, the central stars gradually cool down, decrease their luminosity and become white dwarfs. This mechanism was described by Paczyński (1971), and was confirmed by detailed evolutionary tracks calculations by Schoenberner (1979) and Wood & Faulkner (1986) and summarised by Kwok (2008). Older PNs are prone to develop instabilities by interactions with the ambient interstellar medium (ISM), and are subjected to the passage of photoionization fronts. This leads to obscuration of the underlying symmetries and geometries imposed early on Sahai et al. (2011). The core mass is one of the key factors that determines the transition time between the AGB and PN stage. A high mass star evolves relatively fast whilst illuminating the nebula for a relatively short time, a low core mass star evolves too slowly to ionise the circumstellar nebula before it dissipates into the interstellar medium. The overall mass loss in the PN stage is a few orders of magnitude lower compared to $\dot{M}$ during the superwind of pPN stage Table 1.2, however it enriches the ISM with heavy elements such as carbon, nitrogen, oxygen and calcium. Due to bright emission spectra, PNs are detectable over large distances and are used to estimate distances to external galaxies. Consequently, not all stars that evolve past the AGB will become PNe Kwok (2008). Eventually the gas in PN is dispersed into space leaving behind a dense, dim white dwarf and the matter ejected by the PN forms new building blocks for the next generation of stars.

1.5 Shock-excited H_2 emission in PPN.

Observationally, the nebula surrounding the central star of pPN can be optically thin or thick, depending on the equatorial wind strength, discussed in more detail in Section 2.3. Optically thin, spherical pPN nebulas are observationally challenging due to the luminosity of the central star $\sim 10^4\,L_\odot$ being $\sim 10^3$ brighter than the reflected nebular light. Hence, most observationally viable pPNs are bipolar reflection nebulas where the central star is obscured by the optically thick torus of dust created by intense equatorial wind with two optically thin lobes of CFW perpendicular to the ring creating the bipolar structure. The surrounding envelope of gas and dust causes light reflection from the central star with effective temperature between $10^3 \sim 10^4$ K.

The abundance of nebular dust causes post-AGB stellar objects to be optically faint, however they emit strongly in the near-IR part of the spectrum due to the AGB molecular environment enveloping the star being shocked by the collimated fast pPN wind. The CFW or jets, operating during the proto-planetary or very late-AGB phase, are also the primary agent for shaping most Planetary Nebulae. Therefore, the properties of investigated post-AGB outflows are dependent on the nature of the interacting winds and the structure of the ambient medium. Observational studies have detected numerous molecular hydrogen envelopes surrounding post-AGB stars. Molecular ro-vibrational H_2 transitions with $\Delta v = 1, 2$ emit at near infrared wavelengths $\sim 2\mu$m located in the K-band. These ro-vibrational transitions become detectable due to fast collimated winds generating shock waves, that pass through the molecular environment. Molecular envelopes of H_2 have also been detected around PNe Jaminet et al. (1991). Protoplanetary nebula being the predecessor of PNe should have similar molecular envelopes and sustain a stable molecular environment due to relatively low surface temperature $T_* < 15,000\,K$ of the central star. pPN's are optically faint and emit strongly in near-IR (J-, H-, K-bands) due to excitation of molecular environment. Shock waves caused by winds interacting with molecular medium act as excitation source, triggering the ro-vibrational energy transitions of H_2 molecule. This process is followed by cooling via collisional de-excitation with ro-vibrational transition energies corresponding to emission in the near-infrared band. Numerous H_2 detections in post-AGB stars have been confirmed Riera et al. (2003).

1.6 Dust and Chemistry from the AGB to PN phase.

The process of re-ignition of the He burning shell at early AGB phase and subsequent re-ignition of H burning shell at TP-AGB phase leads to formation of circumstellar envelopes with rich atmospheres of nuclear processed matter Lagadec et al. (2005). C-rich stars have envelopes composed mainly of

amorphous carbon while O-rich stars have circumstellar envelopes rich in silicates. These envelopes undergo a further chemical transition into more complex organic molecules and inorganic solid-state compounds. In general, stars in a short transitional AGB-PN phase that lasts between 10^2 sim10^4 years undergo a process of crystallisation or aromatisation forming crystalline (O-rich) Figure 1.9 and aromatic (C-rich) Figure 1.10 structures. Therefore, these type of stars serve as laboratories for astrochemistry, providing constrains on the gas-phase and solid state chemical models obtained by observational studies García-Hernández & Manchado (2016). The detection of pre-Solar grains in meteorites as well as high deuterium to hydrogen ratio in dust Messenger (2000) supports stellar-Solar System hypothesis stating that the Solar System objects contain primordial material that have been delivered to the solar nebula from stars.

The evolution of the CSE depends mainly on the star's chemistry i.e the C/O ratio. The C-rich AGB C/O > 1) stars show amorphous carbon and organic solids with mixed aromatic/aliphatic structures i.e kerogen and coal that provide strong dust emission. In the very late stages of AGB evolution, a star develops a super-wind with extreme mass loss. The gas in the stellar wind condenses as it cools away from the star, forming molecules such as water H_2O and silicon monoxide SiO. This can form grains of dust, mostly silicates, which obscure the star at shorter wavelengths, leading to a strong infrared source. Hydroxyl (OH) radicals can be produced by photodissociation or collisional dissociation. H_2O and OH can both be pumped to produce maser emission. OH masers in particular can give rise to a powerful maser action at 1612 MHz and this is regarded as a defining feature of the OH/IR stars that are unusually bright at near-infrared wavelengths. Many other AGB stars such as Mira variables show weaker OH masers at other wavelengths, such as 1667 MHz or 22 MHz.

C rich stars in post-AGB phase are renown for the unique 21 μm feature that has not been seen elsewhere in the ISM that is either due to a solid substance or many other possible candidates such as amorphous carbon (HAC) grains, nanodiamonds, hydrogenated fullerenes, and TiC nanoclusters . The detection of these C bearing compounds suggests that complex organic molecules are formed over the short PPN lifetime and is believed to onset at the late AGB phase with formation of acetylene. A 30 μm feature is also common for C rich PPN with a carrier being either solid MgS with an alternative being a carbonaceous material Kwok (2004). In general C-rich PPN show molecular absorption bands of C_2, C_2 and CN.

O rich PPN show more restricted chemistry and are identified by the presence of the 9.7 μm and 18 μm amorphous silicate feature. Olivine and pyroxene crystalline silicates have also been found. The 9.7 μm feature in PPN is much less prominent compared to AGB stars due to the decline in dust

temperature. Both PPN and PN contain strong infrared features at 3.3, 6,2, 7.7, 8.6, and 11.3 μm that is attributed to aromatic $C-H$, $C-C$ bends and stretches, known as the aromatic infrared bands (AIB), however these features first emerge in PPN. The AIB bands undergo a chemical evolution throughout the PPN stage. The evolution results in the weakening of the 3.3 and 6.9 μm features suggesting a change from aliphatic to aromatic structures, that is a consequence of photochemistry where the onset of UV radiation at PN stage results in bond migrations and transformation into ring systems. On the other hand, the weakening of 12.1, 12.4 and 13.3 μm is a result of hydrogen loss that results in aromatic rings that are more stable compared to alkanes or alkenes.

1.7 Science Goals

Overall, pPN presents a broad range of investigations and are characterised by massive molecular and dust shells that are the result of AGB mass loss Kwok (1993). Within the extended circumstellar envelope, observational studies have revealed kinematics of the molecular outflows locating high velocity bipolar flows reaching up to $100\,\mathrm{km\,s^{-1}}$ Olofsson & Nyman (1999). CO emission observations detected large quantities of molecular gas ranging between $0.1 \sim 1\,\mathrm{M_\odot}$ Bujarrabal & Pardo (2007) in a large fraction (2/3) of investigated pPNe. The emission of thermal dust and reflected star light from Protoplanetary Nebula uncover an observational window at submillimetre, millimetre and centimetre wavelengths, revealing properties such as kinematics of winds, spacial distribution of material and dust grain properties. The resulting features of investigated post-AGB outflows are dependent on the nature of the interacting winds and the structure of the ambient medium. Observational studies have detected numerous molecular hydrogen envelopes surrounding post-AGB stars. Molecular ro-vibrational H_2 transitions occur at near infrared wavelengths $\sim 2\mu$m located in the K-band and become detectable due to excitation source. In case of fast collimated winds, the transition is caused by passing shock waves.

The main characteristics of fast shocks is their ability to dissociate the H_2 that is in high abundance surrounding the post-AGB stars. In this research we modify version 3.5 of ZEUS-3D (dzeus35) fluid code with molecular chemistry that is described by the first three reactions of collisional dissociation in the Appendix B by Smith & Rosen (2003). The collisional dissociation rates for chemical reactions is determined by Shapiro & Kang (1987). A semi-implicit cooling chemistry step is employed to calculate the temperature and the molecular H_2 fraction taking place in those dissociative reactions. The collisional de-excitation rates for resultant line emission is provided by Lepp & Shull (1983); Shull & Beckwith (1982); Hollenbach & McKee (1979). The internal energy equation has been altered

to include an additional cooling term by Shapiro & Kang (1987) from the dissociation of molecular hydrogen. Atomic recombination lines of [OI, Hα, [Si II] and [Fe II] were also generated based on rate coefficients by Reynolds (1989); Dong & Draine (2011); Reynolds (1989); Smith (1994b). The aim of this set-up was to re-create the near-infrared and optical emission lines of pPN by generating synthetic flux maps. The flux analysis at different wavelengths help quantify the origin of the resultant emission and may suggest selection criteria for new surveys. In order to generate the resultant maps, the research was based on two main components: the high resolution hydrodynamics by dzeus35 that enables to provide additional fine structure, accurate shock physics, that help trace expelled shell evolution for different chemical wind and ambient compositions. Second component is with molecular chemistry and cooling that casts macroscopic variables from high resolution radiative shocks that enables to generate synthetic flux maps and PV diagrams. There is a large combination of models discussed in detail here: (1) the wind ellipticity is varied through an anisotropic wind speed with plane-axis aspect (1) the wind ellipticity is varied through an anisotropic wind speed with plane-axis aspect ratios of 1:1, 1:2, and 1:4, (2) the axial speed of the wind is taken as slow $V_w = 80\,km\,s^{-1}$, medium $140\,km\,s^{-1}$, or fast $200\,km\,s^{-1}$, and (3) the wind and ambient medium can both either be molecular or atomic. In theory, the particular set up of the code enables us to simulate pPNe outflows and answer the following questions:

- Question: What is the cause of H_2 excitation on position, what is the trigger for its distribution in an elliptical shape?

  Method: An adequate wind shell resolution has been used to trace H_2 dissociation and shell fragmentation into radial cometary-shaped protrusions.

  Result: Formation of weak oblique shocks at all locations of protrusions yields a constant $2 \rightarrow 1\,S(1)/1 \rightarrow 0\,S(1)$ H_2 ro-vibrational line fraction that explains why molecular content is found at the beam of pPN outflows.

- Question: What are the timescales for dissociative molecular winds relative to pPNe outflow model?

  Method: Tracing the resultant molecular fraction relative to wind velocity, ellipticity and composition models using added molecular chemistry reactions evaluated with collisional dissociation rates.

  Result: Higher wind shell velocities are H_2 dissociative. Spherical model is most dissociative at

high wind velocities due to isotropic velocity field. Increase in ellipticity results in lower radial velocities and molecular fraction.

- Question: What is the contribution to emission produced by forward/backward shock?

  Method: Input density of ambient is configured to match the wind density at 1/2 of axial grid extent. This set-up enables the forward/backward shock to vary in strength. Molecular cooling based on collisional dissociation rates enables synthetic flux map generation and evaluation of line emission strength.

  Result: There is no significant dependence on model type after the initial blast. A range of wind speeds yields constant $2 \rightarrow 1\,\mathrm{S}(1)/1 \rightarrow 0\,\mathrm{S}(1)$ H_2 line ratio $0.1 \sim 0.2$ due to oblique shocks at all locations.

- Question: What is the hydrodynamic and spectroscopic difference between molecular and atomic wind models?

  Method: Evaluation and comparison of hydrodynamical and spectroscopic evolution of different wind models based on pressure (combined shocked layers), density(immediate shock front) and temperature diagrams coupled with synthetic emission line maps and PV diagrams. The 2D grid is configured with cylindrical geometry. This configuration enables to translate the distribution of 2D grid line flux values on to a cylindrical grid thus creating 'pseudo-3D' projection with the line of sight as a user variable.

  Result: The effect of strong molecular cooling in shocked zone promotes growth of protrusions that promote thermal and hydrodynamical instability. The shock surface in molecular models is not smooth but rough and broken down into a large total area of weak oblique shocks. The shock speed begins to oscillate and produce layers of strong cooling that propagate from the shock front toward the interface. The interaction layer between reverse and forward shock is almost twice as thick in molecular models compared to pure atomic H wind/ambient case due to stronger local pressure and density variations. Compressions, rarefactions and sub-shocks form protrusions in shape of fingers are formed in molecular models where cold dense layers are encompassed by warm regions with strong shocks confined to the tips. In case of pure atomic model with no H_2 present in wind and ambient, the gas corresponds more coherent to sudden changes, the shell is not fragmented, and is dominated by Rayleigh–Taylor instability resulting in irregular pattern containing knots and filaments within a slowly thickening turbulent layer.

- Question: What are the assumptions and code limitations of the numerical study?

  Limitations: When matching the numerical results to observations, limitations imposed on simulated physics and dynamics is taken into account in order to set the boundaries within which the generated results and the real data can be compared. One of such limitations is cylindrical symmetry that influences growth of perturbations and how fingers appear in projection. We also assume no background radiation and no photoabsorption, thus implying an optically thin medium.

- Question: Comparison to observations?

  Result: High line ratios between $0.3 \sim 0.5$ were detected in NGC 7662, and it was proposed that the emission is induced by UV from the central star. However the results computed in this work found that isolated hot shock zones can produce similar values at early stages of expansion. The molecular simulations here generate the same morphological structures of shell disintegration, similar to cometary shaped knots (CK) or dense globules found in high resolution images of the Helix and Fried Egg nebula. The presence of molecules in a dense, neutral globule has been observed in the Helix nebula and molecular formation has been investigated by Howe et al. (1994) and stating that instabilities that create large fragmentations in the shells remain into the PN phase. The work by Howe et al. (1994) suggests that the dusty 10^5 to $10^6\,\mathrm{km\,s^{-1}}$ cold $10 - 25\,\mathrm{K}$ clumps are in pressure equilibrium with the ionised gas. Therefore the molecules in these knots are shielded from photodissociation and stay intact despite the UV radiation.

  Conclusion: The specific case studied here corresponds to elliptical winds of high mass outflow into stationary, uniform, dense ambient medium. The proposition is that the shells must be temporary, otherwise if they stayed intact whilst expanding, the pressure would drop and the shell material would be subjected to the radiation from the ISM leading to dissociation of complex chemistry. The results from this research suggest that partially molecular shells are not uniform, they disintegrate into protruding fingers and loose their integrity. The H_2 is conserved due to shell disintegration and formation of weak oblique shocks that partially dissociate molecular content at the tips of cometary shaped protrusions. This is in contrast with warm atomic shells that remain intact. This provides vital clues about how carbon and other heavy materials are transferred and re-used in Universe. Our civilisation happens to exist where the generation of recycled material is at its highest. This is probably no coincidence.

1.8 Thesis Outline

In this thesis we present numerical studies of interaction of winds with molecular environment present in Protoplanetary nebulas.

Chapter 1: Post-AGB Stars and Winds

Description of low-to intermediate mass stars evolution and science goals.

Chapter 2: Physics and Morphology of PPN outflows

Shock waves & emission sequence, GISW model, PPN morphology, spectroscopy and galactic distribution.

Chapter 3: Wind Parameters & Code Adaptations

Description of radiative loses via cooling mechanisms, algorithm implementation with ZEUS-3D.

Chapter 4: Molecular Cooling & Atomic Recombination

Summary of K-band and optical integration routines.

Chapter 5: Hydrodynamical & Line Emission Study

Results of molecular fractions and integrated emission PV maps.

Chapter 6: Discussion

Chapter 7: Conclusions & Future work

Appendix A: pPNe mass-loss model parameters

Appendix B: List of cooling rates

Appendix C: Equations of hydrodynamics

Appendix D: 2D cross-sectional distributions of pPNe

Bibliography

Figure 1.9: IRAS 09371 + 1212 known as Frosty Leo Nebula, unusually located at 900 *pc* above the plane of the Galaxy in the constellation of Leo, unique due to deep ice absorption band near 3.1 μm Geballe et al. (1988). The picture is a combination of 606 nm optical and 814 nm infrared band. Image credit ESA/Hubble & NASA.

Figure 1.10: CRL 618, IRAS 04395 + 3601, the central star is concealed by the nebula, and is ejecting dense molecular gas with a terminal velocity of $\sim 200\,\mathrm{km\,s^{-1}}$ Cernicharo et al. (1989). The picture includes combination of exposures of 547 nm, 606 nm, 673 nm, 658 optical and 953 nm infrared spectrum, showing the dim glow coming from the elements in the cloud. Image credit ESA/Hubble & NASA.

Chapter 2

Physics and Morphology of PPN outflows

2.1 Shock wave & Emission sequence

K-band H_2 emission, presented in this work is computed with collisional de-excitation scenario driven by J-shock environment. The shocked outflows reveal the pPN nebula via molecular emission in the near-infrared band. A common physical phenomena in the interstellar medium is shock waves, which is a consequence of supersonic motion that exceeds the velocity of sound in the surrounding medium. This results in the upstream material not being able to respond dynamically to the shocked material before it arrives. The physical conditions for shock are derived from a rapid change in gas macroscopic properties: pressure, density, and temperature. The shocked medium undergoes compression, heating and acceleration. The post-shock cooling is carried through emission of line photons, which further compresses the medium. Shock waves were first experimentally investigated around 1886 by Ernst Mach who derived the Mach angle equation

$$\sin\alpha = \frac{c_s}{v},\ v > c_s, \tag{2.1}$$

where v is the velocity of the shocked material, c_s is the speed of sound in the surrounding medium, α is the opening angle of the resulting bowshock if $v > c_s$. Figure 2.1 shows a propagating sound wave travelling at different velocities. Upon exceeding the threshold value of the sound speed, the sinusoidal pattern is destroyed, resulting in a discontinuity, or simply a shock wave. An increase in entropy occurs over a nearly infinitesimal region. The region itself

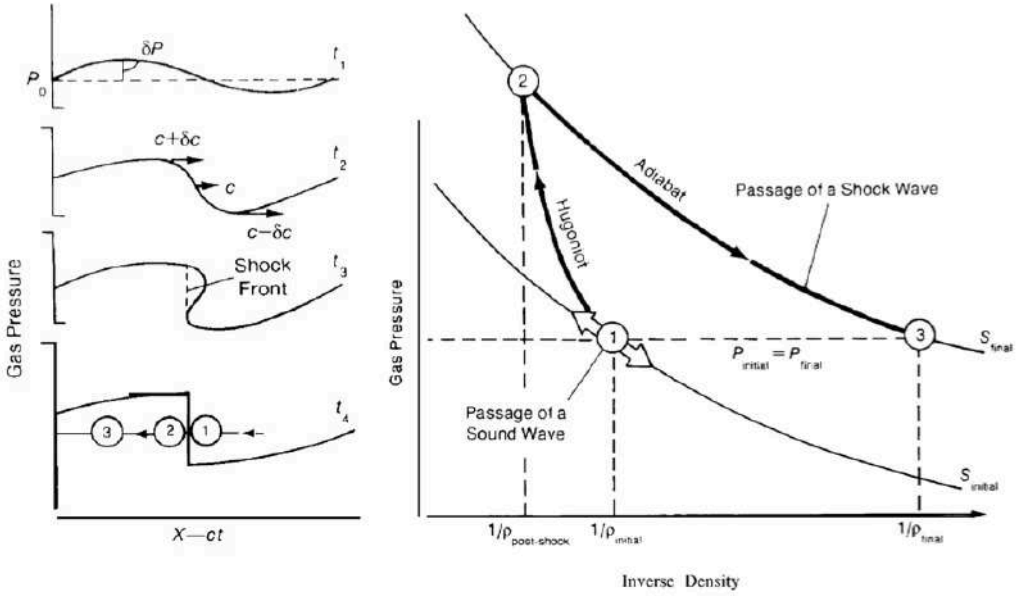

Figure 2.1: Left: Creation of a shock wave. Right: Pressure versus $1/\rho$ plot, regions 1, 2 and 3 correspond to the labelled time t_1, t_2, t_3 positions Norman & Winkler (1985).

is constructed with a control volume established around the shock wave with two distinct zones allocated as: post and pre-shock sides. Upon receiving thermal energy, particles move to an adiabat of higher energy. This process is governed by the relationship between the two states on both sides of the shock wave, the Rankine-Hugoniot jump conditions. The interstellar shocks are split into two types: Jump J-shocks and Continuous C-shocks.

2.2 J-Shock

In case of fast J-Shocks, the gas is subjected to a sudden halt and is heated to high temperature. As a result, insignificant radiative cooling and non-radiative relaxation can take place. This results in the shock front being much thinner compared to the post-shock relaxation layer. The cooling time is much shorter than the evolution time, 1 or 10 years compared to $\sim 10^3$ years. Subsequently, the thickness of shock is small compared to hydrodynamical length scales. The equations of energy, momentum and mass are cast in terms of jump conditions that relate the pre-shock and post-shock quantities of velocity, density and temperature. Assuming homogeneous conditions upstream and steady injection flow, i.e no slowing down of gas as it flows through the post-shock cooling zone. The equations of mass, momentum and energy take form of jump Rankine-Hugoniot conditions, relations that hold at a discontinuity or i.e abrupt change. Starting with the conservation of mass flux or continuity, i.e the mass flow per unit area must hold over the control volume that includes the shock. Effects of viscosity are negligible on the scales larger than the mean free path, hence the jump conditions do not include viscosity terms. Considering

a propagating shock wave in the rest frame of the shock i.e contact discontinuity, the unshocked ambient gas ρ_a approaches from the positive radial direction with velocity $V_w - U$ as presented in Figure 3.3 moving faster than its sound speed and passes through the shock.

- Pre-shock conditions: $\rho_0 = \rho_a, \quad v_0, \quad \mathrm{T}_0 = \mathrm{T}_\mathrm{a}, \quad P_0 = P_a.$
- Post-shock condition: $\rho_1 > \rho_0, \quad v_1 < v_0, \quad T_1 > T_0.$

In a reference frame of the terminal shock, the mass conservation

$$\rho_0 v_0 = \rho_1 v_1, \qquad \left[\mathrm{gm\,cm^{-2}\,s^{-1}}\right] \tag{2.2}$$

The incoming ambient material approaches the contact discontinuity with wind shell speed U, as presented in Figure 3.3, hence the pre-shock gas velocity becomes

$$v_0 = V_w - U \qquad \left[\mathrm{cm\,s^{-1}}\right] \tag{2.3}$$

where velocities are measured in the reference frame of the terminal shock, hence V_w is the unshocked wind input velocity and V_w is the forward shock wind velocity. The mass entering the shock front per unit time has momentum $(\rho_0 v_0)v_0$ and will emerge with momentum $(\rho_1 v_1)v_1$. Conservation of momentum results in

$$\rho_0 {v_0}^2 + P_0 = \rho_1 {v_1}^2 + P_1, \qquad \left[\mathrm{gm\ cm^{-1}\,s^{-2}}\right] \tag{2.4}$$

The force over unit of area, i.e the pressure of the shock front is P. The overall pressure term is the sum of magnetic $\mathrm{B}^2/8\pi$, thermal $\rho\mathrm{kT}/\mu$, where μ is the mean mass, and other pressure terms (cosmic rays, etc). This work considers only the contribution from the thermal component and ignores other pressure terms (no ambipolar diffusion from magnetic fields), therefore setting up the condition to accommodate a J-shock transition. The energy flux conservation concludes a set of Rankine-Hugoniot conditions, where the energy E_0 of the gas entering the shock front per unit area and per unit time is

$$E_0 = \rho_o v_0 \left(\frac{1}{2}{v_0}^2 + \frac{1}{\gamma - 1}\frac{P_o}{\rho_0}\right), \qquad \left[\mathrm{erg\,cm^{-2}\,s^{-1}}\right] \tag{2.5}$$

the first and second bracketed terms stand for the kinetic and internal energy density respectively Equation 2.24, both per unit mass. The energy difference is equal to the work done per unit

area by the shock front (cooling is unimportant)

$$E_1 - E_0 = P_0 v_0 - P_1 v_1, \tag{2.6}$$

rearranging for the final form of energy conservation

$$\left(\frac{1}{2}v_0^2 + \frac{e_0}{\rho_0} + \frac{P_0}{\rho_0}\right) = \left(\frac{1}{2}v_1^2 + \frac{e_1}{\rho_1} + \frac{P_1}{\rho_1}\right) \tag{2.7}$$

For an ideal gas, the internal energy per unit volume is, i.e internal energy density

$$e = \rho u_{sp} = \frac{P}{(\gamma - 1)} \qquad \left[\mathrm{erg\,cm^{-3}}\right] \tag{2.8}$$

and u_{sp} is internal energy per unit mass, i.e specific. It is possible to express the post-shock values in terms of pre-shock input parameters. Beginning with the expression for pre and post-shock velocity components in terms of thermodynamic variables and combining equations of mass and momentum to rearrange for v_j

$$v_j^2 = \frac{1}{\rho_j^2}(P_1 - P_0)\left(\frac{1}{\rho_0} - \frac{1}{\rho_1}\right)^{-1}, \qquad \left[\mathrm{cm^2\,s^{-2}}\right] \tag{2.9}$$

the subscript $j = 0 \,\mathrm{or}\, 1$. The above expression is substituted into energy equation to get the expression for pre/post shock thermodynamic variables

$$\frac{P_1}{P_0} = \frac{(\gamma - 1)\rho_0 - (\gamma + 1)\rho_1}{(\gamma - 1)\rho_1 - (\gamma + 1)\rho_0} \tag{2.10}$$

and equivalently,

$$\frac{e_1}{e_0} = \frac{(\gamma - 1)P_1 - (\gamma + 1)P_0}{(\gamma - 1)P_0 - (\gamma + 1)P_1} \tag{2.11}$$

Defining the Mach number of the shock

$$\mathcal{M} = \frac{v_0}{c_{s,0}} \tag{2.12}$$

The equation above is used to eliminate ρ_1 in the expression for velocity ${v_0}^2$

$$\frac{P_1}{P_0} = \frac{2\gamma}{\gamma + 1}\mathcal{M}^2 - \frac{\gamma - 1}{\gamma + 1}, \tag{2.13}$$

rearranging in terms of densities

$$\frac{\rho_0}{\rho_1} = \frac{\gamma - 1}{\gamma + 1} + \frac{2}{\gamma + 1}\frac{1}{\mathcal{M}^2} \tag{2.14}$$

Together these conditions imply the temperature relation

$$\frac{T_1}{T_0} = \frac{[(\gamma - 1)\mathcal{M}^2 + 2][2\gamma\mathcal{M}^2 - (\gamma - 1)]}{(\gamma + 1)^2\mathcal{M}^2} \tag{2.15}$$

For the strong shock limit with M $\gg$ 1, the jump conditions for mono-atomic gas with $\gamma = 5/3$ become

$$\frac{\rho_1}{\rho_0} = \frac{\gamma + 1}{\gamma - 1} \rightarrow 4, \tag{2.16}$$

$$P_1 = \frac{2}{\gamma + 1}\rho_0 {v^2}_0 \rightarrow \frac{3}{4}\rho_0 {v^2}_0 \qquad \left[\mathrm{erg\,cm^{-3}}\right] \tag{2.17}$$

the velocity

$$v_1 = \frac{1}{4}v_0 \qquad \left[\mathrm{cm\,s^{-1}}\right] \tag{2.18}$$

the post-shock temperature

$$T_1 = \frac{2\gamma(\gamma - 1)}{(\gamma + 1)^2}T_0\mathcal{M}^2 = \frac{2(\gamma - 1)}{(\gamma + 1)^2}\frac{\mu}{k}{v^2}_0 \qquad \left[\mathrm{K}\right] \tag{2.19}$$

Post-shock pressure component

$$P_1 = \frac{3}{4}{v_0}^2\rho_0 \tag{2.20}$$

Tielens (2005). Properties of shocks:

- In case of pure diatomic gas for example H_2, the specific heat ratio is $\gamma = 7/5$ as $\mathcal{M} \rightarrow \infty$, the gas maximum compression ratio is $\rho_2/\rho_1 = 6$.
- The Mach number before and after the shock is such that $M_1 > 1$ and $M_2 < 1$ respectively.
- A parcel of gas subjected to shock increases its entropy, making it an exclusive region in space where gas parcels undergo entropy increase.

Entropy is a measure of a system's thermal energy per unit temperature that is unavailable for doing useful work. Work is obtained from ordered molecular or atomic motion, therefore the amount of entropy is also a measure of the molecular/atomic disorder, or randomness of a system.

2.3 GISW Model

The fast/slow PN outflows are described in theory by the Generalized Interacting Stellar Winds model (GISW) that was also applied to pPN winds and resulted in mismatch with observational data due to momentum excess. The depiction of the problem in GISW is set with the fast stellar wind interacting with an outer slower wind, enabling the development of two layers of shocked gas separated by a contact discontinuity. To simplify the solution of the set of hydrodynamics equations, the rate of mass loss is a constant quantity for each wind. The solution to the hydrodynamic equations for a blast wave with a leading shock front was considered by Parker (1961), Chevalier & Imamura (1983) deriving self-similar solutions for a $\rho \propto \mathrm{r}^{-2}$ wind density profile.

The mass-loss rate driven by supersonic spherical outflows in AGB stars reaches up to $\sim 10^{-4}\,\mathrm{M}_{\odot}\,\mathrm{yr}^{-1}$ Mamon et al. (1988) and is characterised by dusty, slow wind of the outer shell, expanding at $10 \sim 16\,\mathrm{km\,s}^{-1}$ Loup et al. (1990) yielding common expansion velocity profile values for an AGB's circumstellar envelope. Within the CSE, there is a region of the CFW moving at $\sim 10^{3}\,\mathrm{km\,s}^{-1}$ and a lower mass-loss rate of $10^{-6}\,\mathrm{M}_{\odot}\,\mathrm{yr}^{-1}$ Huarte-Espinosa et al. (2012). The resulting pPNe is formed when the fast collimated wind catches up with previously ejected slow AGB wind, driving a shocked shell through it as shown in Figure 2.2.

The region of interaction between the radiatively driven AGB wind and CFW moves at constant velocity Chevalier & Imamura (1983). The process of interaction is characterised with self-similar solutions that determine the velocity of the shell and thickness of interacting winds. The solutions of this type derive a number of properties present in pPN, in particular the existence of molecular gas.

Assuming a set up for singular wind with spherical symmetry about the centre of the star with radial velocity distribution and neglecting stellar gravitational field, the equations of hydrodynamics by Parker (1961) in spherical form of momentum, continuity and energy are

$$\frac{du}{dt} + u\frac{du}{dr} = -\frac{1}{\rho}\frac{dp}{dr} \qquad \left[\mathrm{cm\,s}^{-2}\right] \tag{2.21}$$

$$\frac{d\rho}{dt} + \frac{1}{r^2}\frac{d}{dr}(r^2\rho u) = 0 \qquad \left[\mathrm{gm\,cm}^{-3}\,\mathrm{s}^{-1}\right] \tag{2.22}$$

$$\frac{dp}{dt} + u\frac{dp}{dr} = \gamma\frac{p}{\rho}\frac{d\rho}{dt} \qquad \left[\mathrm{gm\,cm}^{-1}\,\mathrm{s}^{-3}\right] \tag{2.23}$$

Where u is the radial velocity, density ρ, and pressure p and γ is the specific heat ratio. By

integrating the first law of thermodynamics for internal energy per unit mass u_{sp},

$$u_{sp} = \frac{p}{\rho}\frac{1}{\gamma - 1} \qquad \left[\mathrm{erg\,gm^{-1}}\right] \tag{2.24}$$

the total energy density E of gas becomes

$$E = \frac{1}{2}u^2\rho + \frac{p}{\gamma - 1} \qquad \left[\mathrm{erg\,cm^{-3}}\right] \tag{2.25}$$

Two stellar outflows form an interacting winds structure that is characterised by $\dot{\mathrm{M}}_2$, v_2, c_2 for fast wind and $\dot{\mathrm{M}}_1$,v_1, and c_1 for slow wind. Where c_1 and c_2 are the gas sound speeds. The density of the wind is described with $\mathrm{A}_1\mathrm{r}^{-2}$ and $\mathrm{A}_2\mathrm{r}^{-2}$ for outer and inner winds respectively, where $\rho\mathrm{A} = \dot{\mathrm{M}}/\mathrm{v}$. The two layers of shocked gas separated by a contact discontinuity at $\mathrm{R_c}$ is caused by the interaction of a fast, tenuous wind and outer, slower dense wind. This kind of discontinuity is called a shock. The explication of this problem structure is governed by self-similar solutions. For shock waves in a perfect gas, the jump conditions by Chevalier & Imamura (1983) are

$$\Omega(\eta) = \frac{\rho_2}{\rho_1} = \frac{v_1}{v_2} = \frac{(\gamma+1)\mathcal{M}_1^2}{(\gamma-1)\mathcal{M}_1^2 + 2} \tag{2.26}$$

where $\mathcal{M}_1 = |\mathrm{v}_1|/\mathrm{c}_1$ and $\mathcal{M}_2 = |\mathrm{v}_2|/\mathrm{c}_2$ are the Mach numbers of the pre, and post-shock regions.

$$P(\eta) = \frac{P_2}{P_1} = \frac{2\gamma\mathcal{M}_1^2 - \gamma + 1}{\gamma(\gamma+1)} \tag{2.27}$$

the Mach number $\mathcal{M}_\in$ in terms of $\mathcal{M}_\infty$

$$\mathcal{M}_1 = \frac{s_1 - u_1}{c_1} = u_1/c_1\left(\frac{1}{b_1} - 1\right) \tag{2.28}$$

$$\mathcal{M}_2^2 = \frac{2 + (\gamma-1)\mathcal{M}_1^2}{2\gamma\mathcal{M}_1^2 - (\gamma-1)} \tag{2.29}$$

$$U(\eta) = \frac{T_2}{T_1} = 1 - (1 - b_1)\frac{2\gamma\mathcal{M}_1^2 - \gamma + 1}{\gamma(\gamma+1)} \tag{2.30}$$

and $\mathrm{b}_1 = \mathrm{v}_1/\mathrm{s}_1$, s_1 is the velocity of the outer shock. The equations of hydrodynamics can be represented by a system of ordinary differential equations ODE's for P, U as functions of η. These conditions above enable the similarity equations to be integrated to the contact discontinuity (subscript c), where $\mathrm{U}(\eta_\mathrm{c}) = 1$. The variables of similarity for progressive wave treatment are established by Courant & Friedrichs (1948) along with the boundary conditions from Landau &

Lifshitz (1959).

$$\eta = tr^{-\lambda} = t/r \tag{2.31}$$

$$\rho = Ar^{-2}\Omega(\eta) \tag{2.32}$$

$$v = \frac{r}{t}U(\eta) \tag{2.33}$$

$$p = At^{-2}P(\eta) \tag{2.34}$$

$$C^2(\eta) = \gamma\frac{P(\eta)}{\Omega(\eta)} \tag{2.35}$$

In the simulations generated in this work, we start off with the supersonic outflow i.e the collimated fast wind that gets shocked, and expands into uniform ambient medium which is stationary. This numerical set up does not involve self-similar solutions, with $b_1 = 0$, representing a thick shocked layer. However, a more realistic simulation of pPN environment requires an inclusion of a AGB wind that is followed by the collimated fast wind leading to the interaction region between the two winds with each wind characterised by a constant mass loss rate. Hence, the next step to undertake in this research is the injection of an interacting CFW with AGB wind.

2.4 Wind launching mechanism.

The interaction of post-AGB jets colliding with slowly expanding AGB halo around central stars leads to extreme change in spherical morphology of envelopes, forming multipolar or bipolar lobes. The above shaping mechanisms have been checked by observing many bipolar pPNs in optical Hrivnak et al. (2000), infrared (IR) Kelly & Hrivnak (2003), and radio wavelengths Deacon et al. (2004), and tested by hydrodynamical simulations Huarte-Espinosa et al. (2012).

2.4.1 Radiation pressure vs Observed.

The fast pPN winds require energy and a driving mechanism to transfer energy into collimated outflows. Radiation pressure that drives the AGB wind cannot be a source of energy for CFW in PPN. 21/23 pPNs investigated by Bujarrabal et al. (2001), in CO presented in Table 2.1 show linear momentum Π excess carried by molecular outflows, in some cases $\sim 10^3$ greater than predicted by GISW, which assumes a radiation driven wind. The momentum carried by the outflow in terms of the winds shell velocity U and outflow mass M is

$$\Pi = \mathrm{MU} \qquad \left[\mathrm{gm\,cm\,s^{-1}}\right] \tag{2.36}$$

source	mass $M(M_\odot)$	momentum $P(\mathrm{g\,cm\,s^{-1}})$	kinetic energy $E(\mathrm{erg})$	$\frac{P}{L/c}$ (yr)	comments
Red Rectangle					$L/c = 4.0 \times 10^{33}\ \mathrm{g\,cm\,s^{-1}\,yr^{-1}}$
fast outflow	5.2×10^{-5}	1.5×10^{35}	1.2×10^{41}	38	peculiar dynamics, underestimate?
IRAS 07134+1005					$L/c = 5.4 \times 10^{34}\ \mathrm{g\,cm\,s^{-1}\,yr^{-1}}$
no fast outflow detected		$<1.9 \times 10^{38}$		$<3.5 \times 10^{3}$	
OH 231.8+4.2					$L/c = 4.0 \times 10^{34}\ \mathrm{g\,cm\,s^{-1}\,yr^{-1}}$
fast outflow	0.22	3.9×10^{39}	2.2×10^{46}	10^{5}	well studied, conspicuous bipolar flow
Hen 3–401					$L/c = 1.5 \times 10^{34}\ \mathrm{g\,cm\,s^{-1}\,yr^{-1}}$
fast outflow?	>0.01?	$>9 \times 10^{37}$?	$>3 \times 10^{44}$?	$>6 \times 10^{3}$?	poor data, uncertain analysis
Roberts 22					$L/c = 1.2 \times 10^{35}\ \mathrm{g\,cm\,s^{-1}\,yr^{-1}}$
fast outflow	>0.018	$>2.2 \times 10^{38}$	$>9.2 \times 10^{44}$	$>1.8 \times 10^{3}$	probable underestimate, unique component
HD 101584					$L/c = 1.2 \times 10^{34}\ \mathrm{g\,cm\,s^{-1}\,yr^{-1}}$
fast outflow	0.1	1.5×10^{39}	10^{46}	1.3×10^{5}	well studied, conspicuous bipolar flow
Boomerang Nebula					$L/c = 1.2 \times 10^{33}\ \mathrm{g\,cm\,s^{-1}\,yr^{-1}}$
fast outflow	1.9	6.2×10^{40}	5.1×10^{47}	5×10^{7}	outer shell, spherical?
fast outflow	$\gtrsim$0.07	$\gtrsim 5 \times 10^{38}$	$\gtrsim 9 \times 10^{44}$	$\gtrsim 4 \times 10^{5}$	inner shell, spherical?
He 2–113					$L/c = 2.0 \times 10^{34}\ \mathrm{g\,cm\,s^{-1}\,yr^{-1}}$
fast outflow	$>5.5 \times 10^{-3}$	$>4.1 \times 10^{37}$	$>8.7 \times 10^{43}$	$>2 \times 10^{3}$	probable underestimate, uncertain analysis
Mz–3					$L/c = 2.3 \times 10^{34}\ \mathrm{g\,cm\,s^{-1}\,yr^{-1}}$
no fast outflow detected					poor limit, only ^{12}CO $J = 2$–1
M 2–9					$L/c = 2.2 \times 10^{33}\ \mathrm{g\,cm\,s^{-1}\,yr^{-1}}$
no fast outflow detected		$<1.2 \times 10^{36}$		$<5.5 \times 10^{2}$	
CPD –568032					$L/c = 2.1 \times 10^{34}\ \mathrm{g\,cm\,s^{-1}\,yr^{-1}}$
fast outflow	0.043	6.1×10^{38}	2.7×10^{45}	2.9×10^{4}	
IRAS 17150–3224					$L/c = 4.4 \times 10^{34}\ \mathrm{g\,cm\,s^{-1}\,yr^{-1}}$
no fast outflow detected					poor limit, only ^{12}CO $J = 2$–1
OH 17.7–2.0					$L/c = 1.2 \times 10^{34}\ \mathrm{g\,cm\,s^{-1}\,yr^{-1}}$
no fast outflow detected					poor limit, only ^{12}CO $J = 2$–1
R Sct					$L/c = 1.6 \times 10^{34}\ \mathrm{g\,cm\,s^{-1}\,yr^{-1}}$
no fast outflow detected		$<6.6 \times 10^{35}$		<41	
M 1–92					$L/c = 4.0 \times 10^{34}\ \mathrm{g\,cm\,s^{-1}\,yr^{-1}}$
fast outflow	0.7	3×10^{39}	7×10^{45}	8×10^{4}	well studied, conspicuous bipolar flow
IRAS 19475+3119					$L/c = 5.1 \times 10^{34}\ \mathrm{g\,cm\,s^{-1}\,yr^{-1}}$
fast outflow	>0.026	$>1.6 \times 10^{38}$	$>2.8 \times 10^{44}$	$>3.1 \times 10^{3}$	probable underestimate
IRAS 20000+3239					$L/c = 2.2 \times 10^{33}\ \mathrm{g\,cm\,s^{-1}\,yr^{-1}}$
no fast outflow detected					poor limit, only ^{12}CO $J = 2$–1
IRAS 20028+3910					$L/c = 2.7 \times 10^{34}\ \mathrm{g\,cm\,s^{-1}\,yr^{-1}}$
fast outflow	$>4.1 \times 10^{-3}$	$>2.6 \times 10^{37}$	$>4.3 \times 10^{43}$	$>10^{3}$	probable underestimate
IRAS 21282+5050					$L/c = 2.1 \times 10^{34}\ \mathrm{g\,cm\,s^{-1}\,yr^{-1}}$
fast outflow	0.2	5.8×10^{38}	4.2×10^{44}	2.8×10^{4}	
IRAS 22223+4327					$L/c = 1.5 \times 10^{33}\ \mathrm{g\,cm\,s^{-1}\,yr^{-1}}$
fast outflow	$>4 \times 10^{-4}$	$>2.3 \times 10^{36}$	$>3.5 \times 10^{42}$	$>1.5 \times 10^{3}$	probable underestimate, uncertain analysis
IRAS 22574+6609					$L/c = 6.1 \times 10^{32}\ \mathrm{g\,cm\,s^{-1}\,yr^{-1}}$
no fast outflow detected		$<1.5 \times 10^{37}$		$<2.4 \times 10^{4}$	poor limit

Table 2.1: Calculation of the mass, momentum and kinetic energy for the sources observed in CO by Bujarrabal et al. (2001).

A photon energy divided by the speed of light corresponds to the light's momentum. The total momentum of photons emitted by a star per unit of time is equal to the stellar luminosity divided by the speed of light (L_*/c). The luminosity L_* emitted during the pPN lifetime Δt that corresponds to momentum is

$$(L_*/c)\Delta t \qquad \left[\mathrm{erg\,s^{-1}}\right] \tag{2.37}$$

An example, such momentum excess $\Pi \gg (L_*/c)\Delta t$, is observed in PPN M 1 − 92 with data from Table 2.1 that shows the momentum carried by the molecular outflow is $\sim 3 \times 10^{39}\,\mathrm{gm\,cm\,s^{-1}}$, the central star emits $L_* = 4 \times 10^{37}\,\mathrm{erg\,s^{-1}}$. Rearranging for PPN lifetime yields $\sim 4 \times 10^{34}\,\mathrm{gm\,cm\,s^{-1}}$ yearly momentum to be constantly supplied for $\sim 10^5$ years. In comparison, the dynamical wind

and stellar evolution times are $\sim 10^4$ yr for AGB, $\sim 10^3$ yr for PPN and $\sim 10^4$ yr for PN Kwok (2004). Assuming that overall pPN axial flows are the result of the acceleration model in (GISW) of slow AGB wind and collimated fast outflows with post-AGB material and outer AGB halo by shock interaction, radiation pressure would have to operate at much longer timescales Δt, than pPN lifetime to support the observed linear momentum Π by CO profiles, where most of the gas in pPNe outflow is in a cold molecular state of $10 \sim 20$ K as observed by molecular lines and a much smaller fraction of hot shocked gas observed in near-IR band. Hence, a radiation driven model is untenable as a source of pPNe outflows and other models such as the Magnetic Tower and Magneto-centrifugal launching (MCL) have been a topic for investigation.

2.4.2 Magnetic Tower & Magneto-centrifugal Launch.

Gas flowing from one component of the contact binary to another has a significant moment of rotation due to orbital motion. Therefore, gas particles cannot fall radially onto a star, instead, they move around it in Keplerian orbits. As a result of this motion, a gas disk is formed where the disk velocity distribution must correspond to Kepler's laws: layers located closer to the star will have higher velocities compared to outer layers. However, friction between the gas layers, leads to their velocities being equalized, with the inner layers transmitting part of their angular momentum to the outer layers. As a result, the inner layers approach the star and, ultimately, fall on its surface. In fact, the trajectories of individual gas particles have the form of spirals that twist toward the star. The Magneto-centrifugal Launch mechanism by Blandford & Payne (1982) describes a jet launch model where the outflow is launched from such an accretion disk with energy and angular momentum being removed from the disk with magnetic field lines that start at the disk surface and extend to large distances. Close to corona, the outflow is driven by gas pressure and magnetically dominated corona, whereas at large distances from the disk, the toroidal magnetic field collimates the outflow into a pair of jets propagating perpendicular to the disk. However, since the MCL model has been theoretically described and applied to a large number of 3D magnetohydrodynamic (MHD) simulations of accretion disks and astrophysical jets, the launching mechanism still remains controversial. Mainly due to the fact that MCL model requires large-scale magnetic fields permeating accretion disks. However, such fields are not evident in various astrophysical objects, and their origin is not well understood Kato (2007). Another mechanism, the magnetic tower is proposed by Lynden-Bell (1996) with the magnetic, not centrifugal force that drives and accelerates the flows. The magnetic tower is driven by strong magnetic pressure, that accelerates the outflow in the vertical direction and builds up a, so-called,

tower jet. This magnetic jet is derived from vertically inflating toroidal fields and consists of two component structure: a magnetic pressure dominated plasma threaded with poloidal fields (perpendicular to accretion disk) and the jet itself is surrounded by toroidal fields.

Another important quantity that arises from the momentum carried by the outflows is the timescales for post-AGB wind launching and post-AGB/AGB winds interaction. A study by Bujarrabal et al. (1998) for M 1 − 92 shows wind interaction lasted $\sim$ 100 yr with the upper limit of Δt PPN lifetime $\sim$ 900 yr . This along with the total mass deposited by the molecular outflow implies mass loss rates of $\sim 10^{-5}$ or $\sim 10^{-4}, \mathrm{M}_{\odot}\,\mathrm{yr}^{-1}$ may not be uncommon for PPN outflows Frank et al. (2018), and are used in this research.

2.5 Kinematic AGB-PPN Evolution

Throughout the AGB-PN stages there are three distinct outflow phases each characterised by mass loss rate and expansion velocity. The first phase is the AGB wind. Millimetre observations with CO lines provide quantitative results for systematic measurements of $\dot{\mathrm{M}}_{\mathrm{AGB}} \sim 10^{-5}\,\mathrm{M}_{\odot}\,\mathrm{yr}^{-1}$ in AGB stars showing mostly spherical and isotropic expansion of $\mathrm{V}_{\mathrm{exp}} \sim 5 - 25\,\mathrm{km\,s}^{-1}$ in CSE wind properties Hrivnak et al. (1989), Bujarrabal et al. (2001). The uniform wind temperature of 500 K represents the inner region of the envelope Huarte-Espinosa et al. (2012). Mass loss rates by AGB stars show a systematic increase as they evolve along the AGB track (both luminosity, size, and pulsational activity increase with time, while the core mass decreases). The mass loss rate increase follows with the existense of a final superwind marking the transition between AGB and post-AGB phase. For the case of simpler steady state, spherically symmetric mass outflow, the gas density is a function of radial distance r away from the AGB star's photosphere and is given by

$$n(r) = \frac{\dot{M}_{\mathrm{AGB}}}{4\pi r^2 U m_{H_2}} \qquad \left[\mathrm{cm}^{-3}\right] \tag{2.38}$$

Where $\mathrm{m}_{\mathrm{H}_2}$ is $\sim 3 \times 10^{-24}$ gm, since most AGB gas envelopes are in molecular form (Teyssier et al. 2006).

The second phase is the collimated jet or wind. This phase is present in young PNe or pPN with the general structure and dynamics showing axial symmetry of bipolar flows perpendicular to the disk or torus, surrounded by, and interacting with, previously ejected AGB halo during phase one, depicted in Figure 2.2 (CRL 618 wind schematic) and Figure 2.3 (CRL 618 H_2 number density). The disk and halo have a slow expansion of $\sim 10\,\mathrm{km\,s}^{-1}$ similar to AGB

dynamics. The dense equatorial torus may help in further confinement of fast outflows (Sahai Trauger 1998). The CFW's velocity, temperature and mass loss rate are $30 - 400\,\mathrm{km\,s^{-1}}$, 500 K and $\dot{M} \sim 5 \times 10^{-6}\,M_{\odot}\,\mathrm{yr}^{-1} (= 0.5\,\dot{M}_{\mathrm{AGB}})$, respectively Huarte-Espinosa et al. (2012). These quantities are consistent with momentum excess observed in bipolar outflows and cannot be explained by radiation pressure Bujarrabal et al. (2001).

The third outflow phase is the PN fast wind described by Kwok et al. (1978) with decreasing mass loss from 5×10^{-7} to $5 \times 10^{-9}\,M_{\odot}\,\mathrm{yr}^{-1}$ Perinotto et al. (2004) (and references therein). Simultaneously, the fast wind experiences increase in speed from 200 to 2000 $\mathrm{km\,s^{-1}}$ to conserve the wind's ram pressure. The above three phase structure simulation by Huarte-Espinosa et al. (2012) is complementary to the GISW theory with injection values accountable for momentum excess. The models were able to describe morphologies present in PN and pPN. Starting with fast spherical wind emanating from the central star driving into a slow spherical AGB wind resulting in spherical nebula. An elliptical planetary nebula will result due to interaction of collimated pPN jet with spherical AGB outflow. Finally a fast aspherical wind interacting with spherical AGB halo will result in aspherical nebulae regardless of earlier inclusion of pPN jet. The GISW theory describing PN winds evolution is briefly described in Section 2.2. The observational statistics indicate that (i) approximately 70 to 90% of PPN and young PN are bipolar or more complex shaped Sahai & Trauger (1998); Sahai et al. (2011), (ii) about 20% of mature developed PN are round, 70% are elliptical and about 10% are bipolar Parker et al. (2006); Miszalski et al. (2009); Lagadec et al. (2011), the Planetary Nebula Image Catalogue of Bruce Balick[1], and references therein. More information on pPN morphology is given in Section 2.3.

The research conducted in this thesis does not cover collimated fast winds expanding into the previous $n \propto r^{-2}$ outflow. Instead we simulate simpler model with CFW driving into uniform existing ambient medium, relevant to any ellipsoidal wind expanding into ISM. The goal of this set up is to determine the first approximation sequence of H_2 and optical emission.

[1] http://www.astro.washington.edu/users/balick/PNIC/

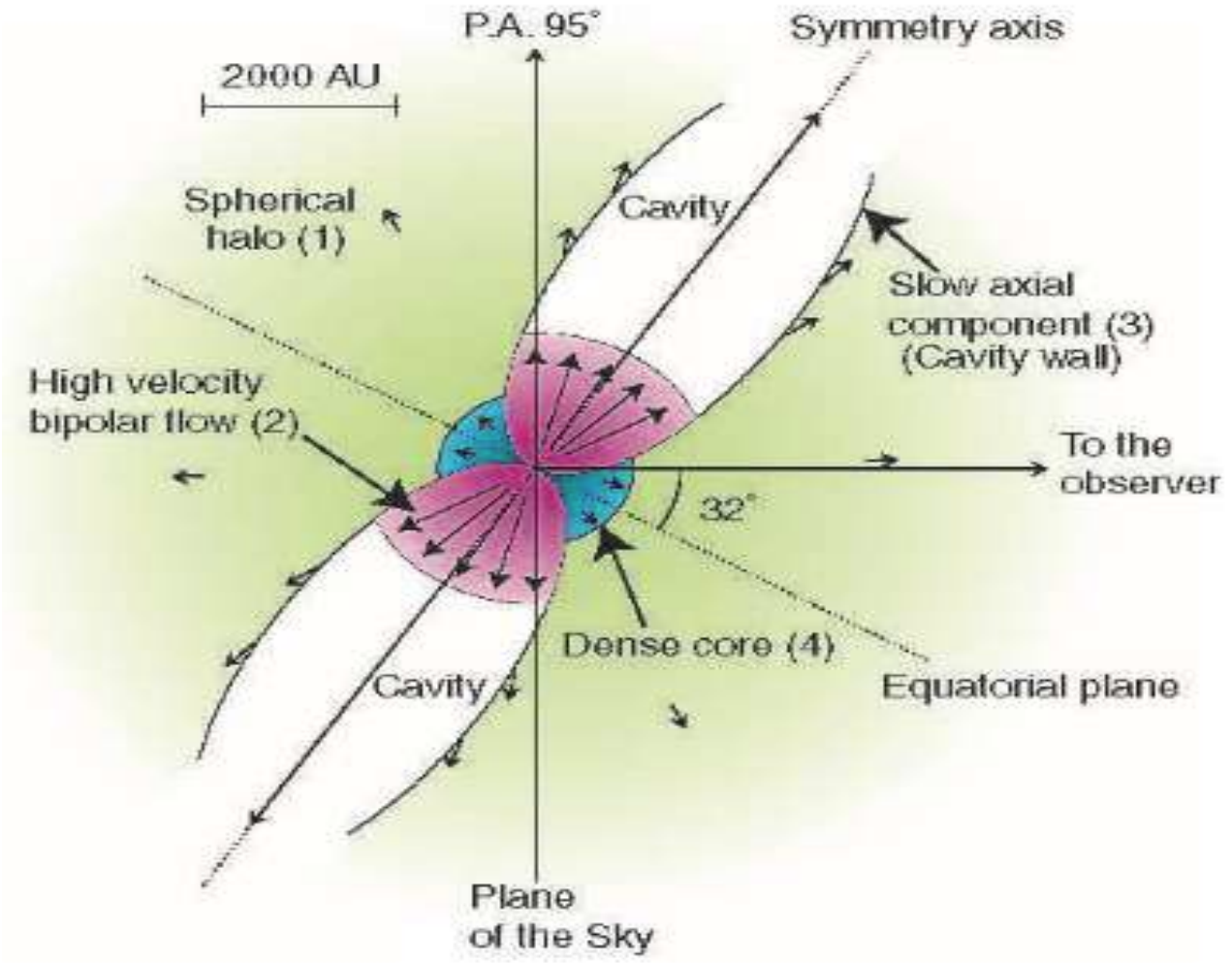

Figure 2.2: Schematic of CRL 618, IRAS 04395 + 3601 by Nakashima et al. (2007). Based on high-resolution interferometric maps, the spatio-kinematic structure of different molecular components is traced with CO data by Sánchez Contreras et al. (2004). The arrows indicate velocity field from different winds: (1) - AGB halo distributed by slow 17.5 km s^{-1} AGB wind, (2) - CFW bipolar outflow 350 km s^{-1}, (3) - two kinematical components expanding at 22 km s^{-1}, (4) - dense, inner torus-like core expanding at a velocity less than 12 km s^{-1}.

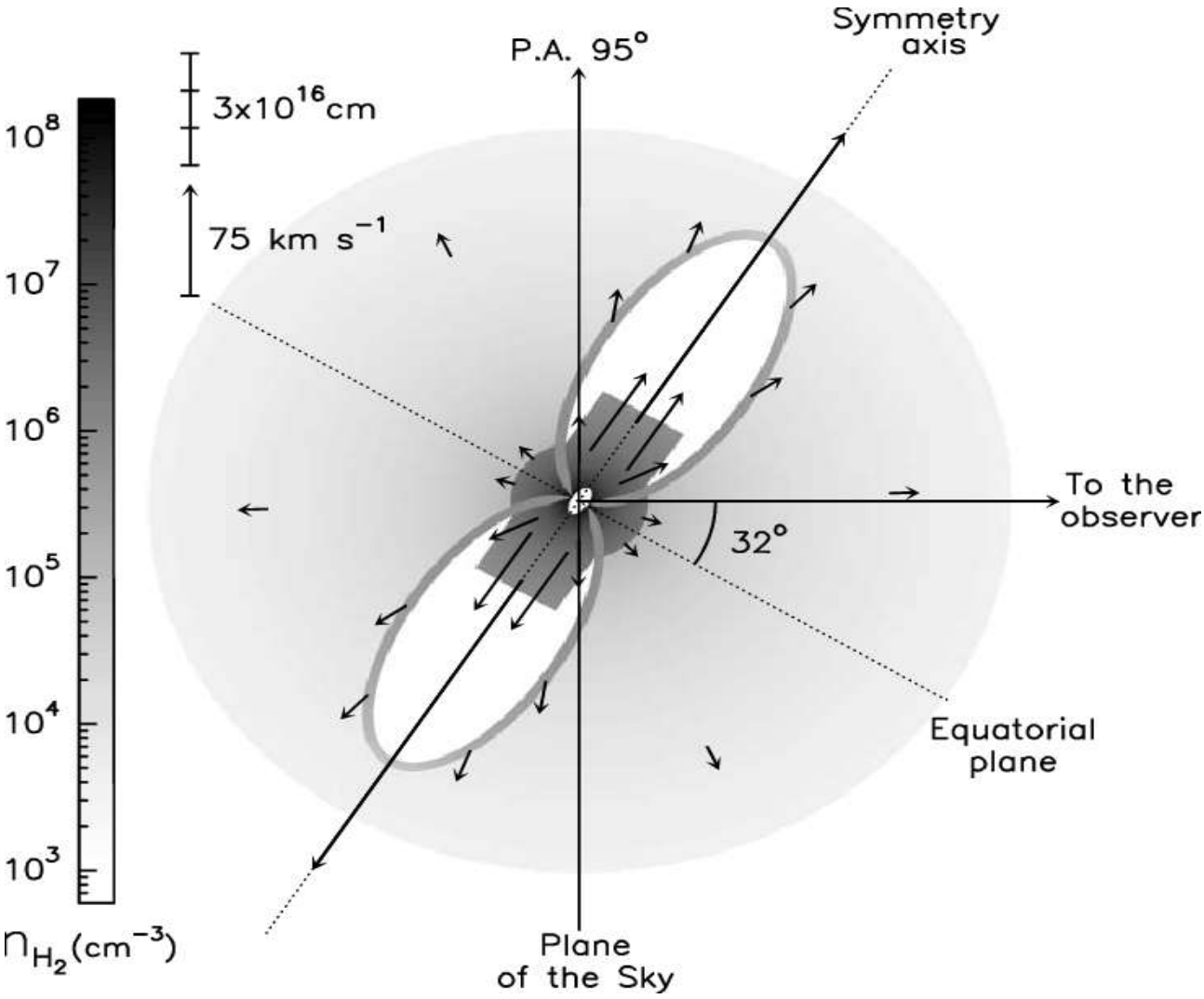

Figure 2.3: Schematic drawing of the density distribution and velocity field of the molecular envelope of CRL 618 by numerical model in Sánchez Contreras et al. (2004). The plot shows a cut of the nebula by a plane that contains the line of sight and the nebula symmetry axis; the north-south direction is perpendicular to this plane (i.e., out of the paper). The arrows represent the velocity field in the nebula. The compact central HII region in which the millimeter continuum emission arises is shown as an elliptical shell.

2.6 PPNe Spectroscopy, Optical Morphology, & Distribution

Axisymmetry in PN seem to originate before the photoionization stage. Hubble Space Telescope (HST) surveys reveal the innermost structure of pPNs using high resolution imaging in optical band of dust shells composed throughout the phase of superwind mass loss Ueta et al. (2000b) resulting in morphological classification of the objects studied in Table 2.5. The survey goal was aimed at observing the circumstellar morphologies originated with AGB superwind phase. The observations by Ueta et al. (2000b) resulted in the classification of two distinct types of optical morphology in PPN reflection nebulosities, the Star-Obvious Low-level-Elongated (SOLE) nebulae and DUst-Prominent Longitudinally-EXtended (DUPLEX) nebulae. SOLE structure corresponds to toroidal type mid-IR emission with two emission peaks marking the limb-brightened torus. DUPLEX type structure is related to core/elliptical type dust emission characterised by compact, unresolved core with broad plateau, shown in Figure 2.4. SOLE contain optically thin dust shells and DUPLEX type nebulas encompass optically thick shells.

2.6.1 Spectroscopy

pPNs are considered to have a post-AGB stars effective temperature between those of AGB and CSPN. The double-peaked spectral energy distribution (SEDs) after the AGB dust envelope detachment signifies neutral nebula. By comparison, the PN is signified by strong HeI and HI recombination lines. Young PN are considered to have properties of pPN as they emit weak recombination lines and/or radio continuum, signifying the beginning of the ionisation stage. In general, obscured sources indicate plane in of the sky orientation of lobes, whilst bright sources suggest face-on orientation Davis et al. (2003). Spectral energy is distinct for both types of pPN. SOLE let the stellar emission pass, converting some into thermal dust emission. DUPLEX nebulae absorb all stellar photons except scattered ones. A post-AGB stellar luminosity of $\sim 10^4\,L_\odot$, is approximately $\sim 10^3$ higher compared with the light reflected by the nebula, therefore making the optically thin, spherical SOLE nebulas observationally challenging to investigate, as depicted in Figure 2.4 (left- SOLE schematic). The central star of bipolar DUPLEX nebula is obscured by the optically thick torus of gas and dust driven by high-density equatorial wind shielding the flux emanating from the star. The optically thin lobes of CFW perpendicular to the ring create bipolar/multipolar structure shown in Figure 2.4 (right- DUPLEX schematic). The surrounding gas and dust envelope leads to reflection of the light from a luminous $10^3 \sim 10^4$ K star. The abundance of nebular dust constructs optically faint post-AGB stellar objects, however they emit strongly in the near-IR part of the spectrum

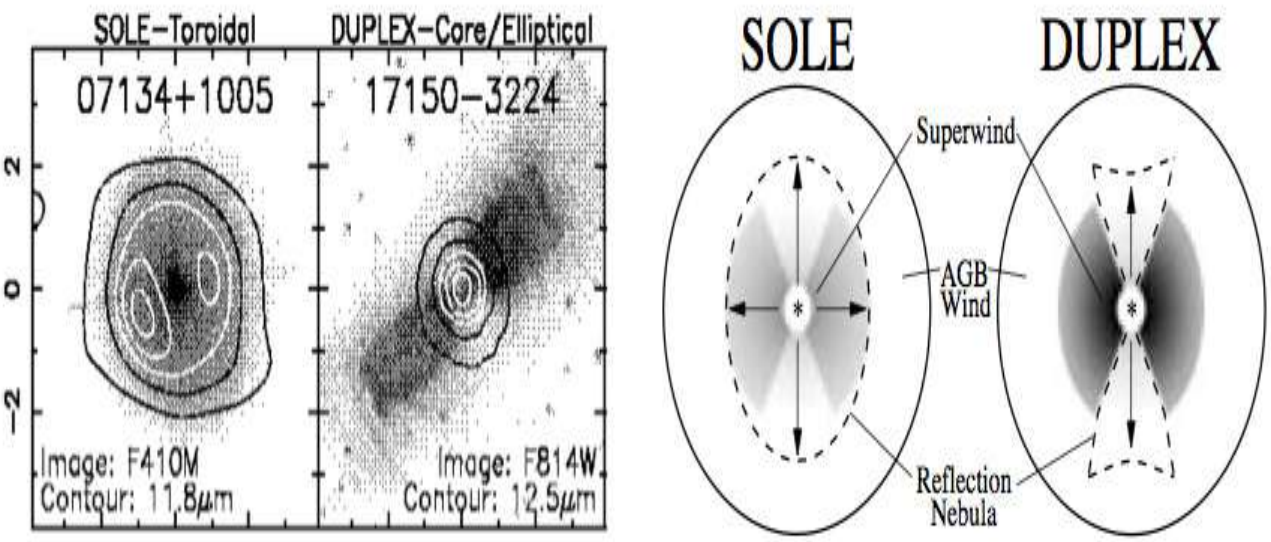

Figure 2.4: (left) Optical/mid-IR overlay images and (right) a schematic of SOLE and DUPLEX. The optical depth of superwind shells determines the morphology of PPN Ueta et al. (2000b).

due to the AGB molecular environment enveloping the star being shocked by the collimated fast pPN winds. van der Veen et al. (1989) identified four types of spectral energy distributions (SEDs) for PPNe. Type I corresponds to a flat spectrum from 4 to 25 μm with a steep fall off at short wavelengths. Type II have a maximum near 25 m and a gradual fall-off to shorter wavelengths. Type III have a maximum near 25 μm, a steep fall off at shorter wavelengths to a plateau between 1 and 4 μm. Type IV have two distinct maxima, one near 25 μm and the second at less than 2 μm. A number of independent studies shows that PPN are axisymmetric therefore the axisymmetry observed in PN might also predate the observed axisymmetry in PPN stage and most likely originates at late-AGB, due to AGB producing spherically symmetrical outflows. There is also a possible link between DUPLEX PPNe and bipolar PN whereas SOLE might be precursors to elliptical PN based on their differences in morphologies and galactic height distributions.

2.6.2 Galactic Distribution & Binarity

It is suggested that DUPLEX type nebula originates from high mass AGB progenitors due to the galactic distribution of pPNe. Figure 2.6 shows the galactic distribution of 326 most likely pPNe candidates provided by the Torún catalogue Szczerba et al. (2007). As depicted in Figure 2.6, the pPNe low-latitude population points to high-mass progenitors, due to observed absence of high-mass stars at high latitudes except runaway cases. Figure 2.7 ([a]) depicts 25 H_2 emitters, defining 8% of pPNes outflows as molecular bearing. The most likely H_2 emitters in terms of

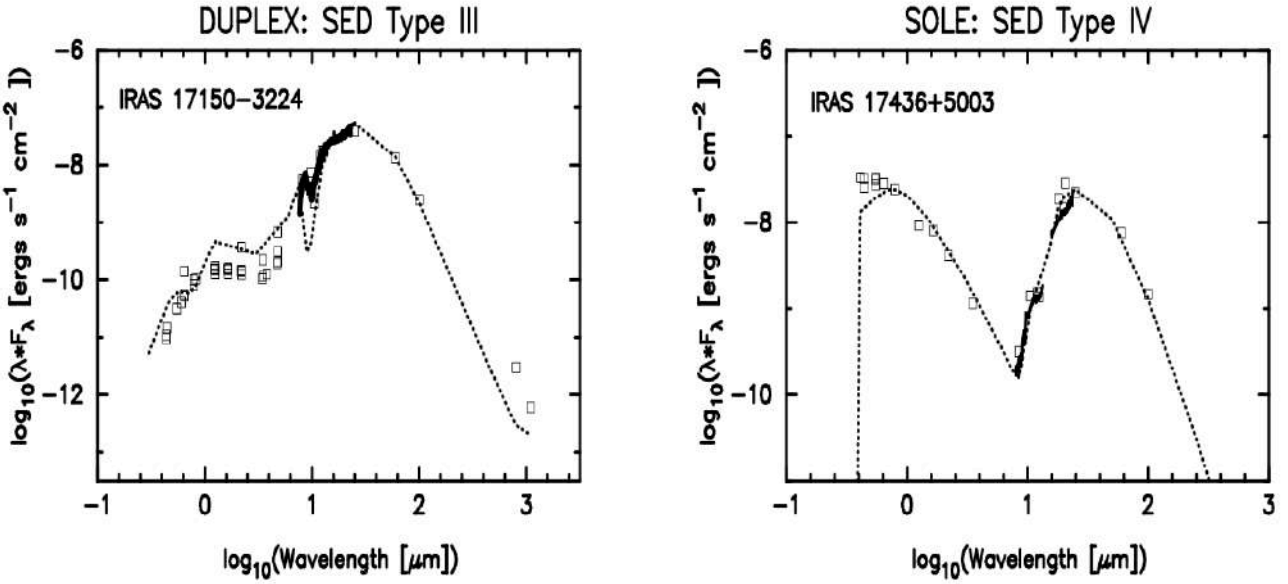

Figure 2.5: The spectral energy distributions for DUPLEX PPN, IRAS 17150-3224 (left) and for SOLE PPN IRAS 17436+5003 (right). Pho- tometry data are the squares, spectroscopy the solid lines and the model presented with dashed lines. From Meixner (2000).

spectral class are B type stars, molecular outflows happen in a variety of spectral types with one significant gap at $10,000$ K A type, that corresponds to accelerated evolution and small value of $\Delta M_{env}/\Delta T_{eff}$ Bloecker (1995). Figure 2.7 ([a], [e]) represents the Galactic distribution of H_2 emitting outflows against entire pPN distribution. The constraints on latitude for H_2 pPNes are $\pm 20°$, and the overall pPN distribution is more expanded at $\sim \pm 70°$. The peak in longitude for molecular pPNs is at $60° - 100°$. In general, pPNe objects are located at low Galactic latitudes near, or in the Galactic plane. Observational statistics also shows that bipolar PPNe begins to show H_2 emission at mid-G spectral types, where these young nebulae the molecular lines are excited by wind interactions at the end of bipolar lobes with weak or absent infrared flux in the torus region. Optically thin SOLE PPNe do not show H_2 line emission at these early spectral types. Therefore, it is possible that thick dust torus present in DUPLEX type nebula might collimate the molecular outflows present in bipolar nebulas.

Another important factor that can influence the mass loss in evolved post-AGB stars is presence of a companion star, i.e binarity. One of the important questions to ask is do all asymmetric PPN that form a majority in their own class involve binaries? Unfortunately, observational statistics cannot provide PPN binarity data due to optical radial-velocity measurements not being successful due to pulsational stellar variability.

An interesting comparison feature arises from PNe having a much higher 40% H_2 emitters Kastner et al. (1996). At first approximation this is counter intuitive due to the fact that

Table 2.2: Protoplanetary Nebular Shape

Class	Shape	% Objects
B	Bipolar	28%
L	Collimated-lobe pair	8.5%
M	Multipolar	19%
E	Elongated	32%
R	Round	3.4%
S	Spiral Arm	3.4%

Data from HST surveys of 119 objects resulting in a detailed morphological classification scheme Sahai et al. (2011).

pPN have more favourable cooler temperature to sustain molecular environment. However this could be due to selection effect of finding out the brightest H_2 bearing pPN. It is also possible that pPN have less H_2 emission on average compared to PNe with combined contribution from shock excited transitions and UV fluorescence. Another possible reason why so little molecular emission is found in pPN is due to the CFW being atomic in nature. Perhaps the H_2 is only in the ambient, previously ejected material in which it has had time for formation on dust. But by the time it has expanded out to the lower density bigger PN, exposed to the UV from surrounding hot stars, the H_2 is destroyed/dissociated by the UV resulting in more emission on average compared to pPN.

- B Bipolar: necessitates the lobes to be pinched-in where they connect with the waist region.
- L Collimated-lobe pair: similar to class-B (except no indication of pinched-in appearance at the point where the lobes join the waist region).
- M Multipolar: not always, but generally distributed in a point-symmetric fashion around the centre.
- E Elongated: the following morphological evolution B > L > E in PNe may result as the lobes fade relative to the waist region.
- R Round: a pPN needs presence of fast wind to carve a cavity and produce shell of reflected light to be observable as a pPN, hence there is a very small number of round pPNs. pPN develops round shape at late stages through radiatively driven fast PN wind.
- S Spiral Arm: binary interaction causes the gas ejected from the pPN to curl outwards

	PRIMARY CLASSIFICATION – *Nebular Shape*
B	Bipolar
M	Multipolar
E	Elongated
I	Irregular
	SECONDARY CLASSIFICATIONS
lobe shape:	
o	lobes open at ends
c	lobes closed at ends
obscuring waist:	
w	central obscuring waist
w(b)	obscuring waist has sharp radial boundary
central star:	
⋆	central star evident in optical images
other nebular characteristics:	
an	ansae present
ml	minor lobes are present
sk	a skirt-like structure present around the primary lobes
point symmetry:	
ps(m)	two or more pairs of diametrically-opposed lobes
ps(an)	diametrically-opposed ansae present
ps(s)	overall geometric shape of lobes is point-symmetric
halo:	
h	halo emission is present (relatively low-surface brightness diffuse region around primary nebular structure)
h(e)	halo has elongated shape
h(i)	halo has indeterminate shape
h(a)	halo has centro-symmetric arc-like features
h(sb)	searchlight-beams are present

Table 2.3: Morphological classification codes Sahai et al. (2007).

toward the stars companion.

Class-B and class-L can appear like class-E due to insufficient angular resolution and unfavourable orientation.

IRAS name	f25/f12	Imaging Refs.	Chem.[a]	Morphology
Well-Studied PPNs				
AFGL 618[b]	2.3	1	C	Mcw,ml,h(e,a)
Red Rectangle	1.1	2	C+O	Bow
OH 231.8 + 4.2	11.9	3	O	Bcw,sk
07131 − 0147	1.6	4	O	Bow*
Frosty Leo Neb.	>17	5	O	Bcw(b)*,an,ml,ps(m,an,s)
Roberts 22	5.5	6	C+O	Bcw,ml,ps(s),h(e)
Hen 3-401	9.3	7	C	Bow*,sk
Boomerang Neb.	1.3	8	...	Bow*
16342 − 3814	12.3	9	O	Bcw,ps(s)
Hen 3-1475	4.0	10	O	Bow(b)*,an,sk,ps(an,s),h
M 1-92	3.4	11	O	Bcw(b)*,an
AFGL 2688	...	12	C	Bcw(b),ml,h(e,a,sb)
Less Well-Studied PPNs				
02229 + 6208	3.1	10	C	E
04296 + 3429	3.6	13	C	Bcw(b),h
05341 + 0852	2.2	10	C	Ec*,ps(s),h
06530 − 0213	4.5	10	C	Bc*,ml,ps(s),h(e)
07134 + 1005	4.8	10	C	Ec*,h(e)
07430 + 1115	3.9	10	C	E*,h
08005 − 2356	2.9	10	O	Bc*
16594 − 4656	6.6	14	C	Mcw*,an,ps(m,an),h(a)
17106 − 3046	15.5	15	O	Bw(b)
17150 − 3224	5.6	16	O	Bcw,h(a,sb)
17245 − 3951	13.3	14	O	Bcw,h(sb)
17436 + 5003	30.1	10	O	Ec*
17441 − 2411	4.5	17	C	Bcw,h(e,a)
18095 + 2704	2.8	10	O	Bc,h
19374 + 2359	4.2	10	O	B,h(e)
19477 + 2401	4.9	14	C	E,h(e)
20028 + 3910	5.0	18	C	Bcw(b),h(e,a,sb)
22272 + 5435	4.1	10	C	Ec*,h(a)
22574 + 6609	3.3	14	C	Bwh(i)
23321 + 6545	6.3	10	C	Ec

Table 2.4: Properties of Previously Observed, Well-Resolved Preplanetary Nebulae Sahai et al. (2007). spectral energy distributions (SEDs) of a large fraction of these objects indicate a lack of hot dust (25-12 μm flux ratio F25/F12 > 1, implying a lack of dust hotter than $\sim$ 450 K and subsequent cessation of the dense AGB mass-loss process less than a few hundred years ago.

Number (1)	*IRAS* ID (2)	Object Type (3)	Mid-IR Morphology[a] (4)	SED Type (5)	Spectral Class (6)	Chemistry[b] (*/CS) (7)	b^c (deg) (8)	z^c (pc) (9)
				SOLE Sources				
1	02229+6208	PPN	Unknown	IVa	G8–K0 Ia	C/C	1.5	60
2	04296+3429	PPN	Unresolved	IVa	G0 Ia	C/C	−9.1	650
5	05341+0852	PPN	Unresolved	IVa	G20–Ia	C/C	−12.2	2100
6	06530−0213	PPN	Unresolved	IVa	F0 Iab	C/C?	−0.1	4
7	07134+1005	PPN	Toroidal	IVb	F5 Iab	C/C	10.0	520
8	07430+1115	PPN	Unresolved	IVa	G50–Ia	C/C	17.1	90
16	17436+5003	PPN	Toroidal	IVb	F3 Ib	O/O	30.9	620
18	18095+2704	PPN	Unresolved	IVa	F3 Ib	O/O	20.2	660
19	19114+0002	PPN?	Toroidal	IVb	G5 Ia	O/O	−5.0	350
23	20462+3416	PN	...	IVb	B1 Ia	O/...	−5.8	290
25	22272+5435	PPN	Toroidal	IVa	G2 Ia	C/C	−2.5	130
	21282+5050	PN	Toroidal	III	...	C/C	−0.1	6
				DUPLEX Sources				
9	08005−2356	PPN	Unresolved	II	F5E	C/O	3.6	250
10	09452+1330	AGB	...	I	C9.5	C/...	45.1	140
13	16342−3814	AGB	Core/elliptical	III	M	.../O	5.8	220
14	17150−3224	PPN	Core/elliptical	III	G2	.../O	3.0	130
15	17423−1755	PN	...	II	...	.../O	5.8	510
17	17441−2411	PPN	Unknown	III	...	.../C?	2.2	110
20	19374+2359	PPN	Core/elliptical	II	...	.../O	1.0	90
21	20028+3910	PPN	Unresolved	II/III	...	.../C	4.1	240
26	22574+6609	PPN	Unresolved	II	...	C/C	6.0	520
27	23321+6545	PPN	Unresolved	II/III	...	.../C	4.3	...
	04395+3601	PN	Core/elliptical	III	B0	C/C	−6.5	190
	06176−1036	PPN	Core/elliptical	III	B8 V	C/O	−11.8	70
	AFGL 2688	PPN	Core/elliptical	III	F5 Iae	C/C	−6.5	140
				Stellar Sources				
3	04386+5722	PPN	Unresolved	IVa	M	.../...	7.5	...
4	05113+1347	PPN	Unresolved	IVa	G8 Ia	C/C	−14.3	1200
11	10158−2844	RCrB	Unresolved	...	B9.5 Ib–II	C/...	22.9	270
12	15465+2818	RCrB	Unresolved	...	F0–F8pe	C/...	51.0	1500
22	20043+2653	AGB	Unresolved	I	...	O/...	−2.7	...
24	22142+5206	YSO	Unresolved	II	...	C/...	−3.6	280

Table 2.5: Morphology of detected pPNs, by Hubble survey Ueta et al. (2000a). Morphology classification a, Chemical composition of Photosphere and CS-Circumstellar shell b, Galactic latitude b^c, used with average distance to the object to estimate the Galactic Height, z.

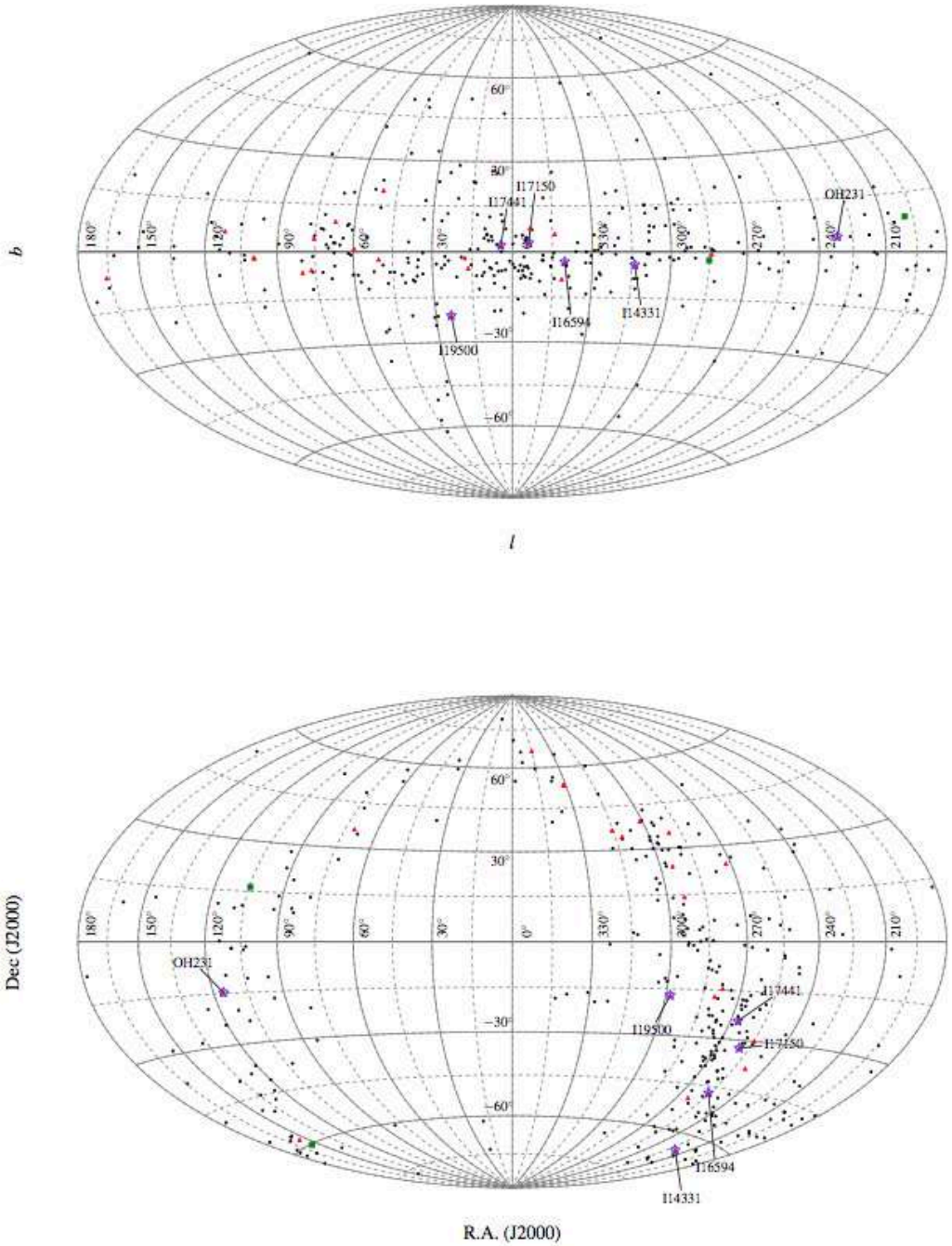

Figure 2.6: (top) positions of pPNe in Galactic coordinates. H_2 bearing pPNs are marked with red triangles, black circles denote other most likely pPNe candidates as presented by the Torún catalogue Szczerba et al. (2007). (bottom) same data as above displayed in Equatorial coordinates.

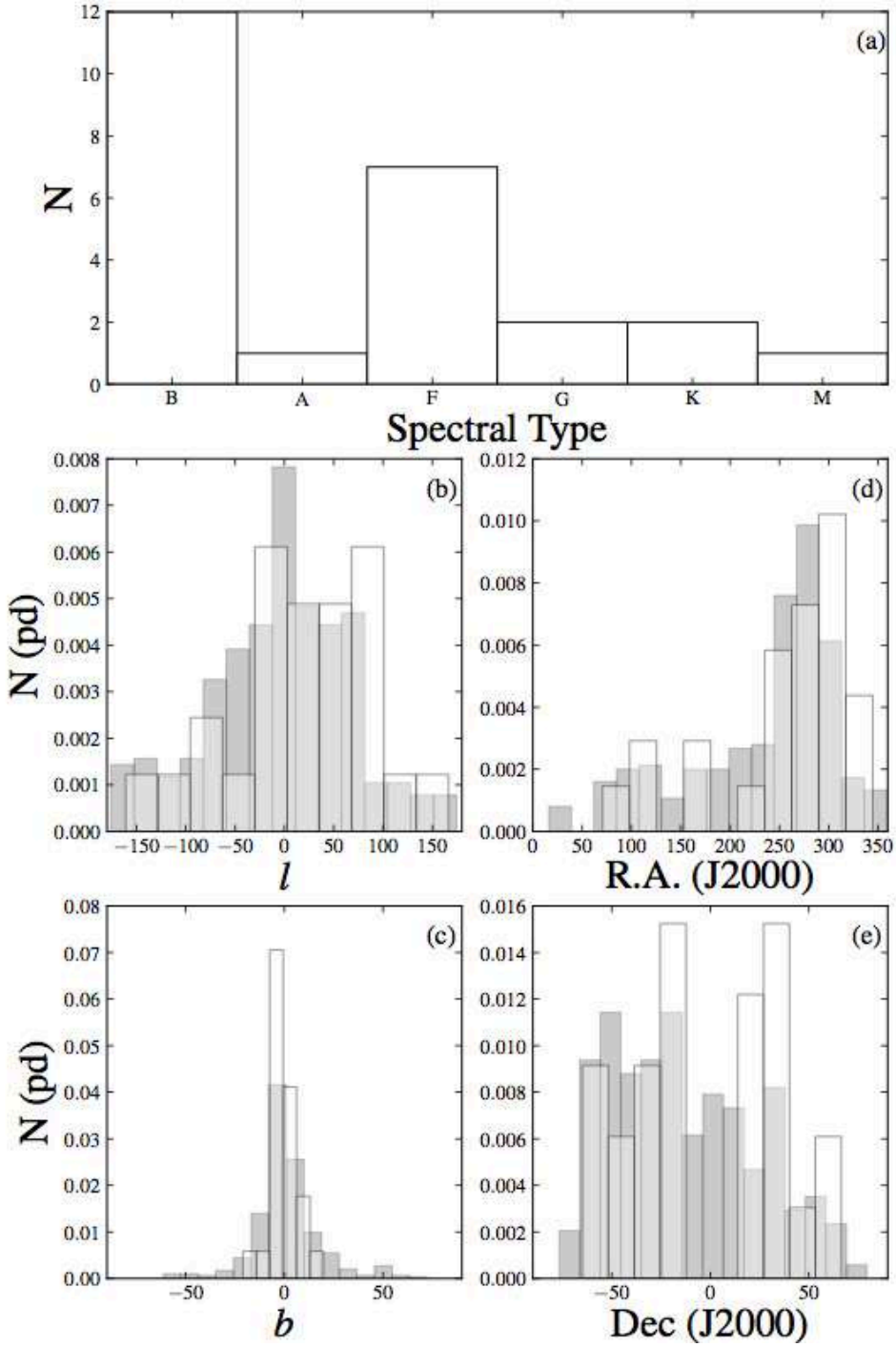

Figure 2.7: (a) The top diagram displays Galactic pPNs that exhibit molecular H_2 emission in terms of spectral types. (b) Longitudinal Galactic distribution for all pPNs. (c) Galactic latitude distribution. (d) Right Ascension distribution and (e) Declination distribution. White histograms show pPNs with H_2 outflows, and grey histograms show all defined pPNs. The Y axis is scaled to show normalised number of objects and form probability density to enable comparison of distributions Forde (2013).

Chapter 3

Wind Parameters & Code Adaptations

3.1 ZEUS 3D Modification

The goal of this work is to re-create pPN wind conditions using hydrodynamic codes, coupled with near-infrared and optical line emission algorithms. The re-created emission maps can be used for comparison with pPN surveys. Equations of hydrodynamics provide macroscopic parameters of temperature, nucleon density and molecular fraction, necessary to generate molecular and atomic line emission via cooling & recombination mechanisms discussed in the next chapter. This chapter describes the scaling used for the hydrodynamical part of simulation and code configuration of 2D axisymmetric computational grid. The numerical code employed for the work presented in this thesis is ZEUS-3D (version 3.5)[1], released in May 2008 and developed by M.L. Norman and the Laboratory for Computational Astrophysics (LCA)[2]. For the current problem it is set up as a semi-implicit, operator-splitting, finite difference, Eulerian code. It is modified and differs from otherwise fully explicit Eulerian scheme used by regular ZEUS-3D fluid code by incorporating chemistry (molecular dissociation) and molecular cooling & atomic recombination functions. Chemically reactive flows are incorporated into ZEUS via molecular chemistry reactions of collisional dissociation of H_2 with H and with itself, described by Smith & Rosen (2003) and given by Equation 4.2. The chemical reactions are governed by collisional dissociation rates from Shapiro & Kang (1987) that are listed in equation 4.16 & 4.17. The

[1] http://www.astro.princeton.edu/∼jstone/zeus.html
[2] http://www.ica.smu.ca/zeus3d

molecular cooling from dissociation Equation 4.14 determines the gas non-conservative internal energy, where the gas molecules radiate energy away in quantum steps by releasing photons of certain energy, therefore generating H_2 emission lines of certain wavelength. The molecular emission lines are generated by a process of collisional de-excitation where H_2 looses energy via collisions with itself or H_2 atoms given by collisional de-excitation rates in Table 4.2. In case of atomic recombination lines, we use a constant abundance of ionised atomic species relative to atomic hydrogen cell abundance to generate optical emission lines. Molecular infra-red and atomic optical emission line calculation is discussed in more detail in section 4.1.3 and 4.2 respectively. We have also chosen 2D axially symmetrical cylindrical grid, where the viewing angle is set up as a user variable, this enables the 2D grid values to be translated on to a cylindrical grid and create line emission and position-velocity diagrams in pseudo-3D.

3.2 Semi-Implicit approach for Cooling & Chemistry

The cooling and chemistry are solved semi-implicitly, this method has been first tested by multi-dimensional simulations of molecular jets in Suttner et al. (1997). After that, it has been extensively tested for stability in Smith & Rosen (2003) in one-dimensional mode, and has been further applied in various environments including 3D simulations of protostellar outflows in Rosen & Smith (2004b) and slow-precessing protostellar jets in Smith & Rosen (2005). In all of the above numerical simulations, cooling and chemistry is solved using semi-implicit scheme that enabled to generate synthetic line emission maps of H_2. The above synthetic molecular emission line calculation has not been applied for PPN outflows before, however this code set up is relevant for being used here due to the fact that PPNe are encompased by molecularly rich envelopes and are also known to launch H_2 collimated jets . The temperature and molecular fraction are evaluated implicitly. For example, the next $n+1$ value of molecular fraction f due to dissociation chemistry is evaluated with the current n known value of molecular fraction coupled with next $n+1$ value of density taken from the ordinary explicit approach. After evaluating molecular fraction (chemistry dissociation reactions) and temperature grid values, cooling Λ that is T, f, ρ dependent is also evaluated implicitly and is used by the internal energy equation for molecular line-emission generation. Overall, the method uses both implicit (temperature, molecular fraction, cooling) and explicit (density, pressure, velocity) step evaluation and is therefore called semi-implicit. Newton-Rapson method is employed at each time step for re-iteration of molecular fraction and temperature values until sufficient accuracy is reached by convergence. The time step size is set with the Courant number. Symmetry is assumed along the axial axis,

hence our models are two-dimensional. The calculations are carried out on the (R, Z) cylindrical plane. Therefore, an operator-splitting method is employed due to all above quantities being calculated in 2D, i.e $\mathrm{T}, \mathrm{f}, \rho$ is solved for axial direction (R), followed by consecutive solution of those three terms for radial direction (Z), and finally solved for cooling $\Lambda(\mathrm{T}, \mathrm{f}, \rho)$. After that, the above three steps are repeated again until the final timestep of simulation.

3.3 Finite-differencing

The principle of finite-differencing is based on Taylor series. The function $\mathrm{f}_{\mathrm{x_{i+1}}}$ can be expanded around the point $\mathrm{x_i}$ to $\mathrm{n^{th}}$ order where h is the *small* step separating x_i and x_{i+1}. The Taylor series can be written as

$$f_{x_{i+1}} \approx f_{x_i} + f^{'}_{x_i} h + \frac{1}{2} f^{''}_{x_i} h^2 + ... + \frac{1}{n!} f^{n}_{x_i} h^n, \tag{3.1}$$

by only taking into account the first two terms of the Taylor series, and defining the third term in the expansion as the truncation error

$$\epsilon = \frac{f^{''}_{\xi}}{2} h^2 \tag{3.2}$$

with ξ being an unknown value that lies in the interval $\mathrm{x} < \xi < \mathrm{x} + \mathrm{h}$. Hence, rearranging Equation 3.32 and obtaining the expression for the first derivative, i.e the forward difference scheme (FDS) as

$$f^{'}_{x_i} = \frac{f_{x_{i+1}} - f_{x_i}}{h} + \mathcal{O}(h) \tag{3.3}$$

Also, introducing the backward difference scheme (BDS) wit the subscript $\mathrm{i} - 1$ as we are expanding around $\mathrm{x} - \mathrm{h}$

$$f^{'}_{x_i} = \frac{f_{x_i} - f_{x_{i-1}}}{h} + \mathcal{O}(h) \tag{3.4}$$

The expansion error is of order $\mathcal{O}(h)$ for both (BDS) and (FDS). To further reduce the error, second order accurate expression is employed. A combination of (FDS) and (BDS) defines a central difference equation, (CDS)

$$f^{'}_{x_i} = \frac{f_{x_{i+1}} - f_{x_{i-1}}}{2h} + \mathcal{O}(h)^2 \tag{3.5}$$

The truncation error is now of lower second order of h. Therefore, the central difference gives scheme enables a better estimate at point x. The first two methods are known as first derivative

Euler or Runge-Kutta 1 (RK1) method. A family of the Runge-Kutta approximations is a numerical recepie that use more than one term of the Taylor series. The objective is to make use of weighted average of gradients calculated at different points in order to estimate the change in f_x. In general, n^{th} order of Taylor series is $\mathcal{O}(h)^n$ accurate and the error decreases with increasing order of magnitude in h.

3.4 Equations of Hydrodynamics

ZEUS-3D ordinary routine solves equations of hydrodynamics numerically by applying a method of 'finite-differencing' with 'time-explicit' multi-step 'operator-splitting'. Differential equations of hydrodynamics, are transformed with the above method into a set of algebraic equations that are solved over the domain of computation. At each time step, a set of variables is calculated to be used for computation taking place throughout the next time-step, i.e 'time-explicit'. The solutions to the partial differential equations PDEs are split into parts, with each part corresponding to a single term from the equations. Numerical simulations are based on equations of hydrodynamics. The set of differential equations below for conservation of mass, momentum and internal energy for zero viscosity, i.e inviscid flow neglect viscous stress and strain forces and also ignore gravity, thus simplifying Navier–Stokes equations to conservative form of Euler equations:

The continuity equation

$$\frac{d\rho}{dt} + \rho\nabla \cdot \mathbf{V} = 0, \qquad \left[\mathrm{gm\,cm^{-3}\,s^{-1}}\right] \tag{3.6}$$

Euler equation

$$\rho\frac{d\mathbf{V}}{dt} + \nabla p = 0, \qquad \left[\mathrm{gm\,cm^{-2}\,s^{-2}}\right] \tag{3.7}$$

Internal energy conservation (edited in Section 4.1.2) to account for the molecular cooling term Λ.

$$\rho\frac{d}{dt}e + p\nabla \cdot \mathbf{V} = 0, \qquad \left[\mathrm{erg\,cm^{-3}\,s^{-1}}\right] \tag{3.8}$$

where $\nabla \cdot \mathbf{V}$ is the velocity vector in three dimensions and $\nabla = \mathrm{i}\frac{\partial}{\partial \mathrm{x}} + \mathrm{j}\frac{\partial}{\partial \mathrm{y}} + \mathrm{k}\frac{\partial}{\partial \mathrm{z}}$ is the grad operator, ρ is the density, V is the velocity, p is the pressure, e is the internal energy density. The above equation is edited in ZEUS to account for energy loss in form of radiation. The ideal gas equation

$$p = (\gamma - 1)e \qquad \left[\mathrm{erg\,cm^{-3}}\right] \tag{3.9}$$

Appendix C provides derivation of inviscid Eulerian set of equations for conservation of mass, momentum and energy. The above equations do not have analytical solutions but can be solved by numerical methods described in Section 3.4. The simulated problem discussed in this work involves non-conservative Navier–Stokes equations with quadratic artificial viscosity $q_{con} = 1.6$ and linear artificial viscosity $q_{lin} = 0.1$ parameters listed in inzeus in Figure 3.1. The inclusion of the cooling term Λ forms a non-conservative internal energy Equation 3.10 which upon solution leads to shock errors and rarefaction shocks caused by the anti-diffusive terms in truncation errors Zhu et al. (2012). A linear artificial viscosity term is applied throughout the grid and stabilizes continuous structures such as magnetoacoustical and rarefaction waves and has been suggested by Clarke (2010) to remove the anti-diffusive terms to exclude numerical errors. q_{con}, is applied only to regions of strong compression and effectively captures shocks within $q_{con} + 2$ zones. Both parameters serve to implement stable internal energy calculation with molecular cooling and chemistry which otherwise can lead to unstable solutions and cause code to crash at late times and high resolution.

3.5 Courant condition

The Courant–Friedrichs–Lewy (CFL) condition in one dimension is defined as

$$C < \frac{(u + c_s)\Delta t}{\Delta x} \tag{3.10}$$

With dimensionless Courant number C given by the magnitude of flow velocity u, the speed of sound in medium c_s, the time step Δt and the length interval Δx. A necessary condition for the stability of numerical solutions of partial differential equations is determined by the expression above. As a consequence, computer simulations use a time-step that is less than the certain value established by (CFL) restraint. Numerical stability and meaningfulness of physical results is established by the CFL condition. The simulations in this work employ a conventional Courant number setting of $C = 0.5$. However, futrher decrease in the time step Δt does not lead to reduction of numerical errors Brebbia (1991). The size of time step Δt is determined by ZEUS-3D at each cycle from Equation 3.10. The CPU run-time of the code increases significantly for $C < 0.5$.

3.6 Computer system & ZEUS-3D configuration

The Eulerian astrophysical gas dynamics code ZEUS Stone & Norman (1992) is extended to include molecular and atomic cooling functions. Modelling electron transitions in atoms and ro-vibrational transitions in molecules is computationally expensive. Therefore, atomic cooling is represented macroscopically by simple functions of temperature, ion and free electron abundance. The modelled axisymmetric outflows were calculated on a 2–D grid, and expressed in terms of cylindrical geometry. As a result, 2–D grid values are translated onto a cylindrical grid creating a pseudo-3–D projection with the line of sight as a user variable.

The 128 core SGI Altix cluster Forge housed by the astrophysics CAPS group at UKC performed calculations for simulations described in this work. The computer system runs on a version of the SUSE linux operating system. Forge hosts 16 computing nodes, each equipped with 8 cores and and $\sim$ 12 GB of local RAM memory. The hard disk space available for storage is 21 TB. The Interactive Data Language (IDL)[3] software was used to visualise the HDF output files and create plots for this thesis. Before the executable xdzeus is initiated to produce output data which is later used for IDL graphics output as shown in flow chart in Figure 3.2, it must first be compiled and configured. The initial configuration determines the grid dimensions, the coordinate system used and physcis modeules included in computation. The source file dzeus35.s fixes the grid resolution and outputs an executable xdezus and main input file inzeus. The input file hosts the initial variables and sets the simulation total run time t_{lim} along with the time intervals of data output. Re-compilation with source file is not required unless the parameters of the grid are changed, all other input simulation variables can be altered within input inzeus without re-compilation. An extra layer of *ghost zones* is created by ZEUS-3D around the visible simulation domain to enable the wind to leave the grid. The simulation present in this work includes 5 additional ghost zones set in inzeus to let the wind escape the computational domain known as the outflow regime. By definition, ZEUS-3D provides five types of boundary conditions that can be implemented into the grid:

- **Reflecting**: Not included in simulations present here. Values of ghost zones are set to equal the neighbouring active ones, and the velocity component is reflected in the next ghost zone.

- **Symmetry**: Used for our axisymmetric simulations, (R.Z) boundary is set to symmetry

[3] http://www.ittvis.com/idl

```
$iocon   iotty=0, iolog=2                                    $
$rescon  dtdmp=-1e11, idtag='ar', resfile='zr00ar'          $
$ggen1   nbl=3200, x1min=0.0, x1max=6.171356e17, igrid=1, x1rat=1.0
     , lgrid=.t. $
$ggen2   nbl=1600, x2min=0.0, x2max=3.085678e17, igrid=1, x2rat=1.0
     , lgrid=.t. $
$ggen3   nbl=1, x3min=0, x3max=1, igrid=1, x3rat=1.0
     , lgrid=.t.  $
$pcon    nlim= 9999999, tlim=8.8162e10, ttotal=800000.0, tsave=10.0  $
$hycon   qcon=1.6, qlin=0.1, courno=0.5, iord=2, istp=0, icool=2
     , itote=0  $

$iib     niib(1:1605,1)=9                                    $
$oib     noib(1:1605,1)=9                                    $
$ijb     nijb(1:1,1:3205)=1                                $
$ojb     nojb(1:1,1:3205)=9                                  $
$ikb     nikb(1:3205,1:1605)=9                                 $
$okb     nokb(1:3205,1:1605)=9                                 $
$grvcon                                                    $
$eqos    gamma=1.428571                                        $
$gcon                                                      $
$extcon  istretch(1)=3,istretch(2)=23,istretch(3)=10      $
$plt1con  iplt1dir=1, dtplt1=0.0, corl=1
     , plt1var= 'd ', 'se', 'p', 'v1', 'v2', 'v3'
          , 'b1', 'b2', 'b3', 'bd'                          $
$plt2con                                                   $
$pixcon   dtpix = 0.0, ipixdir = 1,2,3, lpix = 3,18,18, npi=30,30,35
     , npj = 30,35,30, pixvar = 'pb','gp','v2','v3','d2'
     , nlpix = 1,0,0,0              $
$voxcon                                                    $
$usrcon                                                    $
$hdfcon  dthdf = 6.31e9, hdfvar= 'd', 'v1', 'v2', 'p1', 'co' $
$tslcon                                                    $
$discon  dtdis=3.155e8, disvar='v1', jdismn=57, jdismx=68, kdismn=57
     , kdismx=68, idisdir=1, ldis=1   $
$radcon  dtrad = 6.312e7, itype=1, radvar='I ','HH','CO'
  ,x2rdmn=-2.0e16,x2rdmx=2.0e16,x3rdmn=-2.0e16,x3rdmx=2.0e16
  , rorhrad=1, iradmm = 0 ,nlrad=1000,1000,1000
  ,radmax=2.0e29,2.0e28,5.0e25
  ,radmin=2.0e26,2.0e25,,5.0e22                              $
$pgen    djet=3.7627042e-20, damb=1.5050816e-21, e1jet=1.5529523e-09
     , e1amb=2.4847235e-12,  mjet=44.035853, rjet=3.08568e+16
     , cojet = 0.5, coamb  = 0.5 , iwiggle=2, thetaj=0.0
```

Figure 3.1: inzeus input file describing cylindrical computational grid with macroscopical parameters for molecular $140\,\mathrm{km\,s^{-1}}$ wind flowing into molecular medium including 5 additional grid zones enabling outflow scheme.

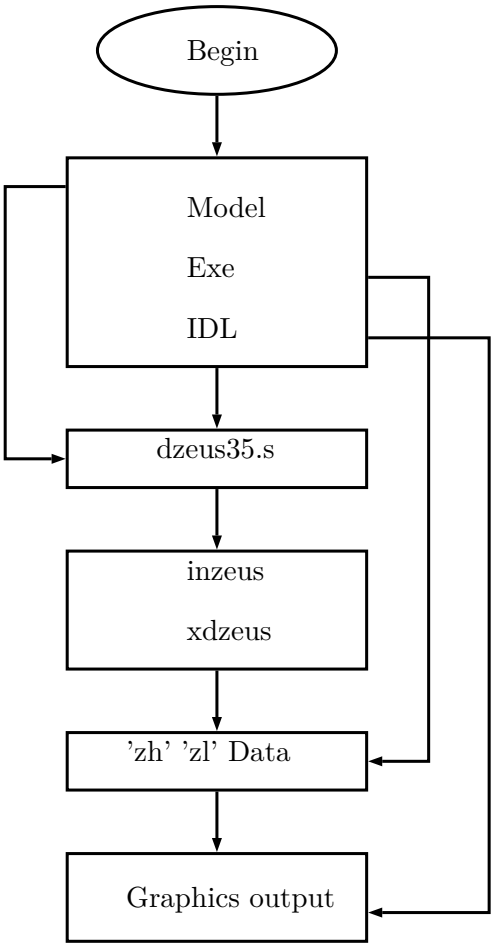

Figure 3.2: A schematic flow chart displaying ZEUS-3D configuration and IDL output. The Model folder contains dzeus35.s which creates input inzeus and executable xdzeus that are stored in Exe folder for HDF output. The IDL folder contains images of HDF output data.

boundary (R,-Z) condition, used to speed up CPU run-time.

- **Inflow**: This condition is used for wind input, with the ghost zones given a fixed variable.
- **Outflow**: The neighbouring ghost zone values are set to the values of the neighbouring active zones. This set-up enables the wind to leave the grid and is used in our simulations.
- **Periodic**: Not present in our simulations. The ghost zones values are taken from the neighbouring active zones, and are repeated on the opposite side of the grid.

Stone & Norman (1992)

3.7 Scaling

Simulations presented here create a jump J-type shock followed by a radiative cooling layer presented schematically in Figure 3.3. This is effectively a combination of J-type forward shock

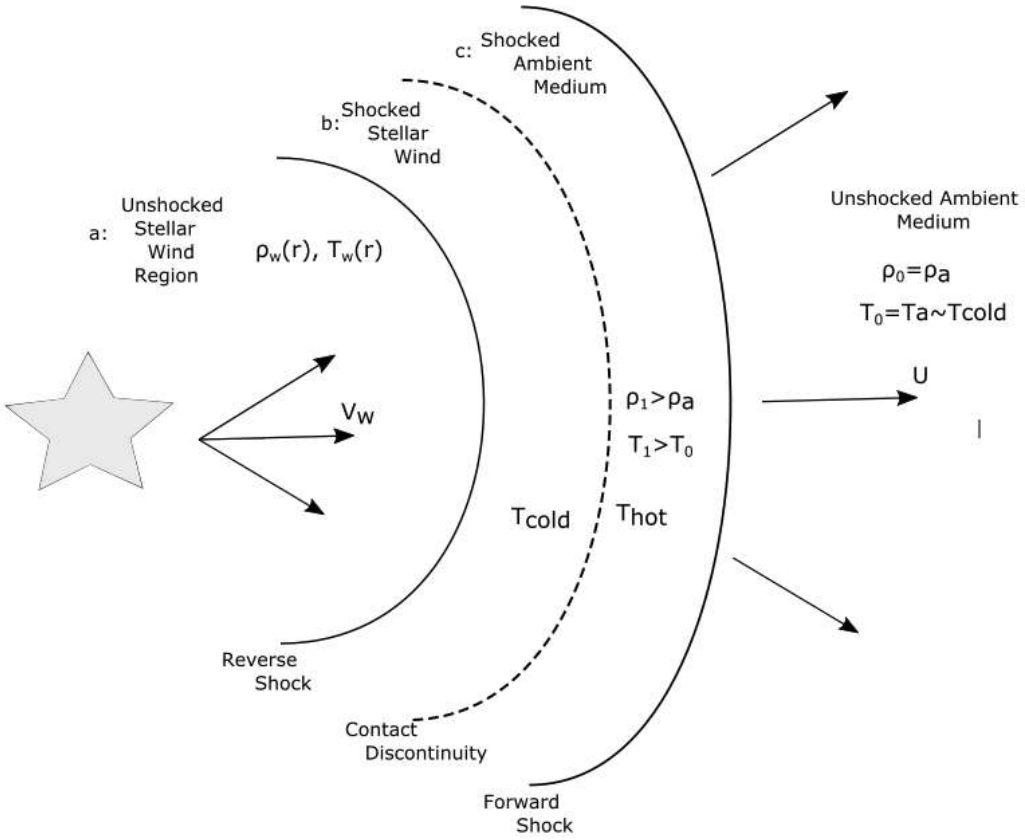

Figure 3.3: A schematic of wind profile showing velocity and temperature distributions of forward & reverse shock structure. The wind from the long-lasting central engine (region 1) passes through the reverse shock (RS) and forms a shocked wind flow (region b). The wind drives a forward shock (region c) into shocked ambient. (region d) is the unshocked stationary ambient. The flow within region b and c is the main goal of the present study where dissociative chemistry and strong cooling takes place, generatig line emission.

where the H_2 is dissociated and K-band emission is produced, with wings of lower shock velocity and temperature in case of non-spherical outflows, where H_2 is exited without dissociation as shown in Figure 4.1.

The Forward shock is the front of the supersonic outflow that accelerates and pushes against the ambient medium. Supersonic material at the back of the outflow is decelerated by the Reverse shock. As the density of the expanding outflow drops, the pressure of the shocked circumstellar medium becomes equal and subsequently exceeds forward ram pressure of the outflow, and a reverse shock is driven into the outflow. The reverse shock propagating inward, slows and shock-heats the material in the outflow that has previously been cooled by adiabatic expansion. In Figure 3.3, the unshocked stellar wind is the input wind material of density ρ_w moving at wind speed V_w. The supersonic wind material propagates into an ambient medium, of density ρ_a with forward shock velocity U. A region between shocked stellar wind and shocked ambient medium is the Contact Discontinuity which separates the shocked ambient medium passed through the forward shock and the wind material shocked by the Reverse shock. In the reference frame

Table 3.1: Initial wind/ambient parameters.

Property	Atomic	Molecular
Wind:		
wind density, $\rho_{\rm w}$(gm/cm^3)	3.76×10^{-20}	3.76×10^{-20}
number density, $n_{\rm w}$(cm^{-3})	1.61×10^{4}	1.61×10^{4}
wind internal energy, $u_{\rm w}$(erg/cm^3)	1.83×10^{-09}	1.55×10^{-09}
molecular fraction, $n(H_2)/n$	0	0.5
specific heat ratio, γ	1.66667	1.42857
temperature, $T_{\rm w}$(K)	500	500
Ambient medium:		
density, $\rho_{\rm a}$(gm/cm^3)	1.51×10^{-21}	1.51×10^{-21}
number density, $n_{\rm a}$(cm^{-3})	6.42×10^{2}	6.42×10^{2}
int. energy, $u_{\rm a}$(erg/cm^3)	2.92×10^{-12}	2.48×10^{-12}
molecular fraction, $n(H_2)/n$	0	0.5
specific heat ratio, γ	1.66667	1.42857
temperature, $T_{\rm a}$(K)	20	20
Element	$\epsilon_{\rm ion} = n_{\rm ion}/n_{\rm H}$	$\chi_{\rm e} = n_{\rm e}/n_{\rm H}$
[a][O I]	3.5×10^{-4}	0.1
[a][Si II]	$\epsilon_{\rm II}$(T)	0.1
[b][Fe II]	1.4×10^{-6}	0.1

Top & middle: Macroscopic wind/ambient parameters for 2:1, 140 km s^{-1}, 10^{-4}M$_\odot$yr^{-1} outflows. Bottom: Ion & Free electron fraction by Reynolds (1989)[a],Smith (1994b)[b],Arnaud & Rothenflug (1985)[c].

of Contact Discontinuity, the separation propagation is given in terms of the velocity of the unshocked wind relative to the inbound forward shock velocity $V_{\rm w} - U$. This interface introduces a sharp temperature and density gradient on each side, but the pressure equilibrium, i.e ram-pressure balance is sustained, this prevents the material from each side of the discontinuity from mixing initially. The separated material can later be mixed through the Kelvin-Helmholtz instability. The Kelvin-Helmholtz instability occurs when there is a velocity shear in a single continuous fluid, or where there is a velocity difference across the interface between two fluids. The theory predicts the development of instability and transition to turbulent flow in fluids of different densities moving at various speeds. Assuming stationary ambient medium, the velocity of the forward shock in terms of the density ratio $\eta = \rho_{\rm w(r)}/\rho_{\rm a}$ and wind velocity, is worked out through ram-pressure balance Equation 3.16 Norman & Winkler (1985).

$$U = \frac{\sqrt{\eta}}{1+\sqrt{\eta}} V_w \qquad \left[\mathrm{cm\,s^{-1}}\right] \tag{3.11}$$

The generated model set-up includes first approximation scenario where an inverse square density wind profile Equation 2.38 is expanding into a stationary uniform ambient medium. We introduce a conserved quantity of hydrogen nucleon density in the wind as $n_w = \rho_w/1.4m_p$ (with 10% helium abundance $n(He) = 0.1n_w$), set on a grid with relatively large injection radius of $R_w = 0.01\,pc$ chosen to resolve input sphere surface and corresponding to the inner radius of the circumstellar envelope (CSE) Gledhill (2005). Grid dimensions and scales are described below with a mass outflow rate set to 10^{-4} or 10^{-5} $M_\odot$ yr^{-1}, and employed to determine the initial set of macroscopic parameters generated in Section 3.1.3 and listed in Table 3.1. The outflows vary in wind ellipticity through anisotropic velocity profile with planeaxis aspect ratios of 1:1 spherical, 2:1 and 4:1 with axial speed ranging from $v_w \sim 40 - 200\,km\,s^{-1}$ winds. The computational grid is configured to match ellipticity ratio, with main simulation set to 2:1 and 4:1 amounting to 0.2×0.1 pc and 0.4×0.1 pc of spatial extent respectively, splitting the fixed grid into $3,200 \times 1,600$ and $6,400 \times 1,600$, zones with grid zone size of $\sim 10^{14}\,cm$. Atomic shocks get heated to $10^5\,K$, at shock velocities of $\sim 30 - 40\,km\,s^{-1}$, after which atomic cooling is dominant in high density thick shock front of $\sim 10^6\,cm^{-3}$ and cooling rates of $\Lambda \sim 10^{-13}\,erg\,s^{-1}\,cm^{-3}$ Smith & Rosen (2003), taken from cooling functions displayed in Figure 4.4. The above metric contributes to a characteristic cooling time of $t_{cool} = nkT/\Lambda \sim 10^8\,s$ and cooling length of $\sim 10^{14}\,cm$, same as the grid zone size and proves suitable for resolving emission in the shocked gas region. Within the post-shock zone, the cooling rate is proportional to wind density squared (see Section 4.1.1), resulting in $\Lambda \sim 10^{-15}\,erg\,s^{-1}\,cm^{-3}$, higher cooling time by a factor of 10 and a subsequent cooling length of $\sim 10^{15}\,cm$. Therefore, the chosen computational domain proves to be suitable for entire shock resolution. The axial $v_z = (z/R_w)v_w$ and plane $v_r = \epsilon(r/R_w)v_w$ speed components at (z, r) of inner spherical injection surface also matches the ellipticity ratio with ϵ parameter equal to 1, 0.5 or 0.25. Thus the speed on the surface is fixed by $v_z = v_w cos\theta$ and $v_r = \epsilon v_w sin\theta$ where θ is the polar angle. The ZEUS code does not separately track the abundance of ions, instead it is estimated as an abundance ratio with respect to H, tabulated in Table 3.1. A free electron abundance is set to 0.1 for simplicity. Atomic pPN elemental abundances are indicative and are likely to be different and varied. The input wind follows an inverse square density profile

$$n_{w(r)} = n_w \left(\frac{R_w}{r}\right)^2,\ R_{ppn} \geq r \geq R_w. \qquad \left[cm^{-3}\right] \tag{3.12}$$

With stationary and uniform ambient medium, we have thus chosen

$$n_a = 4 \times n_w \left(\frac{R_w}{R_{ppn}} \right)^2 . \qquad \left[\mathrm{cm}^{-3}\right] \tag{3.13}$$

The chosen ambient density value creates favourable conditions for propagating forward and backwards shocks to vary in strength, as the wind expands over the defined domain. This set-up enables the reverse shock to become dominant after passing through a set distance of $\mathrm{R_{ppn}} = 10\mathrm{R_w}$ in case of 1:1 spherical outflow. The factor of 4 in Equation 3.13 is chosen to slow down the advancing shock to $\sim 1/3\,\mathrm{v_w}$ for reverse shock generation at $\mathrm{r} = \mathrm{R_{ppn}}$ and $\eta_{\mathrm{w(r)}} = 0.25$. Therefore, the introduced winds with particle densities of above $\sim 10^5\,\mathrm{cm}^{-3}$ are highly overdense with respect to the ambient medium with $\sim 10^3\,\mathrm{cm}^{-3}$, resulting in an initial mass density ratio of $\eta_{\mathrm{o}} = \rho_w/\rho_{\mathrm{a}} \sim 25$ at the injection radius and an initial ballistic expansion with advancing shock of $\sim 5/6\,\mathrm{v_w}$ for all ellipticity cases. For non-spherical higher ellipticity outflows, the wind's working surface experiences the same slow down rate and a longer simulation time due to $\mathrm{R_{ppn}} = 20\mathrm{R_w}$ for 2:1 and $\mathrm{R_{ppn}} = 40\mathrm{R_w}$ for 4:1 winds, setting the final working surface velocity to $\sim 1/5\,\mathrm{v_w}$ and $\sim 1/9\,\mathrm{v_w}$ respectively. The temperature of the ambient medium is set to cold 20 K, and the input temperature of the wind is 500 K, resulting in ram-driven wind being over-pressured with respect to the ambient medium by a factor $\kappa_0 \sim 10^3$. We do not hydrodynamicaly involve interaction of He, O, S and Fe atoms, and take 10% helium abundance for determining specific heat ratio $\gamma = \frac{5}{3}$ and $\gamma = \frac{10}{7}$ of atomic and molecular media respectively in Section 3.1.2. The relative abundance of other atomic species shown in Table 3.1 is used in emission routines to determine the line flux, without having the atoms physically present on the computational grid.

3.7.1 Wind Timescales

Wind properties are described by Smith (2004). For a cylindrical outflow structure of constant mass loss rate and surface area $\mathrm{A_w}$, the mass loss is

$$\dot{M} = \rho_w V_w A_w \qquad \left[\mathrm{gm\,s}^{-1}\right] \tag{3.14}$$

Subsequently, inverse square density profile for constant wind velocity yields

$$\rho_w(r) = \rho_w \left(\frac{R_w}{r} \right)^2, \quad r \geq R_w \qquad \left[\mathrm{gm\,cm}^{-3}\right] \tag{3.15}$$

Where $\rho_{\rm w}$ and $\rm V_w$ are the density and terminal velocity at the input surface $\rm R_w$. The density falls off according to spherical symmetry $\rho \propto {\rm r}^{-2}$. The dynamic pressure equilibrium at the forward/back shock yields

$$P_w = (V_w - U)^2 \rho_w(r) = U^2 \rho_a, \quad V_w \gg U, \qquad \left[\mathrm{dyn\,cm^{-2}}\right] \tag{3.16}$$

Substituting wind density profile into ram pressure balance and evaluating for forward shock velocity

$$U = V_w \sqrt{\frac{\rho_w}{\rho_a}} \frac{R_w}{r}, \quad r \geq R_w \qquad \left[\mathrm{cm\,s^{-1}}\right] \tag{3.17}$$

Numerical simulations often cast input parameters in a dimensionless form. From now on the ratio of $\rho_{\rm w(r)}$ and $\rho_{\rm a}$ is defined as parameter $\eta = \rho_{\rm w(r)}/\rho_{\rm a}$. For a 'heavy' wind with $\eta \gg 1,$ and $\rm v_w \gg U$, the wind ploughs ahead. With the initial value of $\eta_{\rm o} = 25$, the leading shock is initially strong, moving with $\sim 5/6\,\rm V_w$. Upon reaching the $\rm r = R_{ppn}$ grid limit in spherical 1:1 case, η falls from 25 to 1/4, and $\rm U \sim \frac{5}{6}\,V_w$ drops to $\rm U \sim \frac{1}{3}\,V_w$. Therefore, these simulations focus on the transition phase in which the shell experiences a strong deceleration. In the latter stage, the timescale for the simulation is given by

$$t_{lim} = \int_{R_w}^{R_{ppn}} \frac{dr}{U}, \quad R_{ppn} \gg R_w \tag{3.18}$$

Final result used as limiting timescale for simulations is

$$t_{lim} = \frac{R_{ppn}^2}{2 V_w \sqrt{\eta_0} R_w} \qquad [\mathrm{s}] \tag{3.19}$$

The timespan of simulated models depends on the initial wind/ambient number density ratio, the velocity of the outflow, the input wind radius and the final axial grid extent. Keeping the constant initial number density ratio and velocity range the same for all three ellipticities restrains the modelled simulations between few 10^2 and few 10^5 years for 1:1 spherical 200 km $\rm s^{-1}$ and 4:1 40 km $\rm s^{-1}$ outflows respectively.

3.7.2 Specific Heat Ratio

Integrating the chemical set up of pPN into the system allows to work out system's γ algebraically and incorporate this important parameter into ZEUS, n is the number of Hydrogen nuclei per unit volume, f is the ratio of the number of Hydrogen molecules per unit volume, to the number of Hydrogen nuclei per unit volume. The total number of hydrogen nuclei present per unit

volume is as follows

$$n(H_{nuclei}) = 2n(H_{mol}) + n(H_{atoms}) \tag{3.20}$$

In terms of number density of hydrogen molecules

$$n(H_{mol}) = 1/2[n(H_{nuclei}) - n(H_{atoms})] \tag{3.21}$$

Therfore the number density ranges between 0 and 1/2. A new useful parameter is introduced that represents the above range with f = 0 being fully atomic, dissociated molecular hydrogen and f = 1/2 corresponds to fully molecular medium, $n(H_{mol}) = fn(H_{nuclei})$. Rearranging Equation 3.21 for number density of atomic hydrogen yields

$$n(H_{atoms}) = (1 - 2f)n(H_{nuclei}) \tag{3.22}$$

Simplifying notation

$$n(H) = (1 - 2f)n \tag{3.23}$$

Adding 10% abundance of helium yields

$$n(He) = 0.1n \tag{3.24}$$

Summing all three chemical constituents in terms of n brings the abundance of H nucleons in wind medium to

$$< n >= n(H) + n(H_2) + n(He) = (1 - 2f)n + fn + 0.1n = (1.1 - f)n \tag{3.25}$$

The system's total specific heat at constant volume c_v is determined by the sum of the individual specific heats of the components that are in tern determined by the number of degrees of freedom.H_2 possesses three translational and two rotational degrees of freedom making five degrees of freedom in total. The additional two degrees of freedom are ignored due to high temperatures of activiation greater than $6,000\,\mathrm{K}$ at which H_2 would undergo complete dissociation into atomic constituents.

$$c_v = c_v(H) + c_v(H_2) + c_v(He) = \frac{3}{2}k_B\frac{n(H)}{< n >} + \frac{5}{2}k_B\frac{n(H_2)}{< n >} + \frac{3}{2}k_B\frac{n(He)}{< n >} \tag{3.26}$$

With k_B representing the Boltzmann constant. Substituting into above equation and solving for c_v yields

$$c_v = \frac{3.3 - f}{2.2 - 2f} k_B \qquad \left[\text{erg K}^{-1}\,\text{gm}^{-1}\right] \tag{3.27}$$

The specific heat ratio $\gamma = c_p/c_v$ together with specific heat at constant pressure $c_p = c_v + k_B$ bring further constraint into the system

$$\gamma = \frac{c_p}{c_v} = \frac{c_v + k_B}{c_v} = \frac{5.5 - 3f}{3.3 - f} \tag{3.28}$$

Hence $\gamma = \frac{5}{3}$ and $\gamma = \frac{10}{7}$ stand for atomic and fully molecular mediums respectively. Specific heat ratio is an essential input parameter in ZEUS-3D. Other elements such as He, O, S and Fe are considered in the code through the cooling functions as tracers to provide diagnostics.

3.7.3 Macroscopic Parameters

In the simulations presented in this work, we have fixed the grid parameters for pPN radius at: $R_{ppn} = 0.1 \sim 0.4\,\text{pc}$; input wind radius, $R_w = 0.01\,\text{pc}$; the initial wind temperature of $T_w = 500\,\text{K}$ and cold ambient medium at $T_a = 20\,\text{K}$. From the Equation 2.38, the density of the wind at R_w is

$$\rho_w = \frac{\dot{M}}{4\pi R_w^2 v_w} \qquad \left[\text{gm cm}^{-3}\right] \tag{3.29}$$

Number of H nucleons in the wind is:

$$n_w = \frac{\rho_w}{m_p(1 + 4he)} \qquad \left[\text{cm}^{-3}\right] \tag{3.30}$$

Where $he = 0.1$ is the 10% helium abundance with respect to H nucleons, yielding to $n_w = \rho_w/1.4m_p$. For ambient medium, the abundance of H nucleons is

$$< m >= n(H) + 4n(He) = n(1 + 4he) \tag{3.31}$$

Substituting the above for ambient medium density yields,

$$\rho_a = m_p n_a < m >, \qquad \left[\text{gm cm}^{-3}\right] \tag{3.32}$$

Yielding to $n_a = \rho_a/1.4m_p$. Ambient and wind medium gas pressure is

$$p_a = \rho_a \frac{kT_a}{\overline{m}} \qquad \left[\text{dyn cm}^{-2}\right] \tag{3.33}$$

$$p_w = \rho_w \frac{kT_w}{\overline{m}} \qquad \left[\mathrm{dyn\,cm^{-2}}\right] \tag{3.34}$$

With $\overline{\mathrm{m}}$ being the abundance ratio of hydrogen nucleons in ambient/wind mediums

$$\overline{m} = m_p \frac{< m >}{< n >} = m_p \frac{(1 + 4he)}{(1.1 - f)}, \qquad \left[\mathrm{gm}\right] \tag{3.35}$$

The speed of sound for ambient $\mathrm{c_a}$ and wind $\mathrm{c_w}$ mediums is

$$\begin{aligned} c_a &= \sqrt{\frac{\gamma p_a}{\rho_a}}, \qquad \left[\mathrm{cm\,s^{-1}}\right] \\ c_w &= \sqrt{\frac{\gamma p_w}{\rho_w}} \qquad \left[\mathrm{cm\,s^{-1}}\right] \end{aligned} \tag{3.36}$$

The relation for the internal energy of ambient medium and wind is

$$\begin{aligned} e_a &= p_a/(\gamma - 1), \qquad \left[\mathrm{erg\,cm^{-3}}\right] \\ e_w &= p_w/(\gamma - 1), \qquad \left[\mathrm{erg\,cm^{-3}}\right] \end{aligned} \tag{3.37}$$

A complete set of initial parameters used in simulations is derived with the above equations and are generated with zeus-energy.pro routine. After which the initial wind/ambient conditions are plugged into the input file, inzeus shown in Figure 3.1 to form the building block of our simulations for further computation by executable xdzeus. The input data is tabulated and summarised in cgs units for convinience and is presented in Appendix A.

Chapter 4

Molecular Cooling

Molecular envelopes of H_2 have been detected around PNe Jaminet et al. (1991). Near-infrared observations have broadened our knowledge of pPN in which H_2 emission has been mapped and compared to the atomic emission Fang et al. (2018). Protoplanetary nebula being the predecessor of PNe should have similar molecular envelopes and sustain a stable molecular environment due to a relatively low surface temperature of central stars $T_* < 15,000\,K$. Davis et al. (2005), have detected H_2 line emission in discrete shock fronts in the bipolar lobes of investigated PN's and pPN's. pPN's are faint and are best observed in the near-infrared due to the domination of emission from radiative shocks, the dust obscuration and the absence of strong photoionisation since the star has not turned on the ultraviolet switch Davis et al. (2005). In the case of fast collimated winds, the excitation is caused by passing shock waves. The shock wave interacts with molecular medium, exciting the gas and populating the lower ro-vibrational levels of the electronic ground state of H_2. Subsequent cooling via radiative decay from excited states results in shocked H_2 near-infrared emission. Numerous H_2 detections in post-AGB stars have been confirmed Riera et al. (2003). Collimated fast winds of post-AGB stars shape and shock their surrounding nebula. We tend to compute K band $\sim 2\,\mu m$ H_2 and optical atomic emission, via collisional de-excitation scenario driven by J-shock environment to properly reproduce the observed HV molecular emission near the source along the body of the lobe of the bipolar outflow such as noted in recent observations of CRL 618 Lee et al. (2009).

We are foremost interested in finding the configurations that can plausibly explain the expanding pPN as seen in H_2 emission lines. Hrivnak et al. (2008) found the emission to be from the walls of the nebula producing an ellipsoidal velocity structure. Gledhill et al. (2011) identified a fast

wind impinging on the cavity walls and tips. van de Steene et al. (2008) detected shock-excited molecular hydrogen emission as well as collisionally-excited emission lines from [OI], [CI], and [FeII]. Finally, Gledhill & Forde (2015) used molecular hydrogen emission lines together with hydrogen and helium recombination lines to explore the distribution of molecular and atomic gas and distinguish a range of evolutionary stages. This chapter will review the structure, and energy transitions of H_2 molecule, discuss the uses of ro-vibrational lines as diagnostic tools for studying post-AGB objects. Additional aim of this study is to computationally investigate whether the high velocity post-AGB winds are also capable of producing strong [Fe II] 1.64 μm and [Si II] 6716 λ forbidden lines, the [O I] 6300 λ airglow line, and Hα 6563 λ line within the same collisionally-excited scenario with J-shocks as a source of atomic optical emission.

4.1 Shock-Excited H_2

In the shock wave, H_2 is collisionally excited or dissociated and is reformed on grain surfaces in the post-shock gas Wakelam et al. (2017). Molecular hydrogen H_2 undergoes rapid formation in high density regions on dust grains out of HI. AGB outflows are the main source of dust deposition in ISM, hence they also serve as a catalyst for formation of molecular hydrogen. Single HI atomic hydrogen is able to bind to the surface of dust grains by Van der Waals forces 0.04 eV Hollenbach & Salpeter (1971). HI moves on the surface of the grain by quantum mechanical tunnelling until it finds a lattice defect 0.1 eV. An unpaired second HI lands on the grain and forms an H_2 diatomic molecule. With no unpaired e^-, the molecular hydrogen soon detaches from the grain into the gas phase again. The process described above is known as the three-body interaction

$$H + H + grain \rightarrow H_2 + grain \tag{4.1}$$

The collisional dissociation reaction is

$$\begin{aligned} H_2 + H &\rightarrow 3H \\ H_2 + H_2 &\rightarrow 2H + H_2 \end{aligned} \tag{4.2}$$

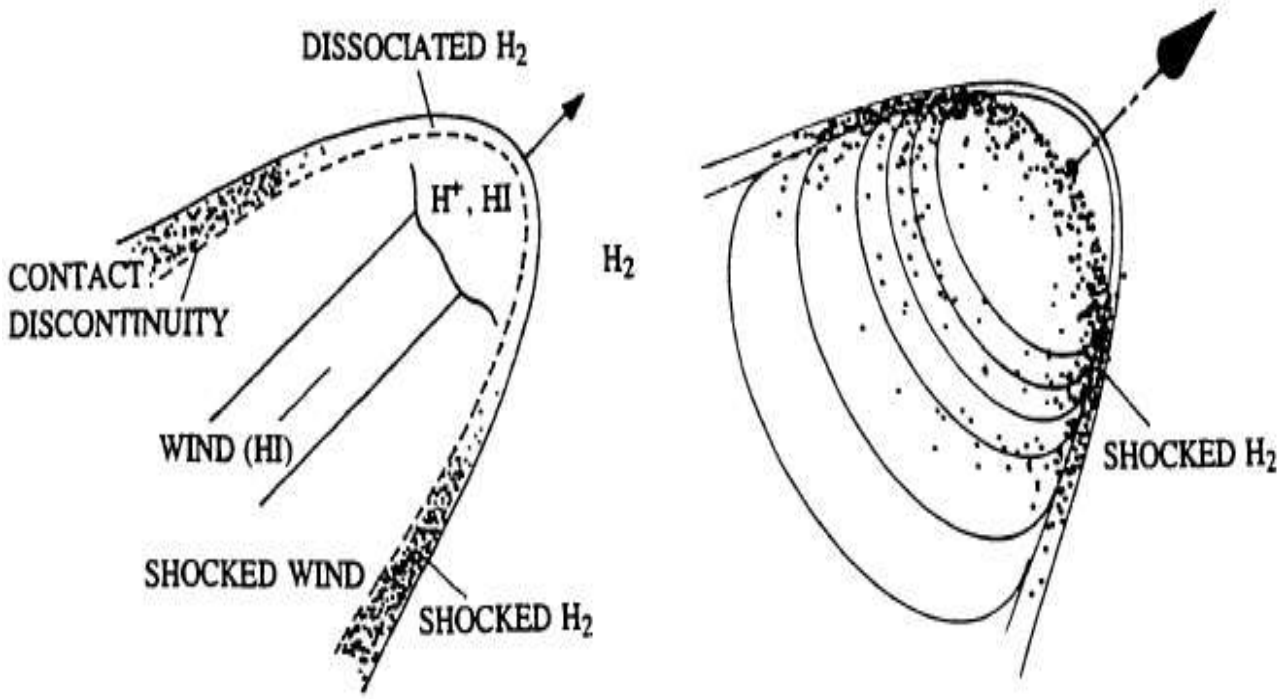

Figure 4.1: A schematic by Bally & Lane (1991) presenting a dissociating J-type shock as seen from an angle of ~ 45 degrees from the propagation direction producing arch-like H_2 emission.

The rate of synthesis of molecular hydrogen by Suttner et al. (1997) presented in Equation 4.2 (top reaction) taking place on grain sufraces is

$$k_R = 3 \times 10^{-17} \left(\frac{T^{0/5}\, f_a}{1 + 0.4(T + T_{dust})^{0.5} + 0.2T + 0.08T^2} \right) \qquad \left[\mathrm{cm^3\, s^{-1}}\right] \tag{4.3}$$

where,

$$f_a = [1 + 10\,000 \exp(-600/T_{dust})]^{-1} \tag{4.4}$$

With T_{dust} fixed at 20 K. Recent studies show H_2 formation on the grain surfaces allows tracing of the magnetic fields in space Andersson et al. (2013). Dust grains experience reaction force from the newly formed H_2 causing the grain to spin and align itself with the magnetic field due to Radiative Alignment Torque. Once H_2 is formed, it can be dissociated/excited by passing shock waves resulting in molecular emission. The process above is similar to atomic emission where electrons transition between quantised energy levels via absorption or emission of photons of certain wavelengths. The molecular and atomic emission is governed by quantum mechanical rules of selection with molecular transitions involving vibrational and rotational transitions of lower energy than electronic transitions in atoms. Rigid rotor model serves for description or ro-vibrational energy transitions of simple diatomic molecules of two point masses at a fixed internuclear distance.

4.1.1 Ro-vibrational H_2 Lines

A simple diatomic molecule has two bound nuclei orbiting each other about their common centre of mass. Assuming no change in internuclear distance between the two particles, therefore establishing rotational energy via classical approach with angular momentum of J = Iω where ω is angular velocity, I is moment of inertia, L is angular momentum and kinetic energy = $^1/_2\, I\omega^2$ yields

$$E_{rot} = \frac{L^2}{2I} \qquad \left[\mathrm{eV}\right] \tag{4.5}$$

With moment of inertia defined as

$$I = \sum m_i x_i^2 \qquad \left[\mathrm{gm\,cm^2}\right] \tag{4.6}$$

And reduced mean mass parameter

$$\mu = \frac{m_1 m_2}{m_1 + m_2} \tag{4.7}$$

Defining moment of inertia with reduced mass yields, where r is the bond length

$$E_{rot} = \frac{L^2}{2\mu r^2} \tag{4.8}$$

Angular momentum is quantised and is related to angular momentum quantum number

$$L^2 = \hbar^2 J(J+1) \qquad \left[\mathrm{erg^2\,s^{-2}}\right] \tag{4.9}$$

Finally, the change in rotational energy is given by

$$\Delta E_{rot} = \frac{\hbar}{\mu r^2}\Delta J \tag{4.10}$$

Rotational levels have been assigned the following labelling scheme: $\Delta J = -2, -1, 0, +1, +2$ corresponding to O, P, Q, R and S branches respectively. Identically, the vibrational energy levels are

$$\Delta E_{vib} = (\Delta v + \frac{1}{2})\hbar\omega \qquad \left[\mathrm{ev}\right] \tag{4.11}$$

Where v is the vibrational quantum number $\nu = 0, 1, 2, 3....$ Shock waves trigger the rotational and vibrational energy levels of constituent H_2 molecules. Molecular hydrogen has no dipole moment and possesses a permanent quadrupole moment enabling rotational transitions in O, Q and S branches, corresponding to change in rotational quantum number ΔJ = -2, 0, 2, respectively.

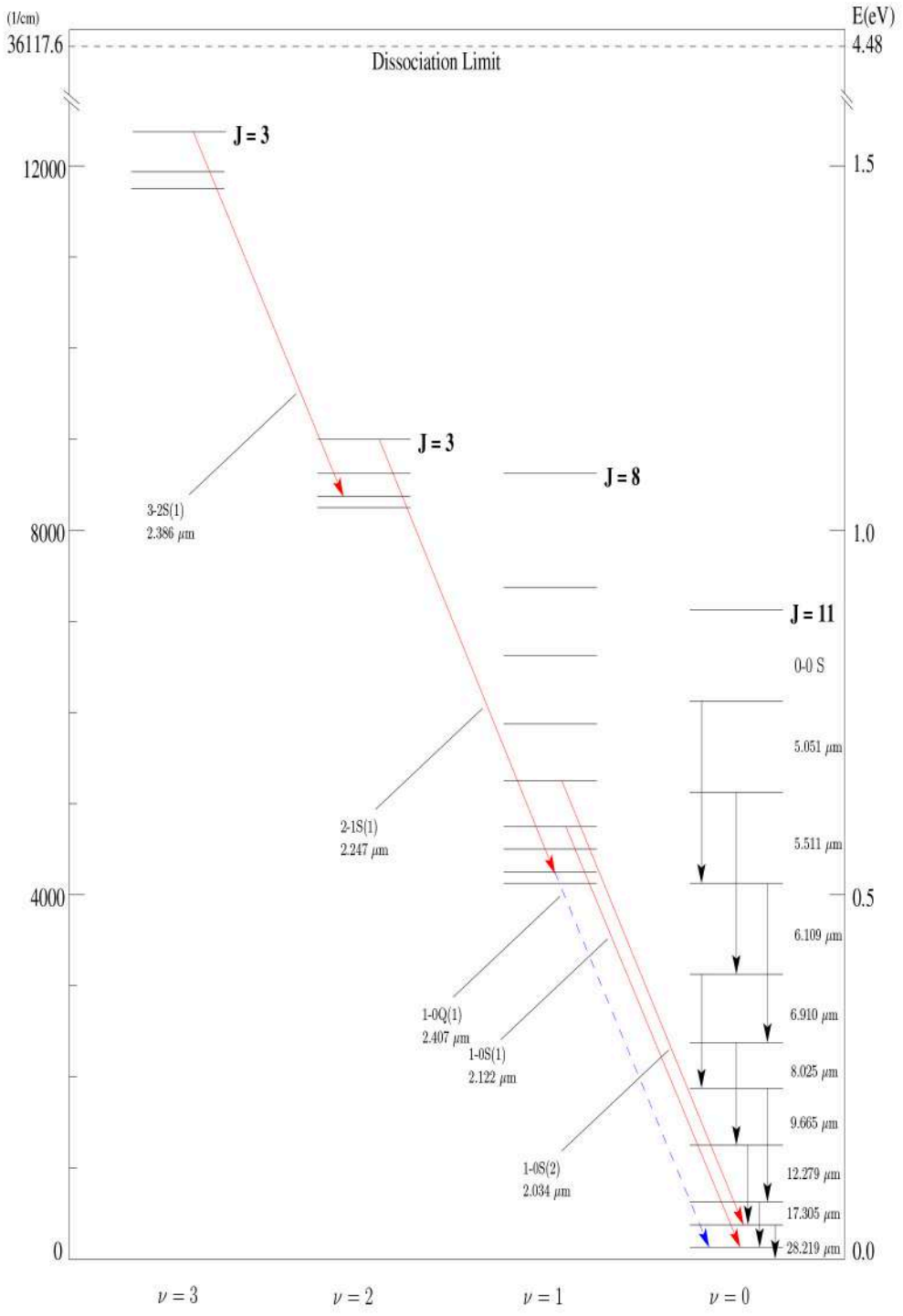

Figure 4.2: The ro-vibrational energy level diagram for the H2 molecule, showing some of the transitions, visible within the SINFONI[1] wavelength range, observed in some PPNe/PNe. The S- and Q-branch transitions are given by the red (solid) and blue (dashed) lines, respectively. Energy diagram by Kwok (2007)[p.62].

Molecule	Wavelength λ	Transition type	Gas Temperature	Shock velocity
H_2	2.121 μm	$1 \rightarrow 0$ S(1) vibrational	6,600K	30–50 km s^{-1}
	2.248 μm	$2 \rightarrow 1$ S(1) vibrational	12,500K	
CO	2.6 mm	$J = 1 \rightarrow 0$ rotational	5.5K	
[O I]	63 μm	$^3P_1 \rightarrow ^3P_2$	230K	
[C II]	158 μm	$^3P_{3/2} \rightarrow ^2P_{1/2}$	92K	
[Fe II]	1.64 μm	$^4D_{7/2} \rightarrow ^4F_{9/2}$	10,000K	>50 km s^{-1}

Table 4.1: Emission line wavelengths, gas temperature and shock velocities. H_2 emission trace high temperature regions locating passing shock waves. CO emission trace cool gas Moraghan (2008).

Of these, the most common observed ro-vibrational transitions which are useful as diagnostics is the $1 \rightarrow 0\,\mathrm{S}(1)$ line at $2.12\,\mu$m with $\Delta\nu = 1 \rightarrow 0$ and $\Delta\mathrm{J} = 3 \rightarrow 1$ and a lower energy $2 \rightarrow 1\,\mathrm{S}(1)$ line at $2.24\,\mu$m with $\Delta\nu = 2 \rightarrow 1$ and $\Delta\mathrm{J} = 3 \rightarrow 1$ labelled in Figure 4.2. Both lines are ortho transitions with equal upper degeneracies and fall within the near-infrared K-band window. H_2 transitions between ro-vibrational levels must satisfy J = 0, ± 2, with J = ± 1 forbidden R branch due to lack of dipole moment. In the above Table 4.1, H_2 $1 \rightarrow 0\,\mathrm{S}(1)$ energy level is at 6000 K, at this value H_2 would undergo quick dissociation, hence the molecule radiates mainly in this line at the temperature of 2000 K. The rise of emission in near-infrared H_2 lines can be contributed to several mechanisms that populate the ro-vibrational levels of the electronic ground state. There are 14 bound vibrational levels possessed by the ground electronic state, with each of those levels being split into a number of rotational levels as indicated in Figure 4.3. Therefore, each electronic state contains a set of ro-vibrational levels identified by a vibrational quantum number v and a rotational quantum number J. The dissociation energy of H_2 is 4.48 eV, which corresponds to a molecular kinetic velocity of $\sim 20\,\mathrm{kms}^{-1}$.

Cold molecular clouds of few ~ 10 K are insufficient to excite the lowest ro-vibrational energy levels corresponding to temperature values of ~ 6000 K. There are several mechanisms that could contribute to the population of the ro-vibrational levels of the electronic ground state and excite the emission of near infrared ro-vibrational H_2 lines. One mechanism is due to UV fluorescence near hot stars, which leads to population of both, high and low v states. In this case, the H_2 molecule transitions into excited electronic state via absorption of UV photons in Lyman and Werner bands with energies between $11 \sim 14$ eV corresponding to UV wavelengths of $0.1\,\mu$m. A subsequent decay leads to molecule dissociation or decay back into ro-vibrational levels of the ground state followed by decays through a cascade of ro-vibrational transitions within the ground electronic state shown in Figure 4.3. Another excitation mechanism is collisional excitation of H_2 molecules in the hot post-shock gas, which is the main topic of interest in this work. The driving engine for this mechanism of ro-vibrational levels population is collisions of H_2 with other

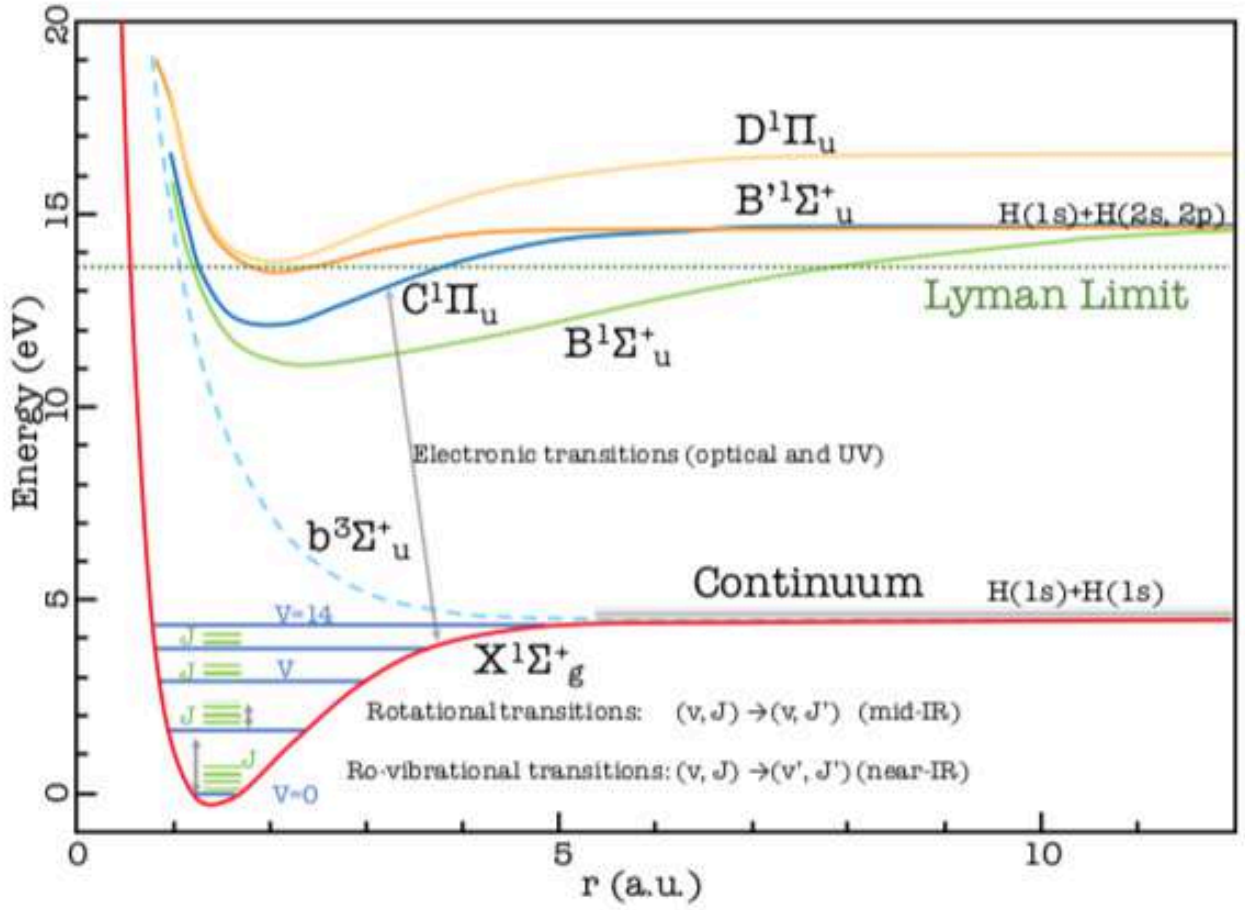

Figure 4.3: Electronic potentials of H_2 as a function of the separation between both atoms. The subscripts g and u stand for gerade (even) and ungerade (odd) symmetries. Vibrational and rotational levels are indicated schematically for the lowest electronic level. Energy levels are indicated with respect to the ground state (v = 0). Levels with vibrational excitation v > 14, in the continuum region, lead to the dissociation of the molecule. Adapted from Le Petit (2002).

H_2 molecules, atoms or electrons. The gas temperature is typically of order $2000 \sim 3000\,\mathrm{K}$, thus collisional excitation tends to populate the lower v vibrational levels, higher temperatures will lead to dissociation as mentioned previously. The signatures of shock-excited H_2 emission are the absence of transitions from high v levels and a low $2 \rightarrow 1\,\mathrm{S}(1)/1 \rightarrow 0\,\mathrm{S}(1)$ line ratio ($\sim 1:10$). The wind causes a hydrodynamical jump i.e J-shock, followed by a radiative cooling layer. This layer is a combination of a hot zone in which H_2 is dissociated, producing dissociative cooling, and generating atomic line emission, followed by the radiative cooling zone, where the remaining H_2 is excited without dissociation as depicted in Figure 4.1. We model an optically thin ambient medium, hence no absorption occurs. The excited molecules then decay via electric quadrupole transitions on time scales of order $10^6\,\mathrm{s}$ Black & Dalgarno (1976).

The line strength ratio comparison enables one to distinguish between the two excitation mechanisms. Shull & Hollenbach (1978) note that above critical densities of $n_{\mathrm{crit}} = 10^5\,\mathrm{cm}^{-3}$, the

line ratio will resemble those expected for a gas in local thermal equilibrium (LTE) with collisional de-excitation becoming important with cooling rate $\Lambda \propto n(H_2)$. In low density regime of $n < n_{crit}$, H_2 molecule in an excited level radiates before being collisionally de-excited, and the cooling rate is proportional to $\Lambda \propto n(H_2)^2$, which is also used to calculate the cooling length in post-shock zones in Section 3.1 and determine grid size resolution. The $2 \rightarrow 1\,S(1)/1 \rightarrow 0\,S(1)$ line ratio can be used as an indicator of shock or fluorescent excitation, for high density $n > n_{crit}$ shocked H_2 gas, the ratio can be ~ 0.1. The ratio values depend on shock velocity and pre-shock gas density, with shocked H_2 capable of producing values as high as ~ 0.25 (Smith, 1995). On the other hand FUV pumping in low density regions produces pure fluorescence value of ~ 0.5, however, in high density gas regions at $n > n_{crit}$ and exposed to high fluxes, FUV pumping line ratio can mimic the ~ 0.1 ratio found in shocked gas Hollenbach & Natta (1995).

4.1.2 Internal Energy & Molecular Cooling

Physical conditions taking place in pPNe is determined with molecular emission and absorption lines. The parameters of density, temperature and velocities is estimated with line flux examination. One of the main aims of this research is an accurate portrayal of chemical reactions taking place in molecular outflows. Modelling actual electron transitions in atoms and ro-vibrational transitions in molecules during a simulation would be computationally intensive. The molecular routines employed by ZEUS-3D used in this thesis is based on equations by Suttner et al. (1997).

The molecular/atomic cooling sequence is as follows: the particles (atoms, ions and molecules) kinetic energy is increased with a passage of supersonic shock wave through a medium, which in turn leads to an increase in collision rates and subsequent excitation energy. For the case of ions and atoms, the electrons transition from more stable energy states to higher, less stable atomic orbitals. Excited states being less stable result in electrons cascade back towards more stable energy states undergoing excess emission in the form of EM radiation. In the case of molecules, the increase of energy results in excitation of ro-vibrational states of molecular bonds, subsequently H_2 loose thermal energy by collisions with other H_2 molecules, atoms, or electrons by a process of collisional de-excitation

$$A + B \rightarrow A + B^* \tag{4.12}$$

$$B^* \rightarrow B + \hbar\omega \tag{4.13}$$

The above reaction depicts two elements A and B in the ground state, where B^* stands for the

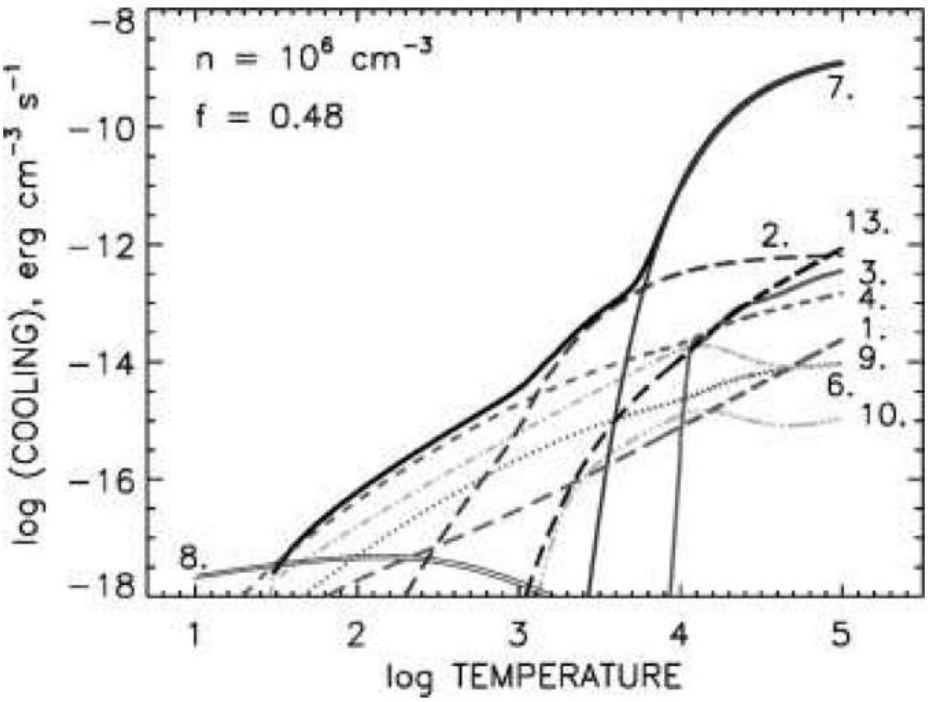

Figure 4.4: A log graph displaying the cooling functions at given density n, and molecular fraction of H_2, f. The temperature determines the cooling rates. The numerical labelling indicates; 1. Gas-Grain cooling, 2. H_2 ro-vibrational cooling, 3. Atomic cooling, 4. H_2O rotational cooling, 5. H_2O and H vibrational cooling, 6. vibrational H_2O and H_2 cooling, 7. H_2 dissociation cooling, 8. H_2 reinformation heating, 9. CO rotational cooling, 10. CO and H_2 vibrational cooling, 11 CO and H vibrational cooling, 12. [O I] 63μm fine structure cooling 13. OH rotational cooling. Figure credit Smith & Rosen (2003)

exited state of element B and $\hbar\omega$ is the energy of emitted photon. To enable further reduction in computational cost, the exponents values of the cooling functions have been previously pre-calculated and tabulated in look-up tables. The temperature threshold is also designed to further increase the speed of the code. Hence, the molecular cooling routine is divided into high and low temperature regime with $T > 3,000\,K$ and $T < 3,000\,K$ respectively to consider certain coolants as important. An example of cooling rates against temperature is presented by Figure 4.4 taken from Smith & Rosen (2003). The added cooling term represents the cooling function, which is a function of three variables, the gas temperature T, density of hydrogen nuclei n, and molecular hydrogen abundance f. The internal energy equation Equation 3.8 is altered by including an additional cooling term in internal energy loss through radiation and chemistry per unit volume Λ.

$$\rho\frac{\partial}{\partial t}e + p\nabla\cdot\mathbf{V} + \Lambda(T,n,f) = 0, \qquad \left[\mathrm{erg\,cm^{-3}\,s^{-1}}\right] \tag{4.14}$$

Cooling from the dissociation of molecular hydrogen with reaction rate coefficients takes the

form

$$\Lambda = 7.18 \times 10^{-12}(n_{H_2}^2 k_{D,H_2} + n_H n_{H_2} k_{D,H}), \qquad \left[\mathrm{erg\,cm^{-3}\,s^{-1}}\right] \tag{4.15}$$

The first term is the 4.48 eV of dissociation energy of H_2 multiplied by reaction rate coefficients. The collisional dissociation rates for Equation 4.2 (middle & bottom reaction) are determined by Shapiro & Kang (1987).

$$k_{D,H} = 1.2 \times 10^{-9} \exp(-52400/T) \times [0.0933 \exp(17950/T)]^{\beta}, \qquad \left[\mathrm{cm^3\,s^{-1}}\right] \tag{4.16}$$

$$k_{D,H_2} = 1.3 \times 10^{-9} \exp(-53300/T) \times [0.0908 \exp(16200/T)]^{\beta}, \qquad \left[\mathrm{cm^3\,s^{-1}}\right] \tag{4.17}$$

With coefficient β being the fraction of thermally released energy.

$$\beta = \left\{1.0 + n\left[2f\left(\frac{1}{n_2} - \frac{1}{n_1}\right) + \frac{1}{n_1}\right]\right\}^{-1}. \tag{4.18}$$

The following two approximations represent critical densities for dissociation by collisions of molecular hydrogen with atomic hydrogen, n_1, and with itself, n_2.

Collisional heating in shock waves triggers the rotational and vibrational excitation of constituent H_2 molecules. The separate vibrational and rotational cooling functions were listed by Smith & Rosen (2003) and take the form

$$\Lambda_{col} = n_{H_2}\left[\frac{L_v^H}{1 + (L_v^H)/(L_v^L)} + \frac{L_r^H}{1 + (L_r^H)/(L_r^H)}\right] \qquad \left[\mathrm{erg\,cm^{-3}\,s^{-1}}\right] \tag{4.19}$$

Where the vibrational L_v^H, L_v^L and rotational L_r^H, L_r^L cooling coefficients of high and low density are provided in Appendix B along with a set of 13 sub-functions for other chemical species by Smith & Rosen (2003).

4.1.3 K-Band Integration & Rate Coefficients

Molecular hydrogen possesses a permanent quadrupole moment $\Delta J = -2, 0, 2$ enabling rotational transition in O, Q and S branches respectively. Of these, the most common observed ro-vibrational transitions which are useful as diagnostics are the $1 \rightarrow 0\,S(1)$ line at 2.12 μm and lower energy $2 \rightarrow 1\,S(1)$ line at 2.24 μm, both lines are ortho transitions with equal upper degeneracies that fall within the range of NIR K-band window and are used as diagnostic in Section 5. Power cooling law coefficients are listed in Appendix B. The line emission properties are

determined from the population density of the upper level N_j. A non-equilibrium chemistry is assumed with non-LTE (NLTE) state, in which the vibrational levels are not distributed according to the Boltzmann distribution. Unlike the vibrational levels, rotational levels within each rotational band are assumed to be in LTE and follow the Boltzmann distribution due to much lower radiative transition rates. The time in between collisions in NLTE is long enough to allow for radiative decays to lower levels via spontaneous radiative transitions. This possibility reduces the LTE upper level population fraction to new NLTE fraction which we call the deviation factor η_j. Since light, symmetric H_2 molecule has small moment of inertia with weak quadrupole transitions and widely spaced rotational levels leading to large energy difference of 512 K for J = 2 to J = 0. Hence the deviation factor is calculated in a stepwise fashion for subsequent ro-vibrational transitions.

$$\eta_j = \frac{V_1/V_0}{1 + V_1/V_0} \tag{4.20}$$

where V_1 and V_0 are the populations of the first and ground vibrational levels and V_1/V_0 is given by

$$V_1/V_0 = \frac{\Gamma_{1,0} \exp(-T_v/T)}{\Gamma_{1,0} + A_{1,0}} \tag{4.21}$$

$$V_2/V_1 = \frac{V_{2up}}{V_{2down}} \exp(-5648/T) \tag{4.22}$$

V_1/V_2 is given as a ratio of upper and lower population levels within v = 2

$$V_{2up} = \Gamma_{2,1} + (1 + A_{1,0}/\Gamma_{1,0})\,\Gamma_{2,0} \tag{4.23}$$

$$V_{2down} = \Gamma_{2,1} + \Gamma_{2,0} + A_{2,0} + A_{2,1} \tag{4.24}$$

$$\Gamma_{j'j} = k^{j'j}_{H_2}\, n(H_2) + k^{j'j}_{H}\, n(H) \tag{4.25}$$

$\Gamma_{j'j}$ is the Einstein coefficient for J → J − 2 transition and $T_v = 5987$ K is the temperature difference between the upper and lower vibrational levels and $A_{j',j}$ is the radiation coefficients or electric quadrupole spontaneous transition probability by Turner et al. (1977) that are averaged for J level in the given v state: $A_{1,0} = 8.3 \times 10^{-7}\,s^{-1}$, $A_{2,0} = 4.1 \times 10^{-7}\,s^{-1}$ and $A_{2,1} = 1.1 \times 10^{-6}\,s^{-1}$; $g_0 = g_1 = g_2 = 1$ and transition energies; $E_{1,0}/k = E_{2,1}/k = 0.5\,E_{2,0}/k = 5860$ K by Hollenbach & McKee (1979). $k^{j',j}_{H_2}$ and $k^{j',j}_{H}$ are the de-excitation rate coefficients for collisions with H_2 and H tabulated in Table 4.2. These parameters form a three-level cooling system for v = 0, 1, 2 vibrational levels with condensed rotational levels of a given vibrational state. Since the excitation energy of the first vibrational state is $T < 6000$ K and vibrational coling is also below that

energy at $T < 4000\,\mathrm{K}$ and can be approximated with the above condensed level system without the need for considerable computational expense of treatment of each individual excited level. N_j is then given by

$$N_j = \frac{\mathrm{g_j}\, n(\mathrm{H_2})\, \eta_j \exp\left(-T_r/T\right)}{\mathcal{Q}\left(T\right)} \quad \left[\mathrm{cm^{-3}}\right] \tag{4.26}$$

where $\mathrm{g_j} = (2I+1)(2J+1)$ is the degeneracy of the level satisfying the exclusion principle $\mathrm{I} = 0$ para states are paired with even J, while $\mathrm{I} = 1$ ortho states are paired with odd J, hence the line intensity is proportional to the statistical weight of 21 for both transitions and $\mathrm{T_r} = 1015\,\mathrm{K}$ is the temperature difference between the upper and lower rotational levels within $\mathrm{V_j}$. $\mathcal{Q}\left(\mathrm{T}\right)$ is the molecule partition function which is taken as $\mathcal{Q}\left(\mathrm{T}\right) = \left(\mathrm{T}/40.75\right)\left[1 - \exp\left(-5\,987/\mathrm{T}\right)\right]^{-1}$ for H_2. The radiation contribution for each shock element can then be determined from

$$\dot{E}_{1,0} = \frac{N_j \mathrm{Z_j\, h\, c}}{\lambda_j} \qquad \left[\mathrm{erg\,s^{-1}\,cm^{-3}}\right] \tag{4.27}$$

$$\dot{E}_{2,1} = 1.35\,\frac{\mathrm{V_2}}{\mathrm{V_1}}\,\dot{E}_{1,0} \quad \left[\mathrm{erg\,s^{-1}\,cm^{-3}}\right] \tag{4.28}$$

where h is Plank's constant, c is the speed of light respectively and $\mathrm{Z_j}$ is the spontaneous radiative decay tabulated by Turner et al. (1977) $\mathrm{Z_{1,0}} = 3.47 \times 10^{-7}\,\mathrm{s^{-1}}$ and $\mathrm{Z_{2,1}} = 4.98 \times 10^{-7}\,\mathrm{s^{-1}}$. The $\dot{\mathrm{E}}$ K-band spectra is then integrated over the $\pi/2$ degrees due to cylindrical symmetry, thus maintaining a constant volume for each element of gas that is projected on to the 2–D CCD image in Section 5.9. The total volumetric emission is summed up through the whole grid and multiplied by the zone size cubed resulting in the dissipation of energy from the whole bow in Figs 6.9 - 6.11. A 3–D data cube is constructed along with the velocity information to produce PV diagrams in section 6.2.

Table 4.2: H_2 collisional de-excitation rates.

Collision type	Rate coefficients ($cm^3\,s^{-1}$)	Reference
Vibrational H-H_2	$k_H^{(1,0)} = \begin{cases} 1.4\times10^{-13}\exp[(T/125)-(T/577)^2], & T < T_v \\ 1.0\times10^{-12}T^{1/2}\exp(-1000/T) & T > T_v. \end{cases}$	1, 2
	$k_H^{(2,1)} = 4.5\times10^{-12}T^{1/2}\exp(-(500/T)^2)$	3
	$k_H^{(2,0)} = 1.6\times10^{-12}T^{1/2}\exp(-(400/T)^2)$	3
Vibrational H_2-H_2	$k_{H_2}^{(1,0)} = \sigma_0\overline{v}\exp(-4.2\Delta E/k)/(T+1200))$	1, 2
	$k_{H_2}^{(2,1)} = k_{H_2}^{(1,0)}$	3
	$k_{H_2}^{(2,0)} = 0$	3

Parameters: $T_v = 1635\,K$, inelastic rotational cross section $\sigma_0 = 10^{-16}\,cm^2$ and $\overline{v} = (8kT/\pi m_H)^{1/2}$ is the average thermal speed of an incident hydrogen molecule with $\Delta E = E(v\prime, J\prime) - E(v, J)$ denoting decrease in de-excitation rates. Tabulated collisional de-excitation rate coefficients are presented graphically in Fig. 4.5.
References: Lepp & Shull (1983)[1], Shull & Beckwith (1982)[2], Hollenbach & McKee (1979)[3].

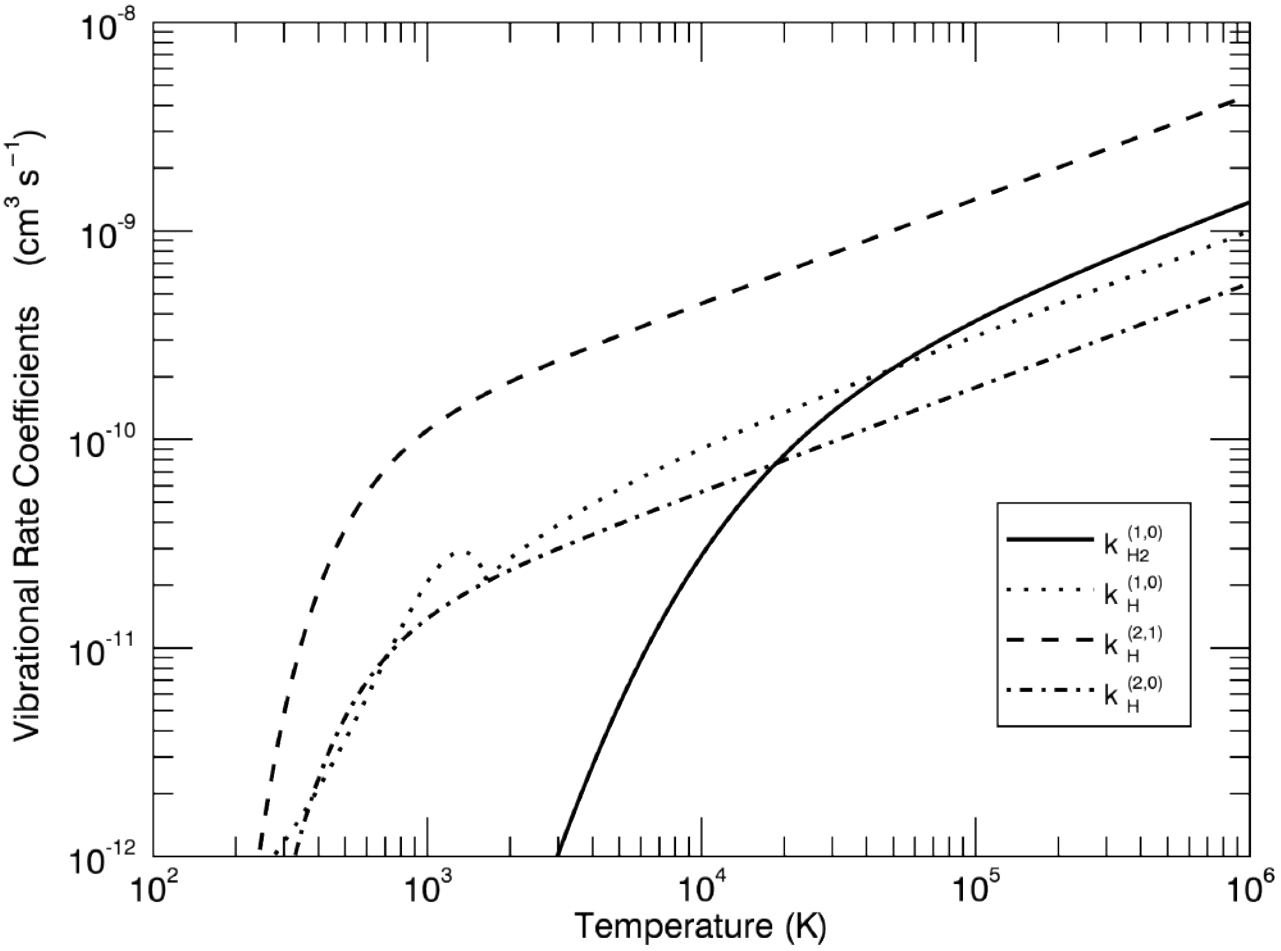

Figure 4.5: Collisional de-excitation rate coefficients for H-H_2 and H_2-H_2 collisions from Table 4.2 indicating higher rates for vibrational H-H_2 collisions in the range of $10^2 - 10^4\,K$ and dominant cooling by collisional dissociation for $T > 4000\,K$.

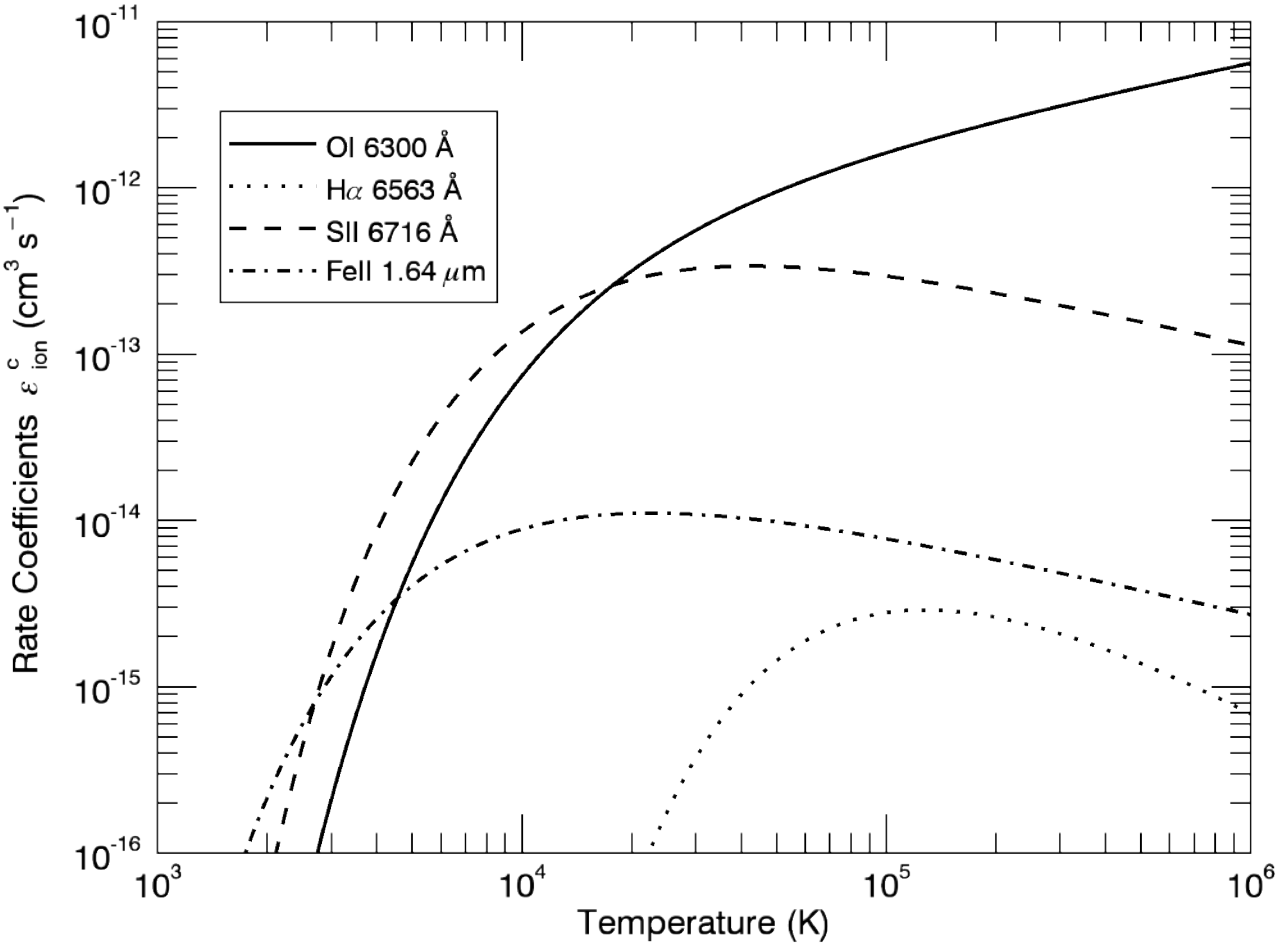

Figure 4.6: Rate coefficients ϵ^{c}_{ion} for recombination and collisions multiplied by relative abundancies for: [OI] Reynolds (1989), Hα Raga et al. (2015), [SII] Reynolds (1989) and [FeII] Smith (1994b)

4.2 Atomic Recombination

The total emission element dL by recombination within a volume element dV is

$$d\mathrm{L} = 4\pi j_{ion} dV \qquad [\mathrm{erg\,s^{-1}}]. \tag{4.29}$$

The emission rate is given by

$$j_{ion} = \frac{h\nu}{4\pi}\,\epsilon_\lambda \quad [\mathrm{erg\,s^{-1}\,cm^{-3}\,sr^{-1}}] \tag{4.30}$$

Thus, the emissivity of atomic elements is dependent on the number densities of free electrons $\mathrm{n_e}$ and ions $\mathrm{n_{ion}}$ (here in units of $\mathrm{cm^{-3}}$), the temperature dependent production rate coefficients for recombination and collisions, $\epsilon^{c}_{ion}(T)$, in units of $\mathrm{cm^3\,s^{-1}}$ as presented in Fig. 4.6, and the emitted photon energy of corresponding wavelength in erg. where ϵ_λ is a photon emissivity of

corresponding ion wavelength

$$\epsilon_\lambda = \epsilon^c_{ion}(T)\, n_e\, n_{ion} \quad [\mathrm{cm^{-3}\,s^{-1}}] \tag{4.31}$$

Given that we know the temperature of the medium and the number densities, we can calculate the emissivity. All four line emission models are described below in detail.

Atomic optical emission correspond to shorter wavelengths compared to molecular emission due to electronic transitions being the highest ∼1 eV. In molecular case, the intermediate vibrational transitions are of order $\sim 10^{-3}$ eV, followed by rotational transitions with lowest order of $\sim 10^{-6}$ eV. The lower mass molecules such as, H_2, have higher energies corresponding to the emission in near infrared i.e $1 \rightarrow 0\,\mathrm{S}(1)$ of 0.58 eV and $2 \rightarrow 1\,\mathrm{S}(1)$ of 0.55 eV, while CO, NH_3 etc are heavier and generate ro-vibrational transitions in the millimetre range typically.

4.2.1 [OI] 0.63 μm Emission

The rate coefficient Reynolds (1989) for [OI] production by spontaneous de-excitation (0.63 μm transition):

$$L_{OI} = h\nu_{oi}\, 5.3 \times 10^{-9} \frac{\Omega(T)}{T_4^{0.5}} \exp^{-2.28/T_4}\, n_e n_{\mathrm{O^0}} \quad [\mathrm{erg\,s^{-1}\,cm^{-3}}] \tag{4.32}$$

where $n_{\mathrm{O^0}}$ is abundance of neutral oxygen, $\Omega(\mathrm{T}) = 0.39\,\mathrm{T}_4^{0.95}$ is the $^3\mathrm{P} \rightarrow {}^1\mathrm{D}$ collision strength by Saraph (1973) for ionised medium of $0.4 < \mathrm{T}_4 < 1.2\,\mathrm{K}$. With $\mathrm{T}_4 = \mathrm{T}/10^4\,\mathrm{K}$ satisfying J-shock condition.

4.2.2 [Hα] 656.28 nm Emission

We have used the rate coefficient for Hα production line by $\mathrm{H^+}$ and $\mathrm{e^-}$ recombination and spontaneous de-excitation as given by Dong & Draine (2011)

$$L_{\mathrm{H}\alpha} = h\nu_{h\alpha}\, 1.17 \times 10^{-13}\, T_4^{-0.942-0.031\ln(T_4)} \exp^{-14.036/T_4}\, n_e n_{\mathrm{H^+}} \quad [\mathrm{erg\,s^{-1}\,cm^{-3}}] \tag{4.33}$$

n_e and $n_{H^+} = n_w$ are number densities of electrons and positrons respectively. The resulting Balmer lines are evaluated by Model 4 (AWAA), which generally indicates greater transition energies, ram pressure and temperatures.

4.2.3 [SII] 671.6 nm Emission

The rate coefficient for [Si II] in the optical range, 6716 λ transition Reynolds (1989)

$$j_{\mathrm{Si\,II}} = h\nu_{si}\, 7.3 \times 10^{-8} T_4^{-0.5} \exp^{-2.14/T_4} n_e n_{\mathrm{S^+}} \quad [\mathrm{erg\,s^{-1}cm^{-3}}] \tag{4.34}$$

$n_{\mathrm{S^+}} = n_w\, \epsilon_{Si\,II}\, \chi_e^{Si\,II}(T)$ and $n_w = n_{\mathrm{H}}$. With the ion abundance value of $\sim 10^{-5}\,\mathrm{cm^{-2}}$ Reynolds (1989), the ionisation fraction $\chi_{\mathrm{e}}^{\mathrm{Si\,II}}$(T) is calculated by logarithmic interpolation, based on Arnaud & Rothenflug (1985).

4.2.4 [FeII] 1.64 μm Emission

Collisional excitation rates for non-dissociative J-shock model by Smith (1994b) for 1.64 μm near-infrared [Fe II] line

$$j_{FeII} = h\nu_{feII}\, 1.9 \times 10^{-3} \exp^{-1.13/T_4} /(1 + 9.74^4 \sqrt{T_4})\, n_e n_{\mathrm{Fe^+}} \quad [\mathrm{erg\,s^{-1}cm^{-3}}]. \tag{4.35}$$

Strong UV radiation at later PN stage combined with heating from H_2 reformation could contribute to the [Fe II] surface brightness. Here, we use a fixed ionisation fraction of 0.1. With $\mathrm{n_{Fe^+}} = \mathrm{n_{Fe\,II}}$ notation.

Chapter 5

Hydrodynamic Properties

5.1 Memory & CPU Run Time

The main numerical code limiting factor is resolution of the computational domain. By establishing high resolution over the computational grid enables us to provide additional fine structure and accurate shock physics. It is essential for the cooling function routines described in Section 4.1 to cast macroscopic variables from high resolution of the radiative shock. A slight variation of input parameters may lead to a significant change in the resulting structure of the downstream flow due to turbulent nature of simulated outflows. As a result, the simulation of high resolution images requires great computational resources, which in turn increases the CPU run-time. Due to the nature of our models requiring input variations of mass-loss, wind profile of pPNe outflows, and wind velocity, all simulations require generation of high resolution images to provide the necessary information for the change in resultant flux-lines.

ZEUS-3D was used to execute the calculations on a 2D grid. The cylindrical coordinate system was used where z and r coordinates were replaced with x and y directions respectively, the azimuthal coordinate ϕ is ignored. The profile of the wind is introduced from a spherical surface of radius R_w. Note that the wind is not introduced from a symmetrical spherical surface due to cylindrical grid and limited resolution used in simulations. If spherical coordinate system was used, the wind would have been launched from a symmetrical spherical surface. The symmetry boundary enables us to calculate half of the produced flow. The bottom half of the wind is a mirror reflection of the top half, this set-up is used for display purposes and also enables us to reduce the CPU run-time of simulations. Following the process of compilation, ZEUS-3D is run

from an executable file xdzeus, the sequence is listed in the flow chart of Figure 3.2. The size of the grid and physics variables included determines the RAM, required for the executable file. The grid itself is constructed of arrays of data that possess the variable values in the grid zones. There are five arrays required for the 3D hydrodynamic simulation: pressure, density and three components of velocity. An additional array is required for molecular cooling. Another additional 11 scratch arrays are used for storage of intermediate values with extra 5% taken up by ghost zones at the grid boundaries. As an example it is possible to calculate the size of the xdzeus executable file. Our 2D axisymmetric hydrodynamic simulations of protoplanetary nebula (pPN) requires seven arrays of variables: density, pressure, and two components of velocity, axial and radial, two spatial coordinates of z and r and an additional array for molecular/atomic cooling. Every variable requires 8 bytes of memory, hence a spherical 1:1 1600×1600 hydrodynamic run would require

$$(1600 \times 1600 \times (7 + 11) \times 8) + 5\% = 378\,\mathrm{MB}$$

Increase in grid zones subsequently increases the size of the executable file. The 2:1 3200×1600 executable requires 774 megabytes and the highest resolution xdzeus occupies 1548 megabytes of RAM.

The executable produces Hierarchical Data Format (HDF) files, where each array variable requires 4 bytes of memory. In order to output the arrays of seven variables at $t_{lim}/\mathrm{dthdf} = 23$ time intervals with dthdf $= 50\,\mathrm{yr}$ is the time between each HDF file dump listed in Figure (fig:inzeus). A complete 1600×1600 simulation run, would require a space of

$$1600 \times 1600 \times 7 \times 23 \times 4 = 1648\,\mathrm{MB},$$

where one HDF file at 1600×1600 grid resolution requires 17.9 megabytes. An individual file at 3200×1600 resolution requires 35.8 megabytes of RAM with 4:1 file occupying 71.6 megabytes. The total RAM needed for different resolutions also depends on the time intervals needed to cover the computational grid, for constant dthdf with 2:1 and 4:1, the number of intervals is 23 and 92 with total space of 11.5 GB and 26.3 GB respectively.

We simulated a $140\,\mathrm{km\,s^{-1}}$ spherical hydrodynamic outflow corresponding to typical CSE expansion profiles of pPNe at the following grid resolutions listed in Table 5.1. Figure 5.3 shows that by increasing the resolution, the flow depicts small structural and eddy details. The overall morphology of the outflow is affected by resolution. A clearer picture of the process is provided

Table 5.1: Resolution vs CPU run time for 2D axisymmetric hydrodynamic simulations.

Resolution	Zone Size (cm)	CPU time
1300×650	4.74×10^{14}	24060 seconds
2600×1300	2.36×10^{14}	N/A
3200×1600	1.93×10^{14}	346380 seconds
3800×1900	1.61×10^{14}	N/A

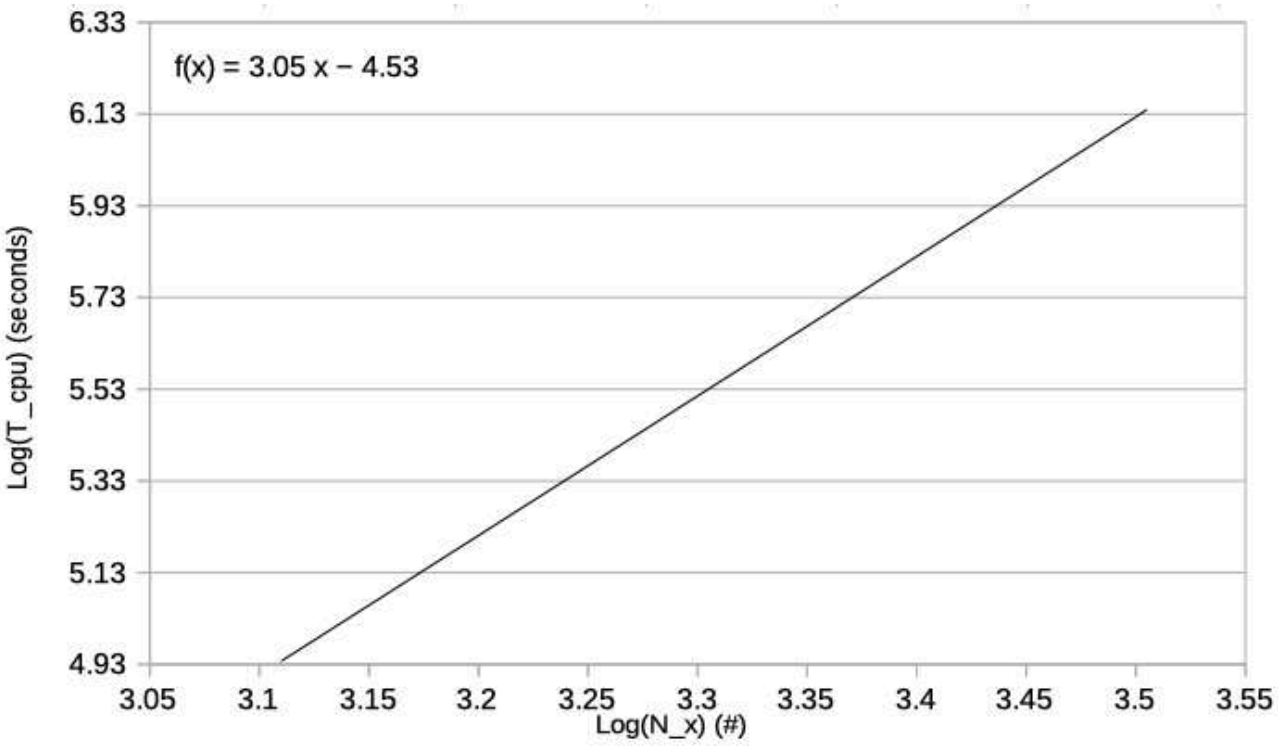

Figure 5.1: A plot of the log of the CPU time against the $\log N_x$. The slope of 3 (D=2, D+1=3) implies that for 2D simulations the run time is proportional to number of zones cubed.

by time sequence animation[1]. It enables the viewer to trace the development of instabilities, shock physics and temperature gradients.

The CPU run-time t_{cpu} is the time it takes in seconds for a computer system to run the complete simulation,

$$t_{cpu} = N_x^{D+1}, \qquad [\mathrm{s}] \tag{5.1}$$

parameter N_x stands for the number of zones in the direction of propagation, D is the number of spatial dimensions and +1 includes time as a dimension. The time values in Table 5.1 were multiplied by a factor of 4 to estimate the true CPU time due to mirroring effects. A slope of 3 is obtained in Figure 5.1 as expected for a 2D simulation. A small discrepancy in the slope may result from the slightly higher sound speed at high resolutions.

[1] `http://astro.kent.ac.uk/~in32/ppn.html`

5.2 Resolution Study

A feature of the molecular simulations, as exemplified in Figure 5.2, are the growth of fingers along the shock surface. The fingers grow through hydrodynamic shell instabilities and we find that the sound speed of the cold shell determines the maximum coherent wavelength. Observationally, there is considerable evidence that shells may turn into shrapnel, after breaking up into filaments and fingers as well as cometary-shaped globules (Taylor et al. 1984; Matsuura et al. 2009; Ueta et al. 2005; Santander-García et al. 2015).

Such protrusions can also arise through the clumpy nature of the ambient medium (Steffen et al. 2013), through variable winds or through hydrodynamical instabilities (Stone et al. 1995). Such hydrodynamic instability also dominates jet-driven molecular interactions in which the advancing bow shock splits up into many mini-bows (Rosen & Smith 2004a). However, these are enhanced in wind-driven flows through the Rayleigh-Taylor instability as the heavy shell rapidly decelerates. In addition, strong cooling in the shocked zone can very easily result in growing protrusions which promote thermal (Smith & Rosen 2003) as well as hydrodynamical instability.

High resolution images generate more structure, however the general outflow profile appears to be independent of resolution simulation as depicted in Figure 5.3. The computational run-time is also factored in, therefore low-resolution studies are commenced for hydrodynamics simulations of overall propagation, whereas high-resolution simulations enable accurate data generation for molecular cooling implementation with zone size becoming a determinant factor for molecular cooling lengths resolution. Generally, the reduction in zone size leads to automatical increase in the time resolution, which in turn generates an increase in CPU run time.

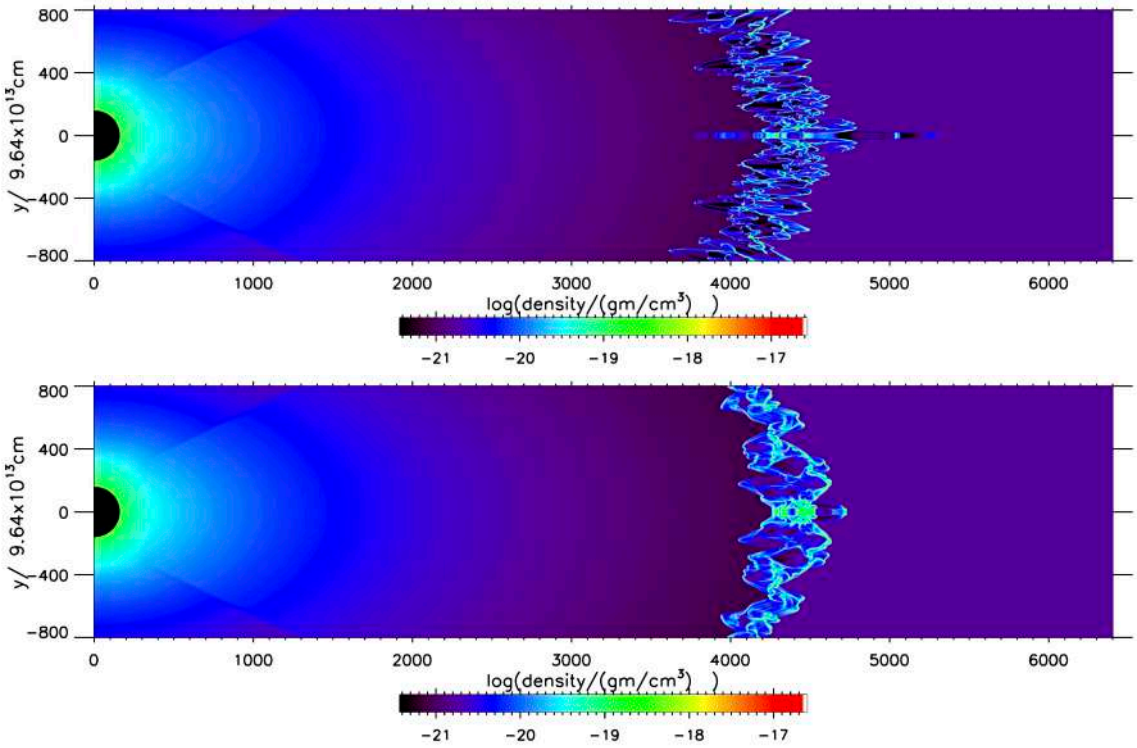

Figure 5.2: Molecular wind/ambient (upper panel) and atomic wind/ambient (lower panel) density distributions for 2:1 elliptical winds of speed $V_w = 140\,\mathrm{km\,s^{-1}}$ along the symmetry axis. Only the displayed portion has been simulated here in order to confirm the detailed features at high resolution of the global winds modelled below. The wind is driven from a shell at 0.01 pc for a time of 1,000 years, onto a grid of length 0.2 pc. An inner mask is superimposed to improve the colour range.

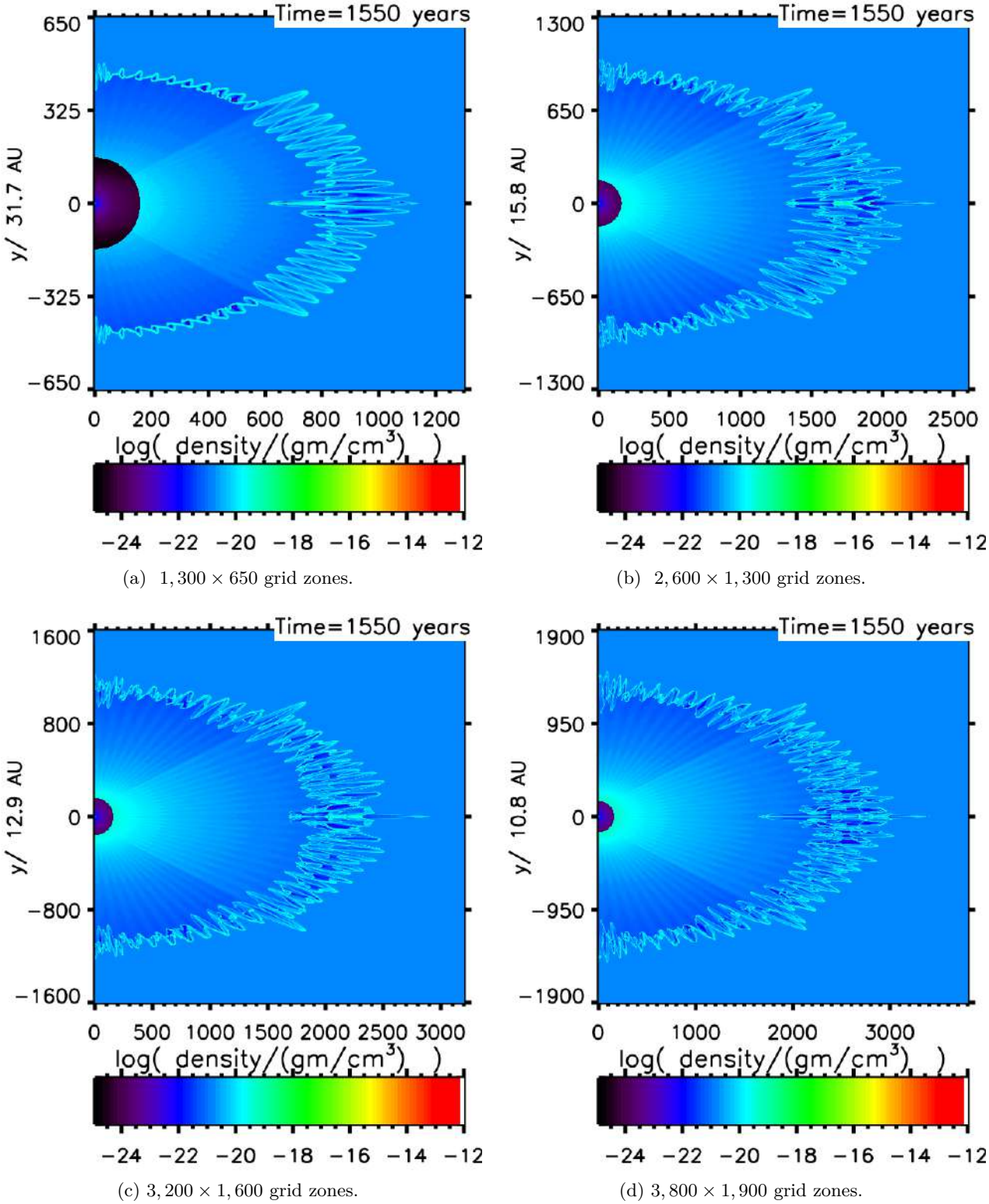

(a) $1,300 \times 650$ grid zones.

(b) $2,600 \times 1,300$ grid zones.

(c) $3,200 \times 1,600$ grid zones.

(d) $3,800 \times 1,900$ grid zones.

Figure 5.3: Cross-sectional distributions of mass density parameters $\mathrm{gm\,cm^{-3}}$ for a 2:1 H_2 140 km s^{-1} wind into H_2 ambient medium at low/high grid resolutions. The lower half of each distribution is the mirror image of the top half. A mask over the central wind region, rmask is set to cover up the radius around the wind input radius, $r_w = 0.01\,\mathrm{pc}$. rmask varies for different resolution used, in case of 3200×1600, rmask ~ 160 grid zones.

5.3 Numerical Errors

Axially symmetrical outflows were computed using cylindrical coordinates. The simulated wind structures produce spikes of unknown origin at $\sim \pi/4$ degress relative to axial axis. The spikes can be either numerical or real in nature. This phenomena can be investigated further with 3D models and gaussian smoothing. Also, at this stage of simulation, the velocity-composition maps Fig. 5.3 show a sharp feature at the forward centre of the bow as a result of cylindrical input structure. Both, the spikes and sharp forward feature are independent of resolution, and could be Rayleigh-Taylor instability coupled with thermal instability. To further resolve the developed structures, 3D simulations should be implemented. As a solution, a narrow conical wind rather than a complete hemisphere can be introduced to enable achievement of wind-ambient interaction at higher resolution.

5.4 Density Corrugation

It is noted that by taking cylindrical symmetry, we achieve the high resolution necessary to study radiative shocks. However, this often introduces well-known numerical artefacts. In particular for this study, the imposed numerical approximation to a sphere is over a finite number of zones. Therefore, in addition, we manually break the spherical symmetry by implementing small wavelength corrugations on to the input density. In so doing, we can verify how far the results depend on the numerical approximation. As shown in Fig. 5.4, imposing perturbations (right panel) does modify the stability of the shell, promoting growth much more uniformly around the shell. The shell structure is not directly related to the imposed oscillations. We thus suggest below that the sound speed in the thin interaction layer determines the wavelength of the perturbations which grow. We also find that the evolving complex shell structure is not significantly influenced when elliptical winds are present. The symmetry of the underlying physical problem is automatically broken.

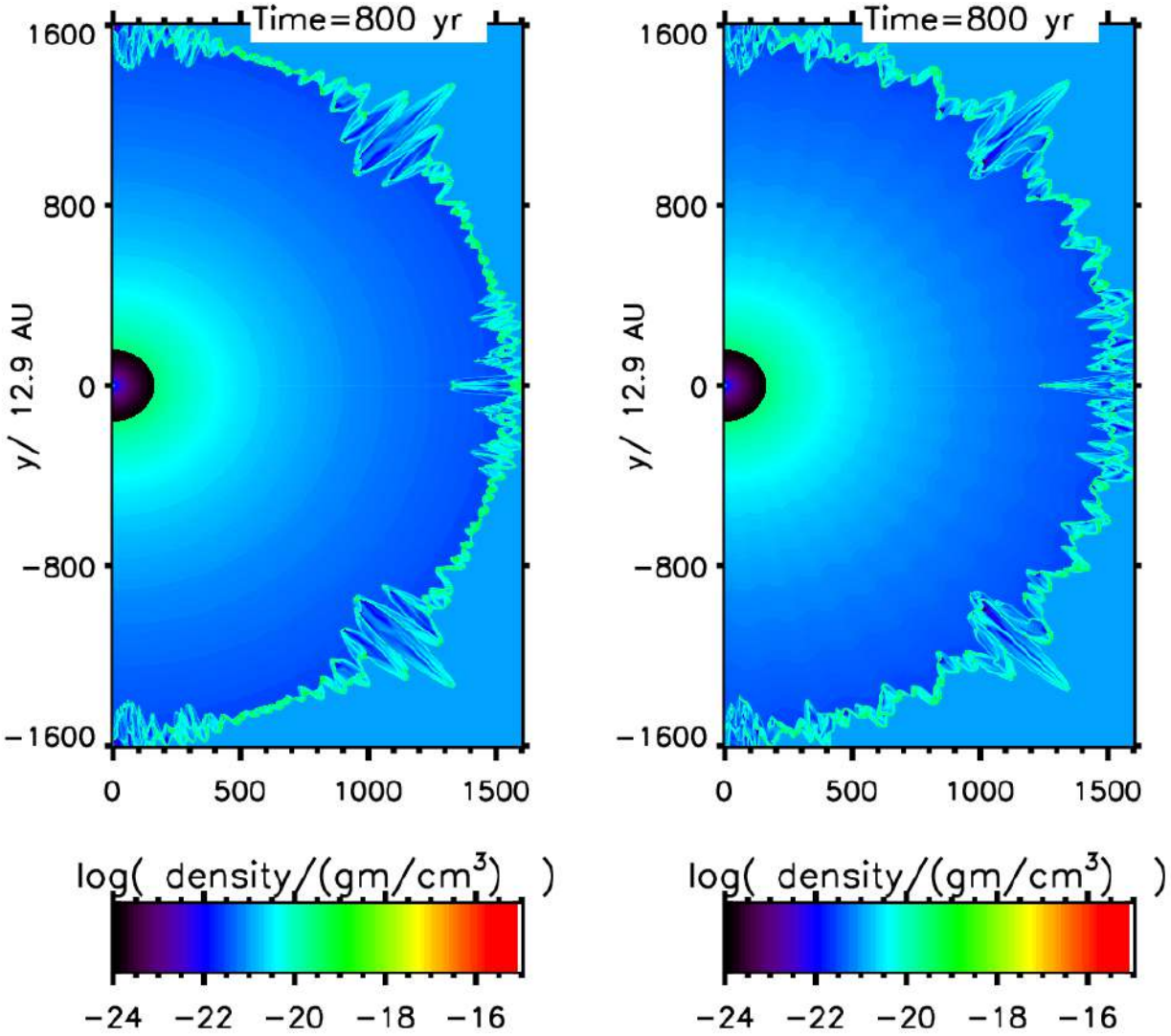

Figure 5.4: Comparison of simulations for a uniform radial wind (left panel) and a density-corrugated wind (right panel). Cross-sectional distributions of the density after 750 years for a spherical molecular wind of radial speed 200 $\mathrm{km\,s^{-1}}$ into a uniform ambient molecular medium. The imposed density corrugations in the wind are of ten sinusoidal waves of amplitude 2.5% between the axis and 90°. The cross-section displayed is 0.1 pc × 0.2 pc and the input sphere is of radius 0.01 pc corresponding to 160 zones.

5.5 Velocity and Compositional Study

The simulation in this work generate highly collimated outflows emerging from the central star of pPN with shock velocities within the range of $80 \sim 200\,\mathrm{km\,s^{-1}}$. The outflow profile was developed with elliptical shape to generate higher velocity values along the axial axis of symmetry. One of the main questions to answer was the following: how is the chemical composition and emission affected by the general propagation?

To provide investigational data, four different compositional models are generated to cover all variations and provide a basis from which to extract the evolution of low to high wind speed and molecular to atomic composition of wind and ambient mediums. The molecular tracers are examined to develop quantitative comparison for the models evaluated in this research.

To enable generation of near-infrared and optical line flux, we have modified ZEUS-3D with molecular and atomic cooling functions discussed in Section 4.4. The generated 2D axisymmetric simulations are executed on 3200×1600 grid zones with the wind radius, $R_w = 0.01\,pc \sim 160$ zones per wind radius. Extent of the 2:1 grid R = 0.2 pc Z = 0.1 pc. The modelled wind is heavy in all cases with $\eta_0 = 25$. For molecular models, the molecular hydrogen abundance is set to 0.5 (fully molecular). The abundance of helium is He = 0.4, Section 3.1.3. The temperature of the ambient medium is set to 20 K, and the input temperature of the wind is 500 K. In all cases the wind is over-pressured with respect to ambient medium. Re-compilation is necessary only if the grid resolution is altered or physics modules and wind profile is modified. The actual input parameter in inzeus corresponding to wind speed is the Mach number,

$$M_w = v_w/c_w, \tag{5.2}$$

where the speed of sound in the wind is c_w. The sound speed for atomic wind ($2.32\,km\,s^{-1}$) is slightly higher than the molecular wind ($1.58\,km\,s^{-1}$) listed in Appendix A.

Figs. 5.5- 5.10, and Figs. 5.15- 5.18 along with Appendix D contain a hydrodynamical distribution visualisation of four different models:

- Model 1 molecular wind/molecular ambient medium MWMA $f_w = 0.5$, $f_a = 0.5$
- Model 2 molecular wind/atomic ambient medium MWAA $f_w = 0.5$, $f_a = 0.0$
- Model 3 atomic wind/molecular ambient medium AWMA $f_w = 0.0$, $f_a = 0.5$
- Model 4 atomic wind/atomic ambient medium AWAA $f_w = 0.0$, $f_a = 0.0$

With each plot containing four panels with a colour gradient scaling. A range of speeds was taken and all macroscopic parameters are tabulated in Table 3.1, more parameters are listed in Appendix A. The panels in Figs. 5.5- 5.10 display the following time-dependent information: panels (a),(b),(c) show molecular fraction grid distribution, i.e the ratio of hydrogen molecules to the total number of hydrogen nuclei ($n(H_2)/n$). This quantity enables us to trace molecular dissociation of shocked H_2. (d) shows the plot of total molecular fraction abundance. In all cases, the density and pressure profiles fall off as $\propto r^{-2}$ and the velocity components stay constant along the radial lines. The spikes appear to be independent of resolution, and could be Rayleigh-Taylor instability combined with thermal instability, numerical issues are also involved.

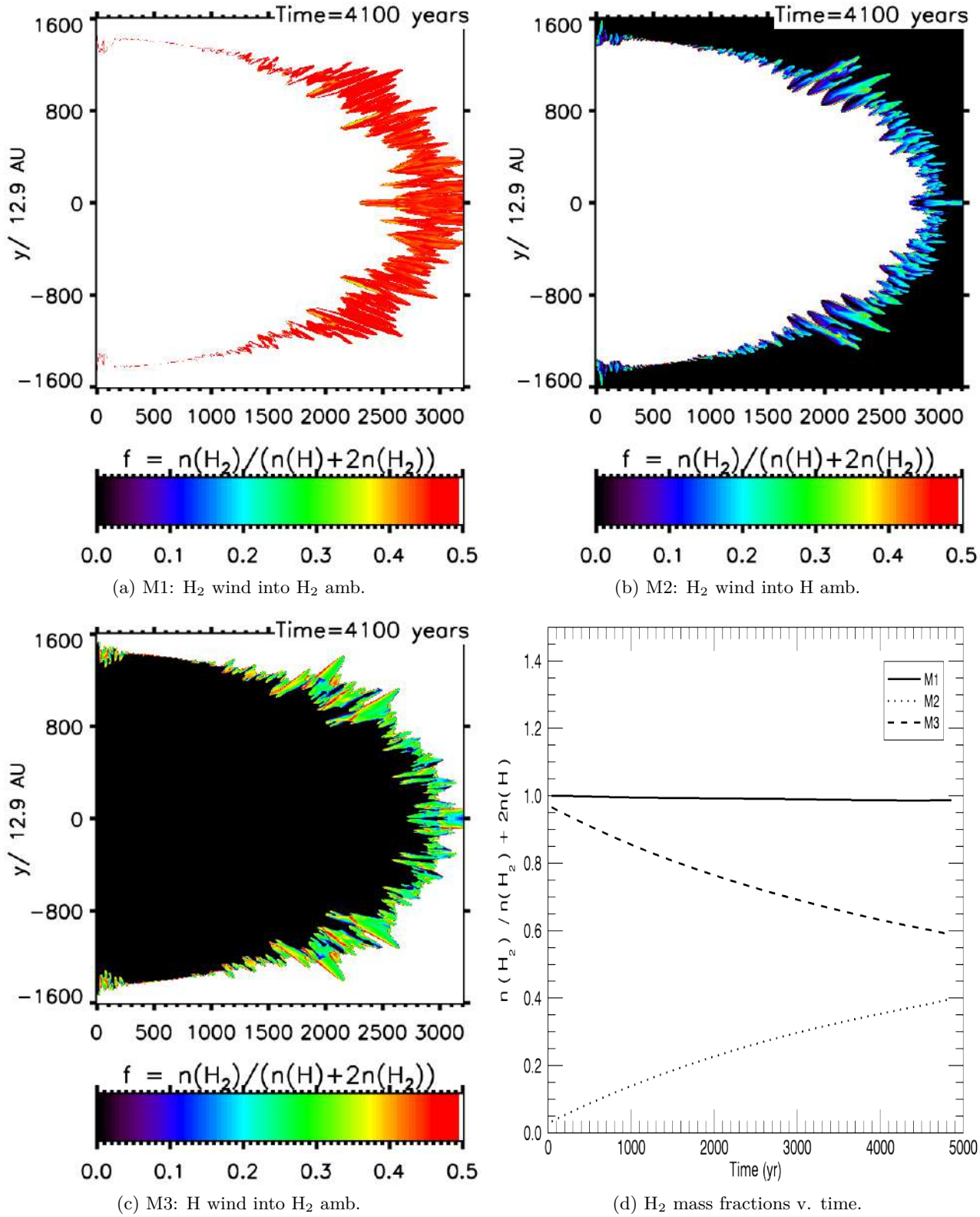

(a) M1: H_2 wind into H_2 amb.

(b) M2: H_2 wind into H amb.

(c) M3: H wind into H_2 amb.

(d) H_2 mass fractions v. time.

Figure 5.5: Cross-sectional distributions of the molecular fraction of 2:1 outflows from a wind with axial speed of 80 km s^{-1}. The displayed region is 0.2 pc^2. The lower-right panel displays the ratio pf total molecular hydrogen mass to the total hydrogen mass as a function of time for the three runs.

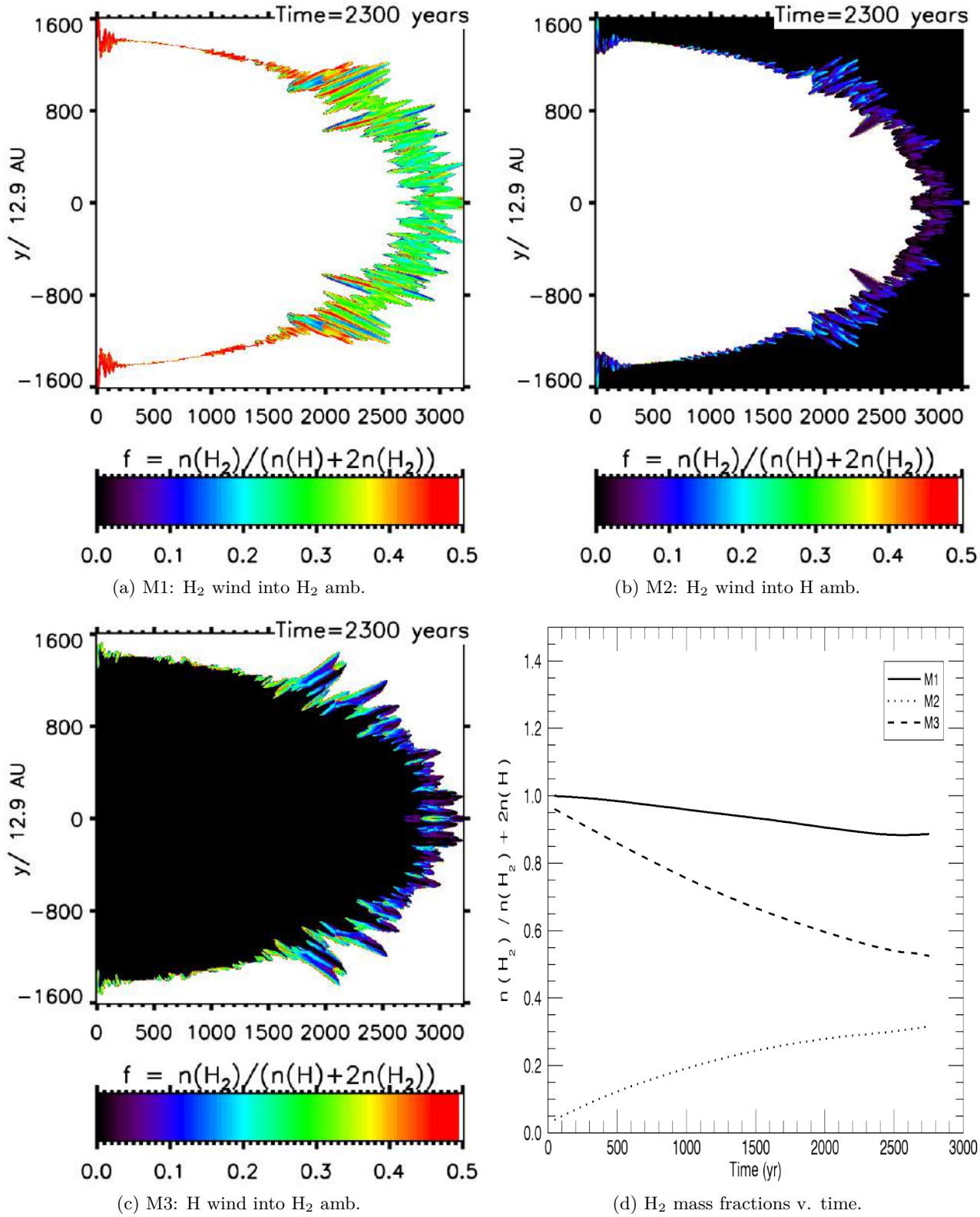

(a) M1: H_2 wind into H_2 amb.

(b) M2: H_2 wind into H amb.

(c) M3: H wind into H_2 amb.

(d) H_2 mass fractions v. time.

Figure 5.6: Cross-sectional distributions of the molecular fraction of 2:1 outflows from a wind with axial speed of 140 km s^{-1}. The displayed region is 0.2 pc^2. The lower-right panel displays the ratio pf total molecular hydrogen mass to the total hydrogen mass as a function of time for the three runs.

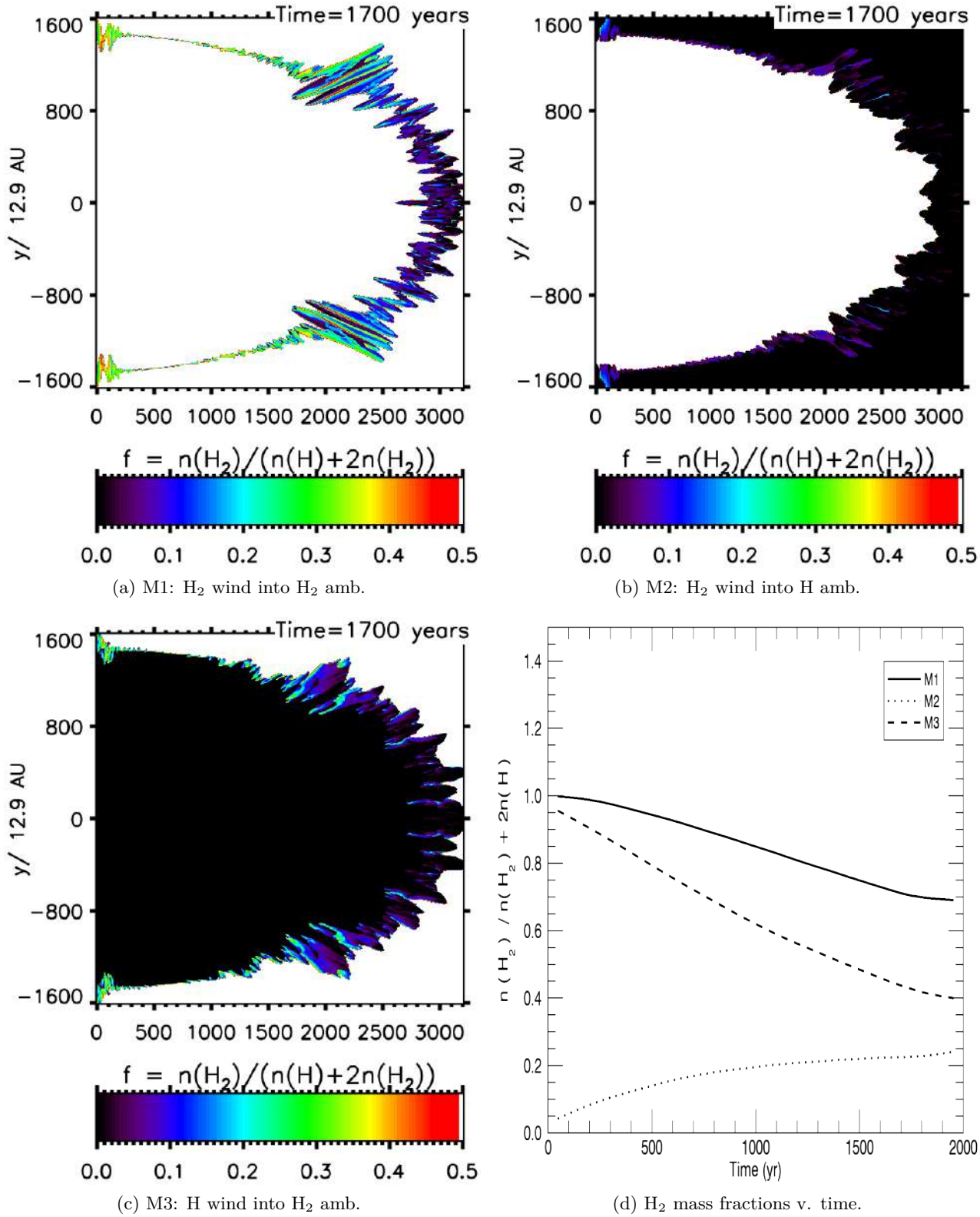

(a) M1: H_2 wind into H_2 amb.

(b) M2: H_2 wind into H amb.

(c) M3: H wind into H_2 amb.

(d) H_2 mass fractions v. time.

Figure 5.7: Cross-sectional distributions of the molecular fraction of 2:1 outflows from a wind with axial speed of 200 km s^{-1}. The displayed region is 0.2 pc^2. The lower-right panel displays the ratio pf total molecular hydrogen mass to the total hydrogen mass as a function of time for the three runs.

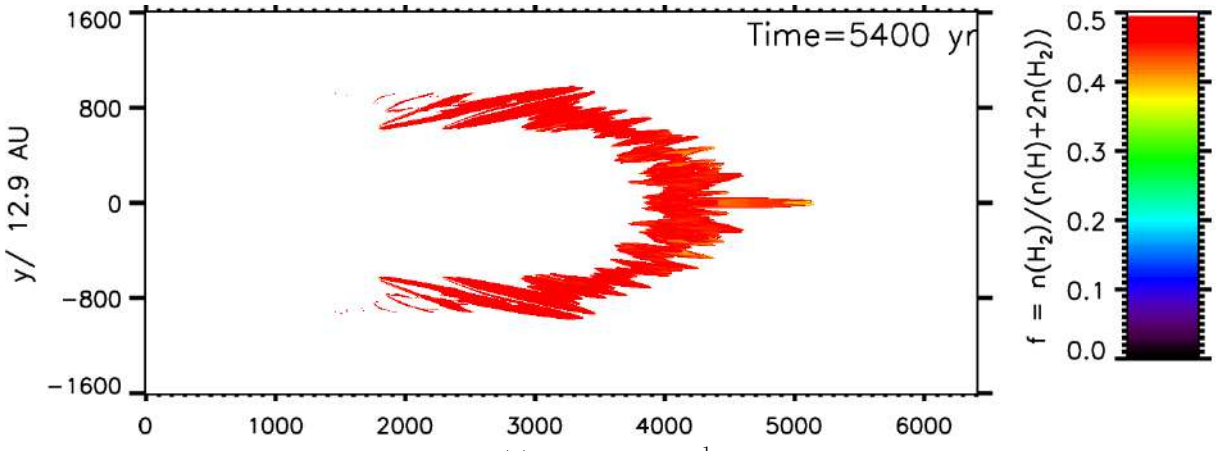

(a) $V_w = 80\,kms^{-1}$

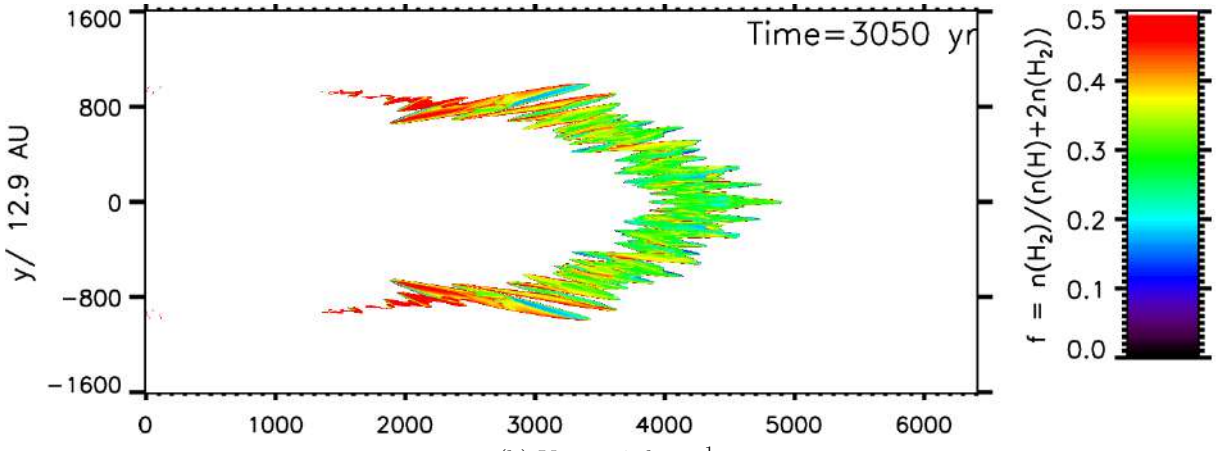

(b) $V_w = 140\,kms^{-1}$

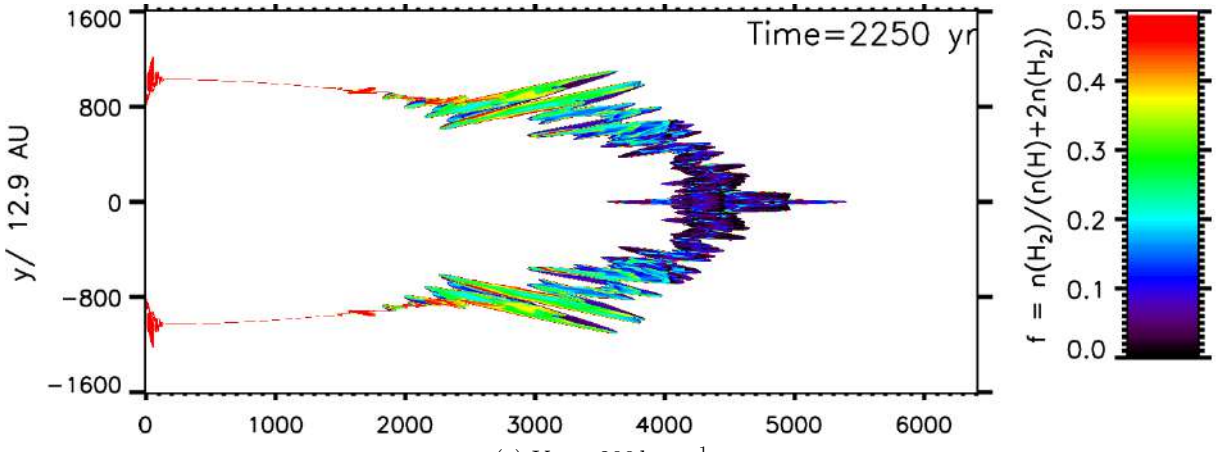

(c) $V_w = 200\,kms^{-1}$

Figure 5.8: M1: H_2 wind interacting with an H_2 ambient medium. Corresponding cross-sectional distribution of molecular fraction produced by 4:1 outflows.

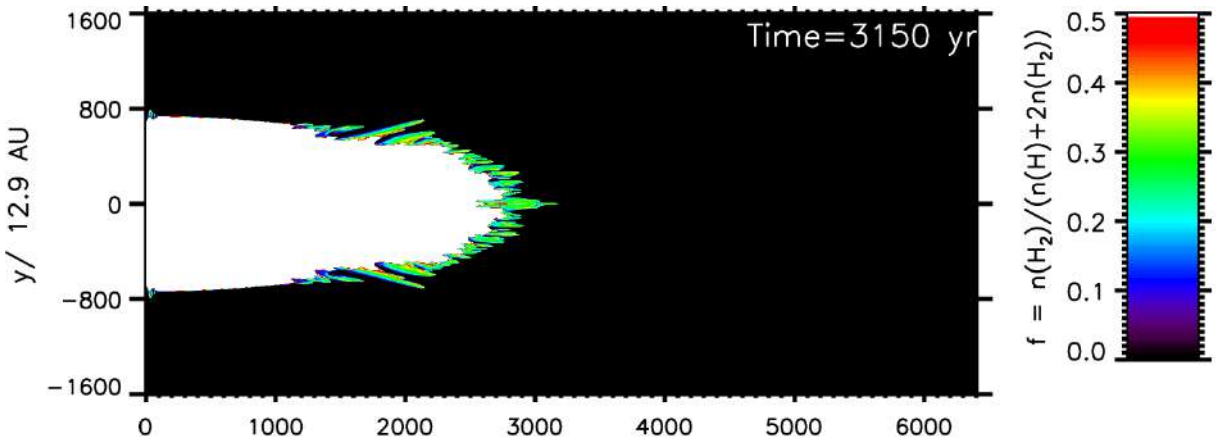

(a) $V_w = 80\,kms^{-1}$

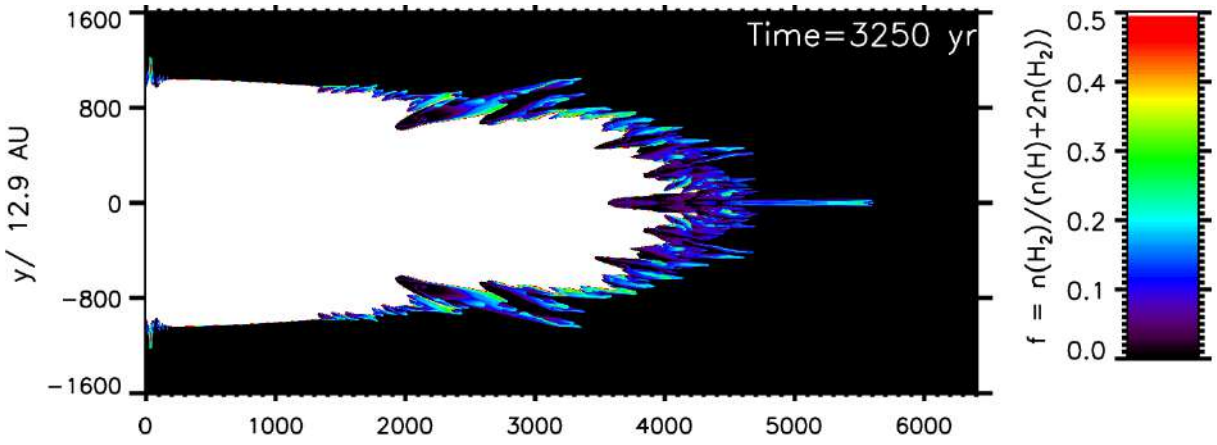

(b) $V_w = 140\,kms^{-1}$

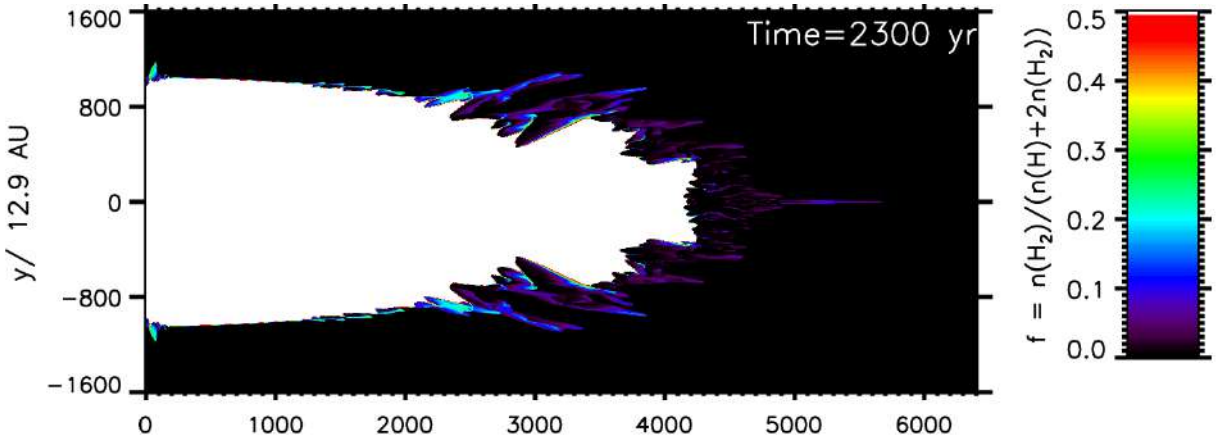

(c) $V_w = 200\,kms^{-1}$

Figure 5.9: M2: H_2 wind interacting with an H ambient medium. Corresponding cross-sectional distribution of molecular fraction produced by 4:1 outflows.

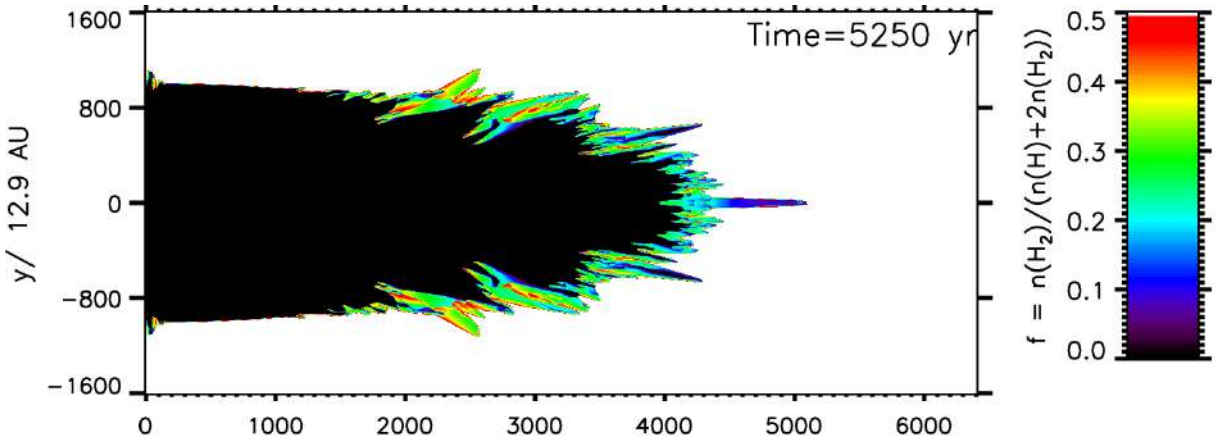

(a) $V_w = 80\,kms^{-1}$

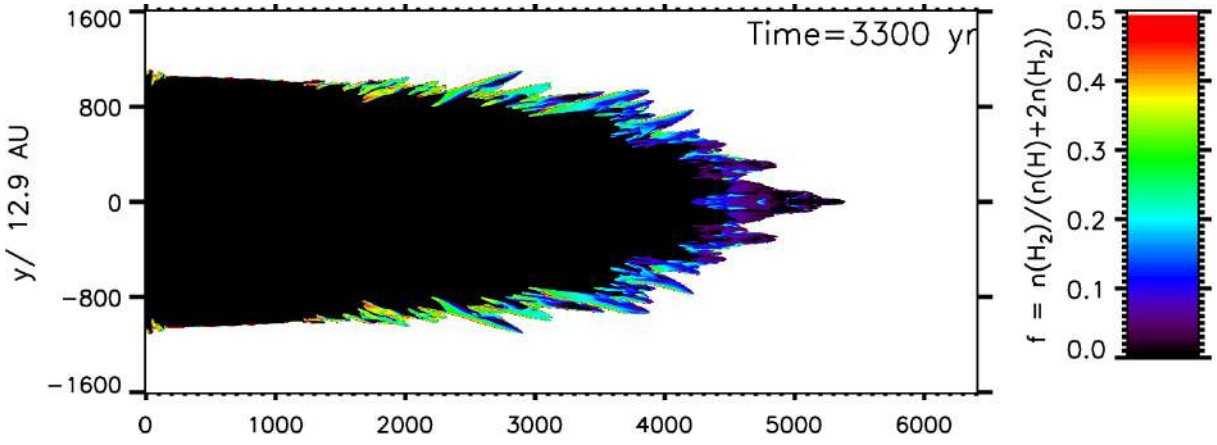

(b) $V_w = 140\,kms^{-1}$

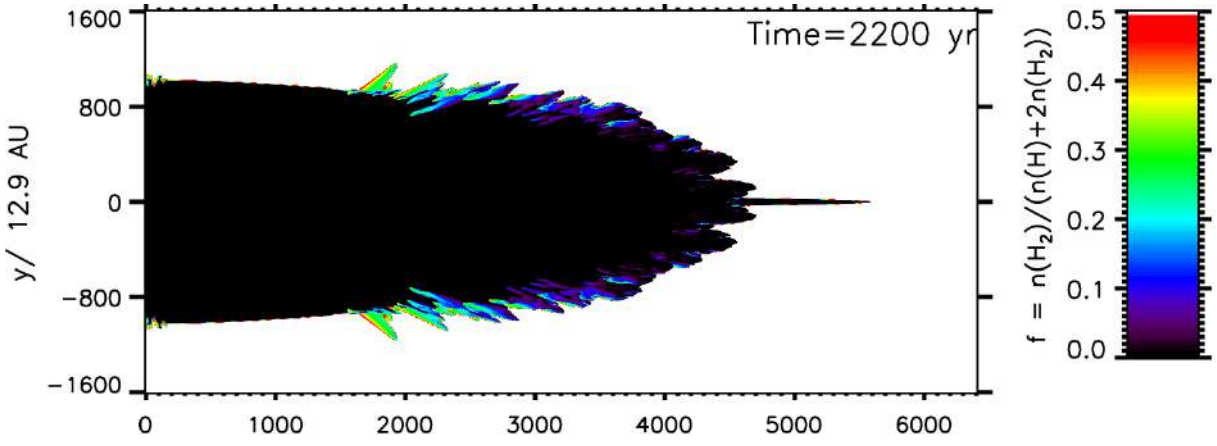

(c) $V_w = 200\,kms^{-1}$

Figure 5.10: M3: H wind interacting with an H_2 ambient medium. Corresponding cross-sectional distribution of molecular fraction produced by 4:1 outflows.

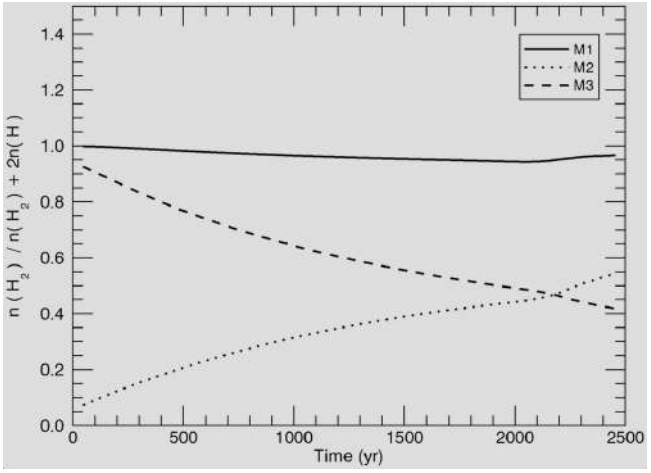

(a) $V_w = 80\,\mathrm{kms}^{-1}$

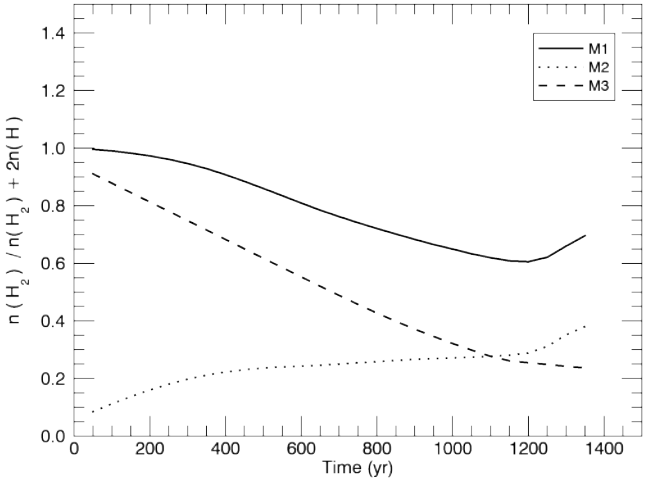

(b) $V_w = 140\,\mathrm{kms}^{-1}$

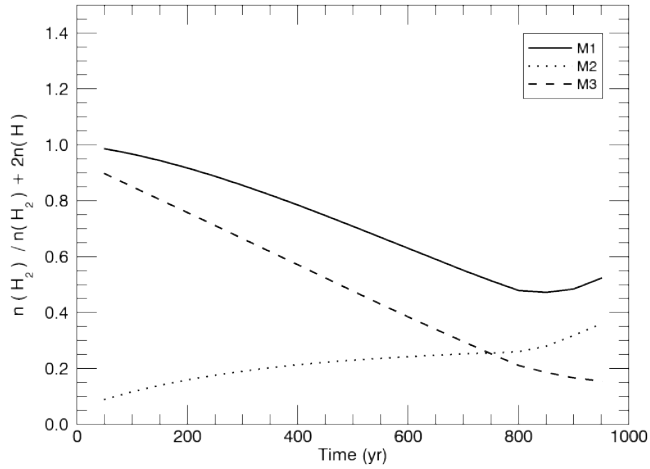

(c) $V_w = 200\,\mathrm{kms}^{-1}$

Figure 5.11: The evolution of the total molecular fraction integrated over the grid as produced by a spherical wind with M1, M2 and M3 outflows, at the three indicated wind speeds from left to right.

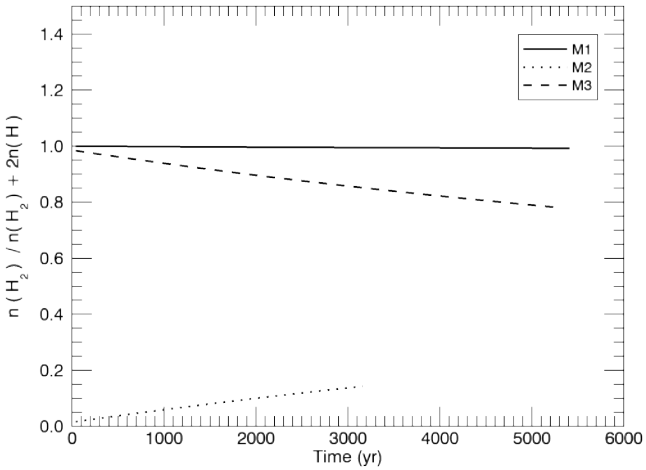

(a) $V_w = 80\,\mathrm{kms}^{-1}$

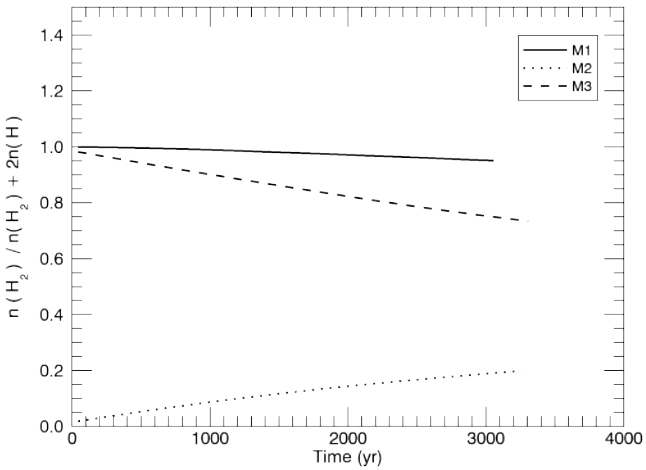

(b) $V_w = 140\,\mathrm{kms}^{-1}$

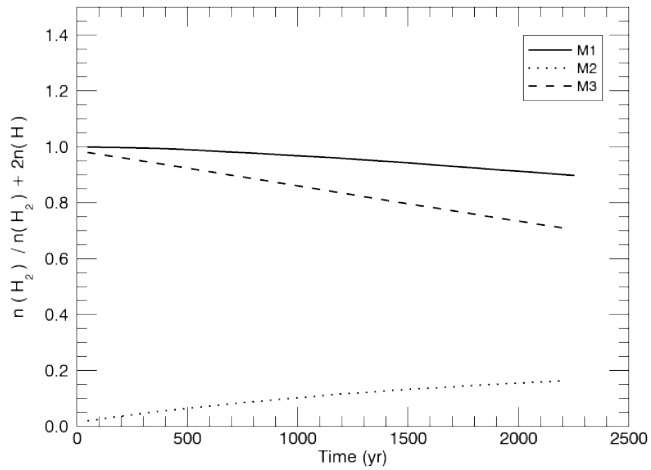

(c) $V_w = 200\,\mathrm{kms}^{-1}$

Figure 5.12: The evolution of the total molecular fraction integrated over the grid as produced by a by a 4:1 wind with M1, M2 and M3 outflows, at the three indicated wind speeds from left to right.

5.6 H_2 Dissociation

All four extreme combinations of atomic and molecular winds into atomic and molecular ambient media have been studied. First, however, we investigate the three combinations in which the molecular fraction changes as hydrogen partly dissociates within the shell.

The molecular tracers are examined in Figs. 5.5, 5.6 and 5.7 for the three speeds with a 2:1 elliptical wind. The cases are easily identified with black representing fully molecular and white corresponding to atomic composition. It is evident that the shell breaks up into fingers in all these cases. The fingers are prominent toward the front section (with no imposed corrugations, the cylindrical coordinates are better aligned to the sphere approximation toward the symmetry plane). The top-left panels exhibit the molecular wind-ambient interactions.

We first take the case in which the axial speed is 80 km s^{-1}, half this speed in the mid-plane, to illustrate the typical flows. Panel (a) displays the molecular wind into a molecular ambient (denoted MWMA). Clearly, moderate dissociation occurs over the entire shell although the front half of the simulation shows extended dissociation within a highly turbulent shell, as expected with the higher jump in speed.

Most significantly, Figs. 5.5 - 5.7 demonstrate that the shock front is not a smooth surface but a rough surface, broken down into a large total area of weak oblique shocks with only a small fraction of strong shock apices. This holds for all three wind speeds. It is also evident that the growing protrusions extend from the interface into the ambient medium. They are generally pockets of wind material channeled into the advancing fingers. Panels (b) and (c) illustrate this for the MWAA and AWMA cases, respectively, since the make-up of the gas can be ascertained. Until the late stages of the flow, however, the leading shock which enters the atomic ambient medium is of course not visible in the MWAA run.

Panel (c) demonstrates that the molecular ambient gas becomes confined to partly-dissociated thin striations embedded in the atomic wind. In contrast, Panel (b) shows that the molecular wind can protrude quite far into the ambient medium, suggesting that these dense molecular fingers are promoted by the Rayleigh-Taylor instability of the decelerating shell.

At the higher speed shown in Fig. 5.7, we see the dissociation is more complete. The fingers are almost completely washed out at the highest speed by the bath of hot atomic gas although some thick fingers do survive in the MWMA case, a few molecular trunks remain in the wind in the

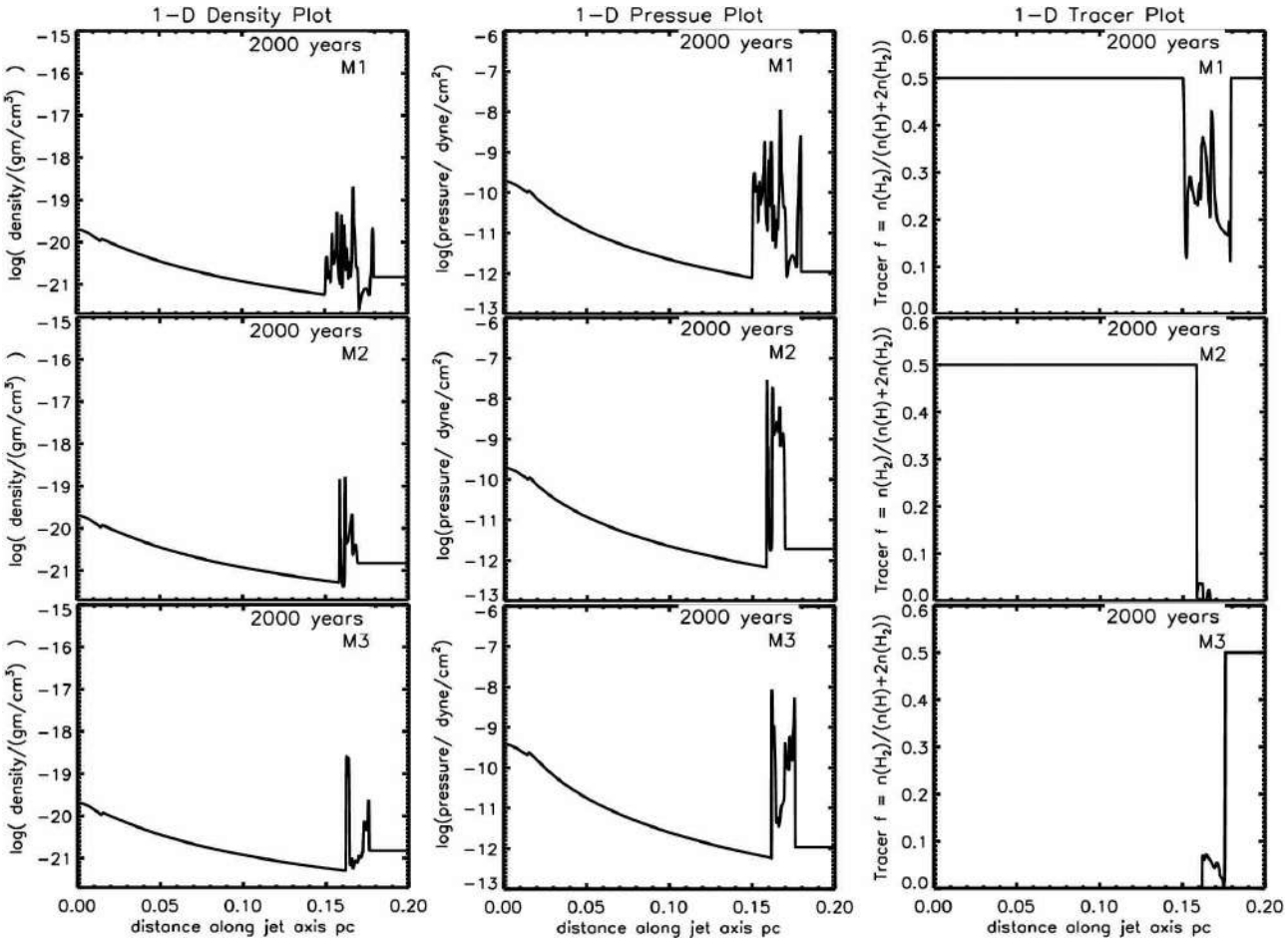

Figure 5.13: One-dimensional plots of the physical parameters for all 2:1 wind models after 2,000 years of evolution of a 140 km s^{-1} wind.

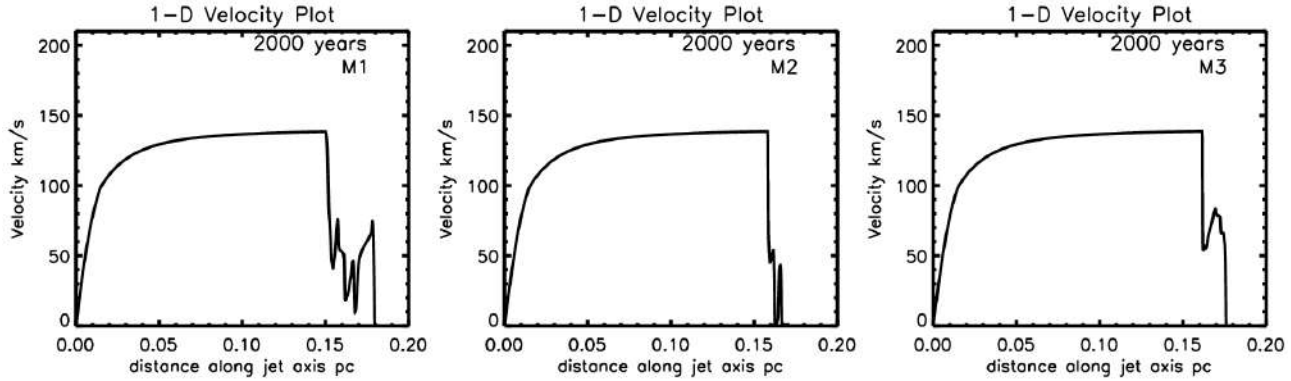

Figure 5.14: One-dimensional velocity plots of the physical parameters for all 2:1 wind models after 2,000 years of evolution of a 140 km s^{-1} wind. The horizontal cut is taken at 200 zones above the symmetry axis in order to avoid on-axis numerical discrepancies. The axial component of the inner part of the wind is thus increasing.

AWMA case, and a few small (blue) wisps are ahead of the main shell in the MWAA case.

A further surprising feature is that the fingers are rarely directed in the radial direction, toward the star. The shells are roughly elliptical with the 2:1 shape as would be expected from the scaling when the shell is driven by a heavy impacting wind. However, at late times as the shell decelerates and is not being driven by a heavy wind, the shape begins to change and the ellipticity decreases. Hence, the wind and ambient fingers are subject to deflection by oblique shocks and will be directed according to the global shape as well as the local conditions.

The displayed change in total mass in molecular hydrogen within the 0.1 pc cylindrical region is instructive. This is shown in terms of the mass fraction in the lower-right panels of Figs. 5.5, 5.6 and 5.7, giving an indication of the nature of the environment surrounding pPN. For example, at the lower speed, the H_2 evolution of MWAA and AWMA appears quite symmetric: the mass enters the environment at a uniform rate and there is a small amount of total dissociation. In contrast, at the high speeds, the molecules added in the wind are dissociated especially at late times when the reverse shock is strong. In summary, the mass fraction in molecules is reduced by 20% across this range of speeds for all model compositions.

The spherical models Fig. 5.11 are most dissociative with the H_2 fraction decrease with increase in the wind's terminal velocity. AWMA outflow is the most dissociative model M3, where ambient hydrogen molecules are being dissociated by the high speed collisions behind the high speed shock. The increase in wind's ellipticity decreases the rate of H_2 dissociation for all models as shown in Fig. 5.12 due to lower radial velocity component, pressure and temperature distribution.

5.7 Pressure, Density & Temperature

The pressure, density and temperature distributions for the 2:1 140 km s^{-1} winds are shown in Figs. 5.15, 5.16 and 5.17. The 2D distributions highlight different sections of the shock structures. The pressure highlights the combined shocked layers, the temperature the immediate shock fronts while the density emphasises the cool compressed gas downstream. Note that the pressure range shown in the colour bars in Fig. 5.15 are identical. Hence, there is a lower pressure in the molecular wind/ambient run, as would be expected with the five degrees of freedom.

These figures confirm that the shock front is a rough surface, broken down into a large total area of weak shock arcs with only a small fraction of strong shock apices. The temperature

plots demonstrate that the shell is dominated by relatively cool gas globally. However, when inspecting the same images in detail, as shown in Fig. 5.18, we see that the individual fingers are topped by hot zones: strong shocks are confined to the tips. This result should impact on the H_2 excitation that would be measured when observations are made even at quite high resolution.

It is also seen in Fig. 5.18 that the purely atomic simulation shows different structure to the other three combinations. The AWAA case displays a thicker surface which remains turbulent or rougher close to the plane. The temperature distributions displayed in Fig. 5.17 provide the interpretation: the shell of the atomic AWAA run remains warm, just below 10,000 K whereas these layers of the molecular-atomic runs are closer to 1,000 K and a few hundred Kelvin for the MWMA run. Therefore, the atomic layer remains partly inflated and less susceptible to dynamic instabilities. The instabilities responsible for the corrugation of the front shock are not sensitive to the width of the shell. As shown by the resolution study in Fig. 5.3, the physical width of the shell is independent of numerical resolution.

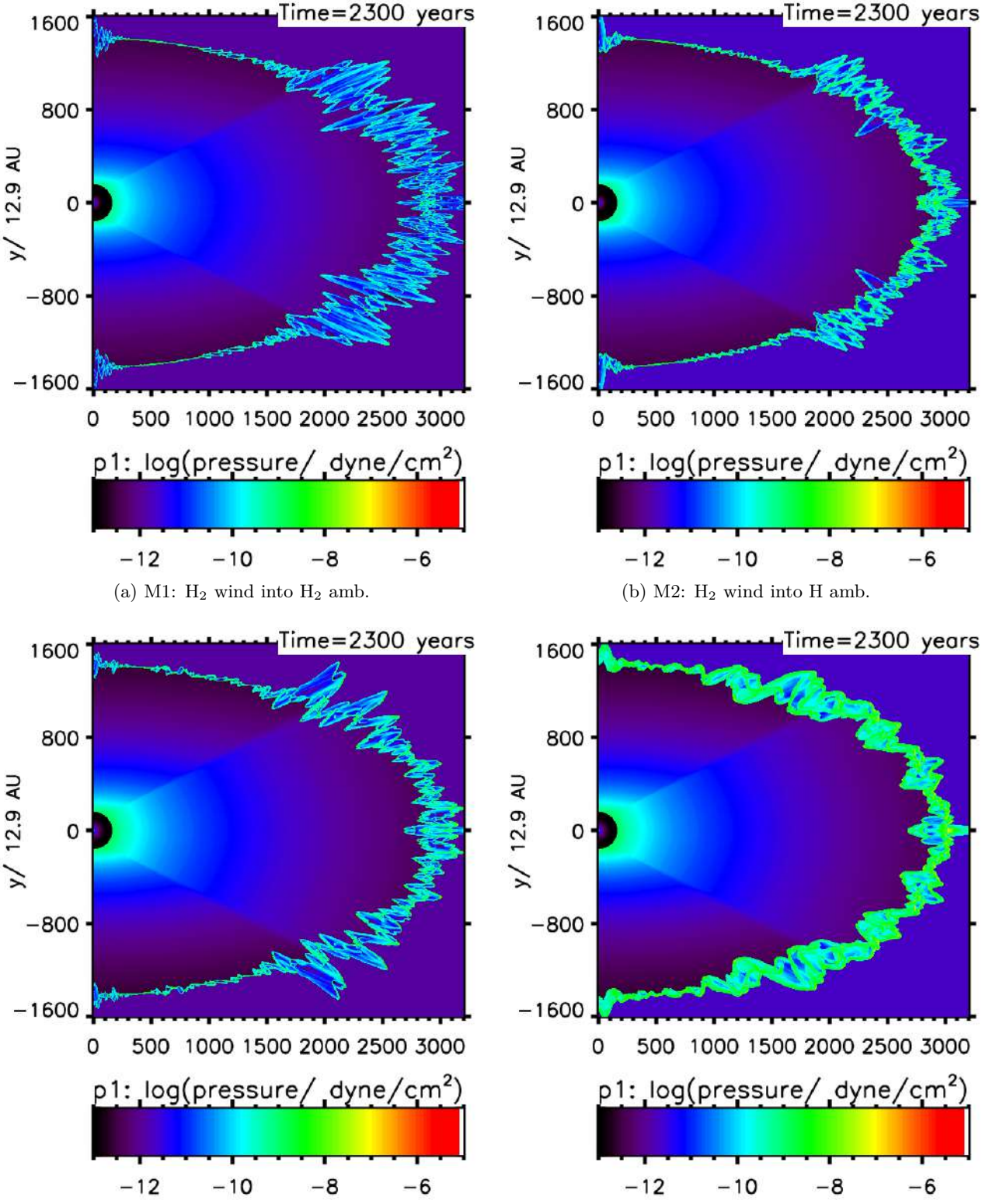

(a) M1: H_2 wind into H_2 amb.

(b) M2: H_2 wind into H amb.

(c) M3: H wind into H_2 amb.

(d) M4: H wind into H amb.

Figure 5.15: Cross-sectional distributions of pressure produced by 2:1 outflows with axial speed of 140 km s^{-1}. The lower half of each distribution is the mirror image of the top half. A mask of 160 grid zones is placed over the central wind region to cover up the radius around a bright star.

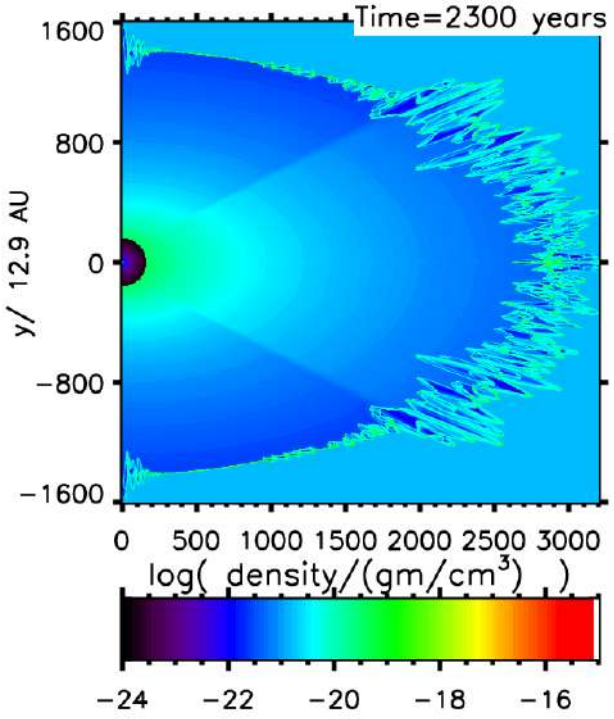

(a) M1: H_2 wind into H_2 amb.

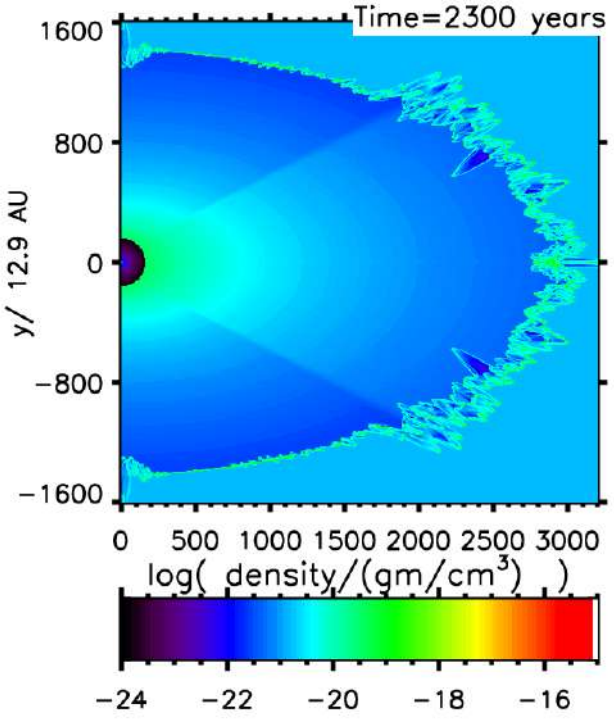

(b) M2: H_2 wind into H amb.

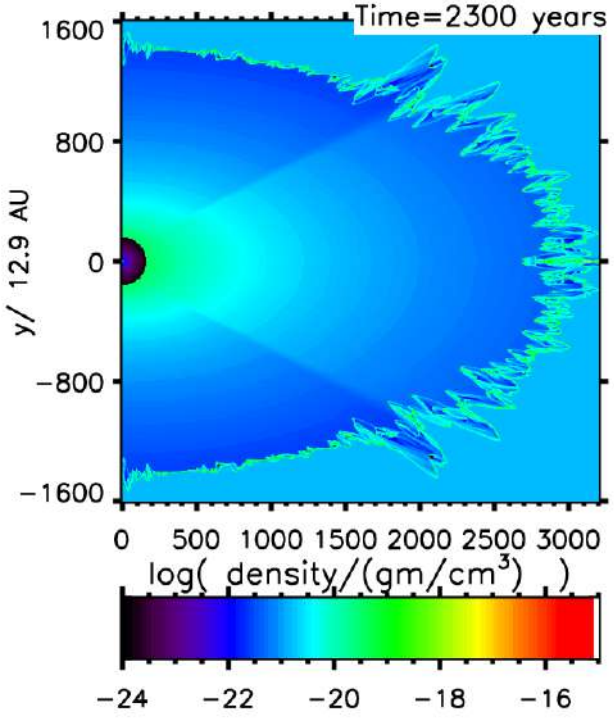

(c) M3: H wind into H_2 amb.

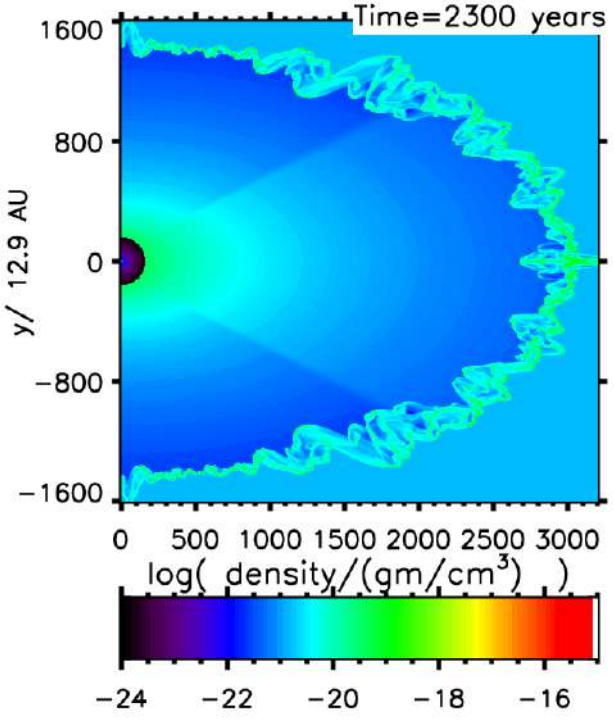

(d) M4: H wind into H amb.

Figure 5.16: Cross-sectional distributions of density produced by 2:1 outflows with axial speed of 140 km s^{-1}. The lower half of each distribution is the mirror image of the top half. A mask of 160 grid zones is placed over the central wind region to cover up the radius around a bright star..

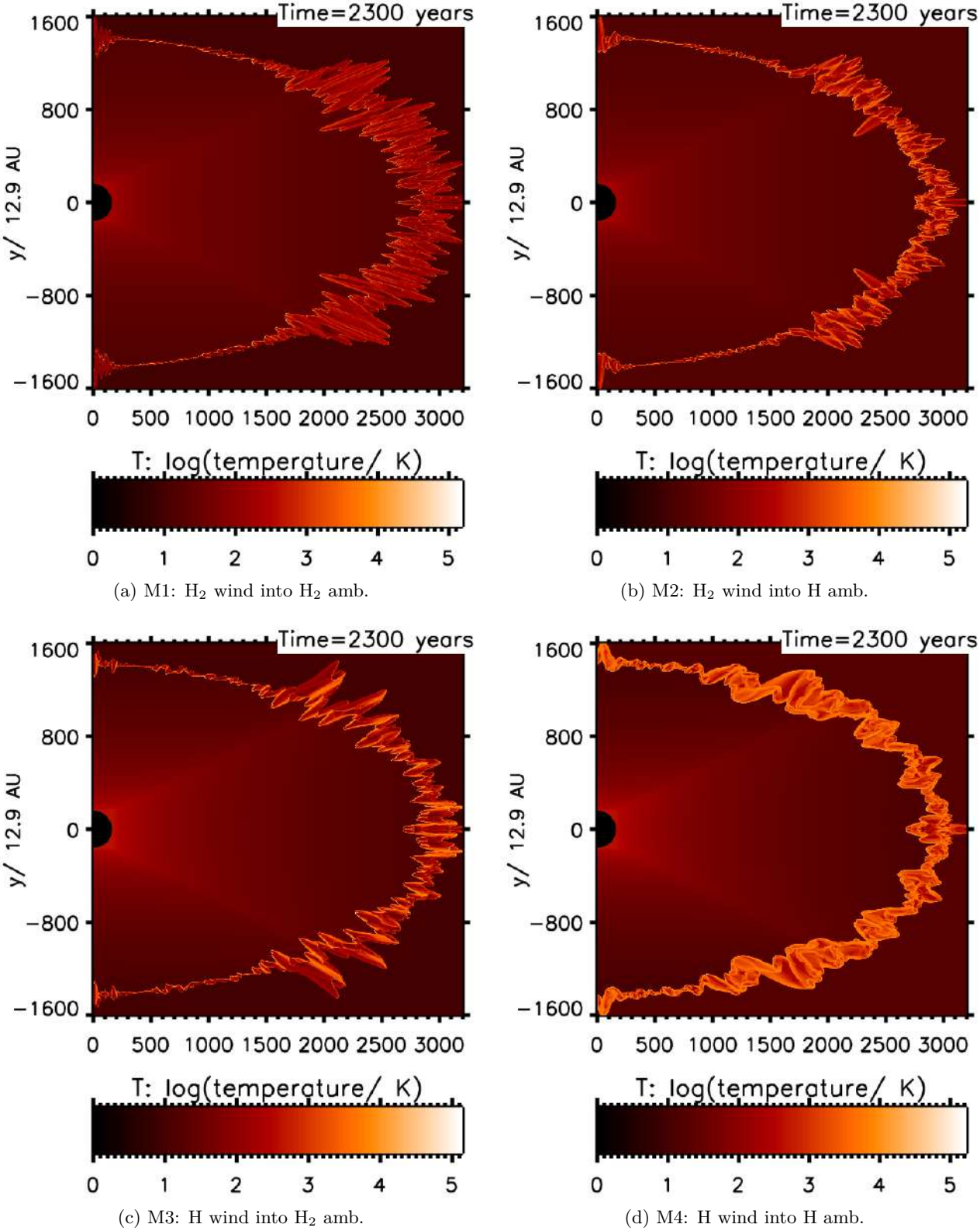

(a) M1: H_2 wind into H_2 amb.

(b) M2: H_2 wind into H amb.

(c) M3: H wind into H_2 amb.

(d) M4: H wind into H amb.

Figure 5.17: Logarithmic temperature maps of 140 km s^{-1} 2:1 wind, all scaled to the atomic model (d). Images indicate maximum temperature for molecular run (a) at $T \sim 3,000$ K, in case of atomic run (d), temperature reaches $T \sim 20,000$ K.

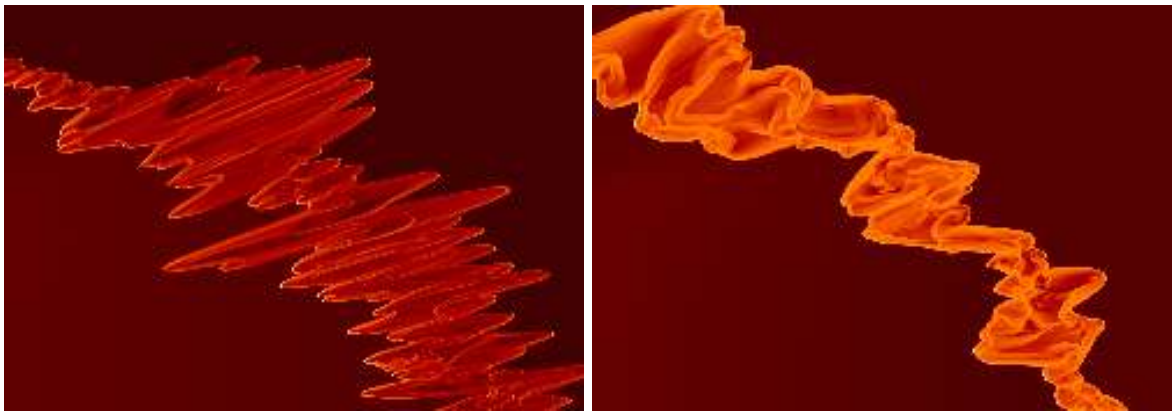

Figure 5.18: Detail from the scaled logarithmic temperature maps of 140 km s^{-1} 2:1 wind, for the pure molecular run (MWMA, left panel) and pure atomic run (AWAA, right panel).

5.8 Structure of collimated winds

The dependence on the wind speed is well illustrated with the 4:1 ellipsoidal wind simulations. The molecular simulation is illustrated in Fig. 5.19 for three speeds. As expected, the highest pressures occur along the axis and in the fastest winds. The shell structure is best shown in Figs. 5.8 – 5.10 for three different axial wind speeds and for all three composition combinations.

The sensitivity of the molecular fraction to the wind speed and the distribution around the shell are prominent here. At low speeds, the dissociation remains at a few percentage along the shell. Large atomic bow-shaped shells result when the axial wind speed is high, even when both media are input as molecular. The bow is again broken up into fingers in cross-section. However, when the ambient medium is atomic (see Fig. 5.10), the fingers become long thin molecular streaks which penetrate into the ambient medium and arc toward the axis. These striations, best observed by zooming in on the panels, are partly dissociated. Moreover, the fingers develop into longer streaks at the higher wind speeds. Generally speaking, the properties are an exaggerated form of the 2:1 case: material does not flow tangentially to the shell but mixes locally.

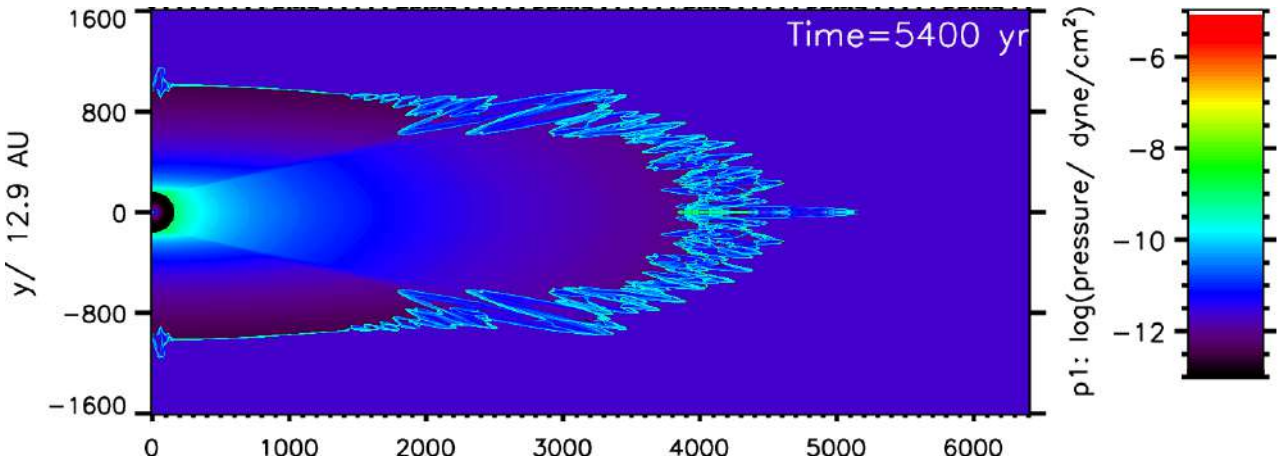

(a) $V_w = 80\,kms^{-1}$

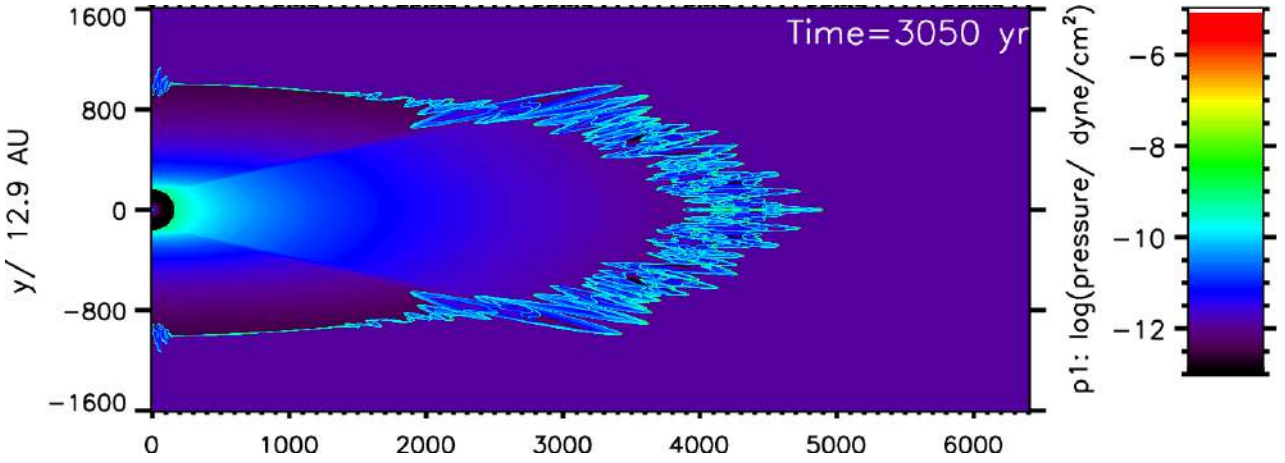

(b) $V_w = 140\,kms^{-1}$

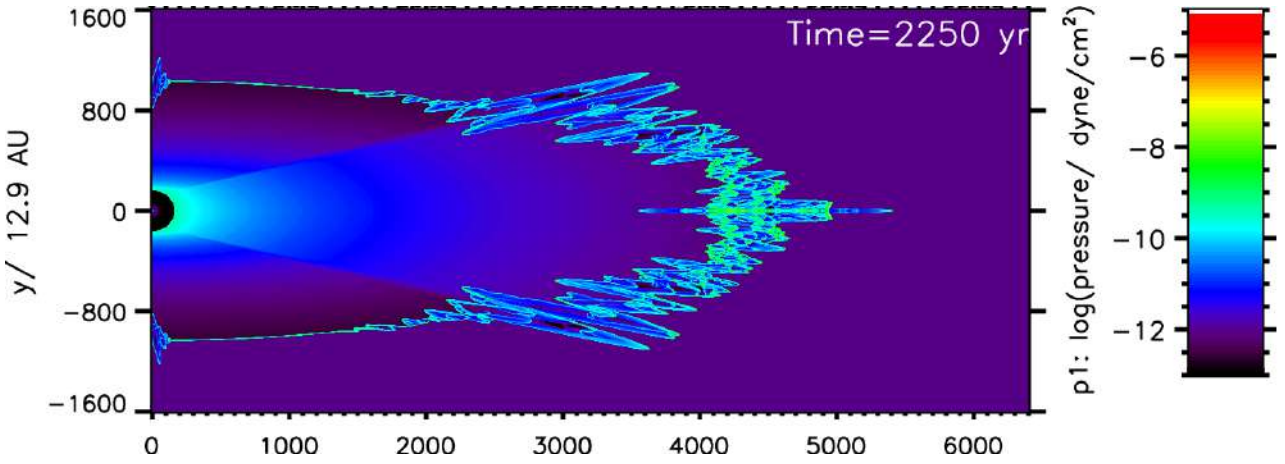

(c) $V_w = 200\,kms^{-1}$

Figure 5.19: Variation of pressure distributions for three axial wind speeds in a collimated 4:1 H_2 wind model interacting with an H_2 ambient medium.

5.9 Nebula shaping: local or global flow?

Significant to further simulations is that, in all cases, there is no flow along the shell toward the apex/axis of the ellipse. This lack of global flow applies to the entire range of wind speeds and compositions and implies that flow details can be usefully investigated through simulations with a constricted opening angle. Furthermore, without a coherent oblique shock front to deflect the wind into a high speed shear interface, it is likely that the sound speed in the shell will determine the maximum length scale for the growth of disturbances. Here, there are two main timescales affecting the evolution of the shell morphology: the thermal gas response time at the sound speed, $t_s = \lambda/c_s$, and the dynamical timescale, $t_d = R_{shell}/U$. Hence the maximum wavelength condition is

$$\lambda < c_s \frac{R_{shell}}{U}, \tag{5.3}$$

which implies that the warmer atomic gas in the shell is likely to lead to wider and thicker coherent shell structures, as found above. The sound speed in the molecule dominated shell is typically between 0.2 and 0.8 $\mathrm{km\,s^{-1}}$, which implies that the fingers may only be a few hundred AU wide.

The growth rate of disturbances on the shell interface with the ambient medium will be controlled by the Rayleigh-Taylor instability and the Vishniac thin-shell instability (Vishniac 1994). However, most shell simulations have had inadequate resolution to follow these instabilities in radiative flows. The cylindrical symmetry does make this feasible and, as shown in several studies (Fryxell et al. 1991; Dwarkadas & Balick 1998; Kane et al. 2000), protruding fingers and streaks are present even at relatively low resolution. Indeed, a number of remarkable observations of radial streaks could be interpreted by the Rayleigh-Taylor instability associated with a decelerating shell (Smith 2013; Matsuura et al. 2009).

The RT growth rate into the non-linear regime is given by $1/\mathrm{t_{RT}} = \sqrt{(\mathrm{gk})}$ where we approximate the deceleration as $\mathrm{g} \sim \mathrm{U^2/R_s}$ and the wavenumber $\mathrm{k} = 2\pi\lambda$ (Blake 1972). This yields a sufficiently short growth time $\mathrm{t_{RT}} = \sqrt{(\lambda/(2\pi \mathrm{R_s}))}$ to ensure that the non-linear regime would be reached.

To elucidate the interface structure, we present one-dimensional cuts through the simulations in Fig. 5.13. The molecular tracer in the lower left panels is instructive and indicates how fragments of partially molecular content become trapped in the evolving flow. In fact, inspection of the

movies [2] corresponding to Fig. 5.14 shows that the speed of the advancing shock at this location falls when the molecular fragment is generated. There is a clear dynamical instability involved.

While thermal instability may contribute to enhance the growth of denser clumps, in general there is little pressure equilibrium within the interface which is dominated by compressions, rarefactions and sub-hocks as cold dense layers become trapped within warm regions. Moreover, we do not expect thermal instabilities alone to trigger such structure since such instability has been shown to be confined to a very narrow range of shock parameters (Smith & Rosen 2003).

A classical sawtooth velocity profile distinguishes the shock sandwiches in one-dimensional simulations (Suttner et al. 1997). These are indeed produced but can only be easily identified early on in the simulations; the shock speed soon begins to oscillate and generate layers of stronger molecular cooling which propagate from the shock front toward the interface. Remarkable density and pressure variations are then sustained. This is particularly noticeable in the molecular wind-ambient simulation: rather than hot atomic gas inflating a thick interface, the molecular case results in stronger local pressure and density variations which act to maintain an interaction layer almost twice as thick.

Finally, we determine the integrated molecular fraction in Fig. 5.11 - Fig. 5.12 where the particle number fraction is presented. As the shock interface sweeps across the grid, the wind contents replaces the ambient medium with a significant fraction of the molecular medium being dissociated. Toward the end of the M1 (MWMA) run, the rate at which new molecular wind enters the grid is faster than the dissociation rate and the decrease in molecules is reversed. This analysis also clearly demonstrates that the sum of fractions for Models M2 (MWAA) and M3 (AWMA) at any given time will approximately yield the fraction for model M1.

[2] http://astro.kent.ac.uk/~in32/ppn.html

Chapter 6

Spectroscopic Properties

6.1 Emission Maps

The simulated images are displayed on an infrared and optical array designed so that all the emission from the simulated 3D cylinder can be projected on to the same array whatever the orientation to the line of sight. Thus, the projected wind origin remains fixed. Due to the axial symmetry and the formation of the warm streaks, the emission tends to form discrete rings in projection which would probably appear as individual bullets or globules in full 3D simulations. Nevertheless, it is instructive to generate these images and determine where the emission is located and how excited the gas is.

6.1.1 K - band

Figs. 6.1-6.3 demonstrates the H_2 emission from a flow in the sky plane. Emission is generated across the entire cylinder although the flux dynamic range is over 1,000. At 60° to the line of sight, Fig. 6.4 for the $1 \rightarrow 0\,\mathrm{S}(1)$ line and Fig. 6.5 for the $2 \rightarrow 1\,\mathrm{S}(1)$ line, we illustrate that the simulated emission does show some significant variation across the three displayed models. Of note is that the fully molecular interaction appears to show less emission from the flanks, although there is no spatial shift of emission close to the apex. The cause for the lower flank emission when fully molecular can be discerned from the H_2 ratio image of Fig. 6.6, which indicates a slightly higher excitation in the far flanks when an atomic component is present.

The peak emission is set back from the leading edge in a similar way for all cases. The suggestion is that the source geometry determines the distribution more than the particular reverse and

advanced shock configuration. Taking a smaller range in flux, appropriate for most observations, it is apparent that the majority of the molecular flux is located at a bow-shaped shock followed by circular cylindrical shells as illustrated in Fig. 6.7. It can be concluded that collimated pPN are produced with the present set up and butterfly-type bipolar nebulae are not generated.

It is interesting to also determine the fluorescent emission that would result from an optically thin gas. Here, in Fig. 6.8, we assume an emissivity proportional to the H_2 density and an inverse square law from a star at the origin (1,600 ,0). Now, the images are very different since a molecular wind generates strong emission from the denser inner parts of the wind while an atomic wind creates a cavity.

A common diagnostic for measuring the excitation is the $2 \rightarrow 1/1 \rightarrow 0\,\mathrm{S}(1)$ H_2 line ratio. One could expect that the excitation would increase toward the apex of the expanding prolate ellipsoid, as found for bow shocks (Smith et al. 2003). However, as shown in Fig 6.6 for the molecular run, the ratio remains between 0.1 and 0.2, typical of moderate shock excitation from gas 1,800 K to 2,600 K. This small range occurs despite the wide range in shell speeds in the 4:1 simulation and can be attributed to the fragmentation of the shock surface into a large number of streaks that encompass weak oblique shocks at all locations.

The flux values and ratios are consistent with a collisional excitation scenario. A fraction of the molecules are abruptly dissociated after the shock front, radiative cooling follows as gas loses heat by radiation, forming dense and cool post-shock relaxation layers (Smith & Rosen 2003). Line map units are in $\mathrm{erg\,s^{-1}\,cm^{-2}}$. These results can be compared to K-band integral field spectroscopy that reveals bipolar ($> 150\,\mathrm{km\,s^{-1}}$) H_2 outflows such as associated with IRAS $16342-3814$ Gledhill & Forde (2012, 2015). A molecular wind can be differentiated from a molecular environment. At early evolution times, the advancing shock is strong. To begin with Model M3, a dense wind pushes easily into the lower density ambient medium. This fast shock dissociates the H_2 in the ambient medium, so making the cap deficient in H_2, in contrast, the cap will be initially bright in model M2. The remaining hot molecular gas generates very high excitation emission in M3 and the 2–1/1–0 ratio exceeds 0.4 over most of the cap. In contrast, the strong molecular wind generates stronger infrared emission in Model M2 with lower excitation.

At later times, the advancing molecular shock has slowed down in Model M3, generating a typical large bow structure in which the excitation declines towards the flanks. On the other hand, this

slow moving shell becomes the wall for strong emission and excitation of the molecular wind in Model M2. The reverse shock appears to generate a moderate excitation of $\sim 0.1 - 0.15$ over almost the entire shell.

The ability to observe pPN in the near-infrared lines is assessed by finding the total pPN emission in the two commonly observed near-infrared H_2 lines as a function of time. These are displayed in Figs. 6.9-6.11 for all three wind speeds and for spherical 2:1 and 4:1 elliptical winds. Particularly high line fluxes are determined for spherical winds with 1–0 S(1) luminosities approaching one solar luminosity for the intermediate wind speed of 140 $\mathrm{km\,s^{-1}}$. At this speed, most shock emission is channelled into the vibrational lines. In addition, it should be noted that the implementation of the ellipticity in the velocity distribution does strongly reduce the energy flux away from the axis and this explains the general trend with ellipticity. However, the emission is also high for elliptical winds but at higher axial wind speeds, which may be expected given the distribution of interface speeds expected across the entire flow.

Overall, H_2 line fluxes remain high once established, throughout the pPN wind phase. The peak H_2 luminosity typically occurs after 500 – 1,000 years which is enhanced when a molecular wind is involved (M1 & M2). However, the flux remains high and slightly increases in the cases involving lower speed winds, corresponding to solid lines.

The overall excitation is best analysed by plotting the 2–1/1–0 ratio as shown in Fig. 6.14 for the 4:1 winds. There is no significant dependence on model type after the initial blast: the excitation is independent of whether ambient streams become trapped and compressed by the wind or vice versa. However, there is a significantly higher vibrational excitation associated with the higher speed wind (right panel), a relationship which holds for all ellipticities studied, shown in Fig. 6.12-Fig. 6.13. The ratio depends on both density and temperature since the H_2 will not possess LTE distributions at the pPN densities but the range displayed between 0.08 and 0.14 corresponds to temperatures of $\sim$ 1,700 K – 2,500 K.

6.1.2 Optical

The emission presented here is purely from shock waves. The spectral types of the stars themselves range from late G to early B with characteristic P-Cygni type profile, strong Hα emission, and narrow absorption components (van de Steene et al. 2000). The emission lines are generated by the circumstellar envelope, whilst the absorption is formed by the fast 100 km $\mathrm{s^{-1}}$ wind, or in the region, where the pPN outflow sweeps up earlier AGB wind. Here, the wind and shell

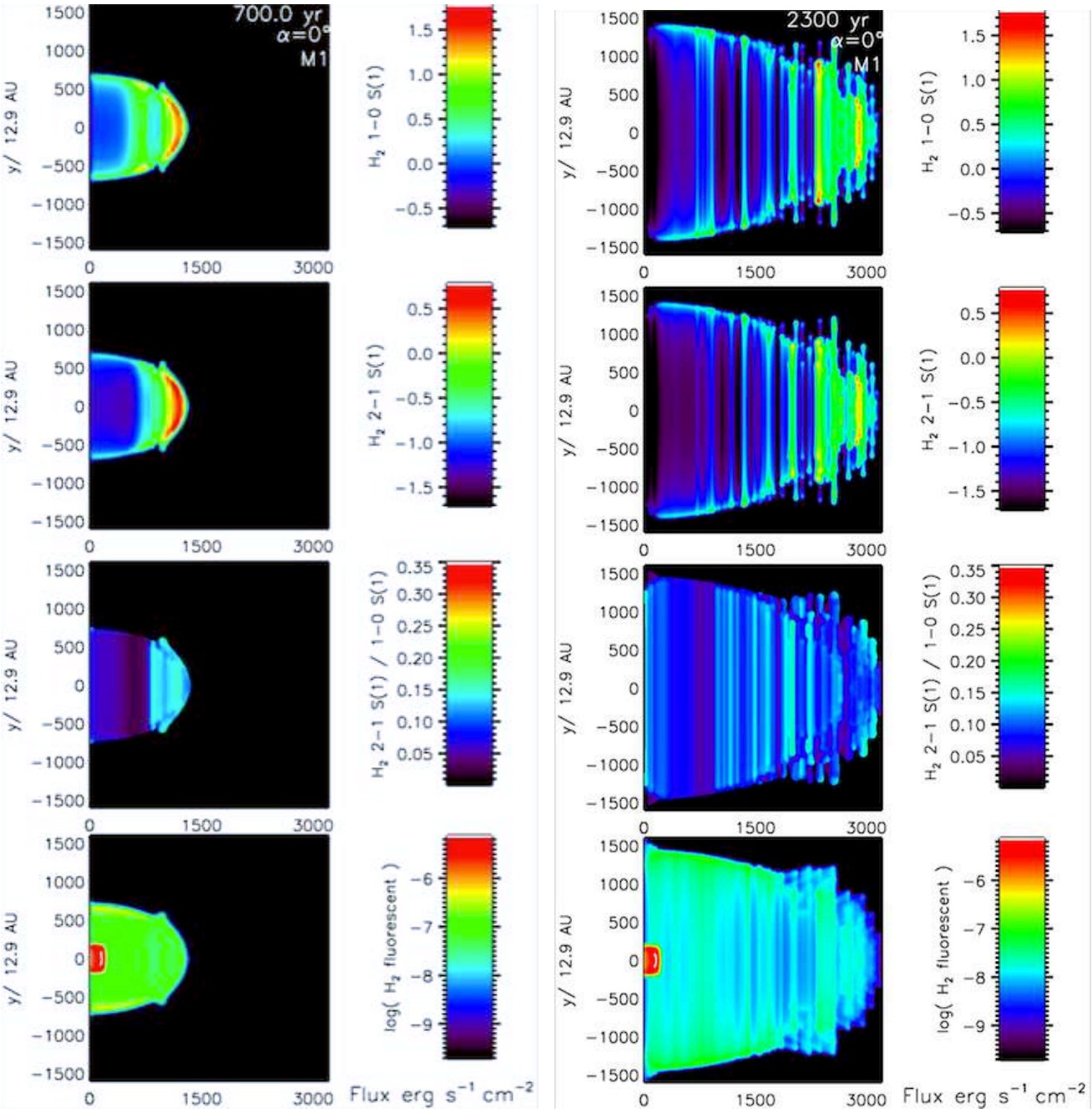

(a) M1: early time, 700 yr.

(b) M1: late time, 2,300 yr.

Figure 6.1: H_2 line emission maps for a molecular wind impacting a molecular medium. Model M1: with a 2:1 $V_w \sim 140\,km\,s^{-1}$ wind in the plane of the sky at the indicated times.

have expanded sufficiently for an optically thin approximation to be valid.

One of the aims of this research is to identify stages of optical emission from strong [Fe II] 1.64 μm and [Si II] 6716 λ forbidden lines, the [O I] 6300 λ airglow line, and Hα 6563 λ emission. The simulated maps resulting from the four chosen atomic transitions are displayed consecutively in Fig. 6.15 - 6.17, modelling 2:1 ellipticity panels of higher peak flux compared to 4:1 ellipticity panels of Fig. 6.18 - 6.21. The resulting emission emanate from three different compositional

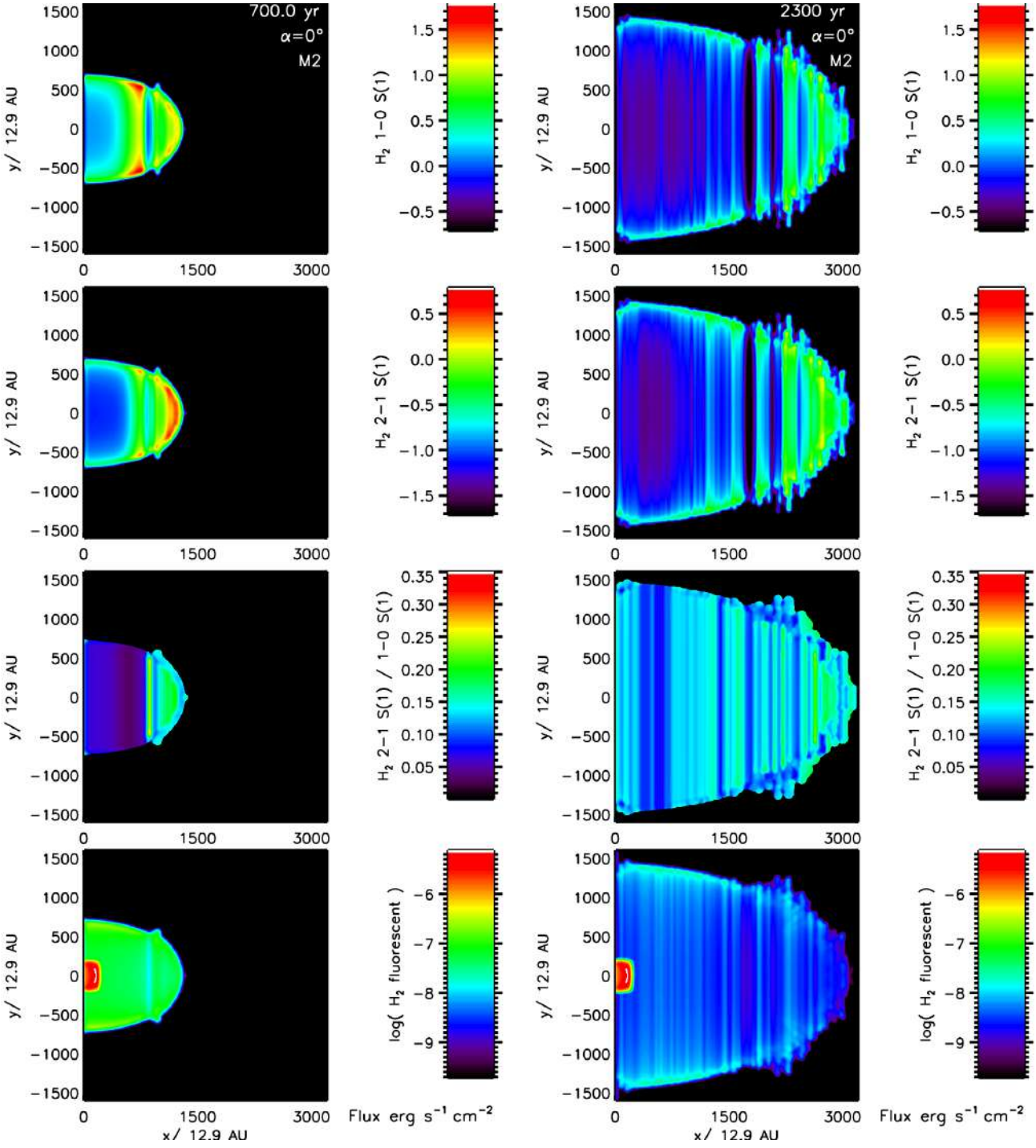

(a) M2: early time, 700 yr.

(b) M2: late time, 2,300 yr.

Figure 6.2: H_2 line emission maps for a molecular wind impacting atomic medium. Model M2: with a 2:1 $V_w \sim 140\,km\,s^{-1}$ wind in the plane of the sky at the indicated times.

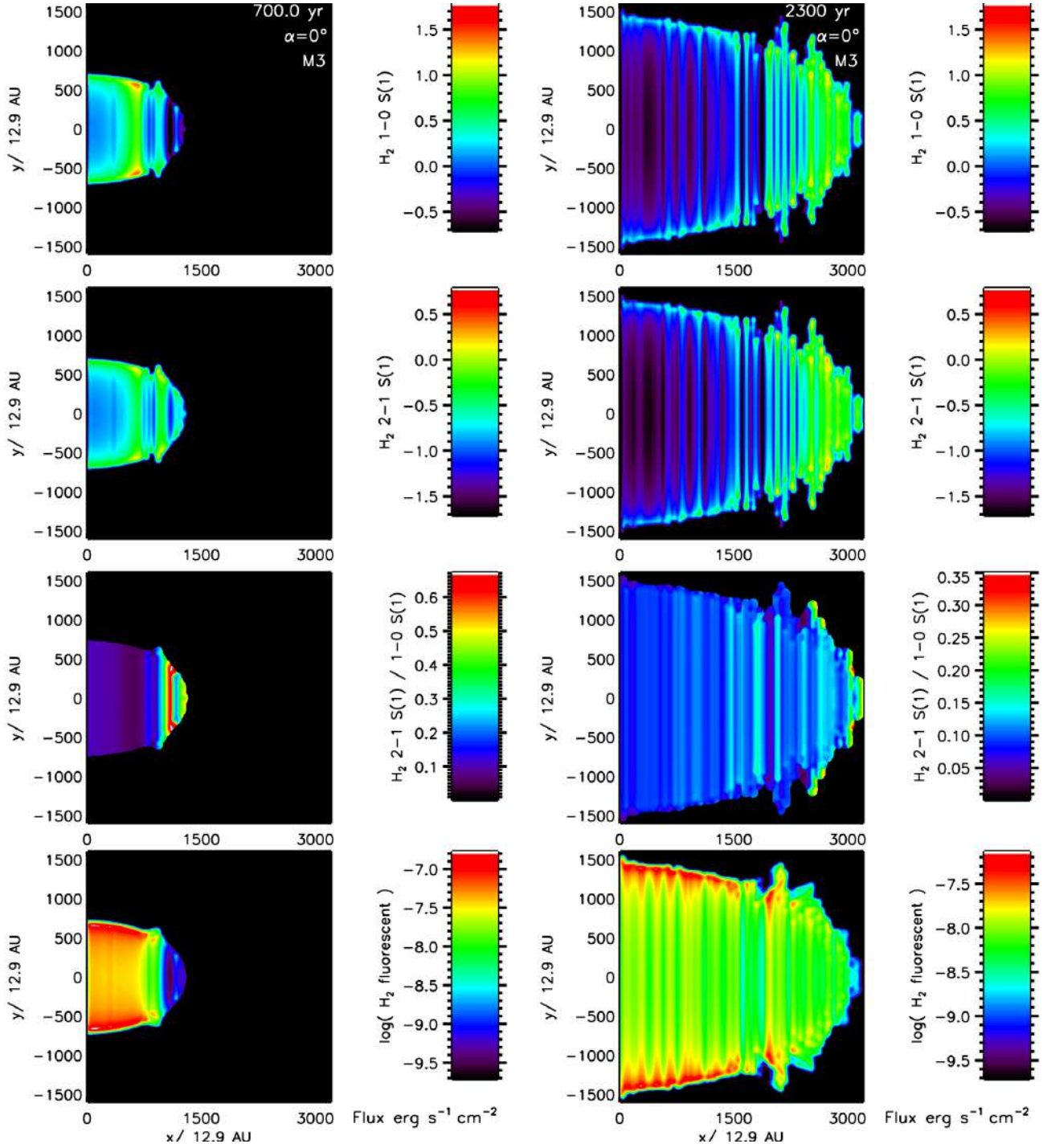

(a) M3: early time, 700 yr.

(b) M3: late time, 2,300 yr.

Figure 6.3: H_2 line emission maps for atomic wind impacting a molecular medium. Model M3: with a 2:1 $V_w \sim 140\,km\,s^{-1}$ wind in the plane of the sky at the indicated times.

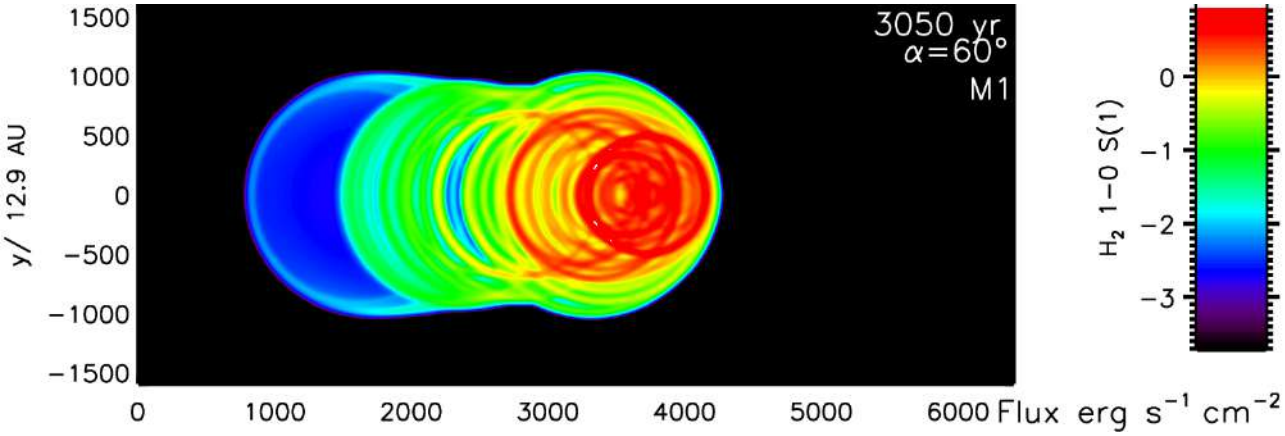

(a) M1: H_2 wind interacting with an H_2 ambient medium.

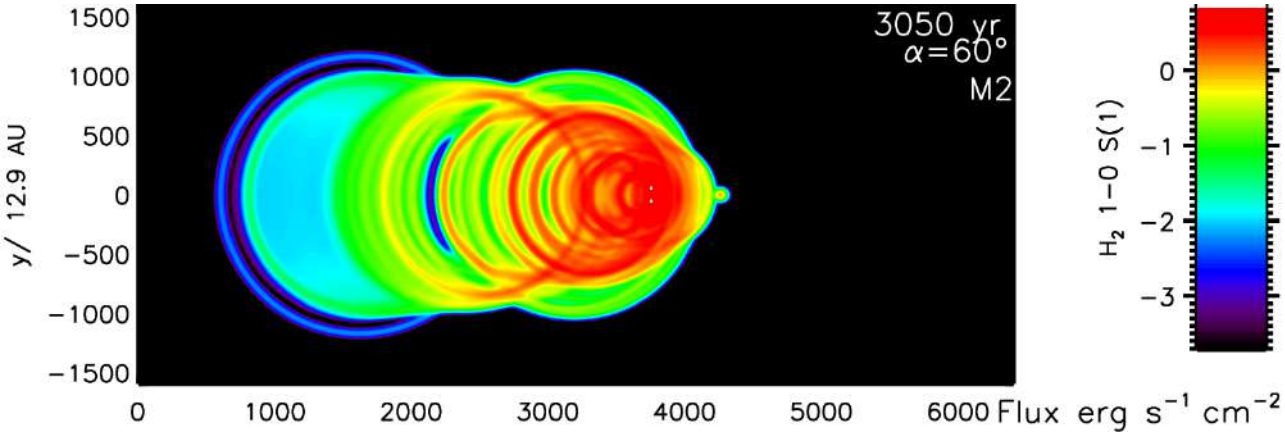

(b) M2: H_2 wind interacting with an H ambient medium.

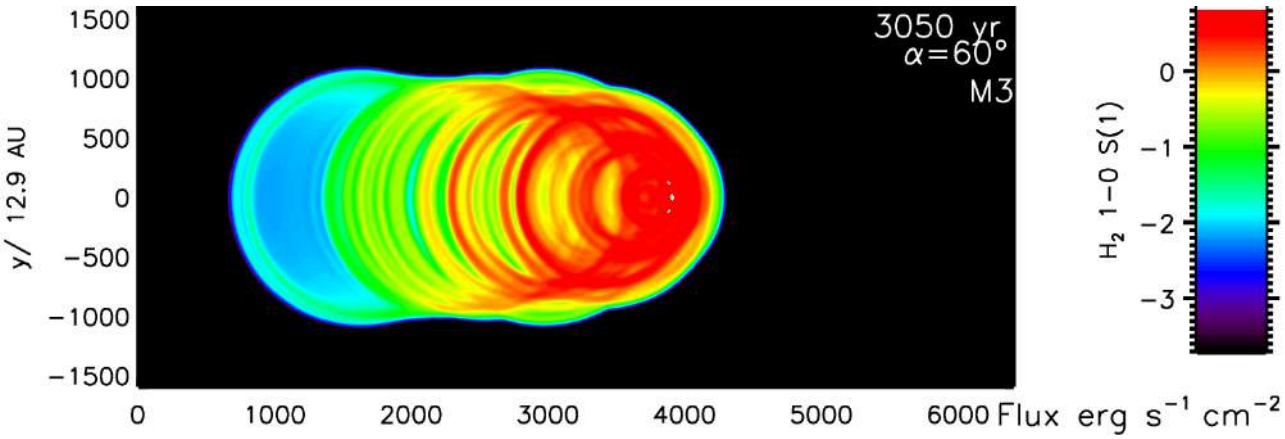

(c) M3: H wind interacting with an H_2 ambient medium.

Figure 6.4: Emission as a function of wind-ambient type. Simulated H_2 emission from the $1 \rightarrow 0$ S(1) line of 4:1 elliptical winds at 60° to the plane of the sky and axial speed of 140 km s^{-1}. The origin of the wind is at zone (1,600,0).

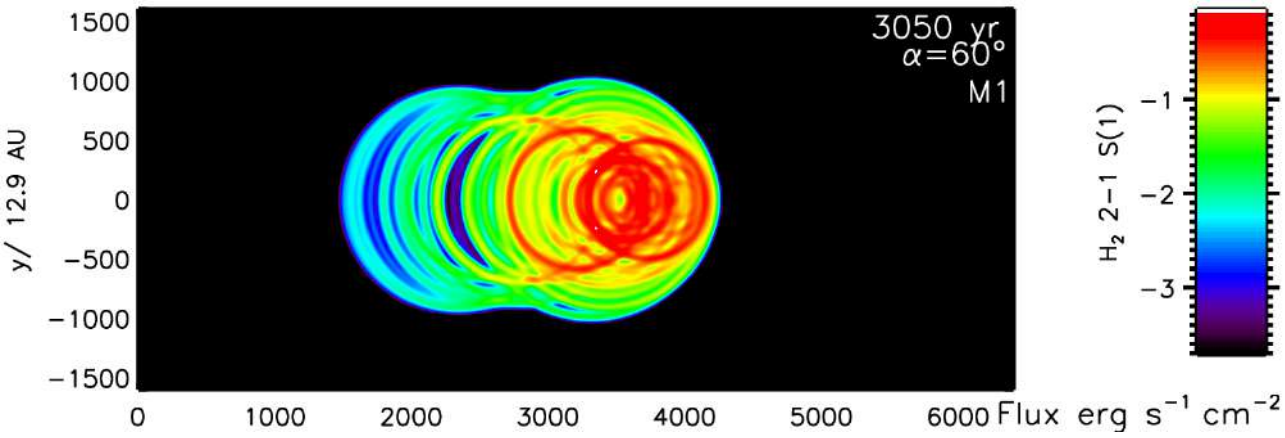

(a) M1: H_2 wind interacting with an H_2 ambient medium.

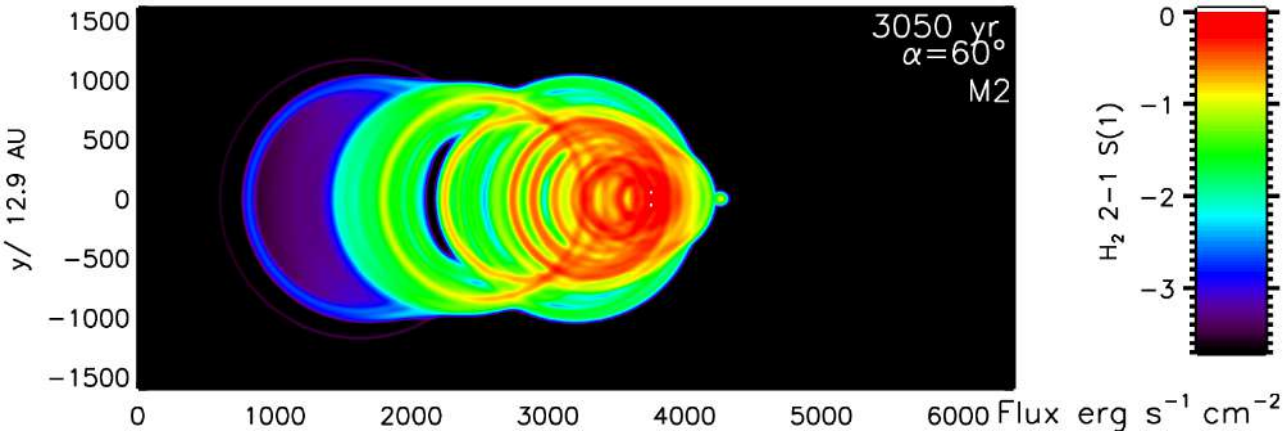

(b) M2: H_2 wind interacting with an H ambient medium

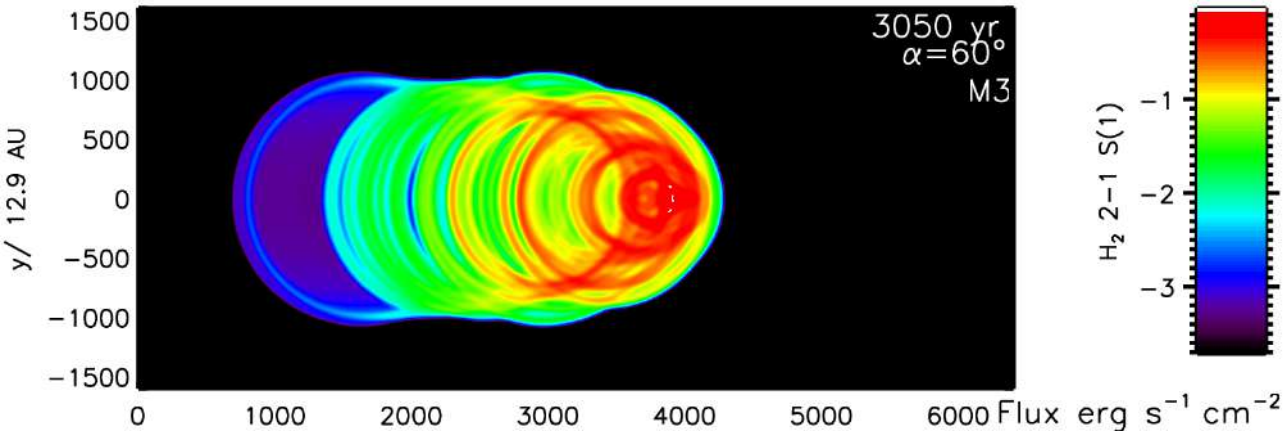

(c) M3: H wind interacting with an H_2 ambient medium

Figure 6.5: Emission as a function of wind-ambient type. Simulated H_2 emission from the $2 \rightarrow 1$ S(1) line of 4:1 elliptical winds at 60° to the plane of the sky and axial speed of 140 km s^{-1}. The origin of the wind is at zone (1,600,0).

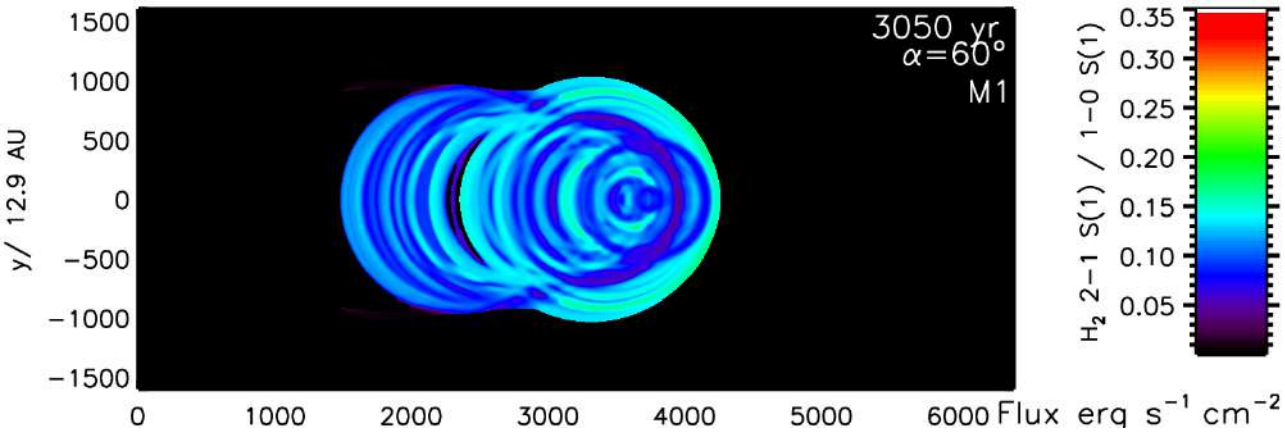

(a) M1: H_2 wind interacting with an H_2 ambient medium.

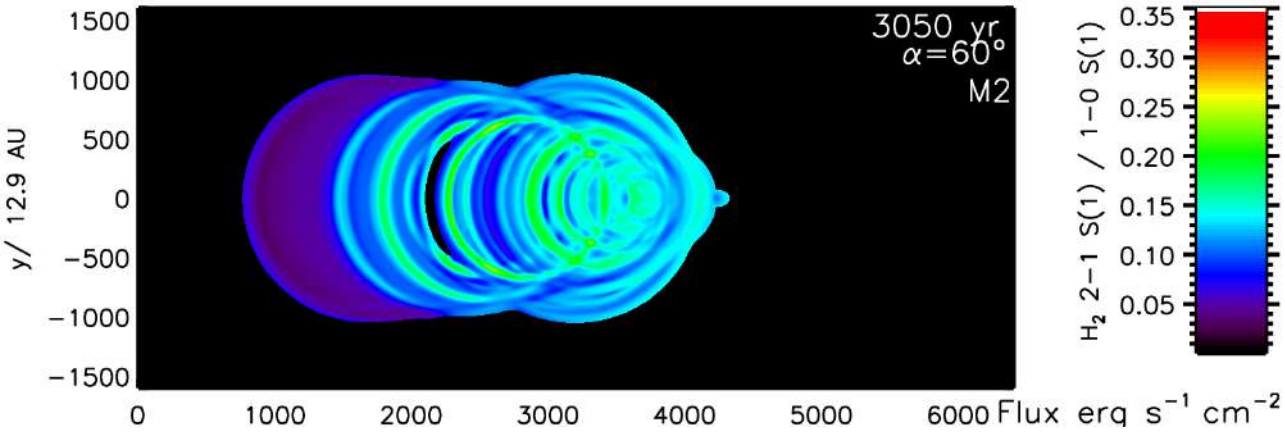

(b) M2: H_2 wind interacting with an H ambient medium.

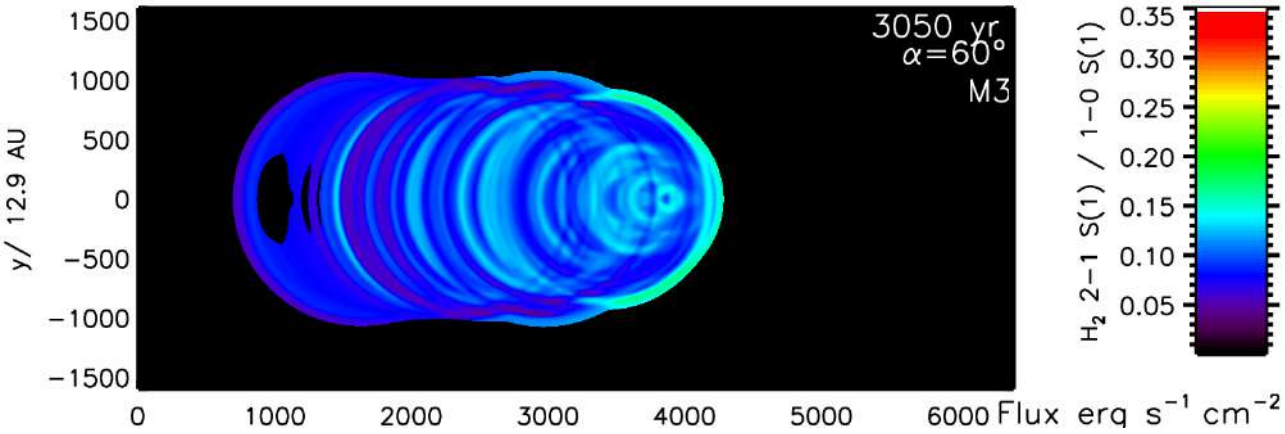

(c) M3: H wind interacting with an H_2 ambient medium.

Figure 6.6: Vibrational excitation as a function of wind-ambient type. Simulated H_2 ratio mapping from the $2 \rightarrow 1\,S(1)/1 \rightarrow 0\,S(1)$ line ratio of 4:1 elliptical winds at 60° to the plane of the sky and axial speed of 140 km s^{-1}. The origin of the wind is at zone (1,600,0).

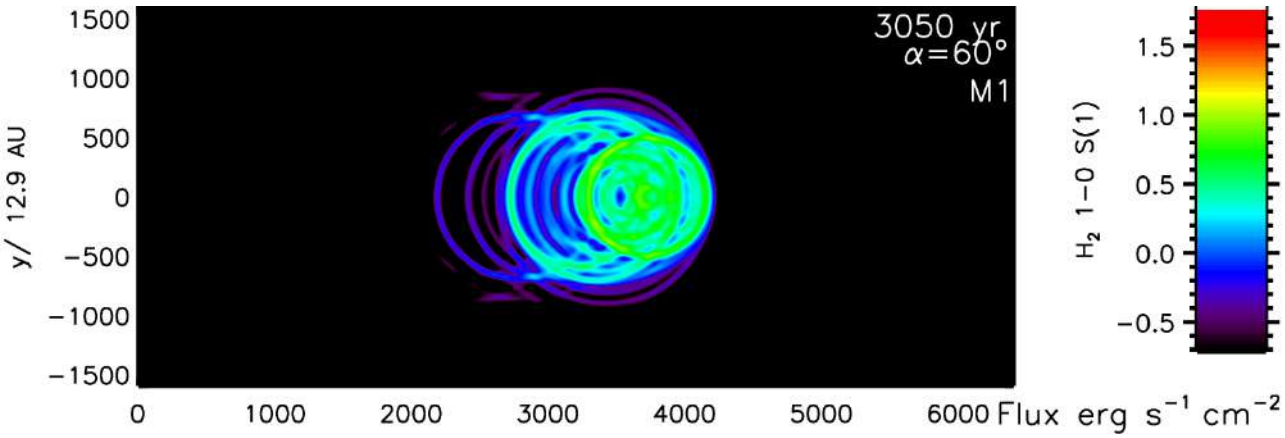

(a) M1: H_2 wind interacting with an H_2 ambient medium.

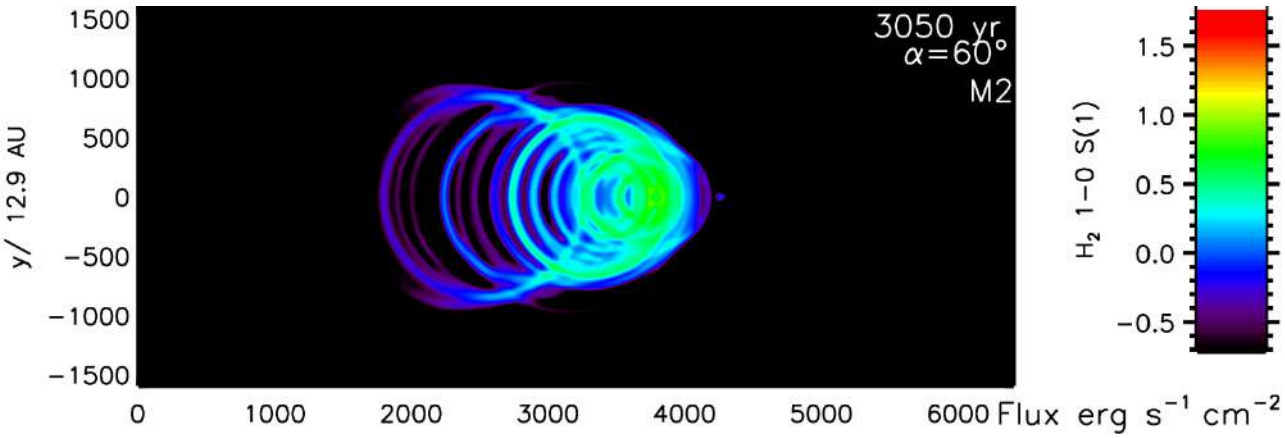

(b) M2: H_2 wind interacting with an H ambient medium.

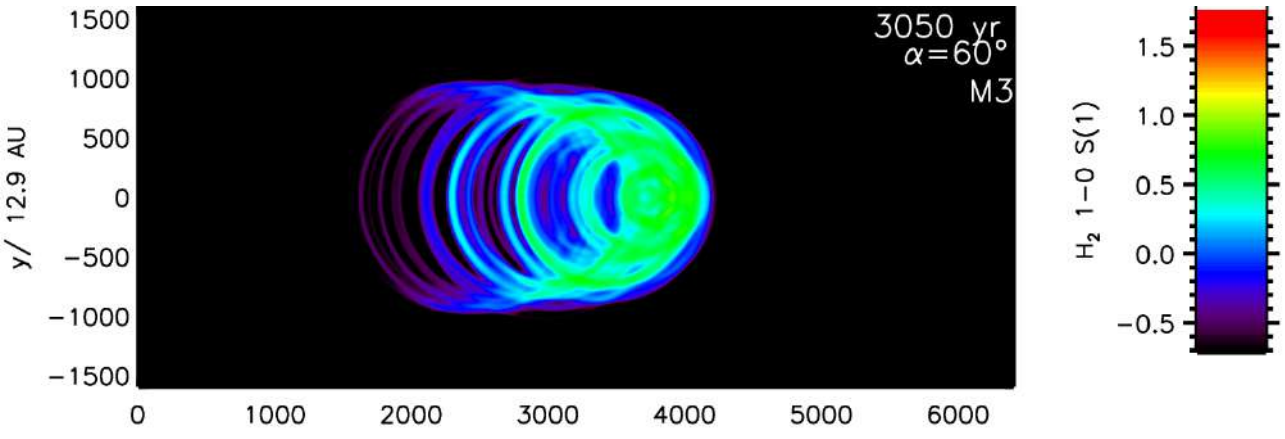

(c) M3: H wind interacting with an H_2 ambient medium.

Figure 6.7: Emission as a function of wind-ambient type. Simulated H_2 emission of smaller range in flux from the $1 \rightarrow 0\,S(1)$ line of 4:1 ellipticl winds at 60° to the plane of the sky and axial speed of 140 km s^{-1}. The origin of the wind is at zone (1,600,0).

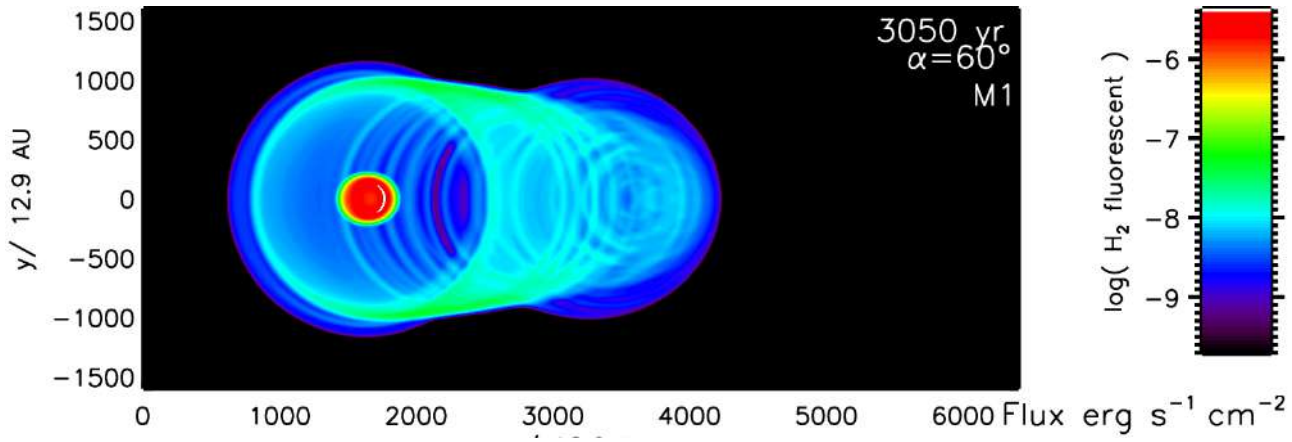

(a) M1: H_2 wind interacting with an H_2 ambient medium.

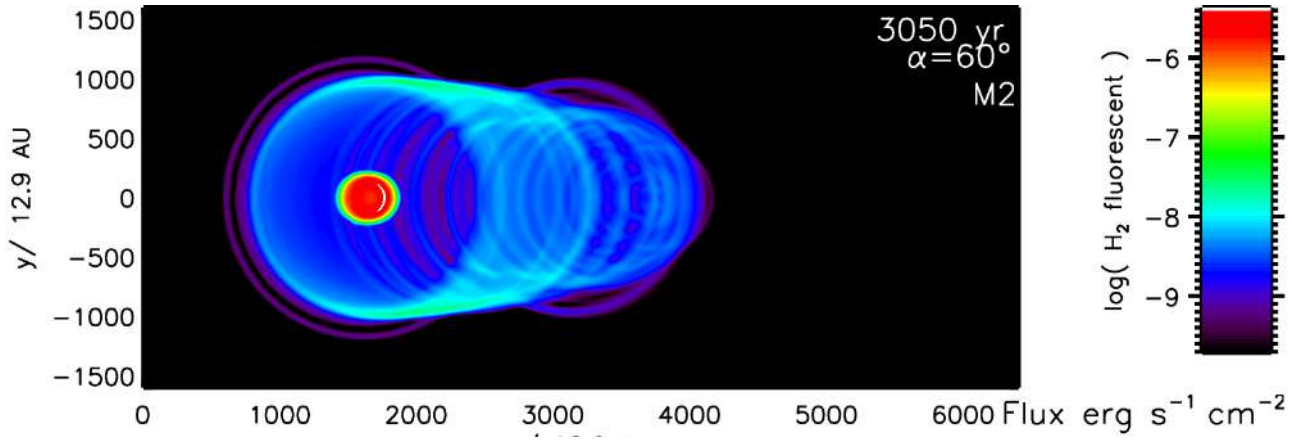

(b) M2: H_2 wind interacting with an H ambient medium.

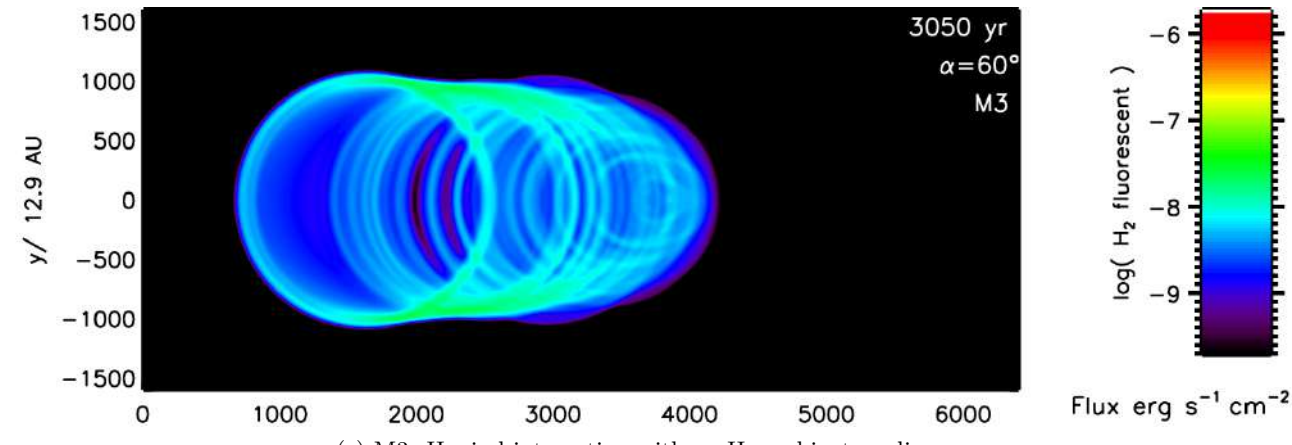

(c) M3: H wind interacting with an H_2 ambient medium.

Figure 6.8: A possible measure of H_2 fluorescence, displayed here is the distribution of $\rho(H_2)/r^2$ where r is the distance from the wind origin (assumed to be the UV radiation source for the fluorescence) measured in arbitrary units.

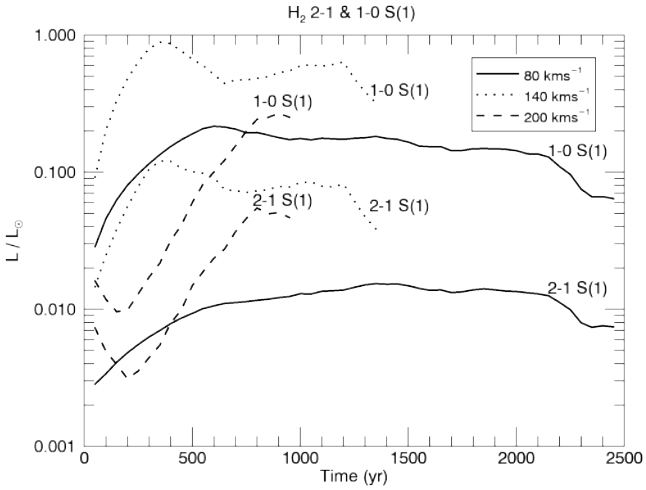

(a) M1: H_2 wind interacting with an H_2 ambient medium.

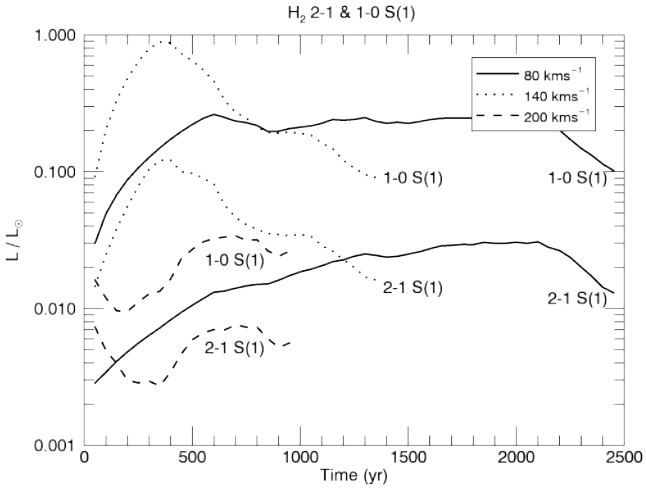

(b) M2: H_2 wind interacting with an H ambient medium.

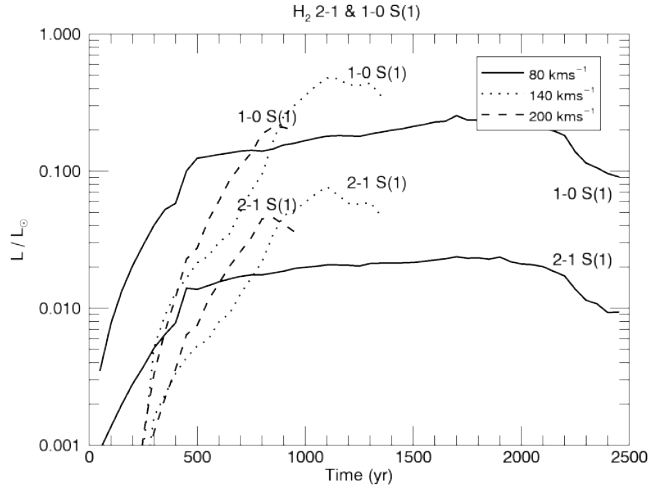

(c) M3: H wind interacting with an H_2 ambient medium.

Figure 6.9: The evolution of the integrated emission in the indicated K-band vibrational transitions produced by 1:1 M1, M2 and M3 outflows for the three axial wind velocities.

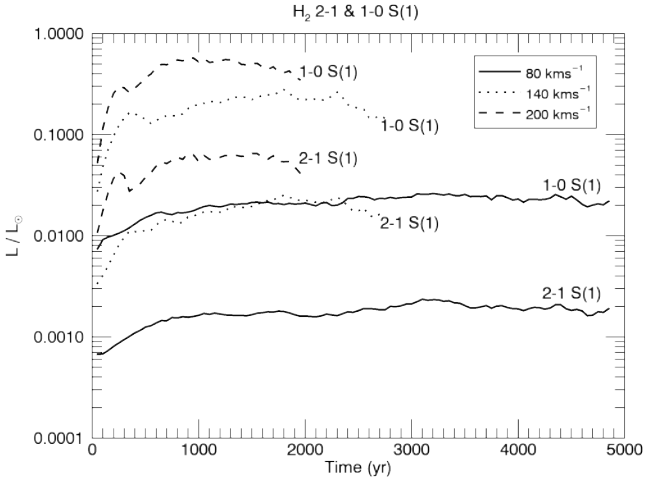

(a) M1: H_2 wind interacting with an H_2 ambient medium.

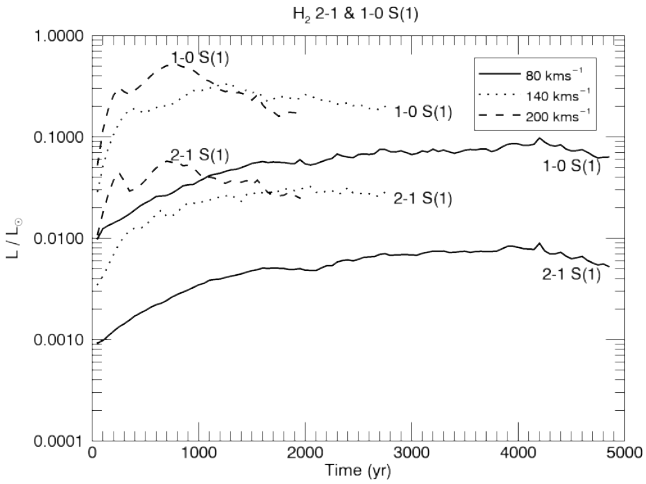

(b) M2: H_2 wind interacting with an H ambient medium.

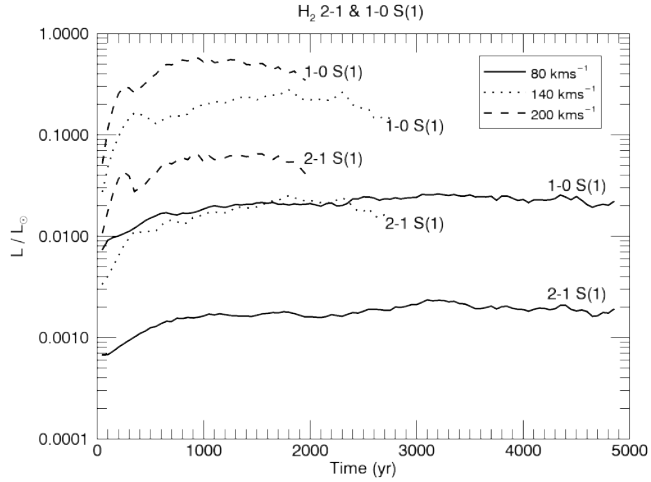

(c) M3: H wind interacting with an H_2 ambient medium.

Figure 6.10: The evolution of the integrated emission in the indicated K-band vibrational transitions produced by 2:1 M1, M2 and M3 outflows for the three axial wind velocities.

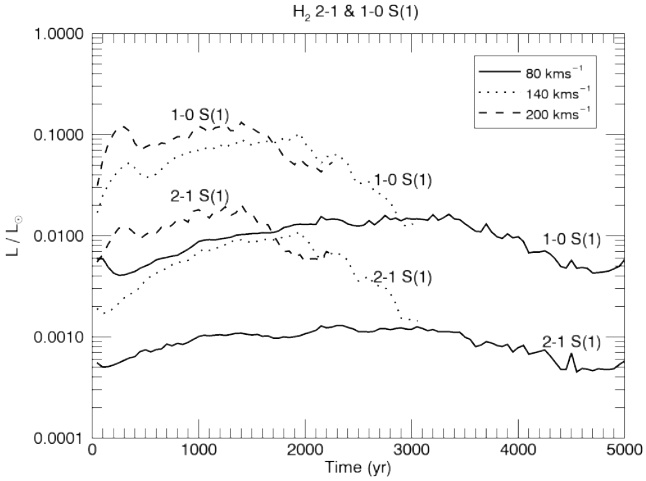

(a) M1: H_2 wind interacting with an H_2 ambient medium.

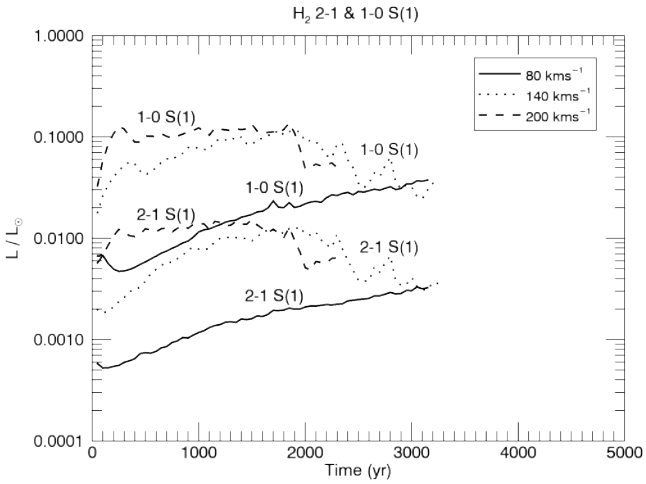

(b) M2: H_2 wind interacting with an H ambient medium.

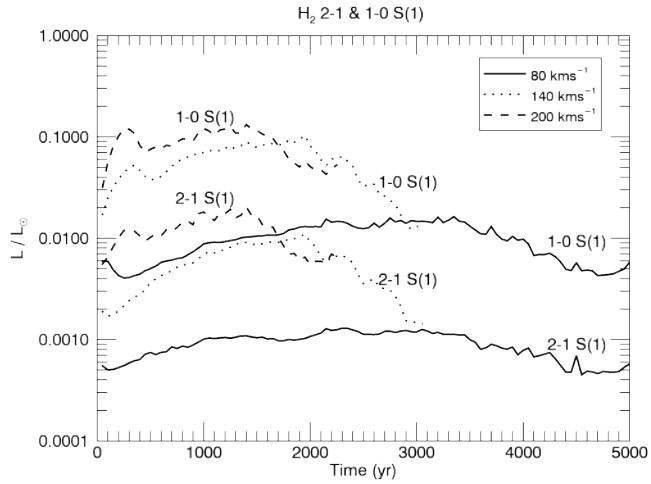

(c) M3: H wind interacting with an H_2 ambient medium.

Figure 6.11: The evolution of the integrated emission in the indicated K-band vibrational transitions produced by 4:1 M1, M2 and M3 outflows for the three axial wind velocities.

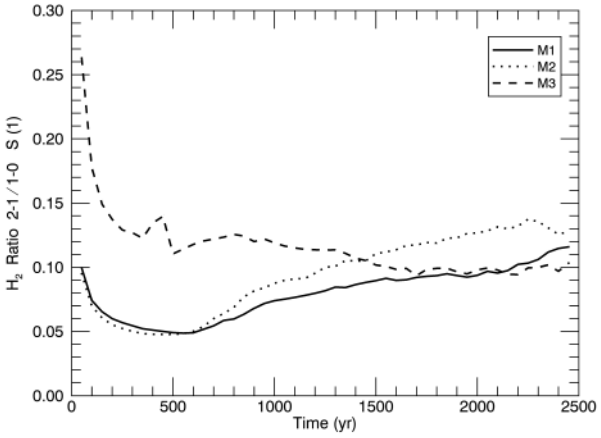

(a) $V_w = 80\,km\,s^{-1}$.

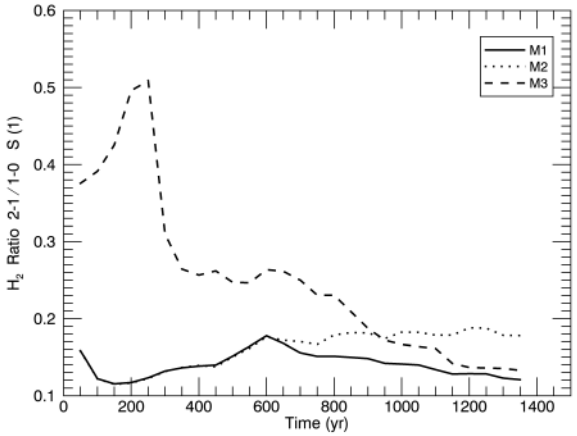

(b) $V_w = 140\,km\,s^{-1}$.

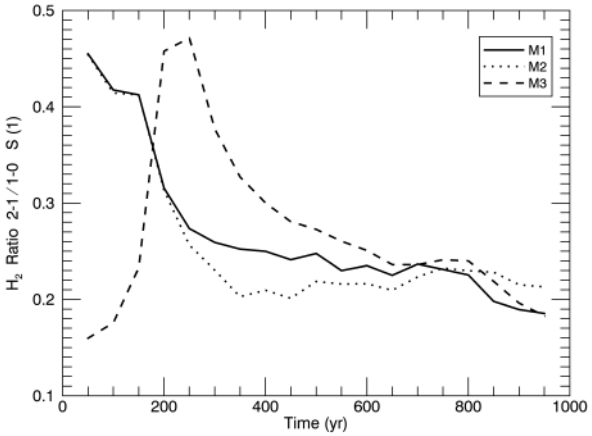

(c) $V_w = 200\,km\,s^{-1}$.

Figure 6.12: The ratio of the emissions from vibration transitions originating from the second and first levels produced by 1:1 M1, M2 and M3 outflows at 80 $km\,s^{-1}$ (top), 140 $km\,s^{-1}$ (middle) and 200 $km\,s^{-1}$ (bottom) wind velocities.

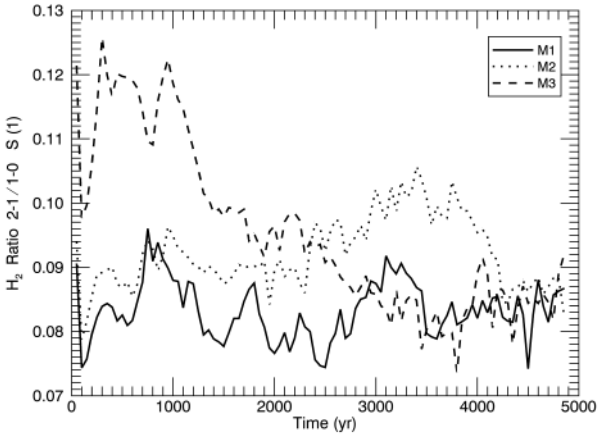

(a) $V_w = 80\,km\,s^{-1}$.

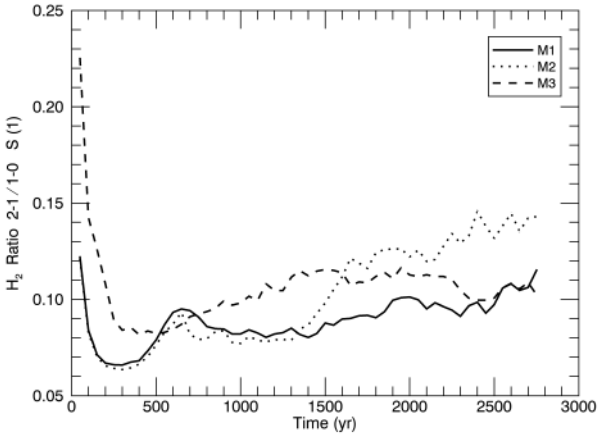

(b) $V_w = 140\,km\,s^{-1}$.

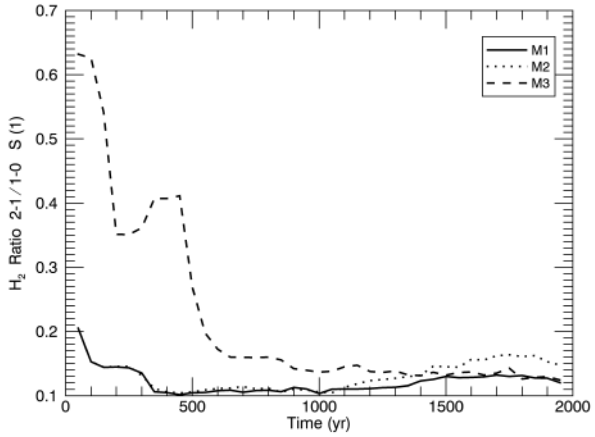

(c) $V_w = 200\,km\,s^{-1}$.

Figure 6.13: The ratio of the emissions from vibration transitions originating from the second and first levels produced by 2:1 M1, M2 and M3 outflows at 80 $km\,s^{-1}$ (top), 140 $km\,s^{-1}$ (middle) and 200 $km\,s^{-1}$ (bottom) wind velocities.

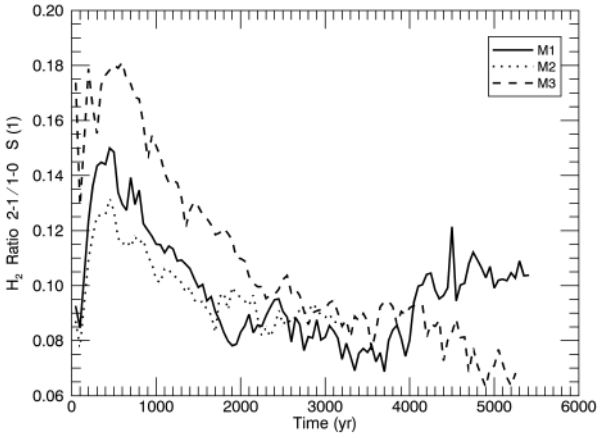

(a) $V_w = 80\,km\,s^{-1}$.

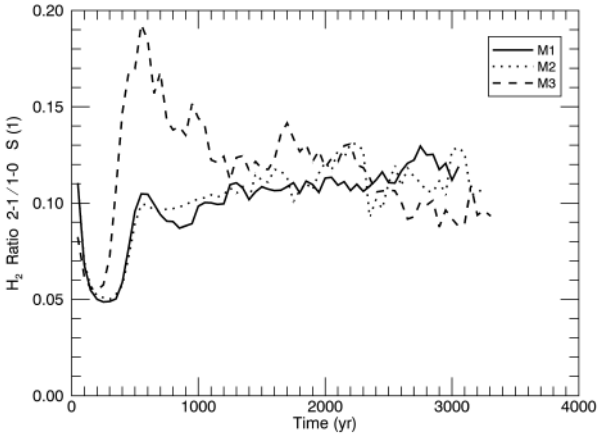

(b) $V_w = 140\,km\,s^{-1}$.

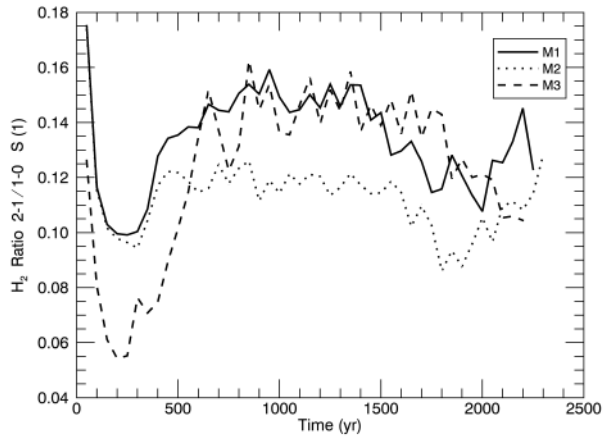

(c) $V_w = 200\,km\,s^{-1}$.

Figure 6.14: The ratio of the emissions from vibration transitions originating from the second and first levels produced by 4:1 M1, M2 and M3 outflows at 80 $km\,s^{-1}$ (top), 140 $km\,s^{-1}$ (middle) and 200 $km\,s^{-1}$ (bottom) wind velocities.

models that are split into the following panels, (a) a molecular wind into a uniform atomic medium (Model M2), (b) an atomic wind into a uniform molecular ambient and (Model M3) (c) an atomic wind-ambient run (Model M4). In each case of Fig. 6.18 - 6.21 the wind is 4:1 ellipsoidal in velocity with an axial speed of 140 $\mathrm{km\,s^{-1}}$ with the axis directed at 60° to the sky plane. The lower ellipticity 140 $\mathrm{km\,s^{-1}}$ wind in Fig. 6.15 - 6.17, is displayed in plane of the sky. A 2–D convolution Gaussian smoothing operator is applied for all models to resolve numerical errors at the forward shock with standard deviation of $\sigma = 20$ zones, and flux spread over 4σ. The above convolution setting enables observation comparison within optimum computational run time.

Regarding Fig. 6.18 - 6.21 the first remark is that the emission occurs in projected rings due to the axial symmetry. Secondly, most emission occurs in case (c) where both atomic wind and ambient media contribute. The peak emission shows a degree of variability corresponding with chemical composition. It is the two higher excitation species that show stronger peaks in Model M4. Uniform ISM simulations presented here show model M4 displaying optical emissions from both the flanks and the leading shock: the surface brightness is much smoother. In contrast, the emission is concentrated toward the faster leading edge of the ellipsoid for all four tracers in Model M2 where only the ambient medium is atomic. The peak emission in all cases is set back from the leading edge, independent of forward/backward shock structure, serving as further evidence to suggest that the emissivity distribution is mainly determined by the source geometry, presented by time-dependent flux animations [1].

The integrated optical emission graphs for each of the four lines are displayed in Fig. 6.22 – Fig. 6.25. Panels show time-dependent luminosity variation with Model type, axial speed and wind ellipticity. First to note is that there is a drop in flux with increase in ellipticity. All computed models show similar ellipticity/velocity flux magnitude sequence. The line luminosities displayed in left-hand panels representing Model M2 all start off with increase in flux. Clearly, the fast molecular wind is sweeping and heating up atomic ambient gas at an increasing rate. However, the wind is hindered and the speed of advance decreases. Therefore, the flux eventually falls, except for the low-excitation lines in the low wind speed case. For Model M3 with the atomic wind, the line luminosities start high but then fall rapidly before reaching steady magnitudes. Overall, Model M3 generates a plateau of emission with time.

At later stages the wind shows least amount of emission from the wings and lower flux values

[1] `http://astro.kent.ac.uk/~in32/ppn.html`

Table 6.1: Ion & Free electron fraction.

Flux line	$\epsilon_{ion} = n_{ion}/n_H$	$\chi_e = n_e/n_H$
[a]O[I]	3.5×10^{-4}	0.1
[a]S[II]	$\epsilon_{[II]}(T)$	0.1
[b]Fe[II]	1.4×10^{-6}	0.1

Abundancies by (Reynolds 1989)[a],(Smith 1994b)[b],(Arnaud & Rothenflug 1985)[c].

from the cap, where the dense molecular wind impinges on atomic medium, this set up enables the wind cap to obtain lower flux values of one magnitude, relative to its inverted counterpart, Model M3. The atomic material surrounding the wind's cap in M2 gets excited and shocked by H_2 molecules in the wind, setting off emission in optical range.

The line luminosities toward the end of these runs, where the pPN has expanded to the scale of 0.1 pc, show a consistent pattern. Generally, the M4 fully atomic run generates more emission than the M2 run by a factor of 10, significantly more than one would expect from adding together the atomic wind component of M3 to the atomic ambient of M2. Hence, the production of the thick turbulent shell intensifies the energy channelled into the strong atomic lines.

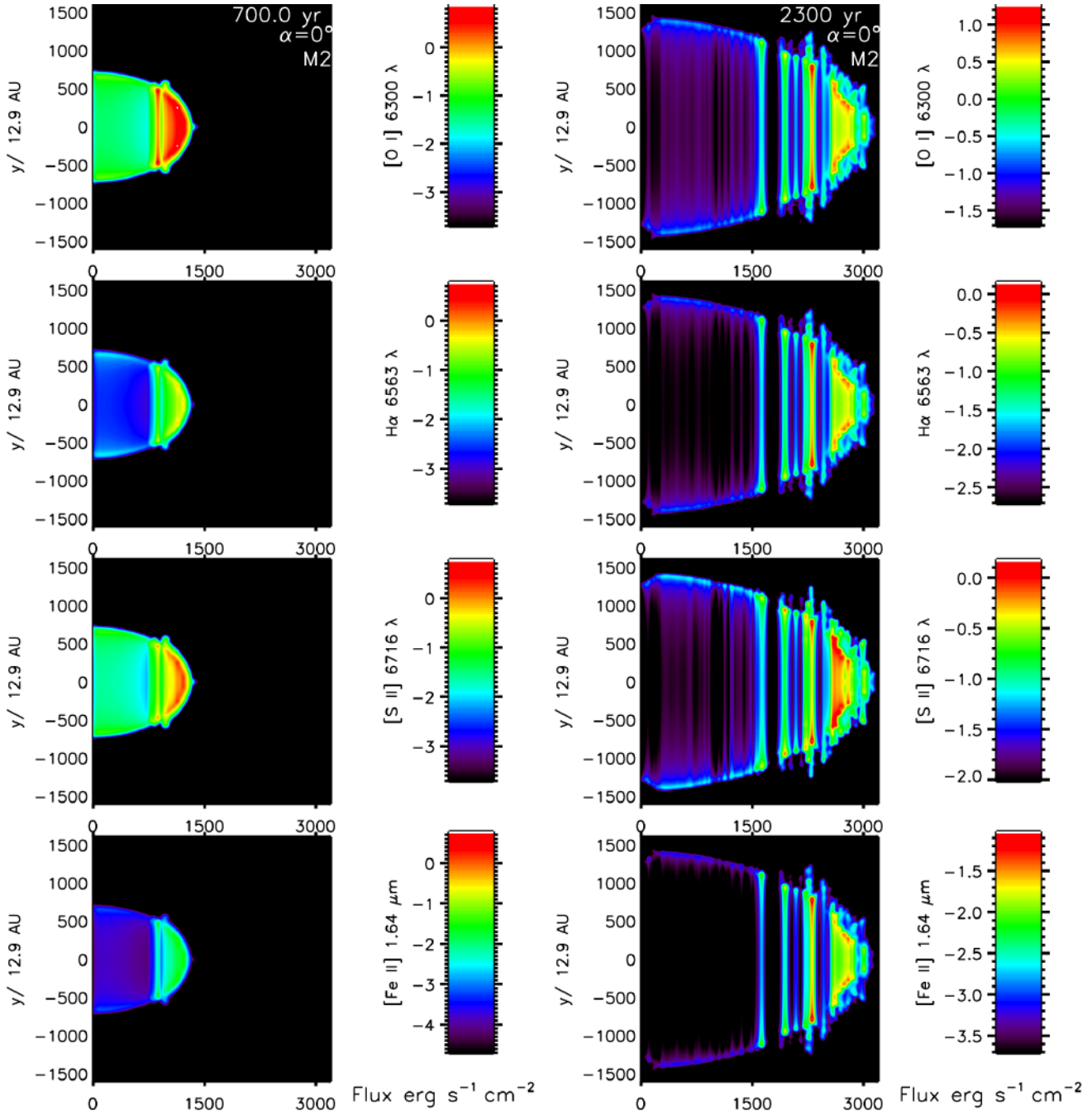

(a) M2: early time, 700 yr.

(b) M2: late time, 2,300 yr.

Figure 6.15: Optical line emission maps for a molecular wind impacting atomic medium. Model M2: with a 2:1 $V_w \sim 140\,km\,s^{-1}$ wind in the plane of the sky at the indicated times.

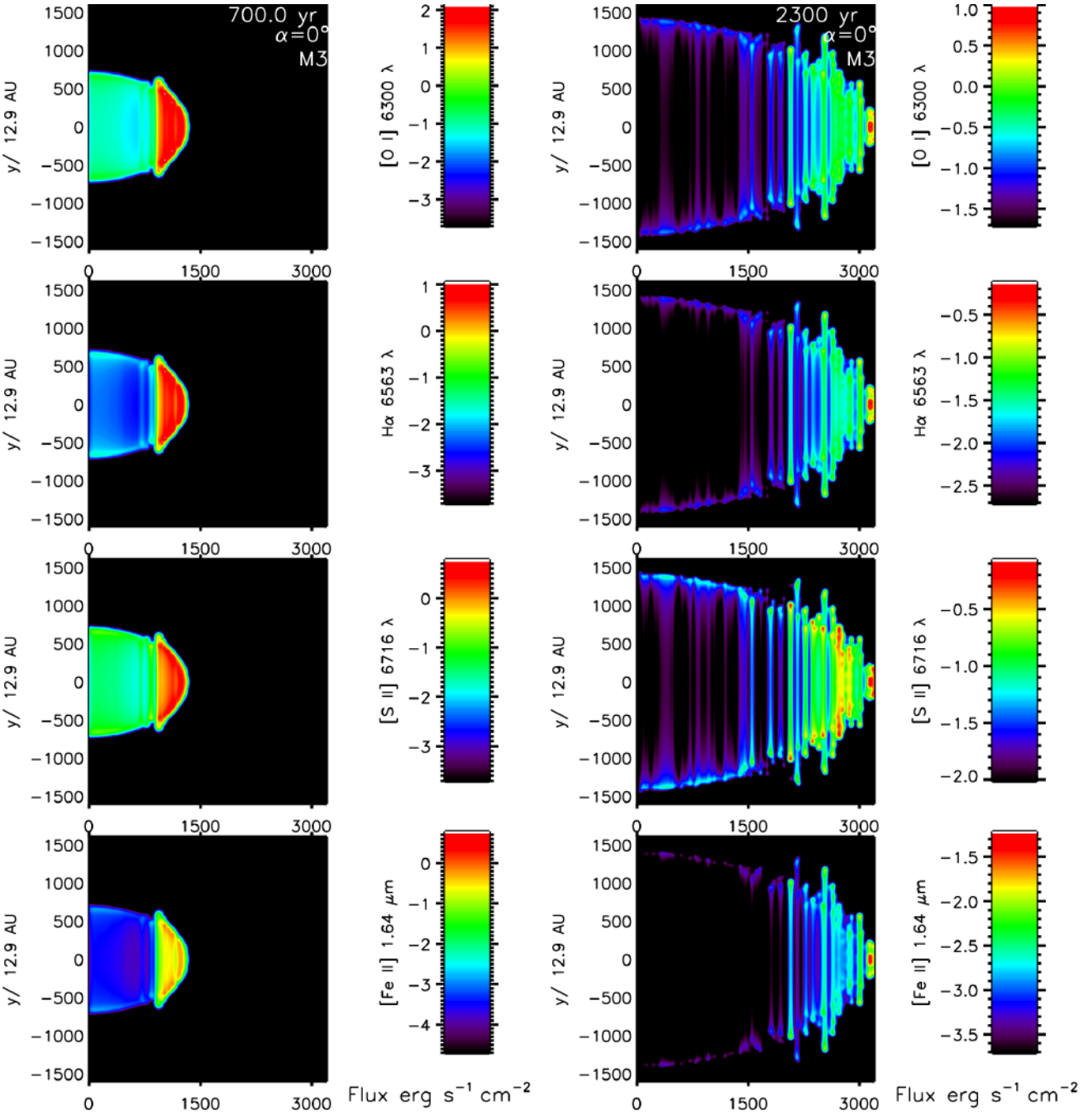

(a) M3: early time, 700 yr.

(b) M3: late time, 2,300 yr.

Figure 6.16: Optical line emission maps for atomic wind impacting molecular medium. Model M3: with a 2:1 $V_w \sim 140\,km\,s^{-1}$ wind in the plane of the sky at the indicated times.

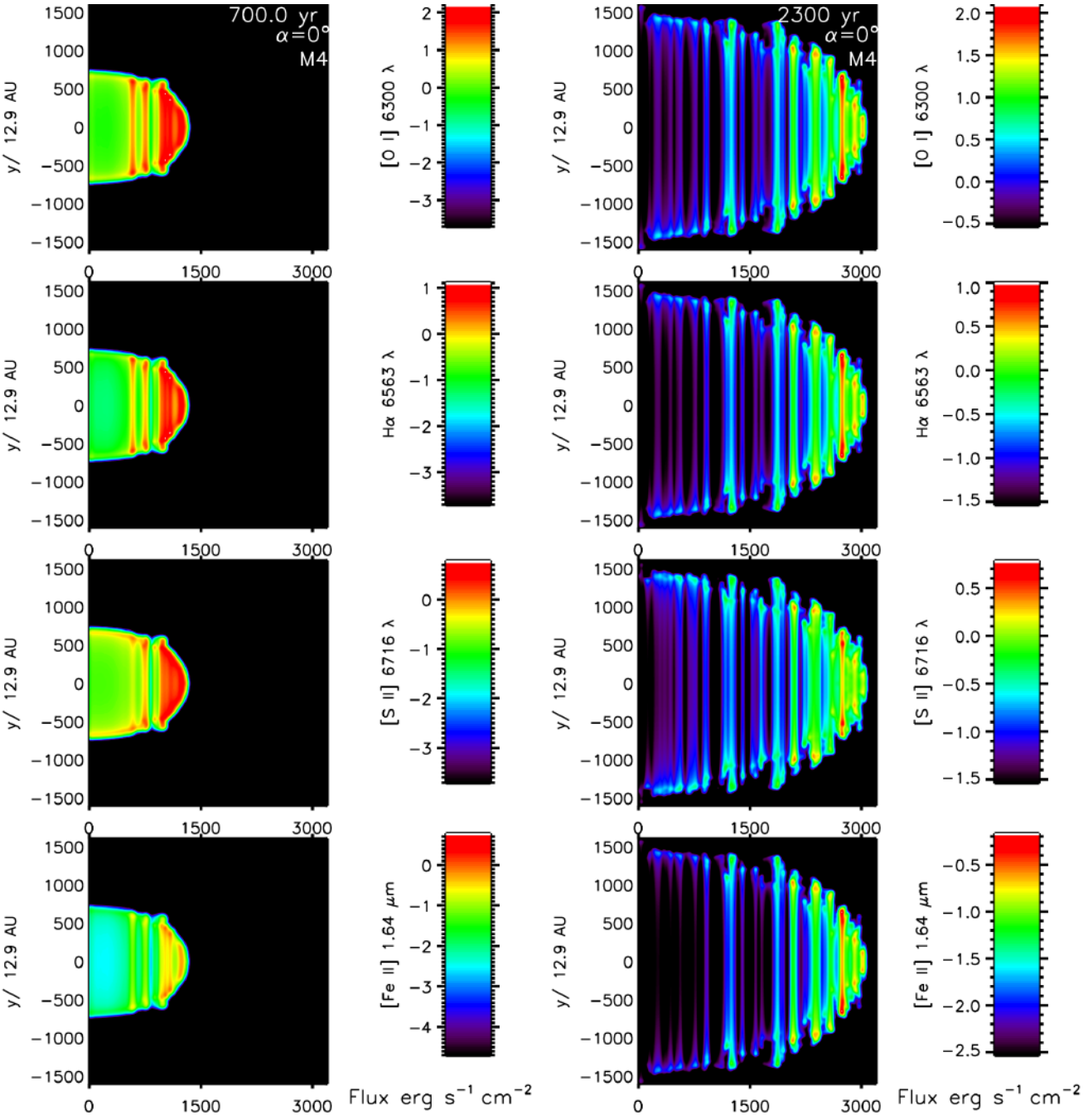

(a) M4: early time, 700 yr.

(b) M4: late time, 2,300 yr.

Figure 6.17: Optical line emission maps for atomic wind impacting atomic medium. Model M4: with a 2:1 $V_w \sim 140\,km\,s^{-1}$ wind in the plane of the sky at the indicated times.

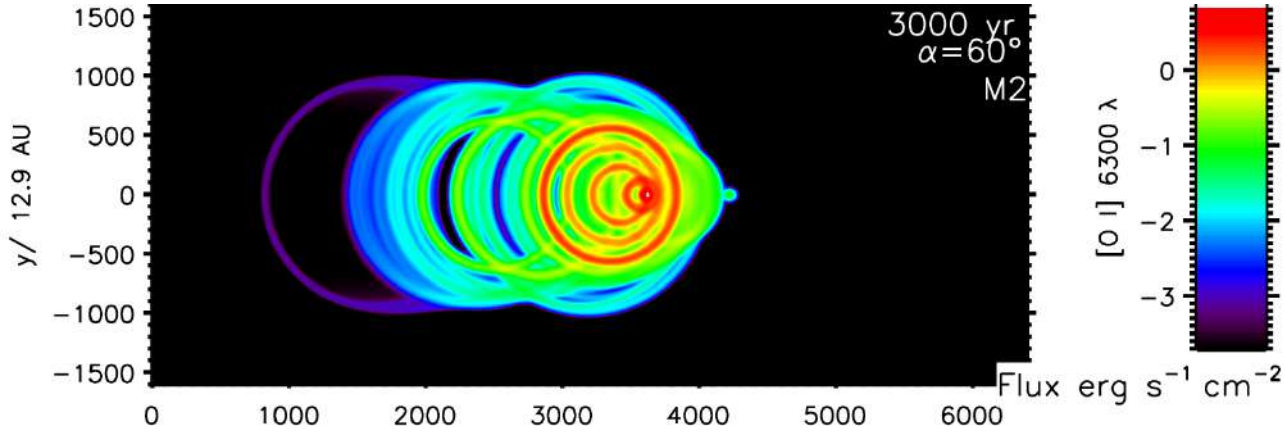

(a) M2: H_2 wind interacting with an H ambient medium.

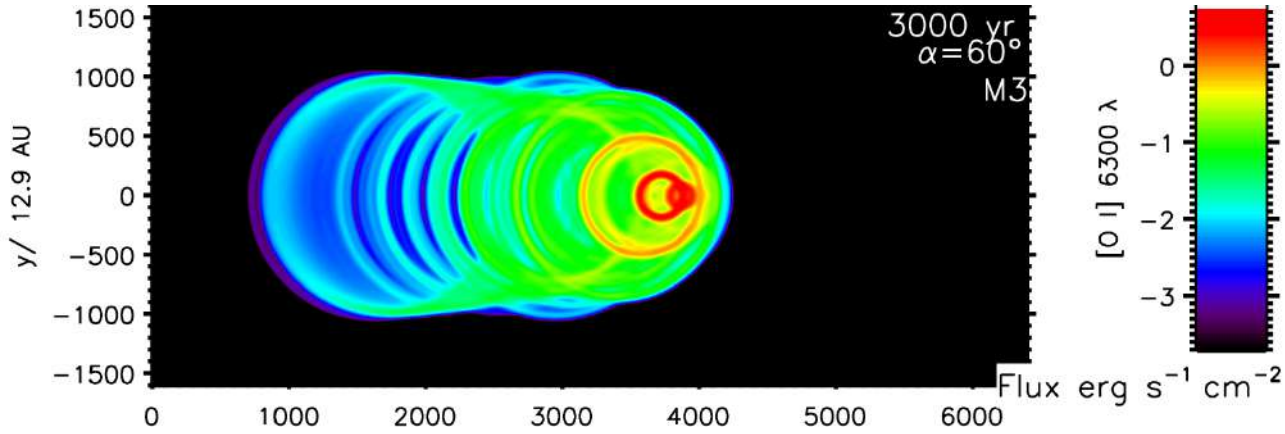

(b) M3: H wind interacting with an H_2 ambient medium.

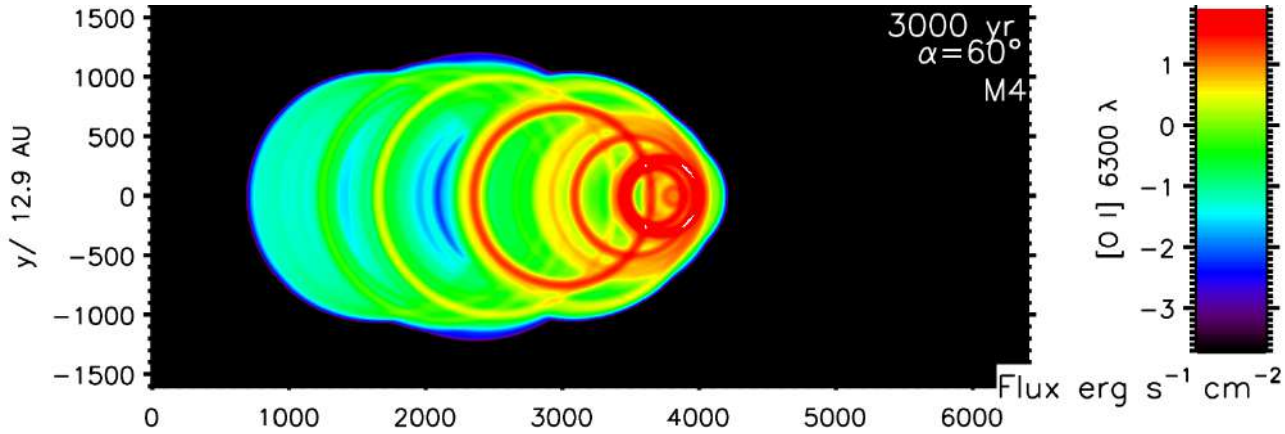

(c) M4: H wind interacting with an H ambient medium.

Figure 6.18: Simulated [O I] 6300 λ airglow line mapping of 4:1 ellipticity winds at 60° to the plane of the sky and axial speed of 140 km s^{-1}. The origin of the wind is at zone (1,600,0).

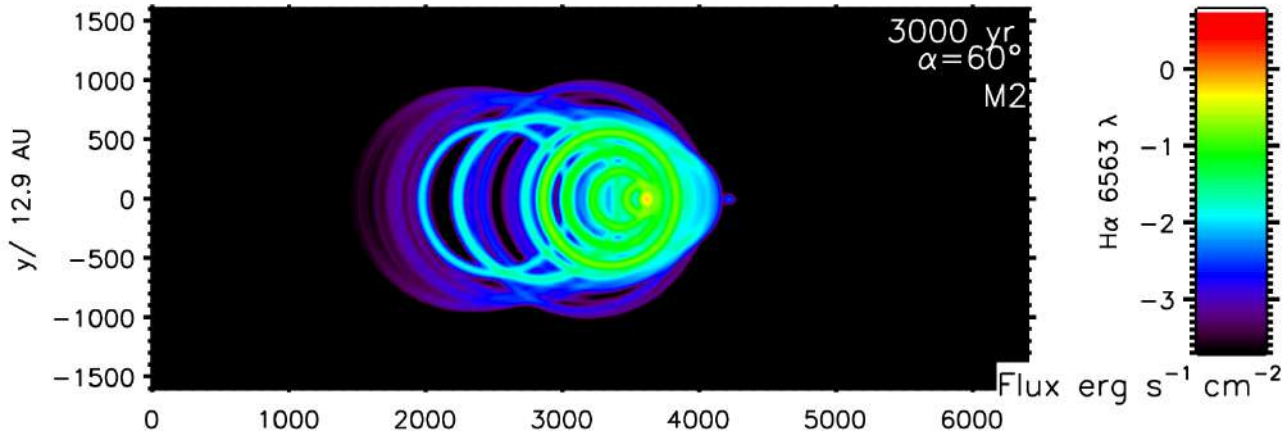

(a) M2: H_2 wind interacting with an H ambient medium.

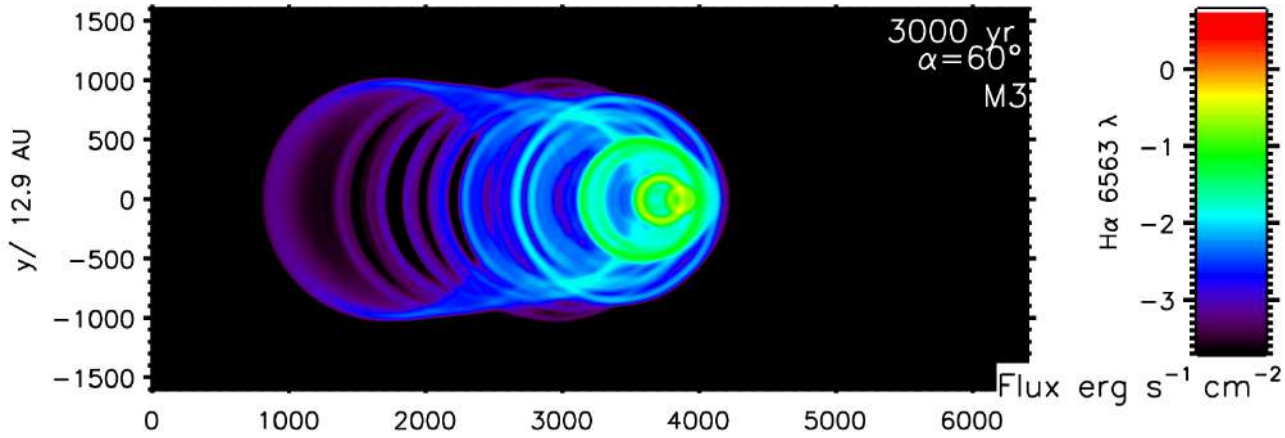

(b) M3: H wind interacting with an H_2 ambient medium.

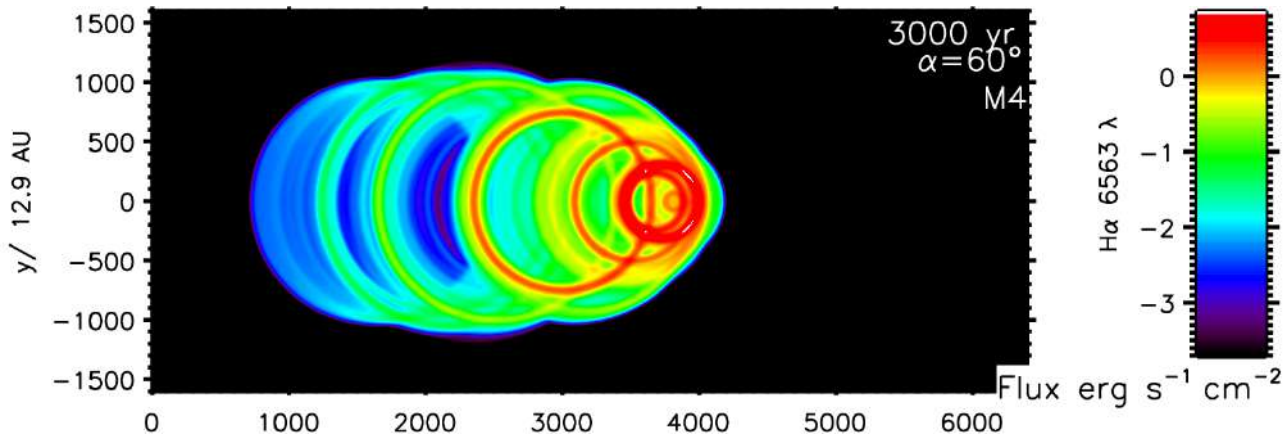

(c) M4: H wind interacting with an H ambient medium.

Figure 6.19: Simulated Hα 6563 λ line mapping of 4:1 ellipticity winds at 60° to the plane of the sky and axial speed of 140 km s^{-1}. The origin of the wind is at zone (1,600,0).

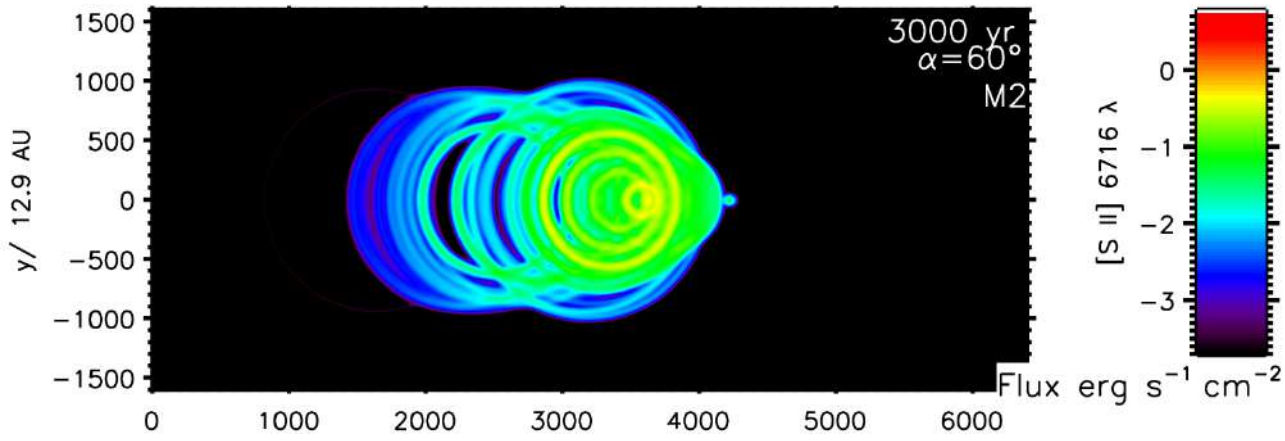

(a) M2: H_2 wind interacting with an H ambient medium.

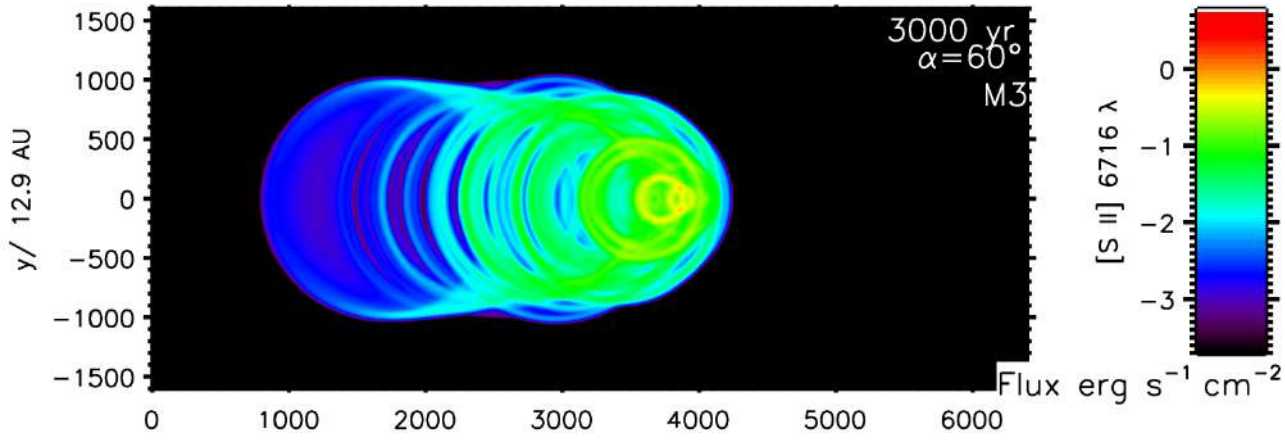

(b) M3: H wind interacting with an H_2 ambient medium.

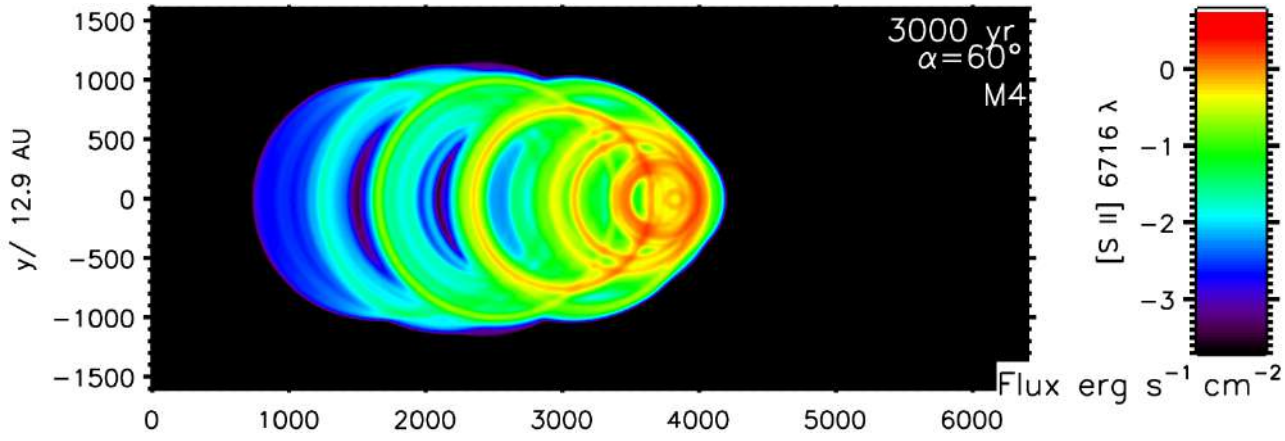

(c) M4: H wind interacting with an H ambient medium.

Figure 6.20: Simulated [Si II] 6716 λ line mapping of 4:1 ellipticity winds at 60° to the plane of the sky and axial speed of 140 km s^{-1}. The origin of the wind is at zone (1,600,0).

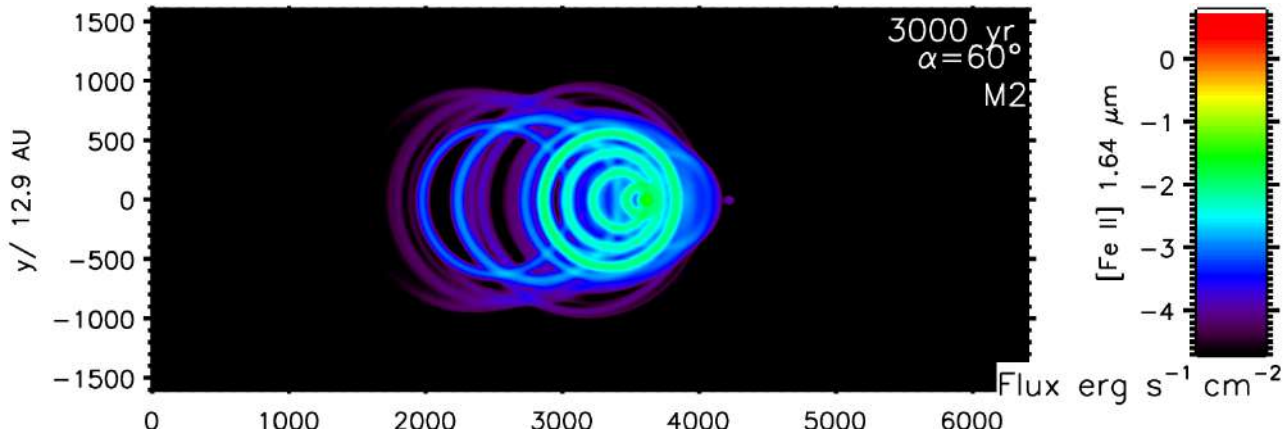

(a) M2: H_2 wind interacting with an H ambient medium.

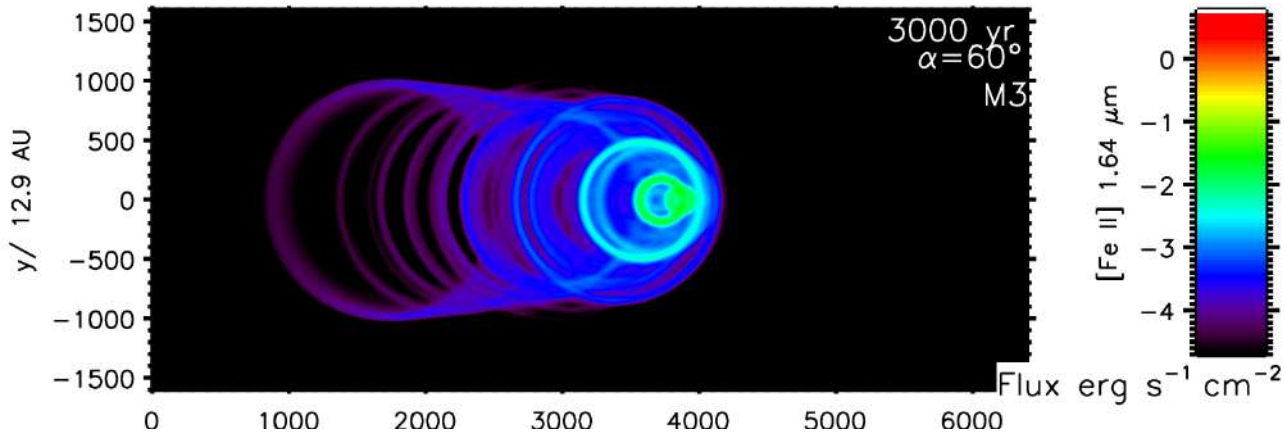

(b) M3: H wind interacting with an H_2 ambient medium.

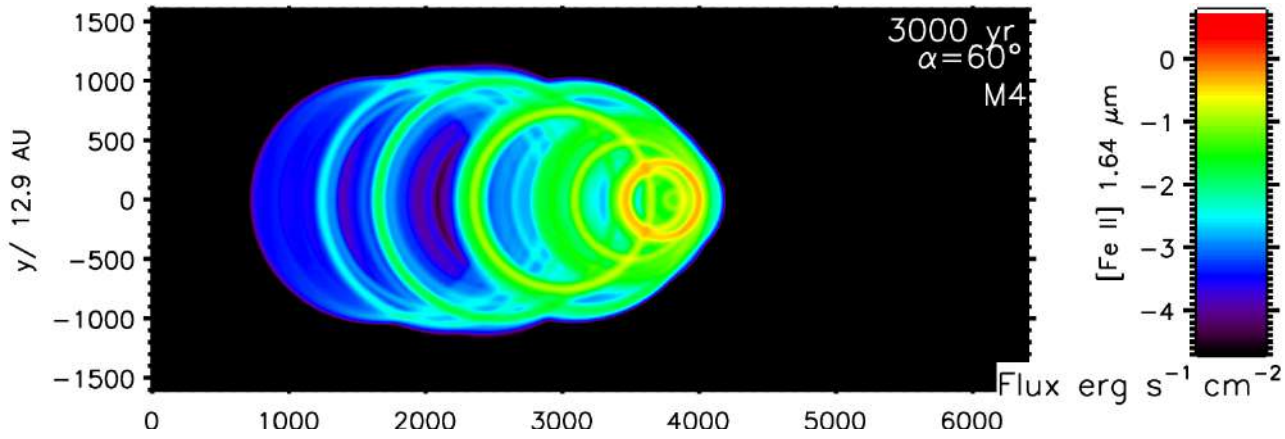

(c) M4: H wind interacting with an H ambient medium.

Figure 6.21: Simulated [Fe II] 1.64 μm line mapping of 4:1 ellipticity winds at 60° to the plane of the sky and axial speed of 140 km s^{-1}. The origin of the wind is at zone (1,600,0).

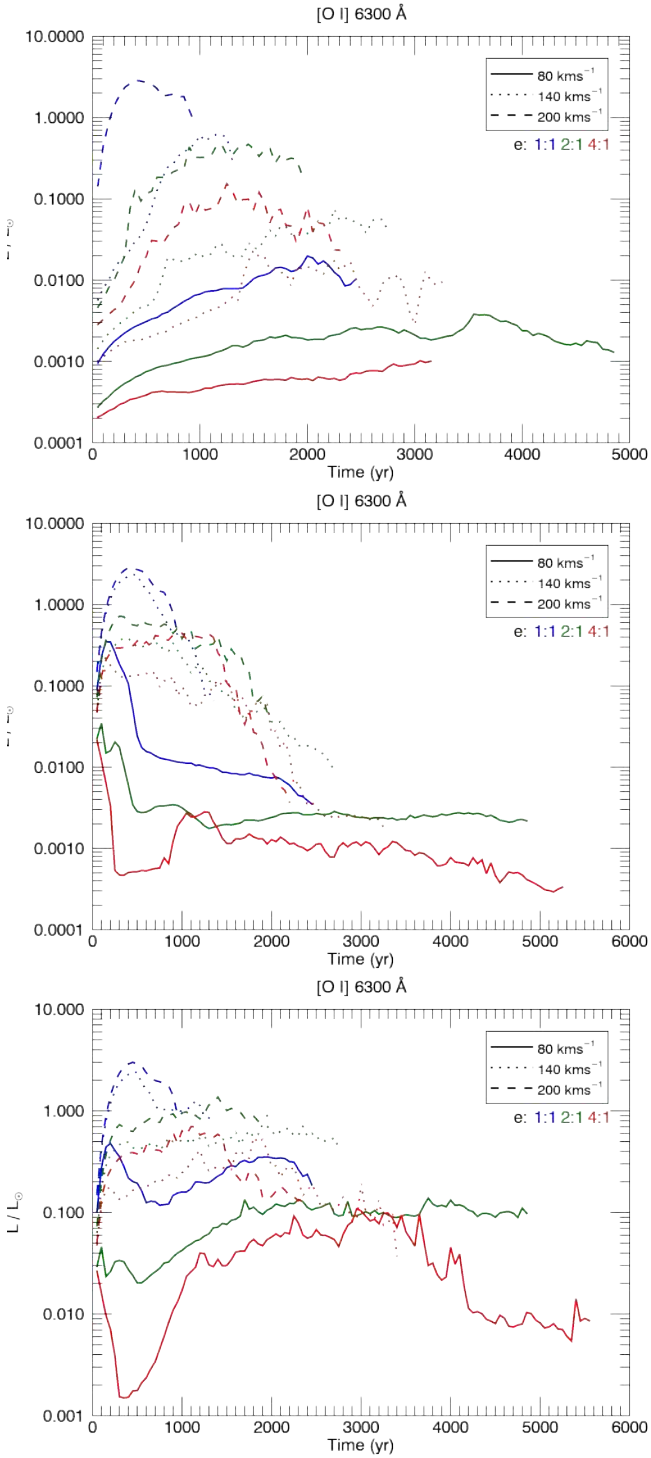

Figure 6.22: Total [OI] emissivities by M2, M3 and M4 outflows at high/low wind velocities for all ellipticities.

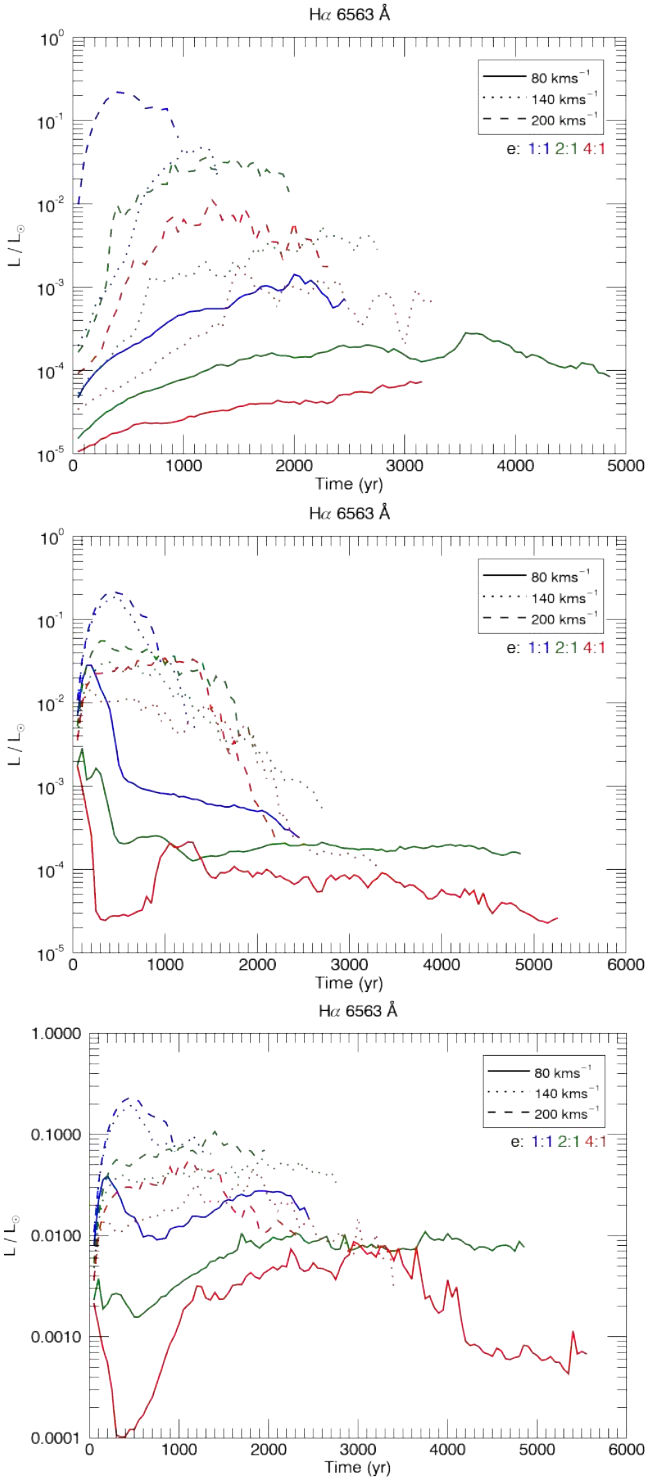

Figure 6.23: Total Hα 6563 λ emissivities by M2, M3 and M4 outflows at high/low wind velocities for all ellipticities.

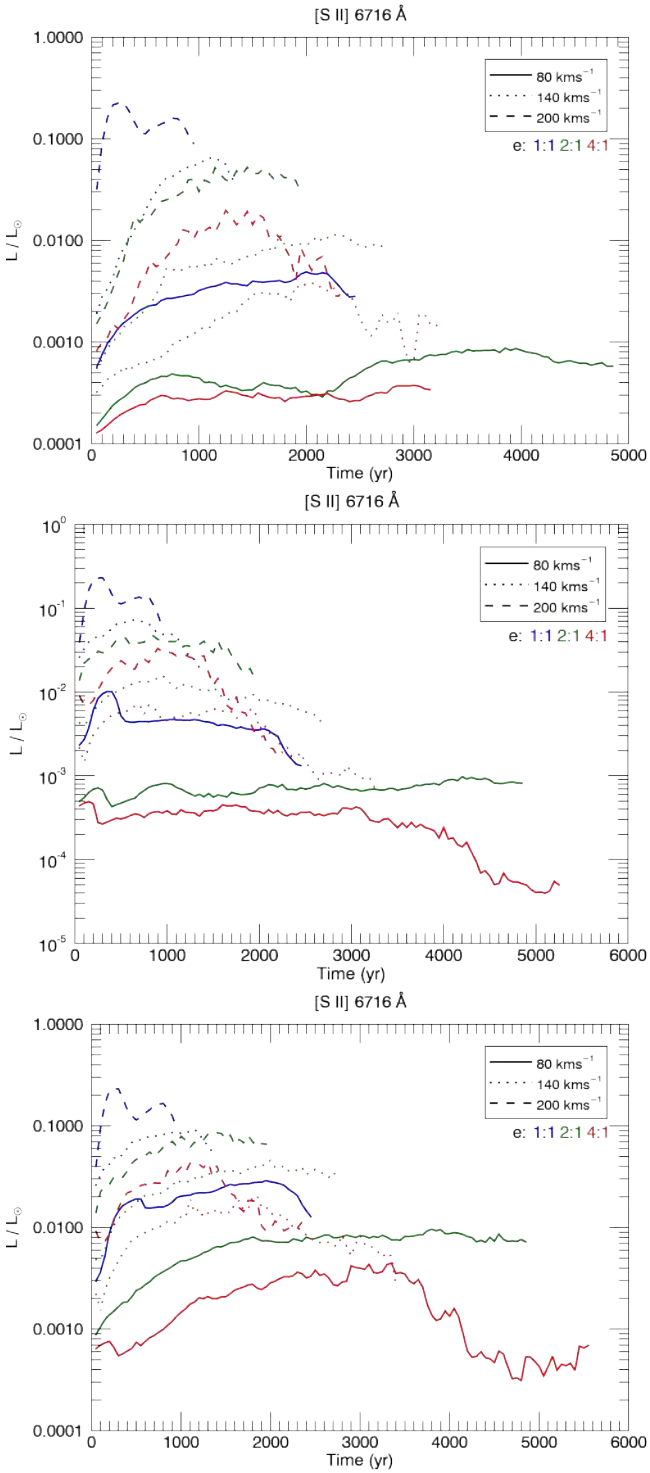

Figure 6.24: Total [Si II] 6716 λ emissivities by M2, M3 and M4 outflows at high/low wind velocities for all ellipticities.

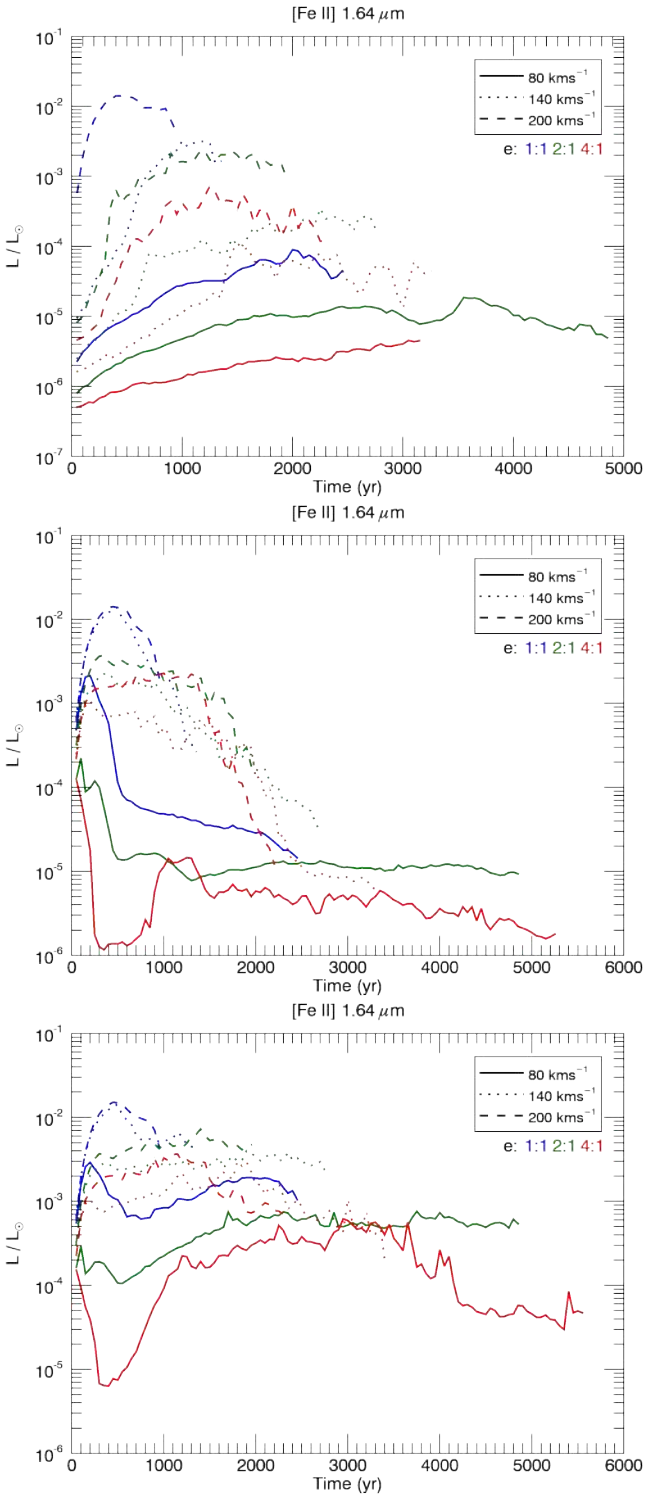

Figure 6.25: Total [Fe II] 1.64 μm emissivities by M2, M3 and M4 outflows at high/low wind velocities for all ellipticities.

6.2 PV Diagrams

6.2.1 K - band

We have generated Position-Velocity diagrams for the H_2 emission, as displayed in Figs. 6.26 – 6.27 for the 2:1 case. We apply a Gaussian smoothing to both the radial velocity and position. However, no explicit thermal Doppler broadening is included. All composition models are shown (from left to right as indicated) at three orientations for the 2:1 wind speed ratio. The origin is set to (0,0) and the position range is set automatically so that the emission remains on the diagram however the axis is orientated. The emission is integrated over the transverse direction within a long slit positioned along the axis with a width of 200 pixels. The radial velocity relative to the star is binned in 1 $\mathrm{km\,s^{-1}}$ intervals.

The narrowest lines are generated in Model 3 (bottom panel) where the wind pushes the distorted shocks into the molecular ambient medium. Since in this work the ambient medium is stationary, the line width is limited, expected to be approximately given by twice the dissociation speed limit on theoretical considerations (Smith 1994a). In shocks that are magnetic-field cushioned with a low ion fraction allowing ambipolar diffusion to dominate (C-type), much narrower H_2 lines are produced. Here we are modelling hydrodynamic jump shocks in which the H_2 emission will mainly occur after the shocked molecular gas has cooled back down to about 2,000 K and accelerated to a high fraction of the shock speed. Hence, we find lines of full width exceeding $80\,\mathrm{km\,s^{-1}}$ in some locations.

The broader lines are generated from the molecular wind model, M2. It is clear that radial speeds can exceed $100\,\mathrm{km\,s^{-1}}$ when the symmetry axis is close to the line of sight. However, during the stage displayed where the pPN has evolved, the emission will still be associated with molecular gas that has been decelerated and compressed within radiatively cooling zones. Therefore, the PV diagrams, as well as the line profiles shown in Fig. 6.29, tend to describe the shocked layer as a whole.

With an orientation close to the line of sight, the blue-shifted emission dominates. The emission is now wider and stronger toward the end of the lobe. This is as expected especially from the 4:1 wind displayed in Fig. 6.28 since the H_2 excitation is much stronger towards the front which is driven by the $140\,\mathrm{km\,s^{-1}}$ wind while this is reduced to just $35\,\mathrm{km\,s^{-1}}$ in the transverse direction.

It is also interesting that the PV diagrams for these elliptical winds are morphologically different

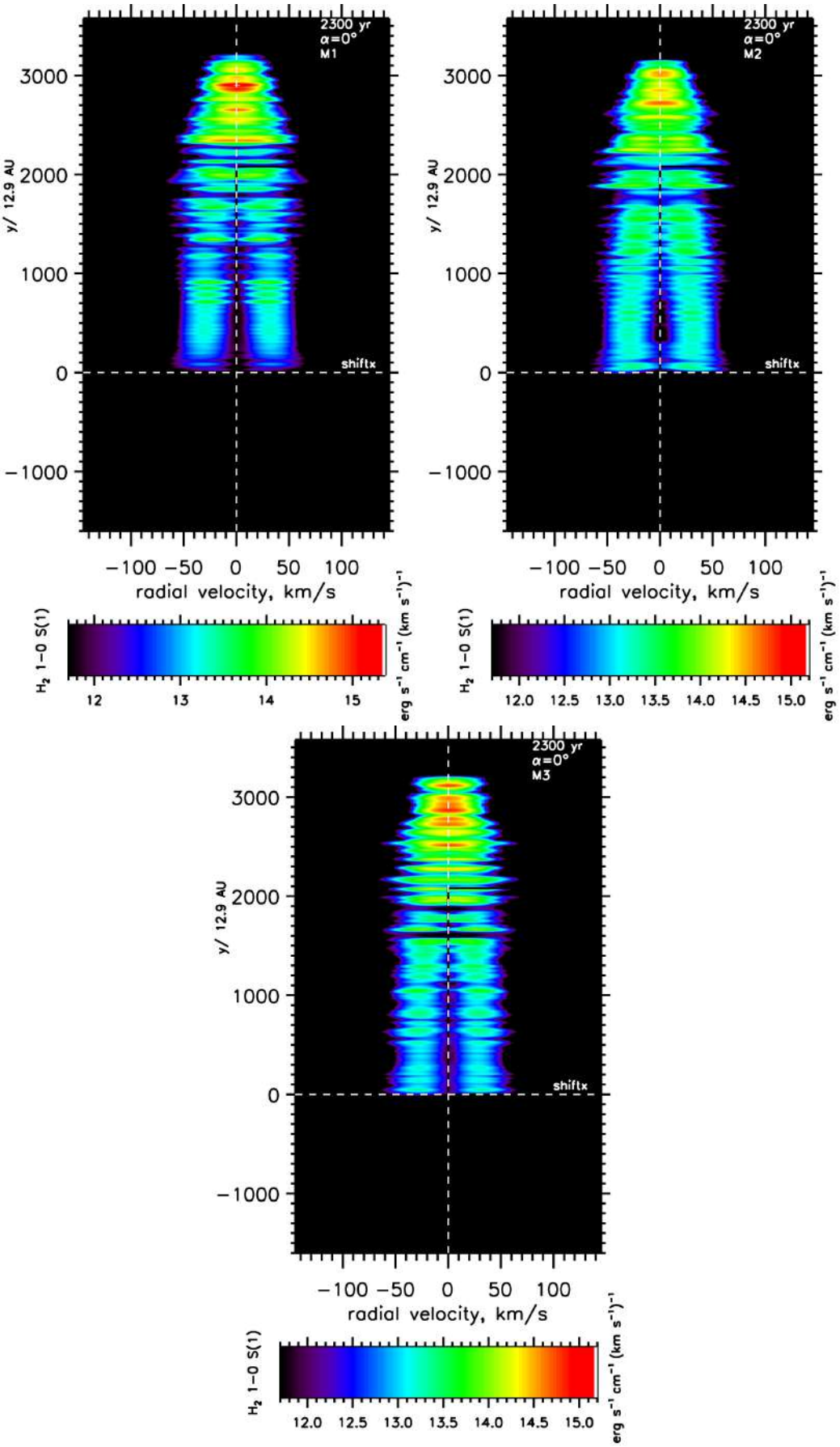

Figure 6.26: Position-Velocity diagrams for the H_2 1–0 S(1) emission from the 2:1 elliptical wind with the long axis in the plane of the sky $\alpha = 0°$ at a late stage of $140\,\mathrm{km\,s^{-1}}$ wind expansion. The three composition models are as indicated.

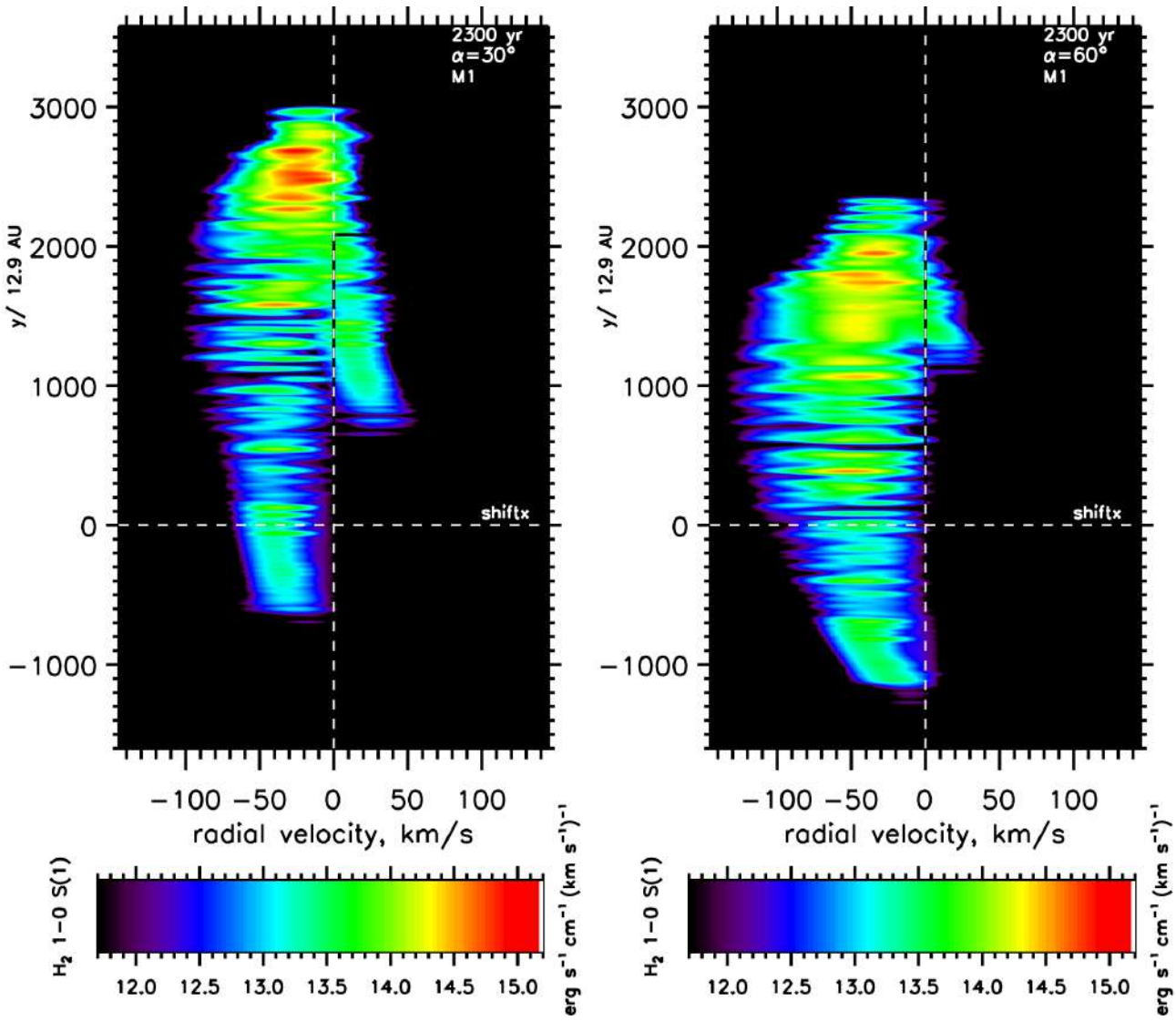

Figure 6.27: Position-Velocity diagrams for the H_2 1–0 S(1) emission from the 2:1 elliptical wind with the long axis $\alpha = 30°$ and $\alpha = 60°$ out of the plane of the sky, at a late stage of 140 km s^{-1} wind expansion. The M1 model for a molecular wind and ambient medium is displayed.

from the jet-driven bows in which both a molecular jet and molecular ambient medium can contribute (Smith et al. 2014). Whereas jet-driven flows generate an apparent acceleration signature termed a Hubble law, the elliptical winds yield a more constant radial speed which is still high at the source location. Imposed on this wide ridge is an S-type meander in the PV pattern with substantial redshifted H_2 at 2.12 μm even when the pPN axis is at 30° to the line of sight.

Finally, we can now also integrate over the entire pPN to obtain a single line profile. Fig. 6.29 displays a characteristic triangular shape when the flux is expressed logarithmically. Once again, the properties appear to be related to the geometry and orientation rather than the Model. The profile peak shifts with orientation by $\sim$ 35 km s^{-1} even with a wind speed four times larger. Line widths are $\sim$ 50–60 km s^{-1} at 10% maximum.

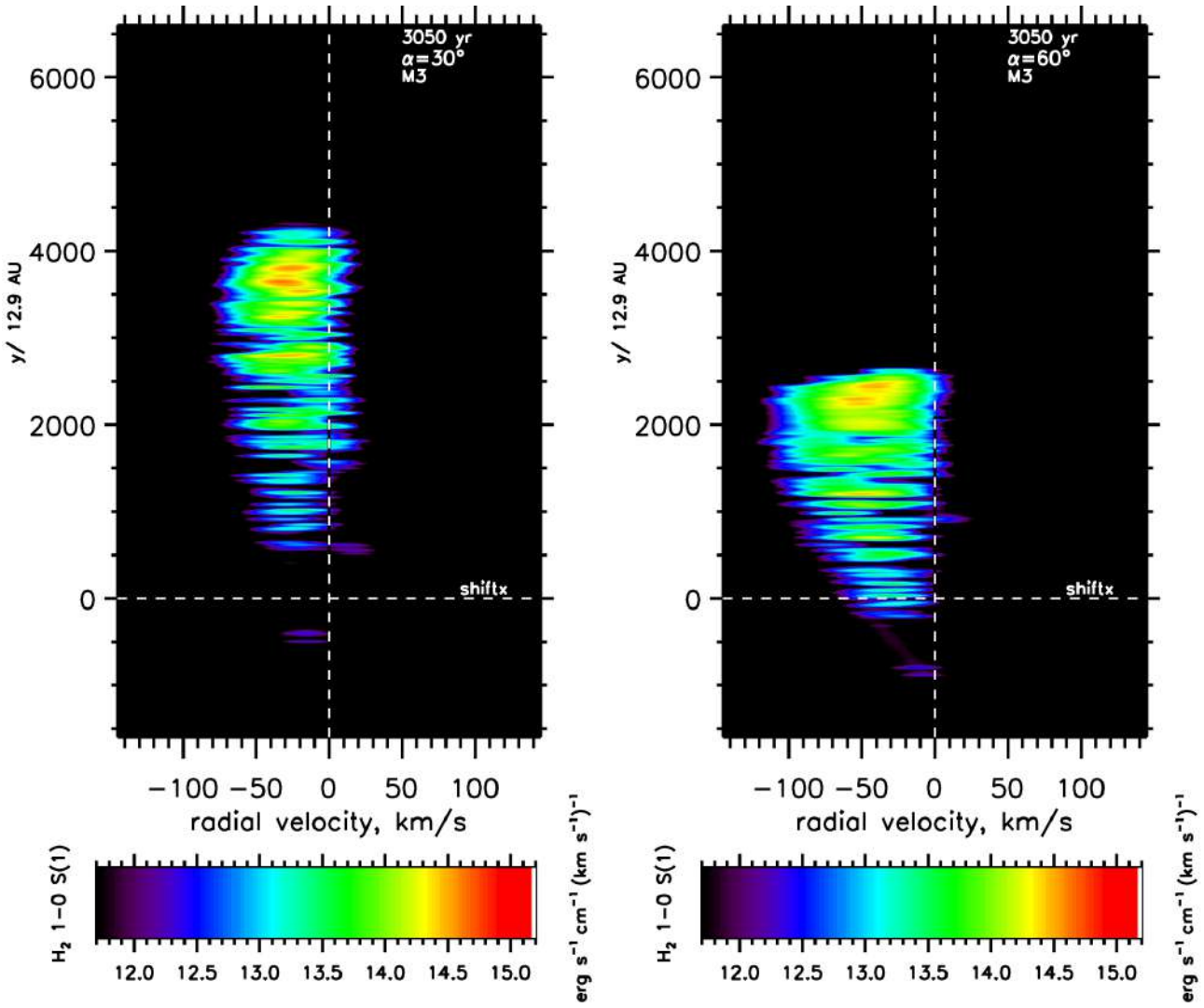

Figure 6.28: Position-Velocity diagrams for the H_2 1–0 S(1) emission from the 4:1 elliptical 140 km s^{-1} wind with the long axis at $\alpha = 30°$ (left panel) and $\alpha = 60°$ (right panel) out of the plane of the sky. Model M3 with a molecular wind is taken as the example here.

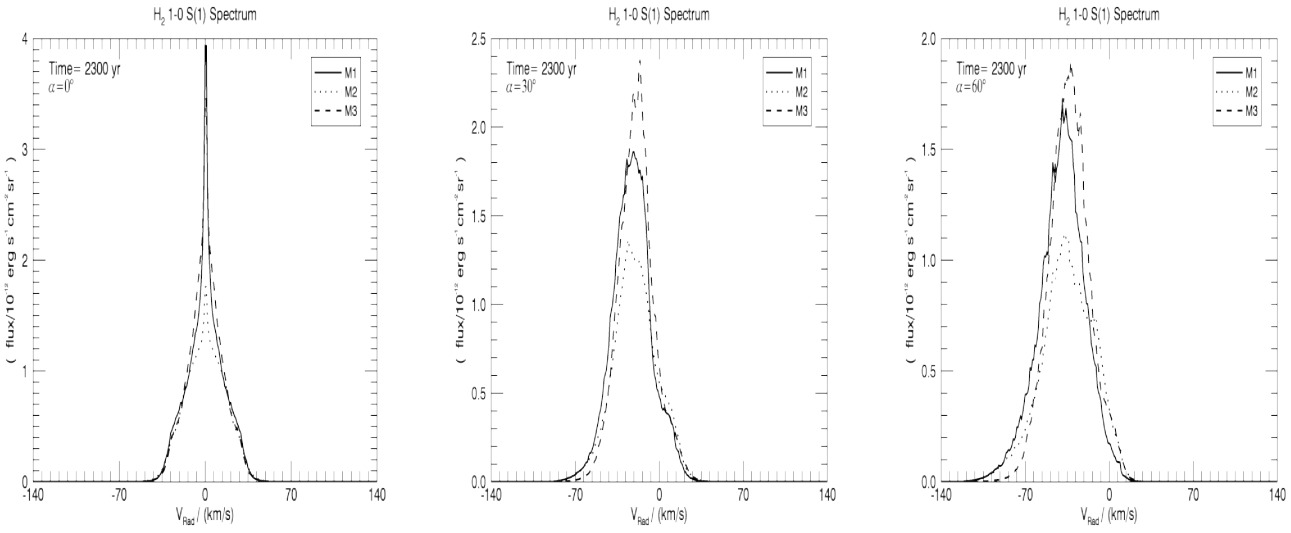

(a) $\alpha = 0°$. (b) $\alpha = 30°$. (c) $\alpha = 60°$.

Figure 6.29: Line profiles of the entire pPN in H_2 1–0 S(1) emission from 2:1 elliptical $V_w = 140$ km s^{-1} wind with the symmetry axis at 0, 30 & 60° to the plane of the sky.

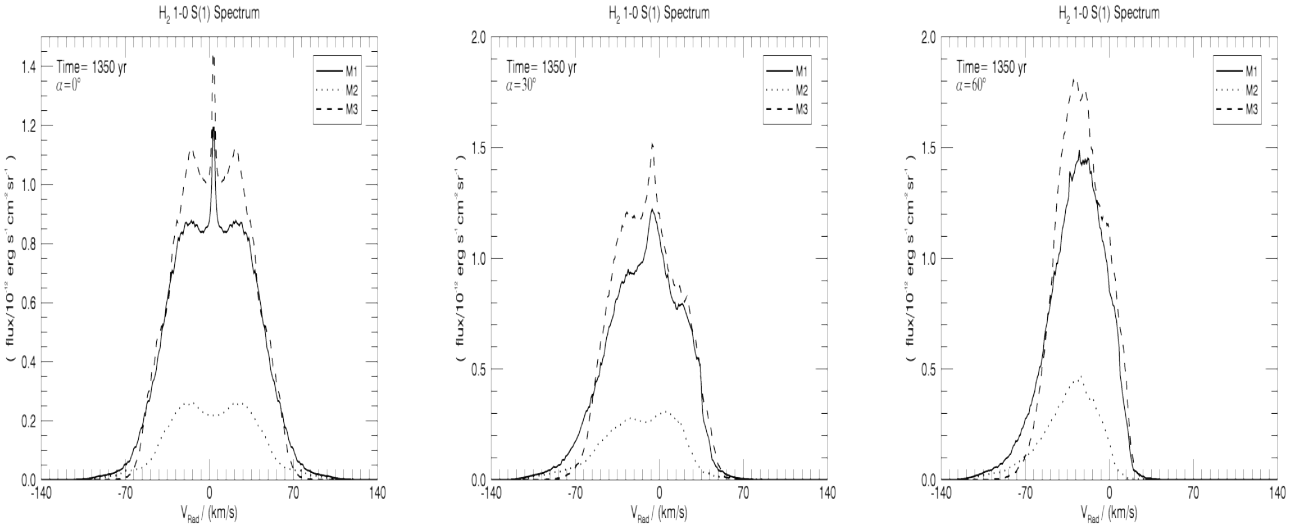

(a) $\alpha = 0°$. (b) $\alpha = 30°$. (c) $\alpha = 60°$.

Figure 6.30: Line profiles of the entire pPN in H_2 1–0 S(1) emission from 1:1 elliptical $V_w = 140\,\mathrm{km\,s^{-1}}$ wind with the symmetry axis at 0, 30 & 60° to the plane of the sky.

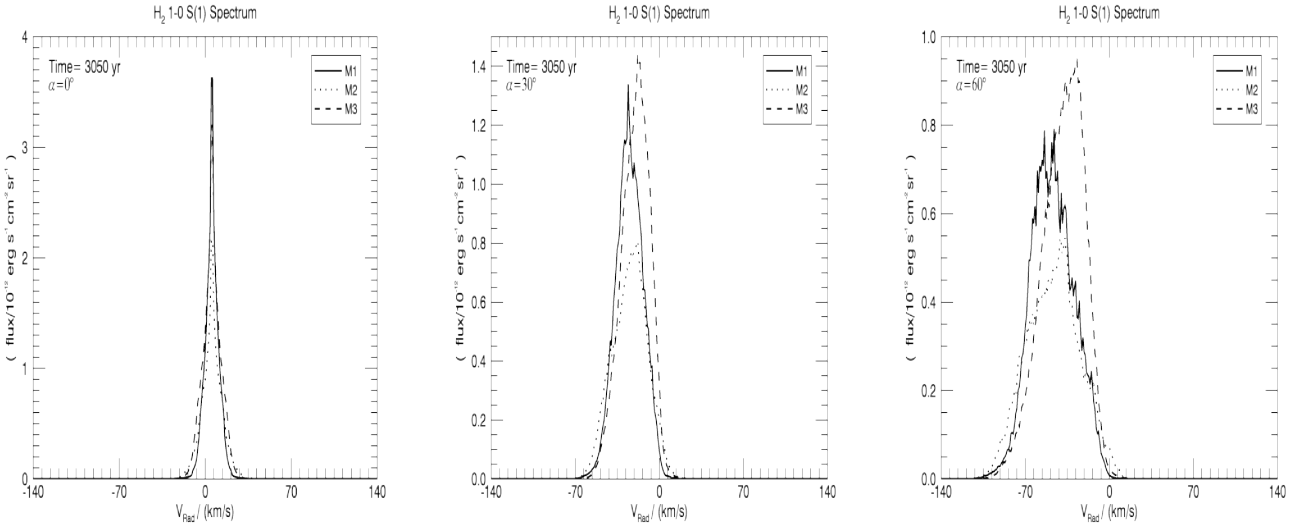

(a) $\alpha = 0°$. (b) $\alpha = 30°$. (c) $\alpha = 60°$.

Figure 6.31: Line profiles of the entire pPN in H_2 1–0 S(1) emission from 4:1 elliptical $V_w = 140\,\mathrm{km\,s^{-1}}$ wind with the symmetry axis at 0, 30 & 60° to the plane of the sky.

Spherical 1:1 line profiles in Fig. 6.30 are at 35% of peak flux value compared to 2:1 counterparts. A triangular profile is replaced with two identical flux peaks disposed from the radial ~ 0 km s^{-1} line of symmetry, in case of M2 at ~ 28 km s^{-1} each and at much lower 18% of peak flux value compared to highest flux model M3. Model M1 and M3 mimic the flux shape of M2 with two peaks at slightly higher radial disposition and a sharp triangular peak at the line of symmetry raising the two models above the M2. At 60° out of the plane, the single peak triangular shape is reobtained with peak shifts of ~ 20 km s^{-1}. The triple peak feature for all models still suggests that in case of spherical outflows the line profile shape is dictated by geometry and orientation whilst the peak values are determined by composition.

The high ellipticity 4:1 line profiles in Fig. 6.31 have triangular shape with narrow line widths and higher peak shifts with orientation compared to spherical and 2:1 outflows. The peaks values are not aligned when disposed from the initial line of symmetry at $\sim$ 0 km s^{-1} radial velocity point with highest shift value reached by pure molecular model M1 at $\sim$ 50 km s^{-1}. The general shape is retained by all models once again with the line width being varied by a change in ellipticity. The line profiles conclude that the variability of line widths is determined by geometry (ellipticity) of the outflow, the composition of wind/ambient factors into flux peak values and the general shape (number of peaks) of profiles is determined by orientation.

6.2.2 Optical

The radial velocity shift of spectral lines often provides the information on the third dimension for objects beyond our reach. Long-slit spectroscopy can be presented as channel maps or more succinctly as Position-Velocity diagrams. Simulated optical Position-Velocity (PV) diagrams of 140 km s^{-1} outflows are displayed in Figs. 6.32 - 6.47. All atomic compositional models are shown at three orientations.

A direct comparison of the three compositional models of [Fe II] 1.64 μm and [Si II] 6716 λ forbidden lines, the [O I] 6300 λ airglow line, and Hα 6563 λ emission is presented and demonstrate that the models can be distinguished. The top left panel in Fig. 6.32 shows a quite narrow line along the slit due to the relatively small acceleration of the ambient atomic gas. In contrast, if the emission is dominated by an atomic wind, as in the right panel, then a broad line appears in the flanks where the fast wind is shocked and decelerated at the interface. The full line width in the flanks can reach 100 km s^{-1}.

The PV diagram in the full atomic simulation differs remarkably, consistent with the different dynamical behaviour. The bottom Hα 6563 λ emission panel in Fig. 6.32 shows that the thickening turbulent shell generates much stronger atomic emission that is distributed far back into the flanks. The radial velocities are moderate and quite centre-filled for the wind orientation displayed. Thus, the pure atomic Model M4 (AWAA) generates higher flux densities for both the wind cap and wings of the outflow with emission being contributed by both ambient and wind.

The Hα 6563 λ PV diagrams are equally interesting when the wind axis is orientated toward the line of sight. As shown in Fig. 6.33 for Model M2, the PV diagram is not only shifted to the blue but also spread more evenly along the axis with several notable peaks spaced out. At 60°

out of the plane, the emission is a distinct arc with the peak well behind the leading edge. The peak is now also blue-shifted relative to the leading edge.

For the atomic wind in Fig. 6.34 displaying Model M3, the blue-shift is much greater and the arc extends back to the star and across to the other side which would be superimposed on the receding lobe. In a symmetric pPN, this would appear as both blue and redshifted arcs close to the symmetry plane or mid-plane of the configuration.

For the full atomic run in Fig. 6.35, the PV diagram displays an arc which remains bright and strong all the way along. It should also be noted that by adding together two lobes of a double source (i.e. the full ellipsoid) would yield a distorted ellipse, rotated off-axis.

In case of higher energy [O I] 6300 λ airglow line, the plane of sky images displayed in Fig. 6.36 are similar in morphology and approximately one flux magnitude higher compared to the Hα 6563 λ. Similar morphological features to Hα also arise at 30° and 60° out of the plane of the sky PV diagrams for both Models M2 and M3 in Fig. 6.37 - 6.38. With M3 obtaining greates blue shift values compared to other compositions of the same emission line. The full atomic run of [O I] at 30° and 60° in Fig. 6.39 is also morphologically identical and is at one magnitude higher flux values compared to Hα emission.

The [Si II] 6716 λ forbidden line in Fig. 6.40 generates a much stronger, spatially filled atomic emission distributed along the entire outflow region with widest 70 km s^{-1} line distribution along the slit compared to other optical plane of the sky PV panels. The overall line emission for all orientations is more filled as shown in Fig. 6.41 - 6.42, the flux range is one magnitude less compared to other optical panels. The emission generates more notable peaks with values similar to Hα lines at 30° and 60° orientation. Model M2 and M3 obtain similar maximum blue shift values. The full atomic run of [O I] in Fig. 6.43 has less peaks distributed into the flanks at 60°, creates blue shift values at that orientation and similar peak morphology at 30° orientation compared to Hα and [O I] lines.

The least energetic [Fe II] 1.64 μm emission line in Fig. 6.44 produces lowest flux values compared to other atomic lines. With M3 in Fig. 6.46 obtaining greates blue shift values compared to M2 in Fig. 6.45 and Fig. 6.47, identical to the other three simulated lines. The full atomic model at 60° orientation is not as spatially filled as M4 for other simulated lines and has greater number of peak emission distributed along the arch of the outflow.

Many of the above properties are confirmed by studying the integrated line profiles, as displayed in Fig. 6.48, where the solid, dotted & dashed lines correspond to the three indicated wind orientations, and the models M2, M3 & M4 are displayed from left to right. It is clear that the atomic wind can create wide lines with shifts approaching the wind speed itself. Even though the wind gets compressed and slowed when passing through the shock, the shock itself is not transverse to the wind, but highly fragmented and distorted into oblique components. Hence the shock-heated wind can maintain a high radial speed. This effect is not prominent in the pure atomic flow because the turbulent shell is not distinctly fragmented. Instead, the energy is channelled into lower-speed turbulence, producing a much higher peak emission, as shown in the right panel.

The highest flux component is reached in plane of the sky view for all atomic model and orientation panels with the highest value of $\sim 120 \times 10^{-13}\,\mathrm{erg\,s^{-1}\,cm^{-2}\,sr^{-1}}$ established by pure atomic model M4 for [O I] 6300 λ airglow line in Fig. 6.51 (right panel) which is also supported by PV diagrams. The lowest flux was achieved by the [Fe II] 1.64 μm emission line at $\sim 0.04 \times 10^{-13}\,\mathrm{erg\,s^{-1}\,cm^{-2}\,sr^{-1}}$ for model M3 , 6.53 (middle panel). This low flux trend holds for compositional model M3 across all optical wavelengths. The greatest blue shift values are also created by AWMA model M3 with 60° orientation compared to other compositional models in Fig, 6.52 - Fig, 6.53.

Finally, it can be noted that many of these properties are apparent in the 4:1 ellipsoidal wind PV and line profile diagrams but not to such an obvious degree although still recognisable.

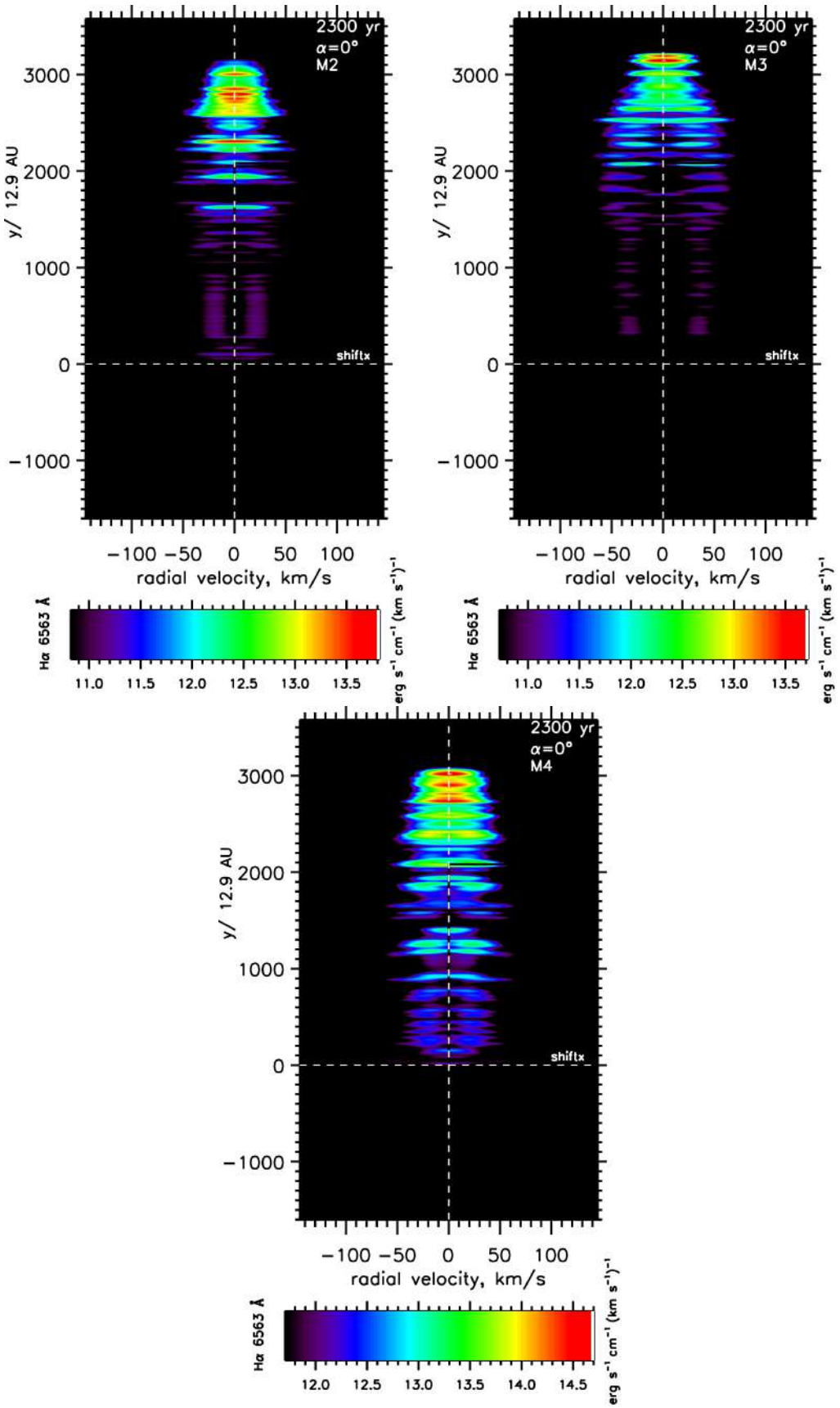

Figure 6.32: Position-Velocity diagrams for the Hα 6563 λ emission from the 2:1 elliptical wind with the long axis in the plane of the sky ($\alpha = 0°$) at a late stage of wind expansion. The three composition models are as indicated.

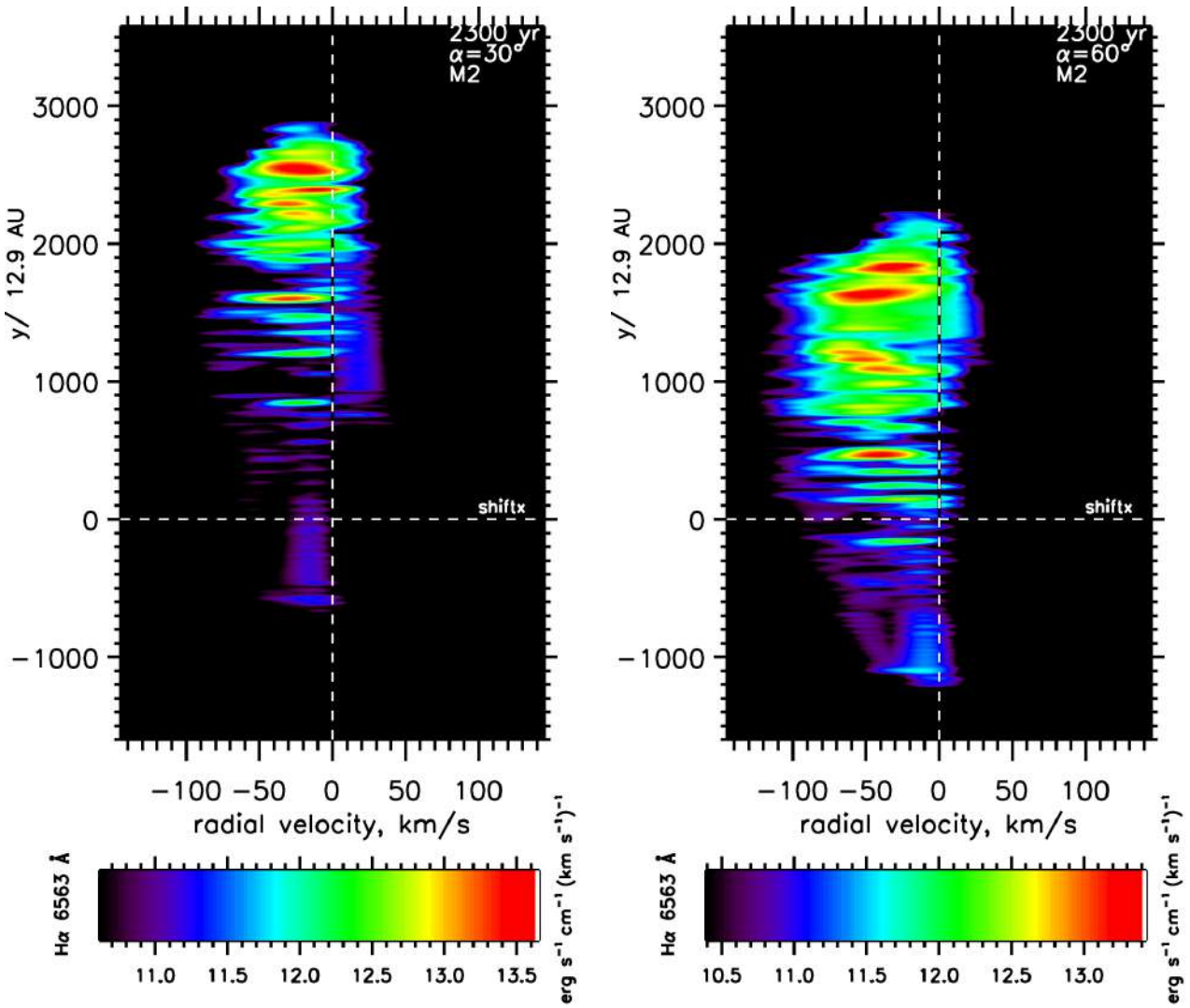

Figure 6.33: Position-Velocity diagrams for the Hα emission from the 2:1 elliptical wind with the long axis $\alpha = 30°$ and $\alpha = 60°$ out of the plane of the sky, at a late stage of $140\,\mathrm{km\,s^{-1}}$ wind expansion. The M2 model for molecular wind and atomic ambient medium is displayed.

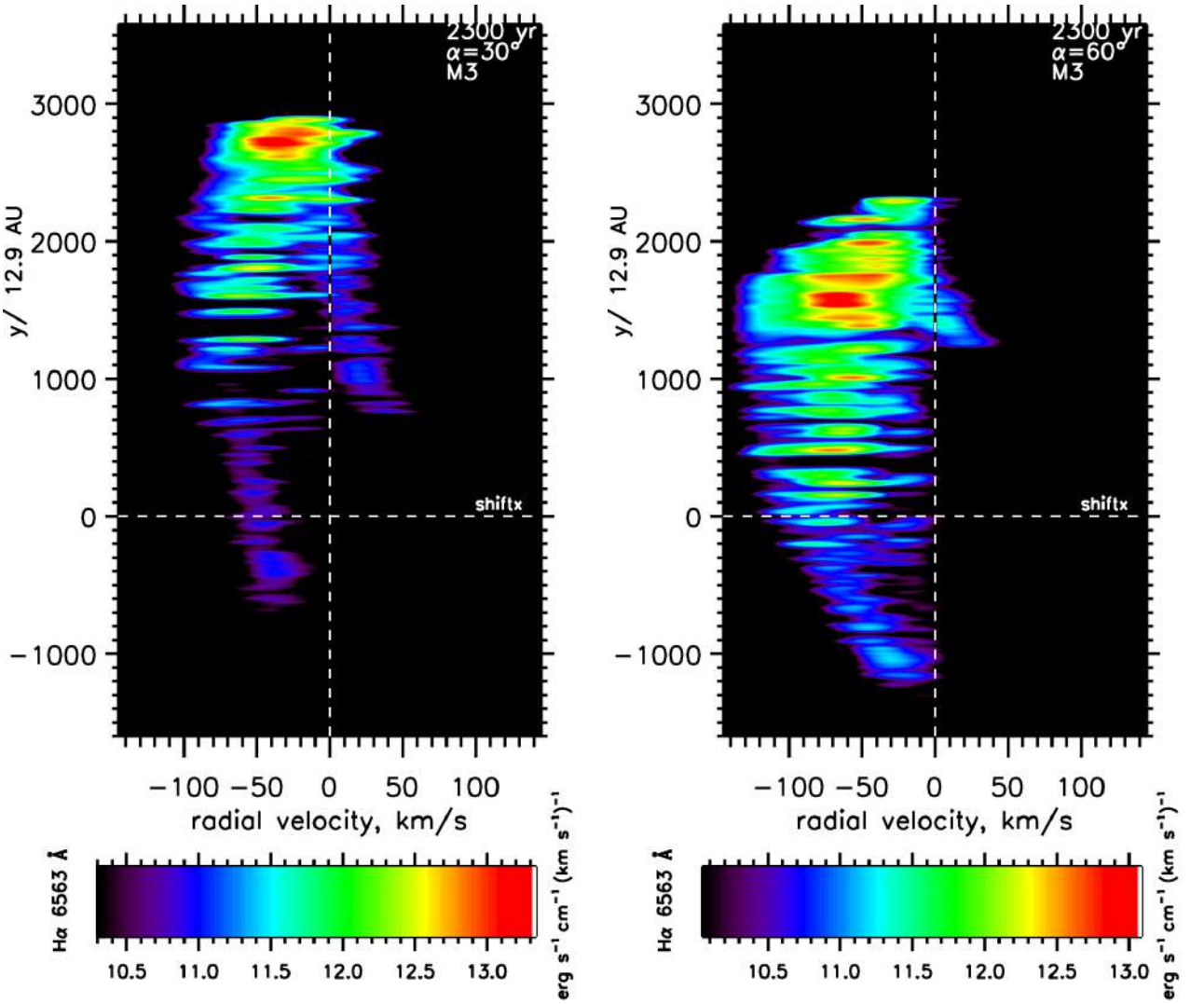

Figure 6.34: Position-Velocity diagrams for the Hα emission from the 2:1 elliptical wind with the long axis $\alpha = 30°$ and $\alpha = 60°$ out of the plane of the sky, at a late stage of $140\,\mathrm{km\,s^{-1}}$ wind expansion. The M3 model for aa atomic wind and atomic ambient medium is displayed.

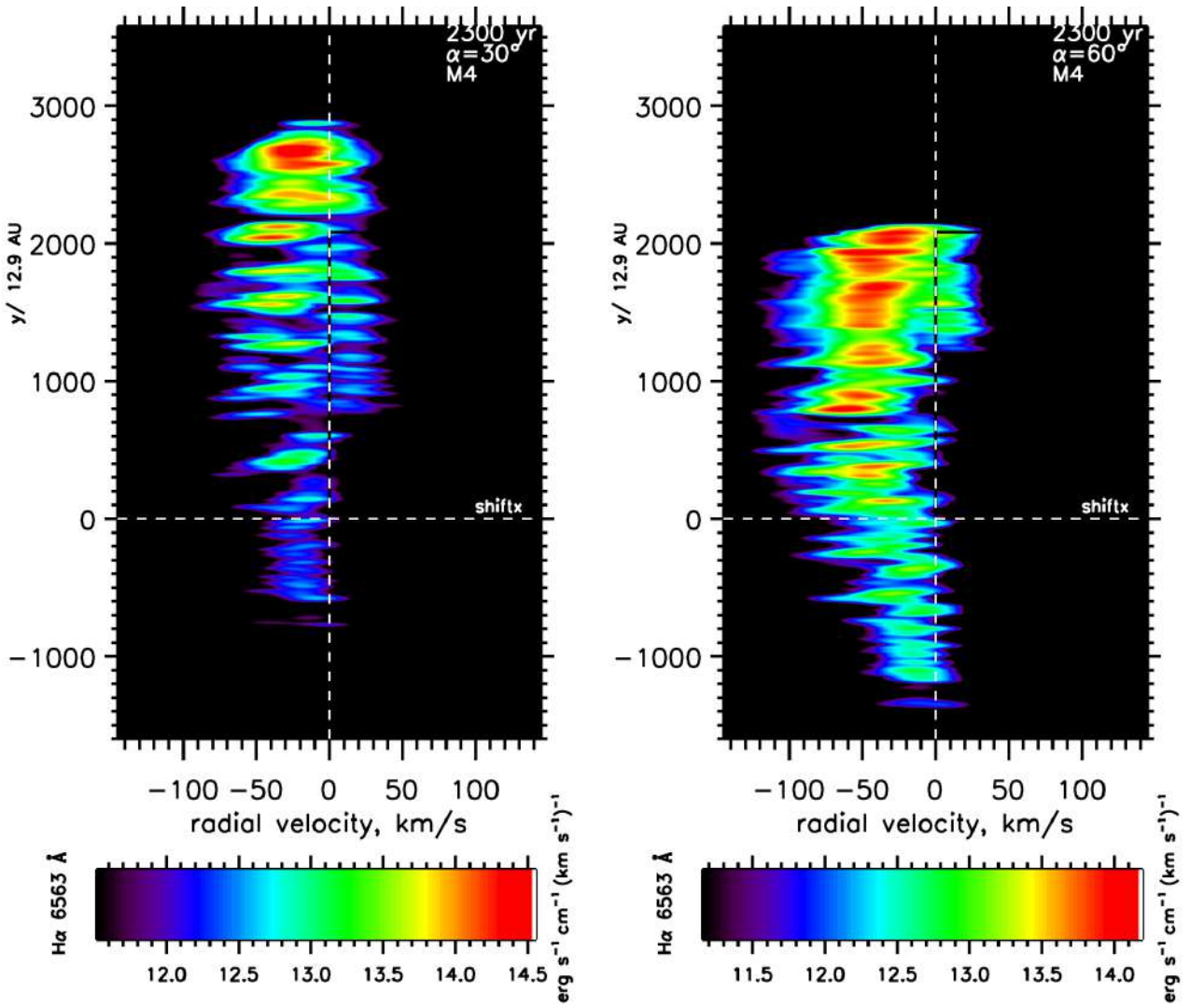

Figure 6.35: Position-Velocity diagrams for the Hα emission from the 2:1 elliptical wind with the long axis $\alpha = 30°$ and $\alpha = 60°$ out of the plane of the sky, at a late stage of $140\,\mathrm{km\,s^{-1}}$ wind expansion. The M4 model for aa atomic wind and atomic ambient medium is displayed.

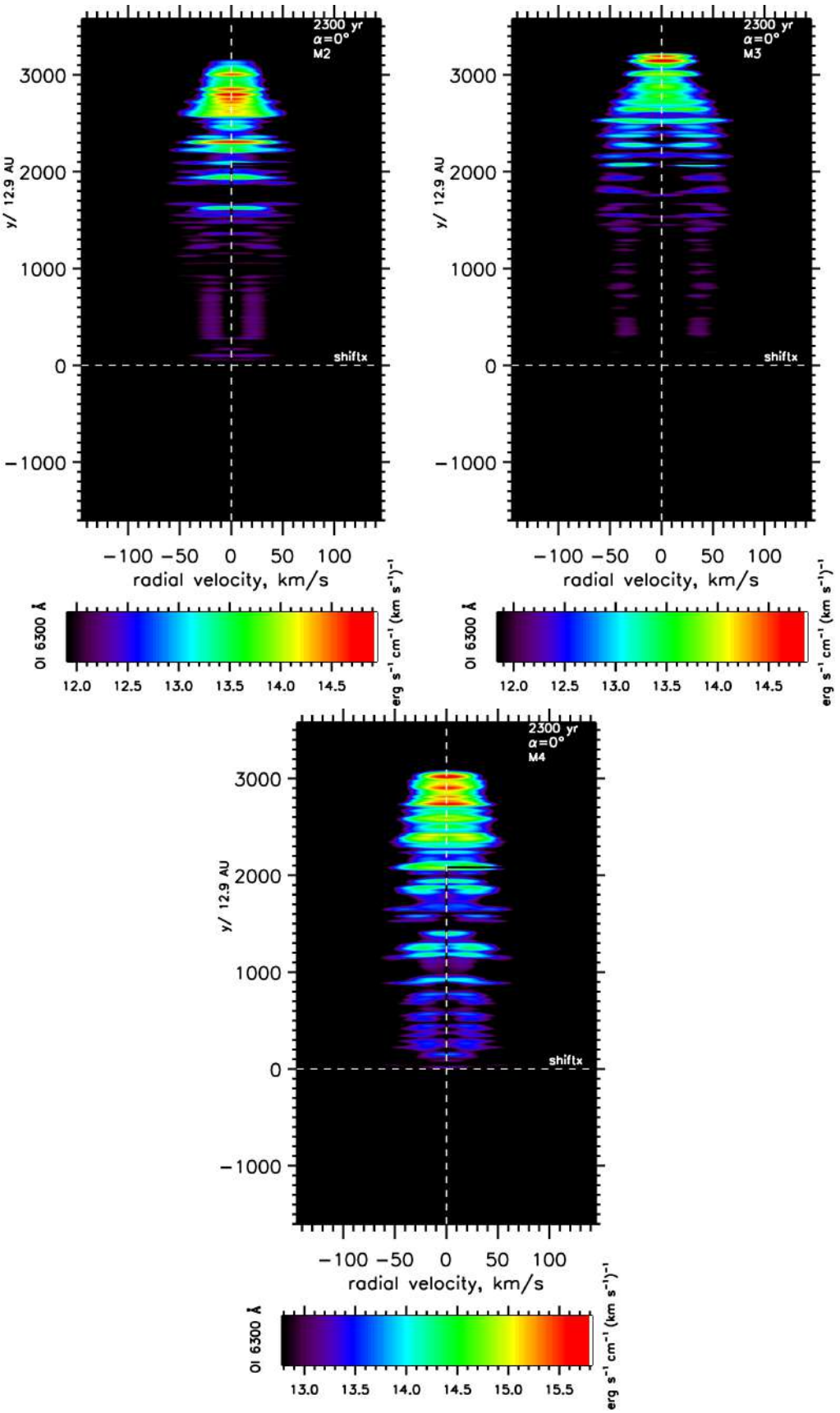

Figure 6.36: Position-Velocity diagrams for the [O I] 6300 λ emission from the 2:1 elliptical wind with the long axis in the plane of the sky ($\alpha = 0°$) at a late stage of wind expansion. The three composition models are as indicated.

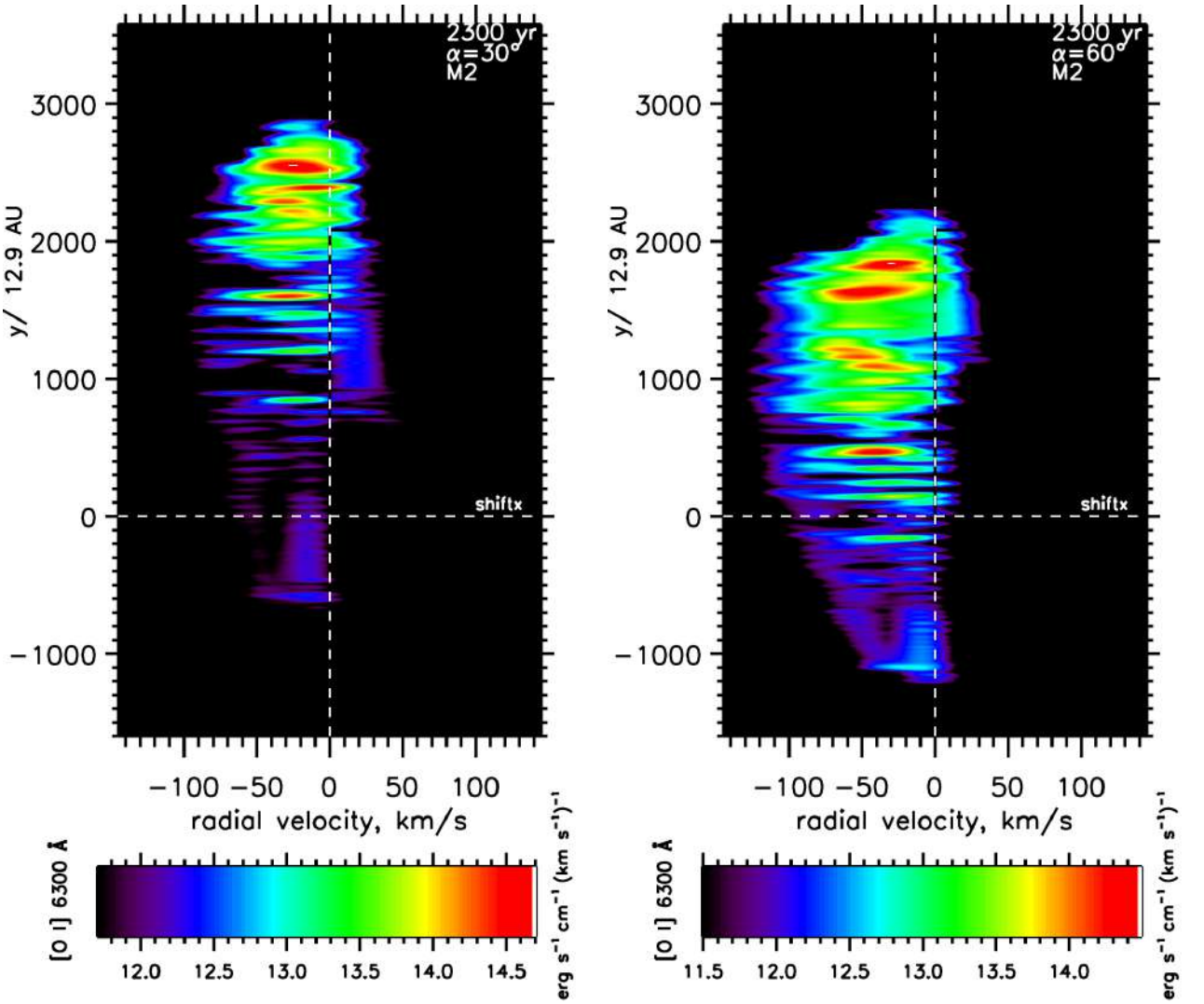

Figure 6.37: Position-Velocity diagrams for the [O I] 6300 λ emission from the 2:1 elliptical wind with the long axis $\alpha = 30°$ and $\alpha = 60°$ out of the plane of the sky, at a late stage of 140 km s^{-1} wind expansion. The M2 model for molecular wind and atomic ambient medium is displayed.

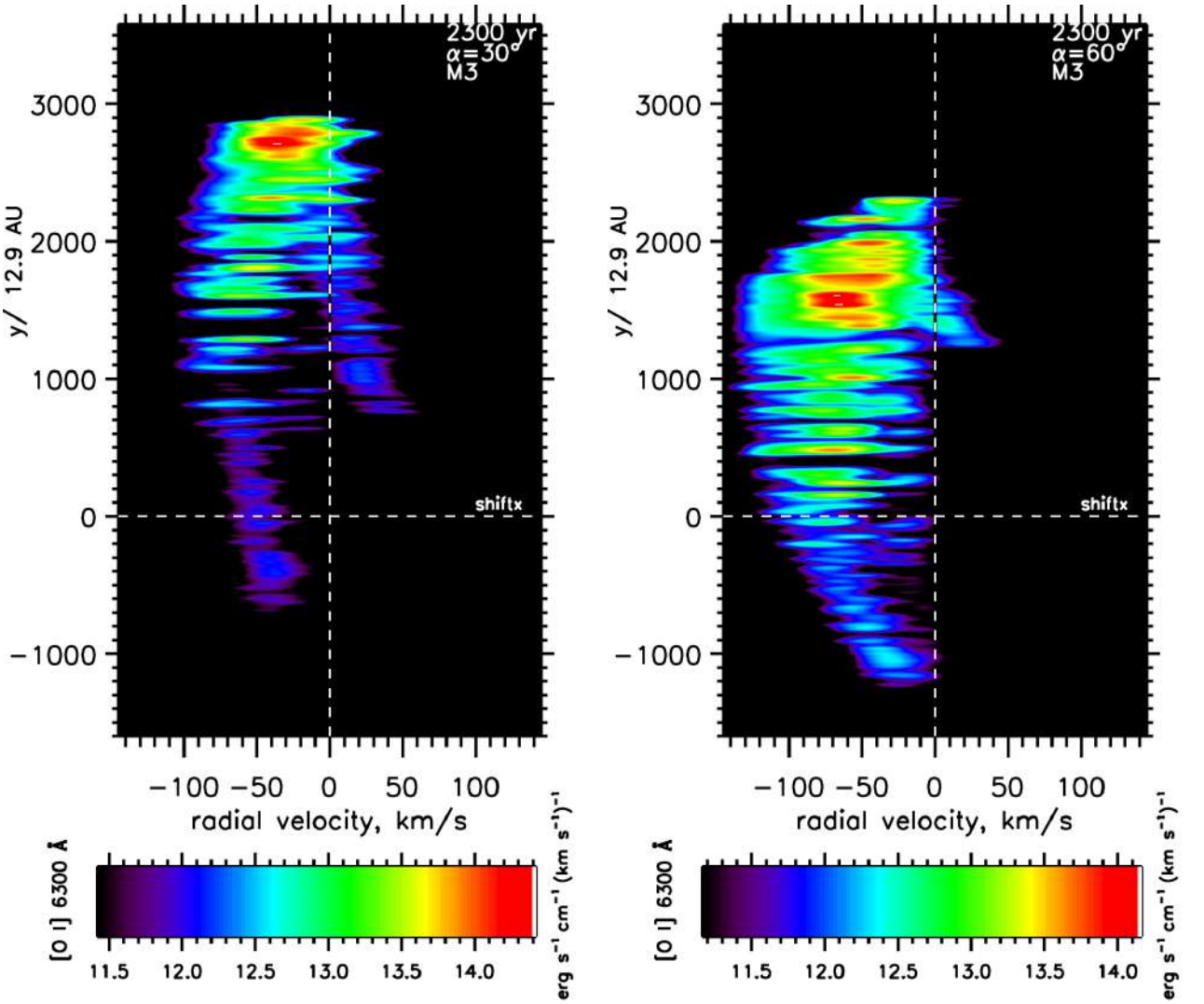

Figure 6.38: Position-Velocity diagrams for the [O I] 6300 λ emission from the 2:1 elliptical wind with the long axis $\alpha = 30°$ and $\alpha = 60°$ out of the plane of the sky, at a late stage of 140 km s^{-1} wind expansion. The M3 model for an atomic wind and atomic ambient medium is displayed.

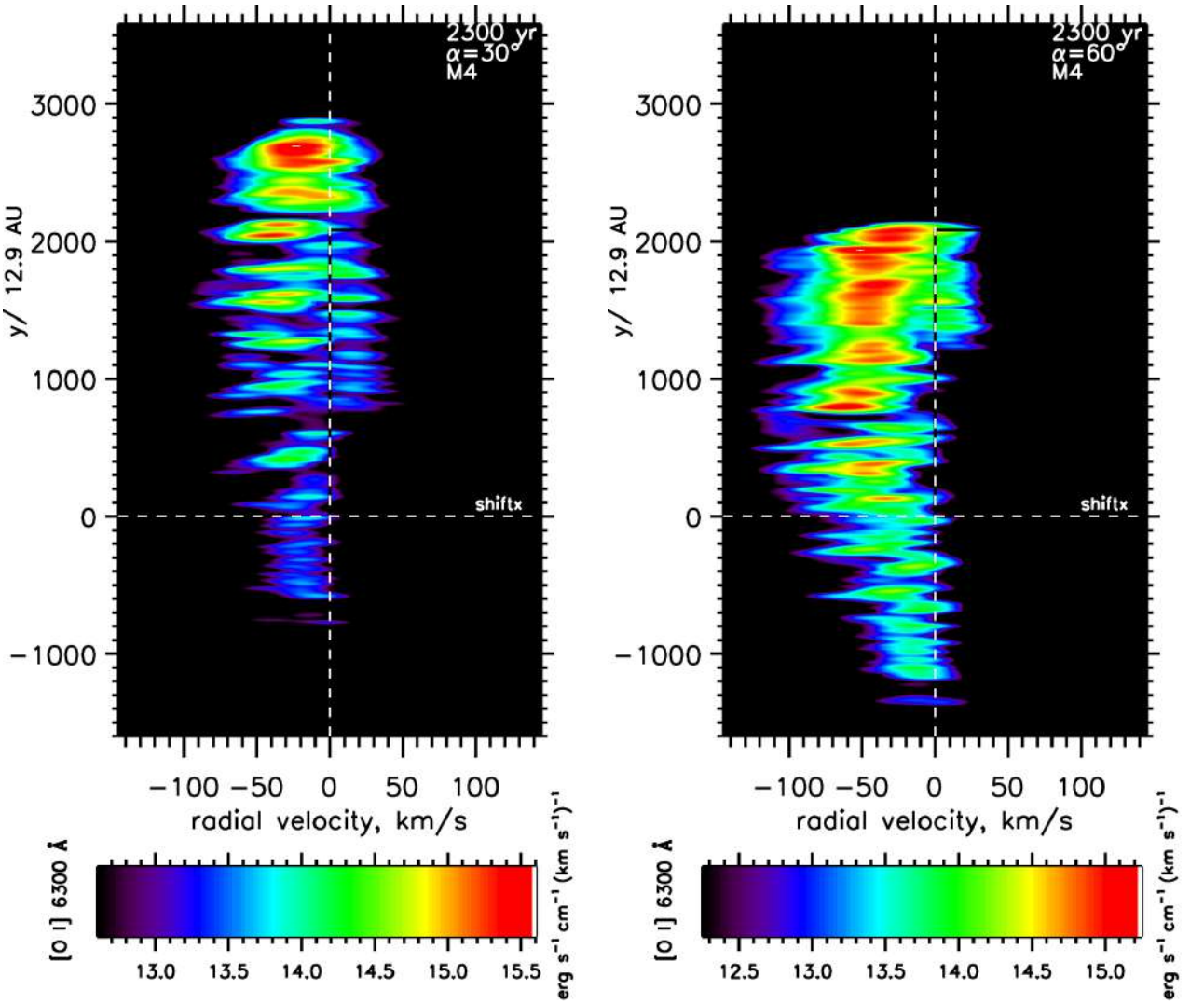

Figure 6.39: Position-Velocity diagrams for the [O I] 6300 λ emission from the 2:1 elliptical wind with the long axis $\alpha = 30°$ and $\alpha = 60°$ out of the plane of the sky, at a late stage of 140 km s^{-1} wind expansion. The M4 model for an atomic wind and atomic ambient medium is displayed.

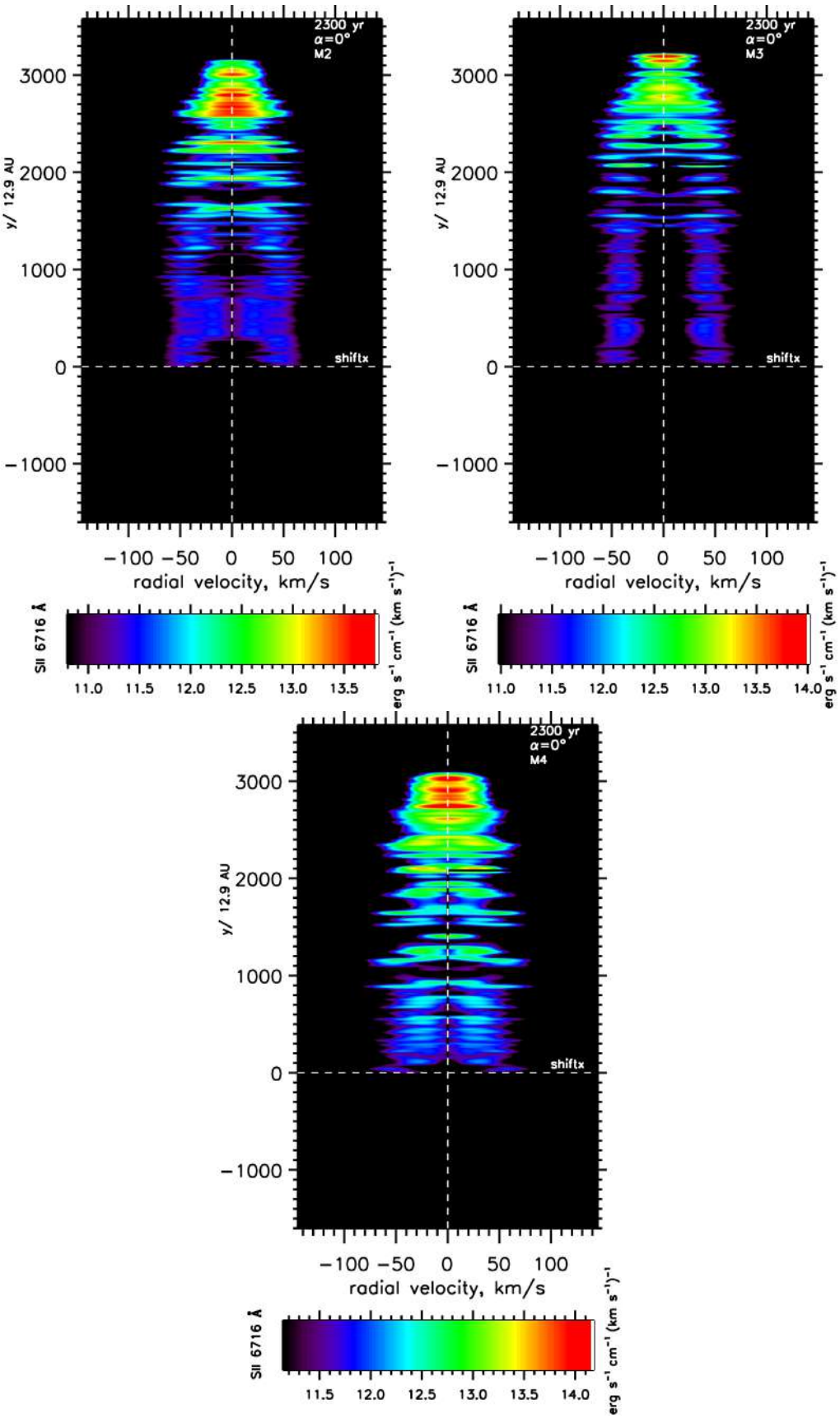

Figure 6.40: Position-Velocity diagrams for the [Si II] 6716 λ emission from the 2:1 elliptical wind with the long axis in the plane of the sky ($\alpha = 0°$) at a late stage of wind expansion. The three composition models are as indicated.

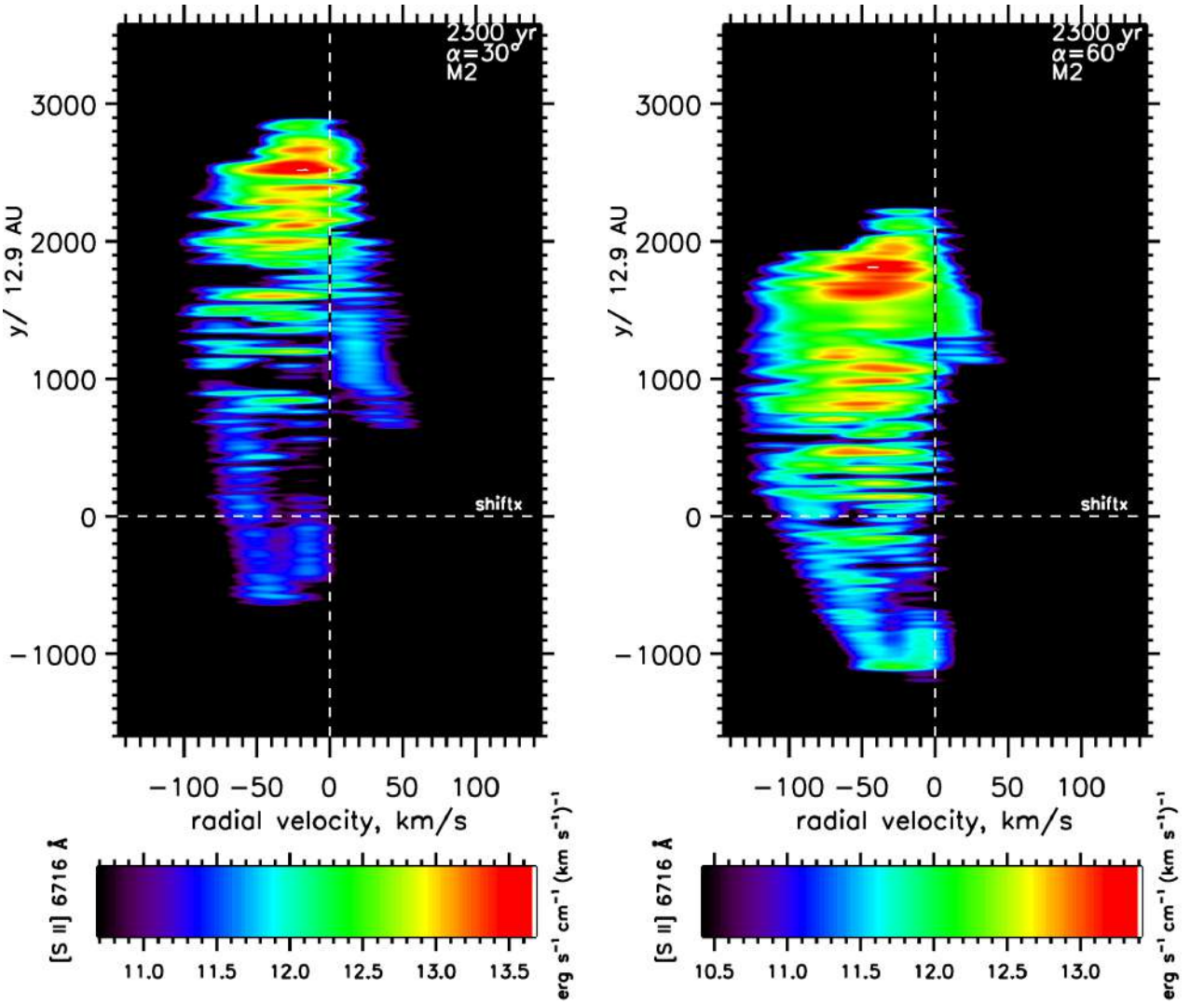

Figure 6.41: Position-Velocity diagrams for the [Si II] 6716 λ emission from the 2:1 elliptical wind with the long axis $\alpha = 30°$ and $\alpha = 60°$ out of the plane of the sky, at a late stage of 140 km s^{-1} wind expansion. The M2 model for aa atomic wind and atomic ambient medium is displayed.

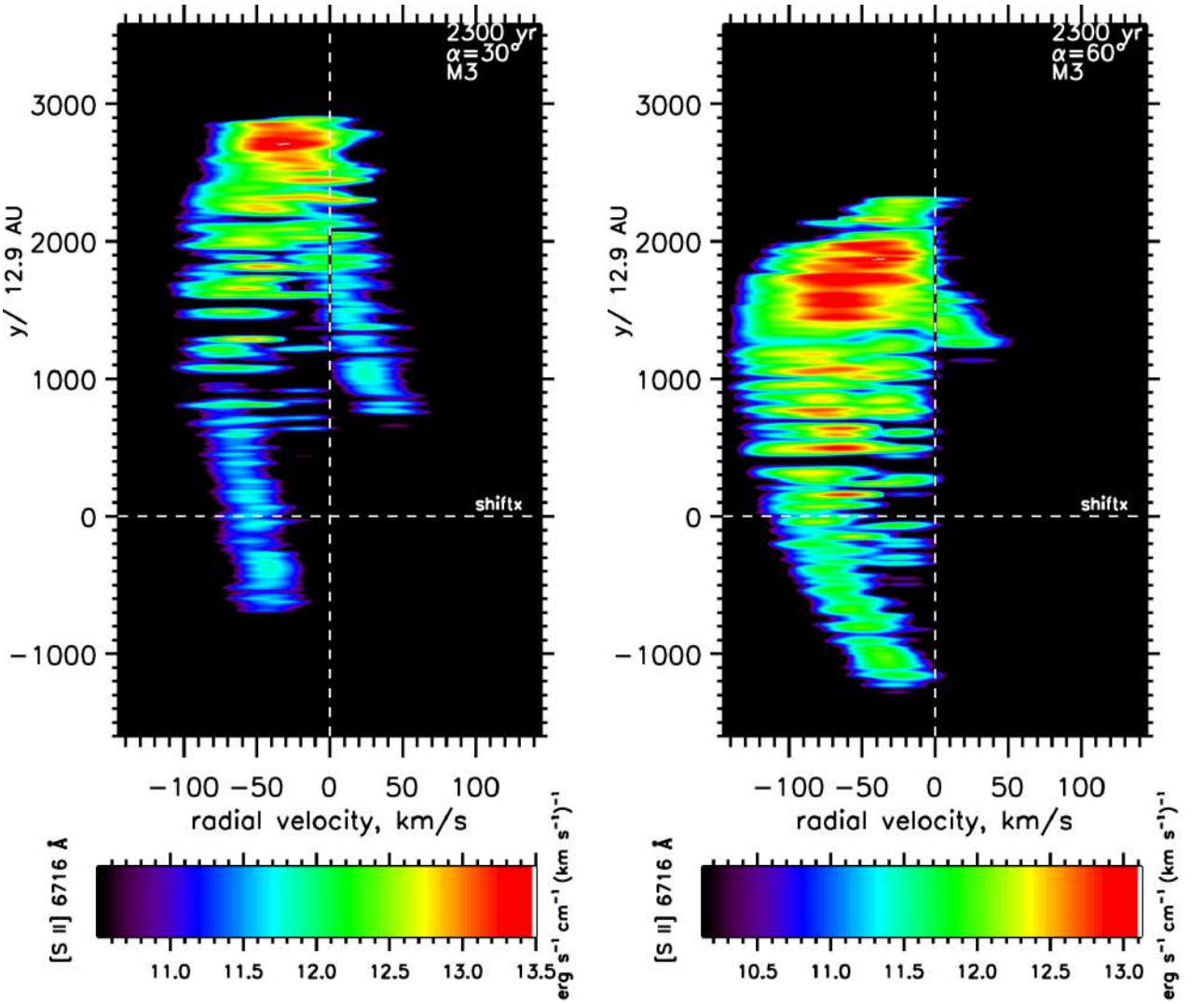

Figure 6.42: Position-Velocity diagrams for the [Si II] 6716 λ emission from the 2:1 elliptical wind with the long axis $\alpha = 30°$ and $\alpha = 60°$ out of the plane of the sky, at a late stage of 140 km s^{-1} wind expansion. The M3 model for aa atomic wind and atomic ambient medium is displayed.

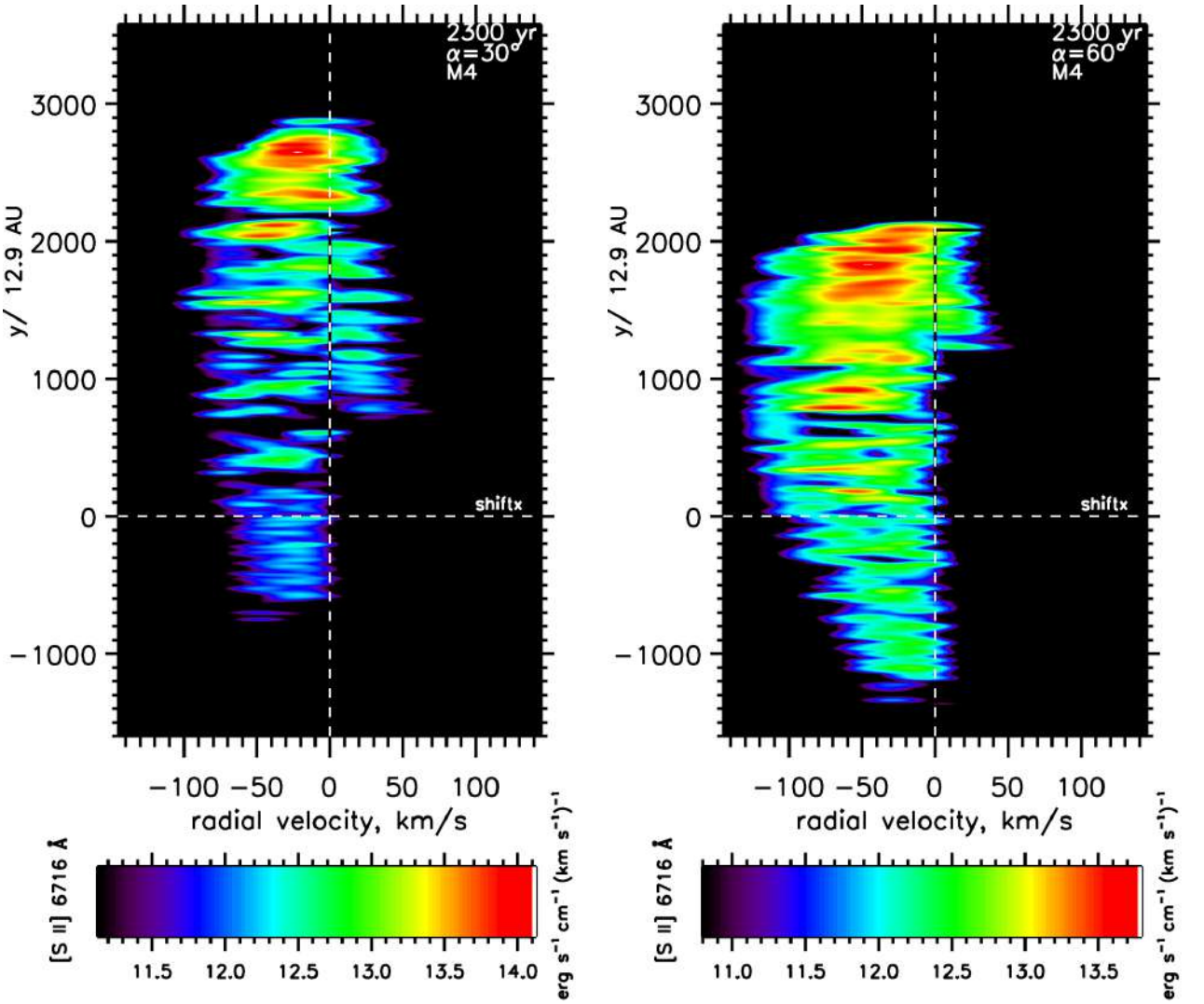

Figure 6.43: Position-Velocity diagrams for the [Si II] 6716 λ emission from the 2:1 elliptical wind with the long axis $\alpha = 30°$ and $\alpha = 60°$ out of the plane of the sky, at a late stage of 140 km s^{-1} wind expansion. The M4 model for aa atomic wind and atomic ambient medium is displayed.

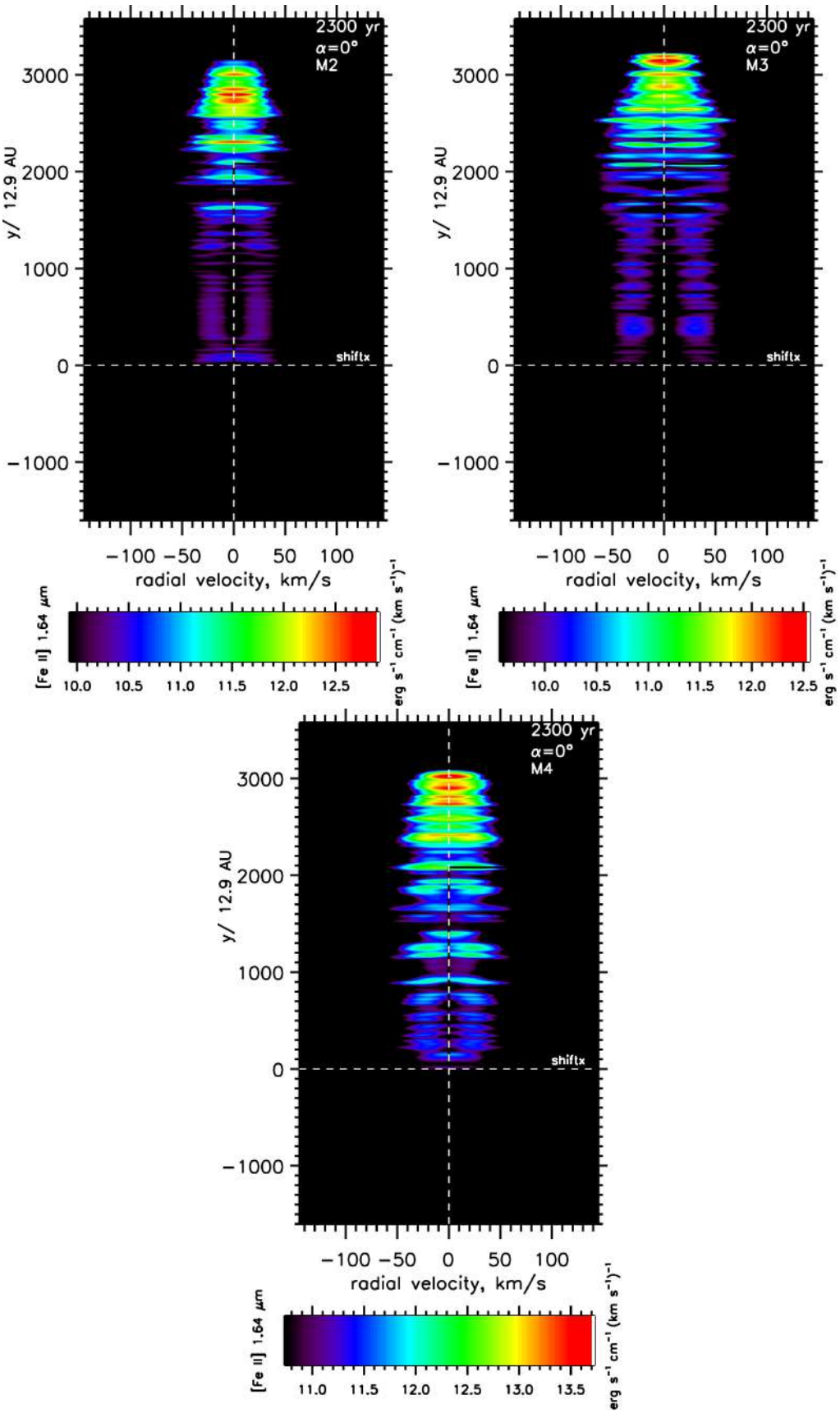

Figure 6.44: Position-Velocity diagrams for the [Fe II] 1.64 μm emission from the 2:1 elliptical wind with the long axis in the plane of the sky ($\alpha = 0°$) at a late stage of wind expansion. The three composition models are as indicated.

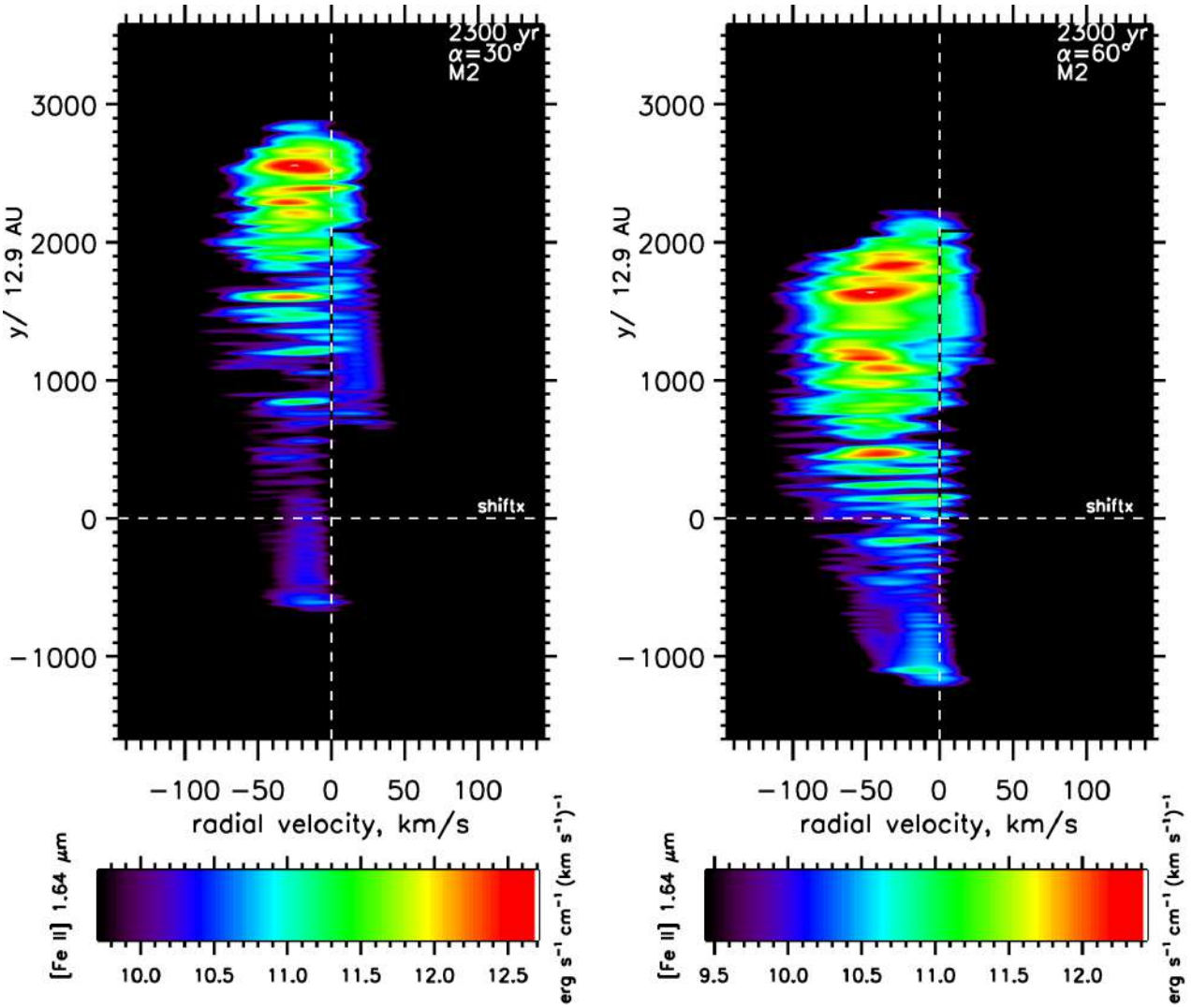

Figure 6.45: Position-Velocity diagrams for the [Fe II] 1.64 μm emission from the 2:1 elliptical wind with the long axis $\alpha = 30°$ and $\alpha = 60°$ out of the plane of the sky, at a late stage of 140 km s^{-1} wind expansion. The M2 model for aa atomic wind and atomic ambient medium is displayed.

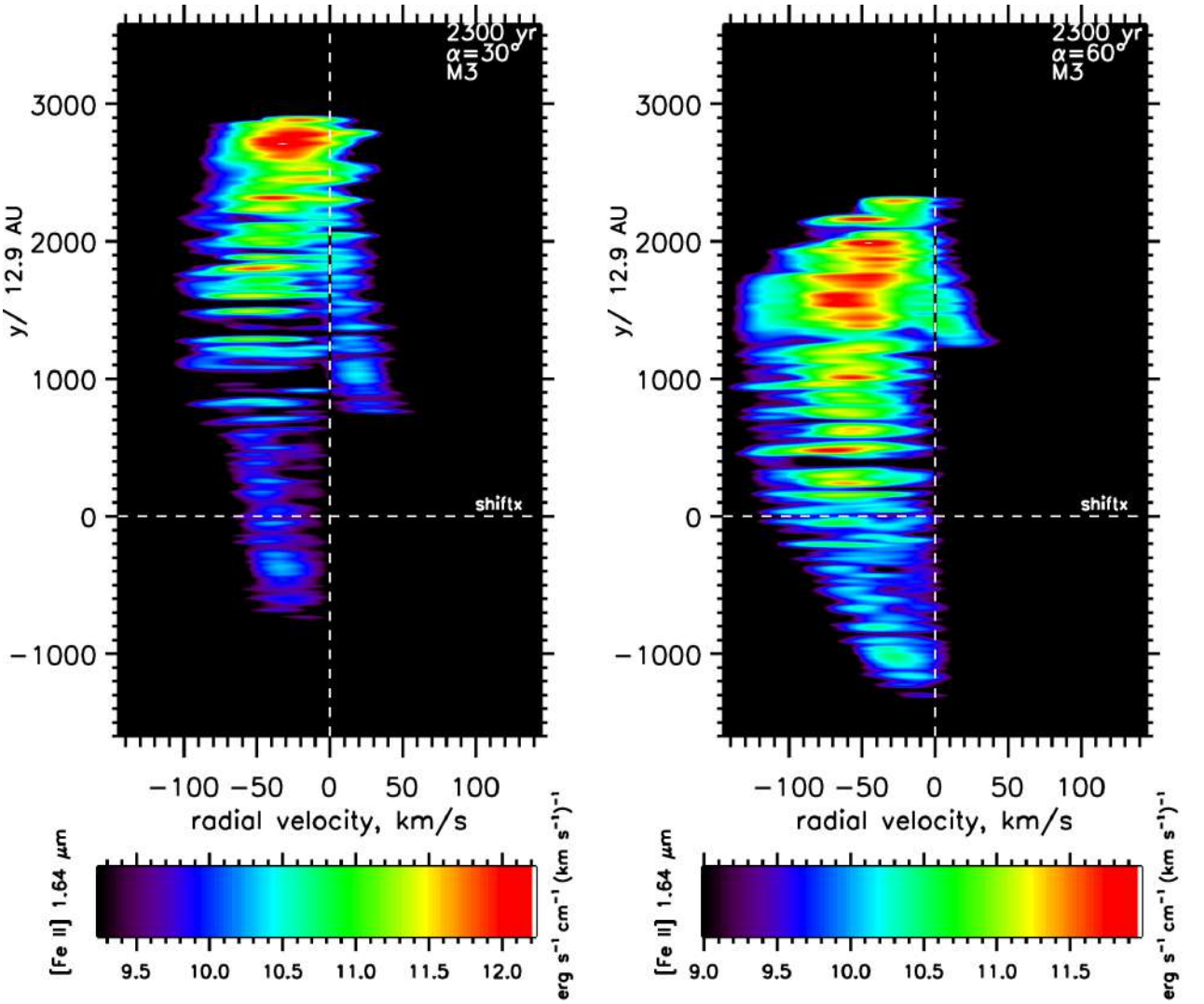

Figure 6.46: Position-Velocity diagrams for the [Fe II] 1.64 μm emission from the 2:1 elliptical wind with the long axis $\alpha = 30°$ and $\alpha = 60°$ out of the plane of the sky, at a late stage of 140 km s^{-1} wind expansion. The M3 model for aa atomic wind and atomic ambient medium is displayed.

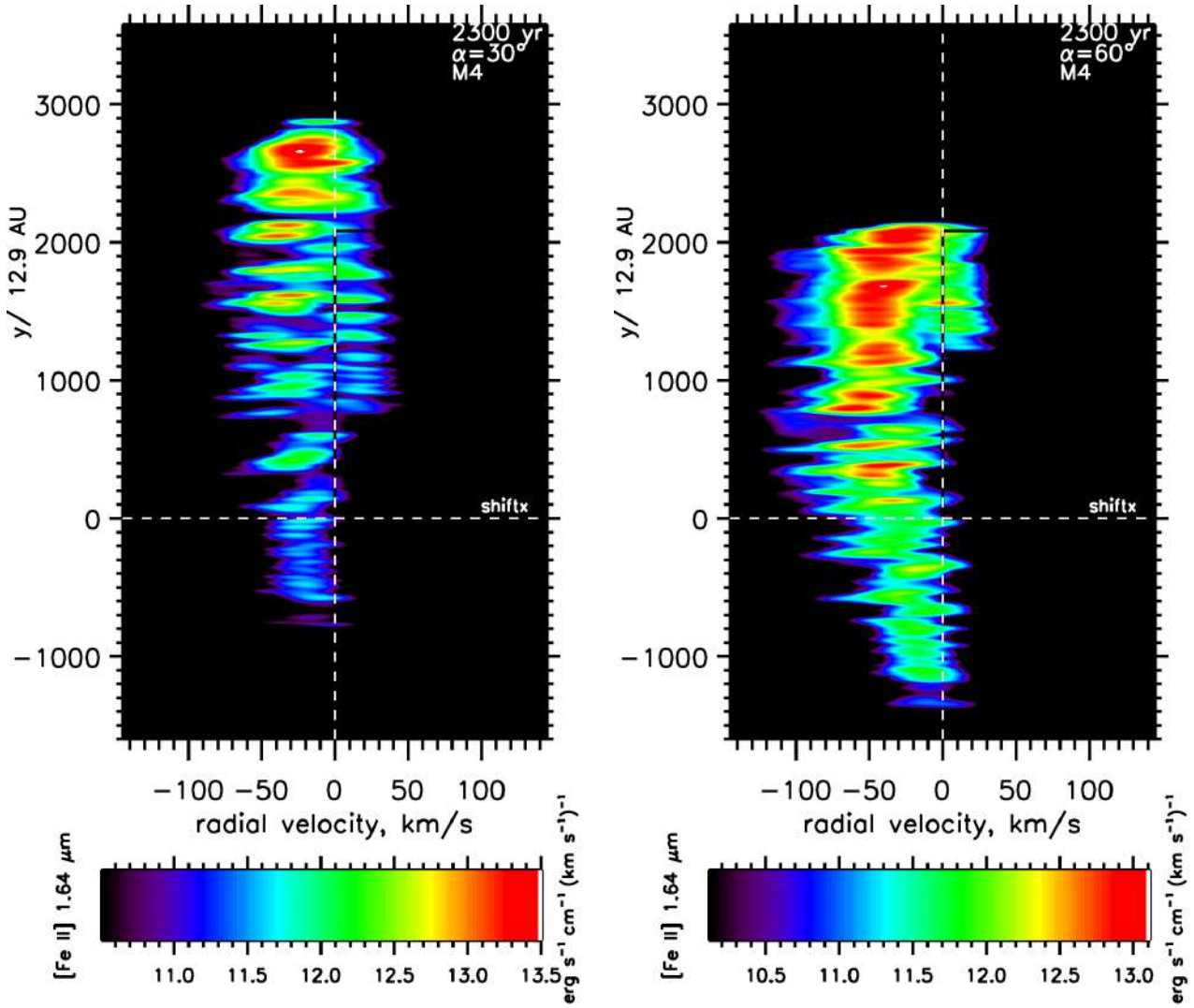

Figure 6.47: Position-Velocity diagrams for the [Fe II] 1.64 μm emission from the 2:1 elliptical wind with the long axis $\alpha = 30°$ and $\alpha = 60°$ out of the plane of the sky, at a late stage of 140 km s^{-1} wind expansion. The M4 model for aa atomic wind and atomic ambient medium is displayed.

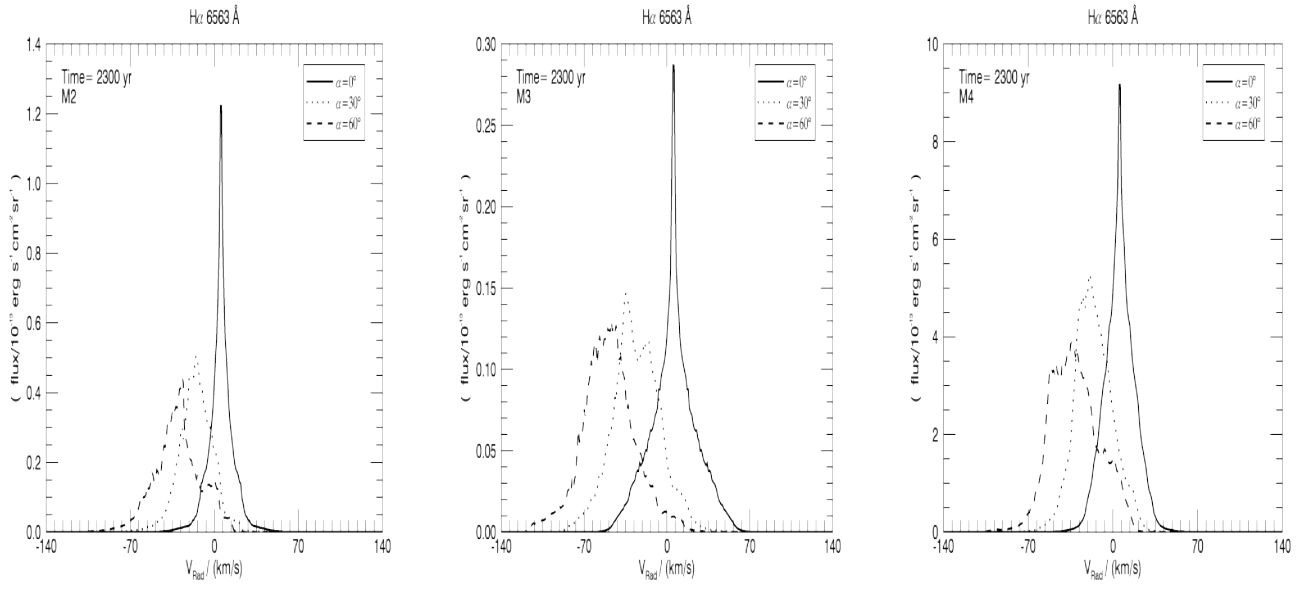

(a) Model M2 (b) Model M3 (c) Model M4

Figure 6.48: Line profiles of the entire pPN in Hα emission from 2:1 elliptical winds with the symmetry axis at 0, 30 & 60° to the plane of the sky.

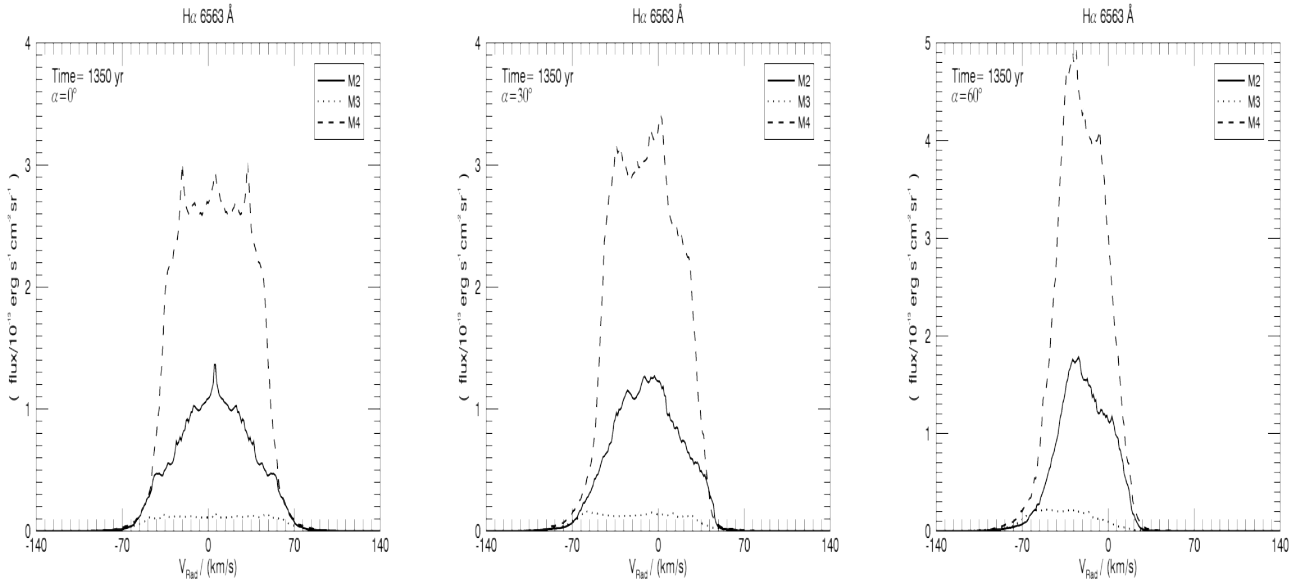

(a) $\alpha = 0°$. (b) $\alpha = 30°$. (c) $\alpha = 60°$.

Figure 6.49: Line profiles of the entire pPN in [Hα] emission from 1:1 spherical wind with the symmetry axis at 0, 30 & 60° to the plane of the sky.

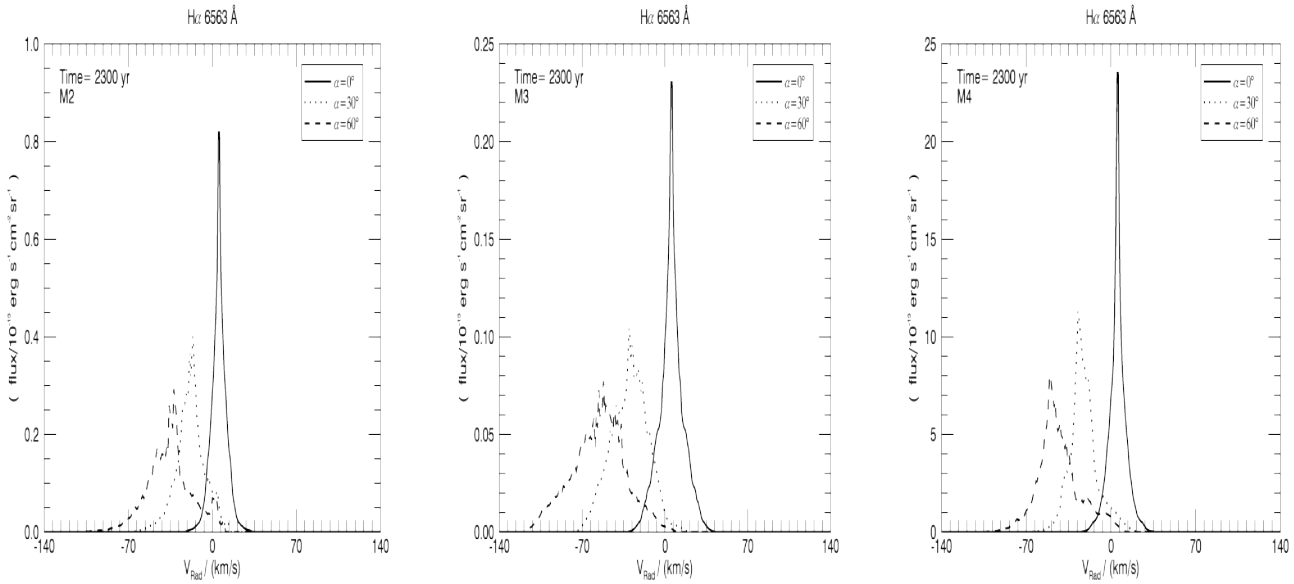

(a) Model M2 (b) Model M3 (c) Model M4

Figure 6.50: Line profiles of the entire pPN in Hα emission from 4:1 elliptical winds with the symmetry axis at 0, 30 & 60° to the plane of the sky.

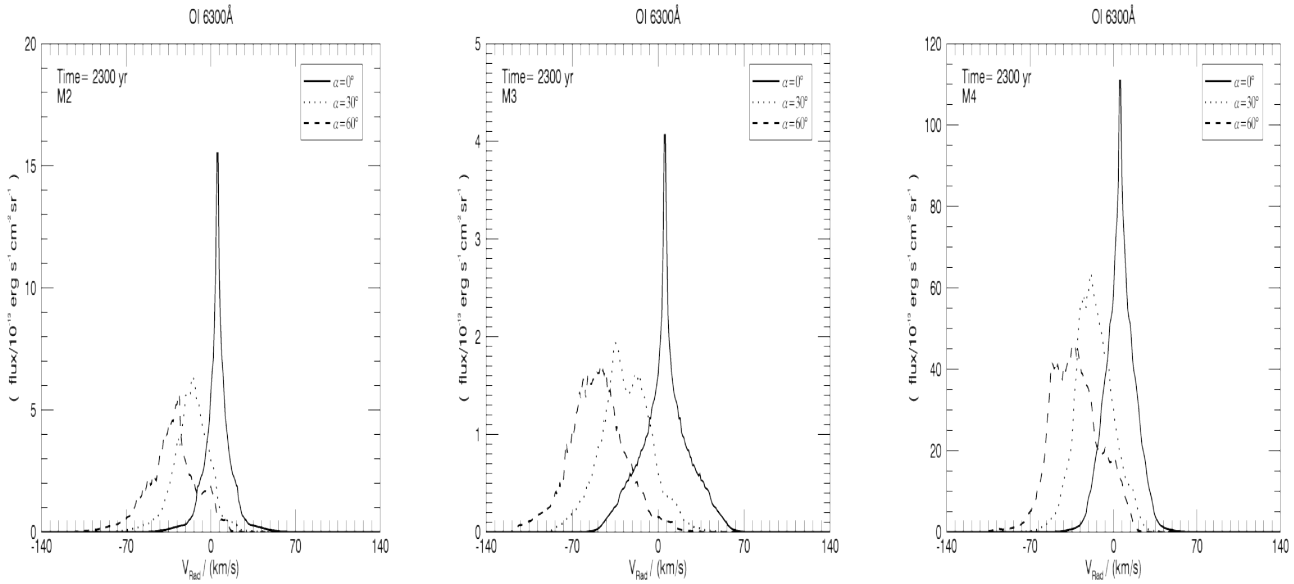

(a) Model M2 (b) Model M3 (c) Model M4

Figure 6.51: Line profiles of the entire pPN in [OI] emission from 2:1 elliptical wind with the symmetry axis at 0, 30 & 60° to the plane of the sky.

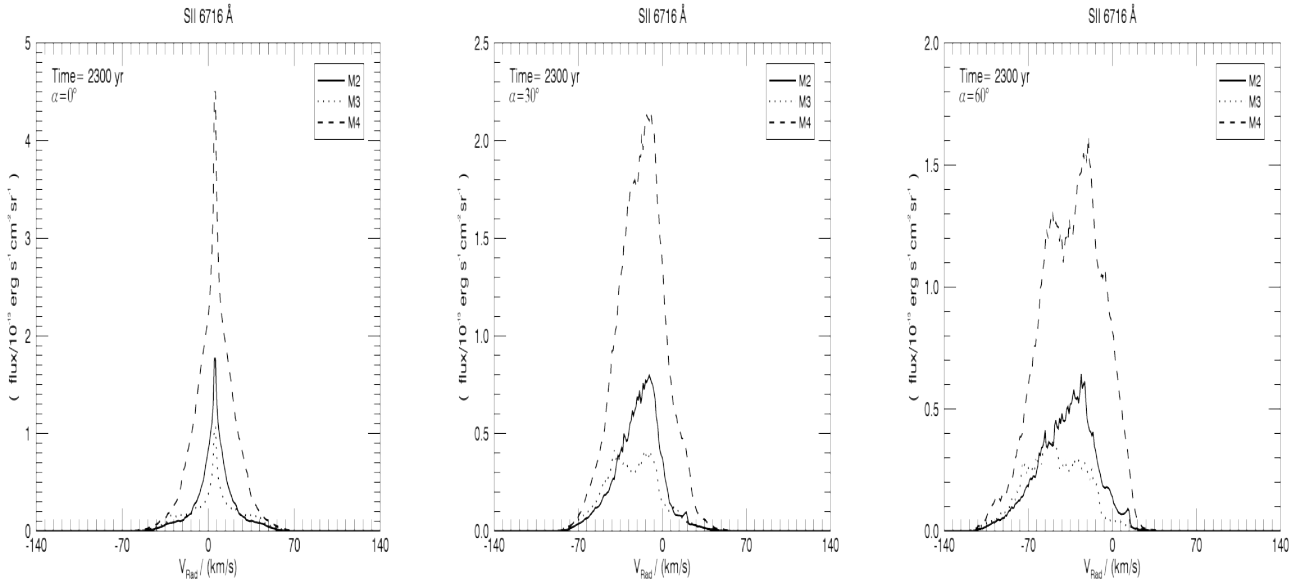

(a) $\alpha = 0°$. (b) $\alpha = 30°$. (c) $\alpha = 60°$.

Figure 6.52: Line profiles of the entire pPN in [SII] emission from 2:1 elliptical wind with the symmetry axis at 0, 30 & 60° to the plane of the sky.

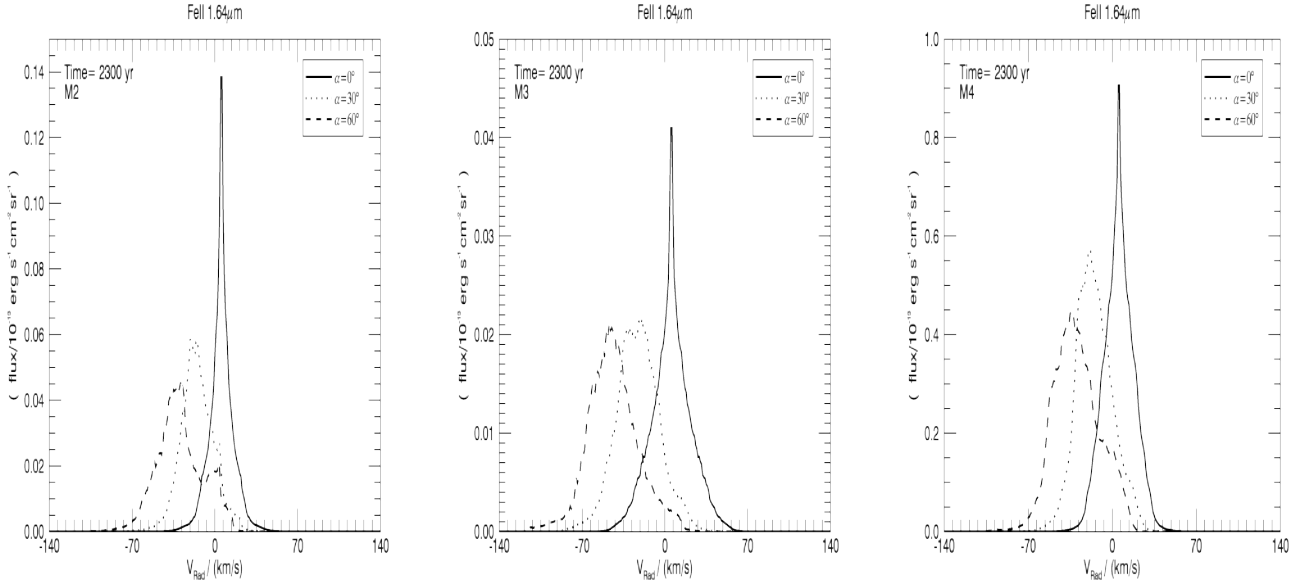

(a) Model M2 (b) Model M3 (c) Model M4

Figure 6.53: Line profiles of the entire pPN in [FeII] emission from 2:1 elliptical wind with the symmetry axis at 0, 30 & 60° to the plane of the sky.

Chapter 7

Discussion

7.1 General

The phase signalled by protoplanetary nebula bridges the AGB and planetary nebula phases. Previously ejected material and swept up ambient gas are subject to the impact of a wind that may have a speed of 60 – 300 $\mathrm{km\,s^{-1}}$, generating a shell expanding at a speed of several tens of $\mathrm{km\,s^{-1}}$. We have made an attempt here to simulate this phase in which molecular shock physics may dominate the observed emission is shock-induced.

Specifically, the inclusion of molecular chemistry and cooling is vital for correct understanding because of the strong cooling and compression within the shock layers which, rather than generating a thin shell, distorts and fragments into molecular streams and fingers. These fingers protrude from the molecular medium across the interface. Thus, classical cometary globules that are exposed to the wind and roughly face the central star or wind-generated bullets advancing ahead of the interface can result. We find that the direction of these streams are not constrained to lie on the radial line to the central star but appear to divert according to the local conditions.

Molecule dissociation is also significant. Overall, we note that in the early stages of wind expansion, the molecules in the ambient medium are destroyed due to a strong forward shock. For the later stages as the pPN radius expands, the situation becomes reversed and it is the molecules in the wind that get dissociated. This shock structure is time dependent and leads to a variety of emission stages that can be followed with emission maps generated by molecular cooling routines.

Planetary nebula that are elliptical could be feasibly generated through a variety of mechanisms. As summarised by Huarte-Espinosa et al. (2012), these include (1) an early jet phase followed by a spherical wind, (2) a wind that is shock-focussed or otherwise redirected by an early AGB equatorial wind or shell and (3) an early spherical AGB envelope or wind with a subsequent collimation axial flow. Here, we simply assume an elliptical velocity distribution, a hybrid jet-wind mechanism. The resulting molecular simulations provide a set of templates against which we can test complex evolutionary scenarios that may be relevant to protostellar outflows as well as pPN.

These wind interactions possess some resemblance in their set up to those occurring in diverging jet or conical atomic outflow (Lee & Sahai 2003) which lead to bow-shock dominated flows, and to collimated molecular winds (Lee et al. 2009) using the same molecular physics as in the original version of the present ZEUS code (Suttner et al. 1997). However, the outcomes are very different since the jet interface is then tangential to the flow and exposed to the ambient medium. Hence, the ratio of the ambient thermal pressure to the wind pressure becomes of crucial importance to the wind/jet expansion.

The comparison to observations must take into account the limitations imposed on the simulated physics and dynamics in order to incorporate the chemistry with moderate accuracy. Firstly, we assume cylindrical symmetry that influences how perturbations grow from an inner spherical surface and how observations of the fingers appear in projection. In addition, magnetohydrodynamics would limit the compression, but possibly introduce ambipolar diffusion effects before ionisation levels are raised sufficiently by the emerging white dwarf. Finally, we have taken the environment to be uniform and homogeneous in this first work. Such an assumption would appear to eliminate the possibility of generating bipolar nebula (with a constricted or hour-glass structure), although this was a priori not necessarily the case, given that a deflected wind or a rotating jet could, in theory, generate candle-flame shapes, if the wind flow were deflected by a 'mid-plane' oblique shock as shown by (Smith 1986).

Molecular hydrogen emission is associated with both bipolar and elliptical nebula (Marquez-Lugo et al. 2013) which may well follow entirely distinct evolutions. There is indeed gathering evidence that the PN phenomenon is heterogeneous; PN are formed from multiple evolutionary scenarios (Frew & Parker 2010). The ejection models may well depend on the progenitor mass, binarity and detailed stellar physics.

Collision shock waves are the dominant source of energy for the H_2 excitation in the least evolved pPN (Davis et al. 2003). Fluorescence, on the other hand, becomes more important at intermediate evolutionary stages (i.e. in 'young' PN when the UV from the exposure to the hot central star first becomes strong), particularly in the inner core regions and along the inner edges of the expanding post-asymptotic giant branch envelope. This is consistent with the finding that, during the developed PN stages, molecular hydrogen remains strongly associated with bipolar nebula rather than elliptical nebula (Hora et al. 1999).

The distribution of H_2 emission in pPN suggests that a fast wind is impinging on material in the cavity walls and tips (Gledhill et al. 2011). Examples of prolate ellipsoidal nebula are found (Hrivnak et al. 2008) even though the bipolar PN are particularly associated with H_2, possibly because of a previously ejected slow molecular wind that possesses an oblate ellipsoidal structure.

The simulations here produce morphological structures similar to cometary knots found in high resolution images of objects such as the Helix nebula (Aleman et al. 2011). The density of the knots present in pure molecular model M1 is found to be significantly denser compared to surrounding ambient and wind media. Knots and filamentary condensations are featured in Hα and $1 \rightarrow 0\,\mathrm{S}(1)\,\mathrm{H}_2$ images, marking the transition region between warm ionised and neutral H.

Knots have also been detected in H_2 emission from low-ionization structures in two planetary nebula (Akras et al. 2017). The H_2 2-1/1-0 S(1) line ratio ranges from 0.1 to 0.14, suggesting the presence of shock interactions, consistent with the predictions here over wide regions of pPN. The strongest line, 1–0 S(1), was also detected in several low-ionization knots located at the periphery of the elliptical planetary nebula NGC 7662. Only four knots of these exhibit detectable 2–1 S(1) and therefore possess high H_2 excitation with line ratios between 0.3 and 0.5. It was suggested that the emission is induced by ionizing ultraviolet from the central star although we have found here that isolated hot-shock zones can possess similar values at early stages. In particular, Model M3 with an ambient molecular medium contains regions of very high excitation even at a later evolutionary stage.

7.2 Comparison of hydrodynamic wind-shell interactions

Persistent supersonic outflows have been the subject of many hydrodynamic simulations with wide applications. The injected flows are allowed to evolve with precession, smooth pulsation and intermittent ejections often imposed or superimposed. Common geometric forms include

ellipsoidal/spheroidal, partly collimated and fully channelled into jets. The simulations then follow the interaction between the outflow and the ambient medium, which may consist of atomic, molecular and/or relativistic gas.

There are two critical factors that will determine the situation being simulated. The first factor is the cooling time in the shell that forms between the shocked wind and the shocked ambient medium. The second factor is the numerical resolution of the cooling layer. Simulations are often not able to resolve the layer and numerical effects rather than the physics that can then determine the outcome. To ameliorate this, the simulations often presume very low densities and high speeds, so increasing the cooling length and stability. These simulations are relevant to the fast winds in the PN stage. We can identify three broad cases from the many outflow simulations, as follows.

In Case 1, the shocked gas of one of the media collapses into a very thin dense shell. The shell breaks up through dynamical instabilities, forming fingers protruding into the opposing medium. Thin-shell instabilities as uncovered in the context of planetary nebula by García-Segura et al. (1999) conform to this picture.

In Case 2, the shocked wind remains hot. A hot cavity forms which will escape through bubbles or de Laval nozzles as jets, depending on the precise configuration (Smith et al. 1981). Thus, extremely low density winds have been shown to create hot bubbles under PN conditions (Balick 1987; Toalá & Arthur 2014).

In Case 3, the thin shell is averted. The cooling is not effective in collapsing the gas into a thin shell because the cooling layer is thermally unstable. In this case, a thick turbulent shell forms and grows without the development of protrusions. Simulations of high resolution are necessary to resolve the compressed shell.

High resolution studies corresponding to Case 3 have been presented by van Marle & Keppens (2012). Here, a fast wind of 2,000 km s^{-1} is shocked to provide a hot cavity that drives a dense shell. The shell is highly distorted and irregular without the formation of dense fingers. The advancing shock front has a speed close to 100 – 200 km s^{-1}, which falls into the range where thermal instability and dynamic overstability are present (Strickland & Blondin 1995). Lower ionisation species such as [Si II] 6716 λ emission from 200 km s^{-1} CFW associated with the pPN CRL 618 was simulated by Velázquez et al. (2014). They show synthetic maps with a flux dynamic range of 10^3 erg s^{-1} $cm^{-2}sr^{-1}$, correlating with images displayed in Fig. 6.20. On

the other hand, predicted PV diagrams for CRL 618 are dominated by the ejected bullets.

The specific case studied here correspond to ellipsoidal winds of high mass outflow into a uniform dense ambient medium Novikov & Smith (2018, 2019). Both the wind and ambient medium will cool in a time scale significantly shorter than the dynamical time of expansion. The outflow speeds and densities correspond to those expected in protoplanetary nebula and protostellar outflows from low-mass stars.

With this simulation set-up, we are modelling the very early stages of outflow development before the fast PN wind such as simulate by Perinotto et al. (2004); Schönberner et al. (2005) is established. The later fast atomic winds, hot bubbles, photoionisation and radiation pressure of planetary nebulae are not simulated with the present parameters.

We thus find that the simulations presented here are consistent with previous studies. A thin collapsed shell of shocked molecular gas under pPN conditions will degenerate into a regular pattern of roughly radial filaments. On the other hand, if only atomic gas is involved, the shell degenerates into an irregular pattern containing knots and filaments within a slowly thickening turbulent layer.

7.3 Comparison to observations

The literature contains many models of planetary nebula that pertain to finding physical parameter fits to specific images. However, models based on full hydrodynamical simulations are rare and often employ resolutions that cannot adequately explore the shell stability or do not have the resolution to explore the range in temperature and density within the shell. Here, the code contains the necessary cooling functions that operate between 10 K and 10^8 K. A compromise remains in the resolution of the hot atomic post-shock gas for which we approximate the ionisation and temperature structure.

The Hα 6563 λ emission in Fig. 6.19 shows features, similar to the ones computated by Velázquez et al. (2004) in Hen 3-1475 with extended bow shock wings produced by collimated fast wind (CFW) of 400 km s^{-1} expanding into uniform ISM. The authors also provide results for the same model expanding into non-uniform r^{-2} density profile ISM producing high emission values close to the central star and seemingly less bow shock emission due to low density medium parameters at large distances away from the stellar surface.

The slightly elliptical planetary nebula NGC 1501 has been modelled as an irregular ellipsoid containing complex filamentary structure. It displays inward-pointing tails (Sabbadin et al. 2000) which suggests that this structure is formed due to Rayleigh-Taylor instabilities and wind-wind interaction. Position-velocity diagrams of Hα show a quite uniform bow-shaped shell with maximum expansion speeds of approximately 55 km s^{-1}. In our case, the corresponding Model M3 shows similar morphological features formed by wind-uniform ISM interaction generating the most well-defined shell structure in the simulated PV diagrams shown in Fig. 6.32. However, it is evident that this nebula has evolved well past the pPN phase and other physical processes are likely to have reshaped the environment.

One can also question if ring structures such as those observed in NGC 6369 (Ramos-Larios et al. 2012) may be related to the ring structures uncovered here in Hα, although it is not clear that such structure would remain in three dimensional simulations and at the later PN phase. This nebula contains outward-pointing protrusions that would correspond to our Model 2 involving a molecular wind ramming into atomic material. Indeed, Ramos-Larios et al. (2012) found that the protrusions contain molecular and neutral atomic gas. This is confirmed in H_2 images that display considerable molecular material interior to the shell. In addition, PV diagrams do show the distorted ellipses predicted here.

Position-velocity diagrams are being increasingly extracted from long-slit and integral-field spectroscopy. A distinct elliptical morphology was found in IRAS 16594-4656 (Hrivnak et al. 2008). A comparison with the PV diagrams generated here indicates an axis very close to the plane of the sky. However, the predicted strong increase of brightness at the leading edge is not detected. While the general expanding-shell structures are very similar to the PV diagrams generated here, the observed velocity width is only $\sim$ 20 km s^{-1}, about half that predicted in Fig. 6.26. PV diagrams for Hen 3-401 display two converging arcs with the radial velocity increasing uniformly with axial distance (Hrivnak et al. 2008). Such a structure is found here at 30° out of the sky plane as shown by Fig. 6.27 if one assumes the redshifted lobe has point-symmetry with the displayed blue-shifted one. Again, however, our models predict a prominent region of high flux at the leading edge of the fast flow along the axis, which is not observed. Position-velocity diagrams were presented from long-slit spectroscopy along the central axis of the PN M2–9 by Smith et al. (2005). These display two components which correspond to the near and far sides of the expanding elliptical structure. However, we cannot distinguish between models presented here since the emission is shell-dominated in all three cases.

While our PV diagrams exhibit shell structures, our simulated images of 4:1 winds do not, being dominated by the fast leading shaped shell. Thus elliptical shell structures such as for NGC 3132 do not fall into place here. One could propose that the shell has been excavated by a fast ellipsoidal wind but which has now been superseded by a spherical wind that applies a similar pressure around the shell. Or, in the later stages, photoionisation has taken over as the excitation mechanism. However, it seems most likely that the elliptical shells are associated with mildly-ellipsoidal winds in which the available shock power is not substantially different. This is also backed up by 2:1 simulations in Fig. 6.15 - 6.17, where a clear shell structure is observed, produced by less elliptic outflows. In fact, the projected turbulent shell of NGC3132 displays an axial ratio of only about 1.25 (Monteiro et al. 2000), consistent with both shock and photo-excitation. Multiple winds will need to be explored with a possible evolution resulting in hour-glass structure present in some post-AGB nebulae such as MyCn-18 and Frosty Leo.

How far can these simulations of pPN be applied to PN? The major difference is in terms of size with our simulations following the expansion up to about 0.2 pc whereas PN extend beyond this typically. Nevertheless, H_2 has now been detected in a large number of PN (Froebrich et al. 2015) and in almost each case (Ramos-Larios et al. 2017). The PN at this stage appear to have evolved to either ring shaped or waist-shaped. The ring-shaped PN appear to be larger and they emit more in the H_2 (Guerrero et al. 2000). Hence, it is probable that some of the pPN are contained by a dense ambient equatorial ring, reducing shock speed and post-shock excitation; fluorescent excitation then dominates. On the other hand, where the pPN is not held back, shock excitation can still dominate within the equatorial plane.

Chapter 8

Conclusions & Future Work

8.1 General

We have investigated the consequences of introducing a supersonic wind with a prolate ellipsoidal velocity distribution into a uniform circumstellar environment. We consider all combinations of fully molecular and fully atomic wind and ambient media. Conditions may be relevant to that of pPN. Early in the runs, the forward shock is dominant and molecules in the ambient medium are partly dissociated. As the wind slows down as it expands, the backward shock begins to dominate and molecules in the wind are dissociated.

We found that an ellipsoidal shell interface forms but fragments into finger-like protrusions, which poke from the molecular medium into the atomic medium. When both media are atomic, the fingers are not apparent. Instead, the atomic shell thickens into a turbulent crust.

To create links to observations, we produced H_2 emission maps for the $1 \rightarrow 0\,\mathrm{S}(1)$ line. By employing 2–D axisymmetric winds, we gain in accuracy and resolution of the temperature and molecular fraction. This, however, means that the simulated structures are limited to ring-like formations. Gaussian smoothing is applied to facilitate a comparison to the observations data with a standard deviation of $\sigma = 20$ zones, and flux spread over 4σ in order to reduce the calculation time for the convolution.

Further spectroscopic studies (position-velocity diagrams) enable us to distinguish between the geometry and orientation. We uncover elliptical and Hubble-like PV diagrams from the same simulation with differing orientations. However, velocity widths are roughly double what has

currently been observed. This suggests that observed pPN are already quite evolved and the advancing shock has further decelerated. Alternatively, magnetohydrodynamic C-shock physics should be considered. The H_2 emission from C-shocks is produced well before the gas is shock-accelerated, as opposed to the J-shocks considered here where the jump occurs before the emission. The result would be lower velocity widths and narrower line profiles if the main source of emission originates from a slow-moving ambient medium.

The model set up here generates lobe-type nebula with a leading bow-shaped region. We have also indicated, however, that fluorescent H_2 distributions would demonstrate a classical bipolar configuration with arcs stemming from the equatorial plane.

There are some significant differences in trends between the models. For fully molecular Model 1 (MWMA), both shocks contribute to the total emission produced which therefore holds quite constant. The increasing reverse shock strength leads to dissociation and raises the overall line ratio, whereas the wind's ellipticity lowers the $1 \rightarrow 0\,\mathrm{S}(1)$ and $2 \rightarrow 1\,\mathrm{S}(1)$ lines and raises the overall line ratio in the low speed flows, but the H_2 excitation remains constant in the high-speed elliptical wind since the major location of vibationally-excited gas gradually moves across the surface with time.

Model 2 (MWAA) with the molecular wind displays more time-dependent emission, obtaining lower flux at the bow shock but more compact overall flux density compared to M1 (MWMA) suggesting that M2 is overall more dissociative. PV diagrams show that the shock front becomes more blunt in the spherical wind case, but stretches out with increasing ellipticity becoming similar to M1 & M3. Model 3 (AWMA), with a molecular ambient medium, displays the most time-dependent integrated emission. The emission falls off quite rapidly in the latter stages. This is related to the diminishing speed of the forward shock front. At the same time, the vibrational excitation remains relatively high consistent with the vibrational temperature of the H_2 being fixed by the collection of shock strengths within the disrupted shell.

Vibrational excitation remains quite constant across the lobes and also in time due to the presence of a full turbulent spectrum of shock speeds rather than a single shock surface. This may help explain the enigmatic absence of high-excitation H_2 where expansion speeds are thought to be highest.

We have applied a hydrodynamic code that includes molecular dissociation and reformation besides molecular and atomic cooling to study protoplanetary nebulae. In this work, we examined

atomic emission line tracers located in the optical and near-infrared bands. This supplements the molecular hydrogen analysis of Novikov & Smith (2018). We do not include the effects of radiation from the central star, the emission is induced after shock excitation.

These simulations provide the platform for more complex dynamical configurations of the global flow. There are two major extreme models considered in the literature. Firstly, we can envisage that the wind speed picks up abruptly, from a slow wind to fast wind (Kwok et al. 1978), generating a fast expanding inner secondary shell, which eventually hits the outer fragmented shell. Secondly, the wind could switch off completely so that there is no further ram pressure support to drive the shell (García-Segura et al. 2006). In this case, the wind cavity is considered to be a hot bubble and the depressurised shell expands back into cavity causing an intricate fragmented structure (Manchado et al. 2015). Both of these cases should be explored with a molecular code in the future.

The ellipsoidal winds into uniform media investigated here produce giant bow-shaped bipolar nebula. In addition, highly ellipsoidal winds generate emission-line structures that resemble bullets. This is because the low speed of the lateral shock does not ionise the gas. Therefore, we do not generate the elongated ellipses often found as a class of planetary nebula. This is expected since such nebula, while physically created by winds, are then ionised by ultraviolet radiation from the central star. Unfortunately, pPN are quite deeply embedded and optical images remain rare. However, we do find that the later pPN (early development of the PN) phase can be interpreted here especially with position-velocity diagrams.

We find that the simulations with a molecular component leads to lower atomic excitation, weaker peaks and integrated atomic emission as the pPN grows. This is due to the shell fragmentation in the molecular cases where the shock surface area is increased and oblique shocks are prevalent. Position-velocity diagrams for the atomic lines indicate that the atomic-wind model may be most easy to distinguish with more emission at higher radial velocities.

Winds and jets have been considered as the drivers behind protostellar outflow, bipolar nebulae and Herbig-Haro flows. The ZEUS 3D modification used here was previously employed in a similar fashion to investigate atomic and molecular jets into molecular environments e.g. Rosen & Smith (2004b) and Smith & Rosen (2007). In the work cited above, it was found that the jet-ambient impact region splits up into protrusions, creating small bullets with leading mini-bows in three dimensions. The difference between a wind and jet is as expected, with the jet impact

region not extending into the flanks. Position-velocity diagrams for jet-driven flows also show a different morphology with a distinct edge of broad radial velocity followed by a trail at low radial speed (Smith et al. 2014). This is in stark contrast to the arc structures which correspond to wind-driven flows. The arcs are caused by the direct wind impact into the flanks.

We conclude that the unstable interface can be produced not only by wind-wind models but also by wind-uniform ISM interaction with formation of clumps and filaments. The subsequent inclusion of GISW model and comparison with resulting morphologies and emission with results from Novikov & Smith (2018) and subsequent Paper II Novikov & Smith (2019) would help trace the differences in kinematic distribution of material and flux densities.

We have thus modelled the initial set-up of post-AGB environments that enable us to generate a set of spectroscopic maps that describe pPN emission features. We can investigate further by the addition of physics modules to approximate wind into wind interaction, i.e the GISW model, in 3–D space for both K-band and optical wavelengths in order to obtain higher resolution of molecular protrusions and atomic turbulent shells. This should be followed by the inclusion of frozen-in magnetic fields as well as field diffusion which may limit shell compression and shock excitation, respectively.

8.2 Interacting winds

Our final aim is to reproduce the most realistic pPN environment by introducing Generalized Interacting Stellar Winds (GISW) model with the addition of an earlier AGB slow wind. Further shaping can be done with precessing jet and pulsations with three-dimensional hydrodynamical simulations. The shock structure can also be altered with the addition of magnetic fields introducing a 'C-shock' environment with lower shock velocities and H_2 excitation. The next step to undertake will be to replace the stationary ambient medium with a wind. An inclusion of a second, dense, slow outflow will enable a systematic study and reveal a variety of flow patterns resulting from the two winds interaction. As a result it will reveal a collection or emission, resulted in process of colliding winds and run comparison diagnostics with current observations. The post-AGB wind will be introduced with an input temperature of 500 K, which allocates the inner region of the envelope (Huarte-Espinosa et al. 2012). An inclusion of outflow precession and a thermal gradient by setting a colder, outer envelope temperatures will resolve in a more realistic set-up. As a consequence, the resultant emission will be altered by the extra temperature dependence.

Another interesting feature to study is inclusion of reassociation coefficient to allow for molecular reformation. Following the research of Suttner et al. (1997), we have adopted the temperature dependent ressociation coefficient k_R and approximated it to be of order $k_R \sim 10^{-17}\,cm^3\,s^{-1}$, hence the relevant ressociation time becomes $t_R \sim (1/k_R\,n)$ with $n \sim 10^5\,cm^{-3}$, t_R becomes few $\sim$ (10^{12} seconds) or 10^4 yr which falls within our simulation time of $10^2 \sim 10^4$ yr. This newly formed H_2 may be subjected to UV fluorescence at the end of pPN stage and beginning of PNe due to $t_{ppn} \sim t_R$. In turn this can also help determine why there is a larger fraction of PNe bearing H_2 compared to pPN by adding ressociation chemistry term in simulations and adding a later PN stage to subject the computated models to additional physics modules such as UV fluorescence to be able to compare the resultant luminosities produced at shock induced H_2 transitions in pPN and H_2 UV fluorescence at later PN stage. Our set up will also enable to predict the luminosity differences based on wind/ambient compositions to further constrain the % difference in pPN/PNe H_2 bearing emitters.

8.3 Magnetohydrodynamic study

One of the promising goals for future research would be an inclusion of C-bow shock, which is a result of J-type bow where H_2 undergoes dissociation turning into atomic gas, which eventually becomes ionised resulting in optical line production coupled with C-type wings of lower density and shock velocity followed by H_2 excitation with no dissociation and subsequent near-infrared emission. ZEUS-MP will enable 3D magnetohydrodynamic simulations implementation with generation of toroidal, poloidal and ambient magnetic fields. Strong toroidal field generates additional acceleration as a result of high ratio of magnetic to thermal pressure leading to a more sharpened cone structure. On the other hand, poloidal field component causes an expansion of the outflow beam (Moraghan 2008).

The developing improvements in computers and numerical methods coupled with advancements in modern telescopes enable researchers to improve understanding of star formation and evolution. These rapid advancements are making it likely to discover and solve old and recent puzzles in the field of Astrophysics, Astronomy & Cosmology. One of the most challenging and recent branches of investigation unfolding for further analysis is numerical simulations of Protoplanetary nebulas. The discussion in this research has helped to clear some of the questions concerning pPNs whilst concurrently developed a foundation for future exploration.

Appendix A

Models	Model 1				Model 2				Model 3			
v_w	40	60	100	140	40	60	100	140	40	60	100	140
Amb												
d_{amb} (gm/cm^3)	5.2677e-21	3.51185e-21	2.1071e-21	1.5051e-21	5.2677e-21	3.5118e-21	2.1071e-21	1.5051e-21	5.2677e-21	3.5118e-21	2.1071e-21	1.5051e-21
u_{amb} (erg/cm^3)	8.6965e-12	5.7976e-12	3.4786e-12	2.4847e-12	8.6965e-12	5.7976e-12	3.4786e-12	2.4847e-12	1.0249e-11	6.8329e-12	4.0997e-12	2.4847e-12
p_{amb} (dyn/cm^2)	3.7271e-12	2.4847e-12	1.4908e-12	1.0648e-12	3.7271e-12	2.4847e-12	1.4908e-12	1.0648e-12	6.8329e-12	4.5553e-12	2.7331e-12	1.0648e-12
c_{amb} (cm/s)	31792.276	31792.276	31792.276	31792.276	31792.276	31792.276	31792.276	31792.276	46496.017	46496.017	46496.017	46496.017
g_{amb}	1.42857	1.42857	1.42857	1.42857	1.42857	1.42857	1.42857	1.42857	1.66667	1.66667	1.66667	1.66667
Wind												
d_{wind} (gm/cm^3)	1.3169e-19	8.7796e-20	5.2677e-20	3.7627e-20	1.3169e-19	8.7796e-20	5.2677e-20	3.7627e-20	1.3169e-19	8.7796e-20	5.2677e-20	3.7627e-20
u_{wind} (erg/cm^3)	5.4353e-09	3.6235e-09	2.1741e-09	1.5529e-09	6.4059e-09	4.2706e-09	2623e-09	1.8302e-09	5.4353e-09	3.6235e-09	2.1741e-09	1.5529e-09
p_{wind} (dyn/cm^2)	2.3294e-09	1.5529e-09	9.3177e-10	6.6555e-10	4.2706e-09	2.8470e-09	1.7082e-09	1.2201e-09	2.3294e-09	1.5529e-09	9.3177e-10	6.6555e-10
c_{wind} (cm/s)	158961.38	158961.38	158961.38	158961.38	232480.08	232480.08	232480.08	232480.08	158961.38	158961.38	158961.38	158961.38
g_{wind}	1.42857	1.42857	1.42857	1.42857	1.66667	1.66667	1.66667	1.66667	1.42857	1.42857	1.42857	1.42857
m_{wind}	25.1633	37.7450	62.9083	88.0717	17.2057	25.8086	43.0144	60.2202	25.1633	37.7450	62.9083	88.0717
η	25	25	25	25	25	25	25	25	25	25	25	25
κ	625	625	625	625	1145.83	1145.83	1145.83	1145.83	340.91	349.91	340.91	340.91
t_{lim}	9778.1 yr	6518.7 yr	3911.2 yr	2793.7 yr	9778.1 yr	6518.7 yr	3911.2 yr	2793.7 yr	9778.1 yr	6518.7 yr	3911.2 yr	2793.7 yr

Table 8.1: Table for solar mass loss of $\dot{M} = 10^{-4} M_{\odot} yr^{-1}$.

Models	Model 1				Model 2				Model 3			
v_w	40	60	100	140	40	60	100	140	40	60	100	140
Amb												
d_{amb} (gm/cm^3)	5.2677e-22	3.51185e-22	2.1071e-22	1.5051e-22	5.2677e-22	3.5118e-22	2.1071e-22	1.5051e-22	5.2677e-22	3.5118e-22	2.1071e-22	1.5051e-22
u_{amb} (erg/cm^3)	8.6965e-13	5.7976e-13	3.4786e-13	2.4847e-13	8.6965e-13	5.7976e-13	3.4786e-13	2.4847e-13	1.0249e-12	6.8329e-13	4.0997e-13	2.4847e-13
p_{amb} (dyn/cm^2)	3.7271e-11	2.4847e-13	1.4908e-13	1.0648e-13	3.7271e-13	2.4847e-13	1.4908e-13	1.0648e-13	6.8329e-13	4.5553e-13	2.7331e-13	1.0648e-13
c_{amb} (cm/s)	31792.276	31792.276	31792.276	31792.276	31792.276	31792.276	31792.276	31792.276	46496.017	46496.017	46496.017	46496.017
g_{amb}	1.42857	1.42857	1.42857	1.42857	1.42857	1.42857	1.42857	1.42857	1.66667	1.66667	1.66667	1.66667
Wind												
d_{wind} (gm/cm^3)	1.3169e-20	8.7796e-21	5.2677e-21	3.7627e-21	1.3169e-20	8.7796e-21	5.2677e-21	3.7627e-21	1.3169e-20	8.7796e-21	5.2677e-21	3.7627e-21
u_{wind} (erg/cm^3)	5.4353e-10	3.6235e-10	2.1741e-10	1.5529e-10	6.4059e-10	4.2706e-10	2623e-10	1.8302e-10	5.4353e-10	3.6235e-10	2.1741e-10	1.5529e-10
p_{wind} (dyn/cm^2)	2.3294e-10	1.5529e-10	9.3177e-11	6.6555e-11	4.2706e-10	2.8470e-10	1.7082e-10	1.2201e-10	2.3294e-10	1.5529e-10	9.3177e-11	6.6555e-11
c_{wind} (cm/s)	158961.38	158961.38	158961.38	158961.38	232480.08	232480.08	232480.08	232480.08	158961.38	158961.38	158961.38	158961.38
g_{wind}	1.42857	1.42857	1.42857	1.42857	1.66667	1.66667	1.66667	1.66667	1.42857	1.42857	1.42857	1.42857
m_{wind}	25.1633	37.7450	62.9083	88.0717	17.2057	25.8086	43.0144	60.2202	25.1633	37.7450	62.9083	88.0717
η	25	25	25	25	25	25	25	25	25	25	25	25
κ	625	625	625	625	1145.83	1145.83	1145.83	1145.83	340.91	349.91	340.91	340.91
t_{lim}	9778.1 yr	6518.7 yr	3911.2 yr	2793.7 yr	9778.1 yr	6518.7 yr	3911.2 yr	2793.7 yr	9778.1 yr	6518.7 yr	3911.2 yr	2793.7 yr

Table 8.2: Table for solar mass loss of $\dot{M} = 10^{-5} M_{\odot} yr^{-1}$.

Appendix B

The description of sub-functions is summarised by Smith & Rosen (2003) and is listed below:

– Λ_1: gas–grain (dust) cooling,

$$\Lambda_1 = n^2 \times \lambda_1 \tag{8.1}$$

Coefficient λ_1 represents standard dust properties, i.e cooling rates after passing shock front with $\mathrm{T_{dust}} = 20\,\mathrm{K}$ therefore assuming cold molecular medium with rapid dust cooling, justified by (Whitworth & Clarke 1997).

$$\lambda_1 = 3.8 \times 10^{-33}\mathrm{T}^{1/2}(\mathrm{T} - \mathrm{T_{dust}}) \times [1.0 - 0.8\exp(-75/\mathrm{T})]\,\mathrm{erg\,s^{-1}cm^3}. \tag{8.2}$$

– Λ_2: collisional cooling,

associated with vibrational and rotational modes in molecular hydrogen, based on equations (7)–(12) in Lepp & McCray (1983).

$$\lambda_2 = n_{H_2}\left[\frac{L_v^H}{1 + (L_v^H)/(L_v^L)} + \frac{L_r^H}{1 + (L_r^H)/(L_r^H)}\right], \tag{8.3}$$

where the vibrational cooling coefficients of high and low density are

$$\mathrm{L_v^H} = 1.10 \times 10^{-18}\exp(-6744/\mathrm{T})\,\mathrm{erg\,s^{-1}}, \tag{8.4}$$

$$\mathrm{L_v^L} = 8.18 \times 10^{-13}\exp(-6840/\mathrm{T}) \times [\mathrm{n_{H_2}k_H}(0,1) + \mathrm{n_{H_2}k_{H_2}}(0,1)]\,\mathrm{erg\,s^{-1}}, \tag{8.5}$$

Collisional excitation rates are represented by the terms $k_H(0,1)$ and $k_{H_2}(0,1)$ with $\Delta v = 1-0$. The exponential term $\exp(-6840/T)$ converts these to de-excitation rates:

$$k_H(0,1) = \begin{cases} 1.4\times10^{-13}\exp[(T/125)-(T/577)^2], & T<T_v \\ 1.0\times10^{-12}T^{1/2}\exp(-1000/T), & T>T_v. \end{cases} \tag{8.6}$$

where the limit $\mathrm{T_v} = 1635\,\mathrm{K}$, and

$$k_{H_2}(0,1) = 1.45\times10^{-12}T^{1/2}\exp[-28728/(T+1190)]. \tag{8.7}$$

The rotational cooling rate coefficient at high density is

$$L_{rH} = \begin{cases} dex[-19.24+0.474x-1.247x^2], & T<T_r \\ 3.90\times10^{-19}\exp(-6118/T), & T>T_r, \end{cases} \tag{8.8}$$

with the limit $\mathrm{T_r} = 1087\,\mathrm{K}$, and $x = log(T/10000K)$. For low density, the coefficient is

$$\frac{L_{rL}}{Q(n)} = \begin{cases} dex[-22.90-0.553x-1.148x^2], & T<T_l \\ 1.38\times10^{-22}\exp(-9243/T), & T>T_l, \end{cases} \tag{8.9}$$

with the limit $\mathrm{T_l} = 4031\,\mathrm{K}$, and the coefficient

$$Q(n) = \left[(n_{H_2})^{0.77} + 1.2(n_H)^{0.77}\right] \tag{8.10}$$

– Λ_3: atomic cooling,

$$\Lambda_3 = n_H^2\times\lambda_2 + 1.42\times10^{-27}(\sqrt{T}) \tag{8.11}$$

With an additional thermal Bremsstrahlung term $1.42\times10^{-27}(\sqrt{T}$ (with Fe=0.5) tabulated in Table 10 of Sutherland & Dopita (1993) added to λ_2. The added term is active for temperatures above $\mathrm{T} > 10000\,\mathrm{K}$

– Λ_4: cooling through rotational modes of water

$$\Lambda_4 = (n_{H_2} + 1.39n_H)\times n_{H_2O}\times\lambda_3 \tag{8.12}$$

$$\lambda_3 = 1.32\times10^{-23}\left[\frac{T}{10^3}\right]^{\alpha}, \tag{8.13}$$

with $\alpha = 1.35 - 0.3log(T/1000)$ which fits the data by Neufeld & Kaufman (1993).

– Λ_5: cooling via water vibrational modes in collision with H_2 and H.

$$\Lambda_5 = 1.03 \times 10^{-26} n_{H_2} n_{H_2O} \times T \exp\left(\frac{-2325}{T}\right) \exp\left(\frac{-47.5}{T^{1/3}}\right). \tag{8.14}$$

Based on Hollenbach & McKee (1989).

– Λ_6: cooling modes of water through collision with atomic hydrogen.

$$\Lambda_6 = 7.40 \times 10^{-27} n_H \lambda_3 n_{H_2O} \times T \exp\left(\frac{-2325}{T}\right) \exp\left(\frac{-34.5}{T^{1/3}}\right). \tag{8.15}$$

again based on Hollenbach & McKee (1989).

– Λ_7: cooling from the dissociation of molecular hydrogen follows Shapiro & Kang (1987).

$$\Lambda_7 = 7.18 \times 10^{-12}((n_H^2)(k_{D,H_2} + (n_H)(n_{H_2}(k_{D,H})). \tag{8.16}$$

The first term 7.18×10^{-12} is the $4.48eV$ dissociation energy of H_2,

$$\mathrm{k_{D,H}} = 1.2 \times 10^{-9} \exp(-52400/\mathrm{T}) \times [0.0933 \exp(17950/\mathrm{T})]^{\beta} \,\mathrm{cm^3\,s^{-1}}. \tag{8.17}$$

$$\mathrm{k_{D,H_2}} = 1.3 \times 10^{-9} \exp(-53300/\mathrm{T}) \times [0.0908 \exp(16200/\mathrm{T})]^{\beta} \,\mathrm{cm^3\,s^{-1}}. \tag{8.18}$$

With coefficient β being the fraction of thermally released energy.

$$\beta = \left\{1.0 + n\left[2f\left(\frac{1}{n_2} - \frac{1}{n_1}\right) + \frac{1}{n_1}\right]\right\}^{-1}. \tag{8.19}$$

The following two approximations represent critical densities for dissociation by collisions of molecular hydrogen with atomic hydrogen, $n1$, and with itself, $n2$.

$$\mathrm{n1} = \mathrm{dex}(4.0 - 0.416\mathrm{x} - 0.327\mathrm{x^2})\,\mathrm{cm^3} \tag{8.20}$$

$$\mathrm{n2} = \mathrm{dex}(4.8451.3\mathrm{x} + 1.62\mathrm{x^2})\,\mathrm{cm^3}. \tag{8.21}$$

– Λ_8: heating from hydrogen reformation is included as another cooling term Hollenbach & McKee (1979):

$$\Lambda_8 = -\lambda_7 \xi \tag{8.22}$$

$$\xi = n n_H (1 - \beta) 7.18 \times 10^{-12} \tag{8.23}$$

Another coefficient λ_7 is defined as

$$\Lambda_7 = (3 \times 10^{-18}\mathrm{cm^3 s^{-1}}) \times \frac{\sqrt{\mathrm{T}}\mathrm{f_a}}{1 + 0.04\sqrt{\mathrm{T} + \mathrm{T_g}} + 210^{-3}\mathrm{T} + 860^{-6}\mathrm{T}^2} \tag{8.24}$$

And f_a is defined as

$$f_a = [1 + 10.000 \exp(-600/T_g)]^{-1} \tag{8.25}$$

– Λ_9: cooling via CO rotational modes Through collisions with molecular or atomic hydrogen as described by equations (5.2)(5.5) in McKee et al. (1982).

$$\Lambda_9 = n_{CO} n \frac{kT\sigma v_T}{1 + n_a/n_{cr} + 1.5(n_a/n_{cr})^{1/2}}, \tag{8.26}$$

where the mean speed of the molecules $v_T = \sqrt{8kT/\pi m_{H_2}}$ with

$$\mathrm{n_{cr}} = 3.3 \times 10^6 \mathrm{T_3^{0.75}\,cm^{-3}} \tag{8.27}$$

$$\sigma = 3.0 \times 10^{-16} \mathrm{T_3^{-1/4}\,cm^{-2} T_3 = T/1000\,K} \tag{8.28}$$

with average density, n_a

$$n_a = 0.5(n_H + \sqrt{2} n_{H_2}). \tag{8.29}$$

– Λ_{10}: CO vibrational cooling from collisions with H_2, as used by Neufeld & Kaufman (1993).

$$\Lambda_{10} = 1.83 \times 10^{-26} \mathrm{n_{H_2} n_{CO} \sqrt{T} \exp(3080/T) \exp \frac{-68}{T^{\frac{1}{3}}}}, \tag{8.30}$$

– Λ_{11}: CO vibrational cooling through collisions with atomic hydrogen

$$\Lambda_{11} = 1.28 \times 10^{-24} \mathrm{n_{H_2} n_{CO} T^{1/2} \exp(3080/T) \exp\left(-(2000/T)^{3.43}\right)}, \tag{8.31}$$

– Λ_{12}: Oxygen cooling through the $63\mu m$ fine structure line

$$\Lambda_{12} = 2.28 \times 10^{-18} n_{CO} \frac{1}{1/f_H + A_{10}/r_L}, \tag{8.32}$$

where $A_{10} = 8.95 \times 10^{-5}$ is the spontaneous transition rate

$$f_H = \frac{0.6 \exp(-228/T)}{1 + 0.6 \exp(-228/T) + 0.2 \exp(-326/T)} \tag{8.33}$$

where $r_l = r_H + r_{H_2}$ are collision rates of atomic and molecular hydrogen,

$$r_H = 4.37 \times 10^{-12} T^{0.66} 0.6 \exp(\frac{-228}{T}) + 1.06 \times 10^{-12} T^{0.8} 0.2 \exp(\frac{-326}{T}) \times (n_H + 0.48 n_H) \tag{8.34}$$

$$r_H = 2.88 \times 10^{-11} T^{0.35} 0.6 \exp(\frac{-228}{T}) + 6.68 \times 10^{-11} T^{0.31} 0.2 \exp(\frac{-326}{T}) \times (n_{H_2}) \quad (8.35)$$

– Λ_{13}: OH cooling Hollenbach & McKee (1989).

$$\Lambda_{13} = 2.84 \times 10^{-28} n^2 T^{\frac{3}{2}} \quad (8.36)$$

Appendix C

8.3.1 Conservation of mass

The conservation of mass also known as the continuity equation, is derived in the following way: the computational domain is divided into an array of grid zones. In 3D space, the grid zones are considered to obtain an infinitesimally small cubic volume. The mass inflow propagating from left to right through surface area $dydz$ is

$$dm_x/dt = (\rho u_x)dydz, \tag{8.37}$$

with ρ being the density of the fluid and u_x is the component of the fluid's velocity in the x-direction. The fluid moves a distance dx, the total mass flow rate out of the right-hand face is

$$dm_x/dt = (\rho u_x + \left(\frac{\partial(\rho u)}{\partial x}\right) dydz, \tag{8.38}$$

with $\frac{\partial(\rho \mathrm{u})}{\partial \mathrm{x}}$ indicating the change in mass flux between left and right faces of the computational volume. The mass is conserved, hence equating the two above equations yields

$$\begin{aligned}(\rho u_x + \left(\frac{\partial(\rho u)}{\partial x}\right) dydz - (\rho u_x)dydz = 0 \\ \frac{\partial(\rho u_x)}{\partial x}dydz = 0\end{aligned} \tag{8.39}$$

By similarity, the mass flow rate in the y direction through $dxdz$

$$\frac{\partial(\rho u_y)}{\partial x}dxdz = 0 \tag{8.40}$$

The net flow in the z direction through $dxdy$

$$\frac{\partial(\rho u_z)}{\partial x}dxdy = 0, \tag{8.41}$$

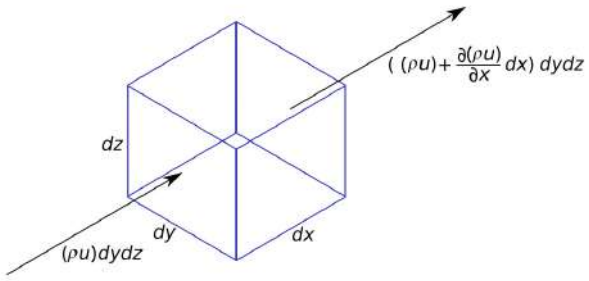

u_x, u_y, u_z are x, y and z components of fluid's velocity. The sum of all three velocity contributions makes up the total mass of the fluid. Summing Equations 7.39 - 7.41 yields

$$\left(\frac{\partial(\rho u_x)}{\partial x} + \frac{\partial(\rho u_y)}{\partial y} + \frac{\partial(\rho u_z)}{\partial z}\right) dxdydz \tag{8.42}$$

The rate of decrease of mass inside a volume is

$$-\frac{\partial \rho}{\partial t}(dxdydz) \tag{8.43}$$

Mass stays conserved, hence the total mass outflow in the volume is equal to the rate of decrease of mass inside that volume, equating Equations 7.42 & 7.43 yields

$$\left(\frac{\partial(\rho u_x)}{\partial x} + \frac{\partial(\rho u_y)}{\partial y} + \frac{\partial(\rho u_z)}{\partial z}\right) dxdydz = -\frac{\partial \rho}{\partial t}(dxdydz) \tag{8.44}$$

Cancelling the volume terms simplifies to

$$\frac{\partial \rho}{\partial t} + \left(\frac{\partial \rho u_x}{\partial x} + \frac{\partial \rho u_y}{\partial y} + \frac{\partial \rho u_z}{\partial z}\right) = 0 \tag{8.45}$$

The above equation can be simplified further by introducing $\nabla \cdot \tilde{u}$, where $\tilde{u}$ is the complete velocity vector in three dimensions and $\nabla = \mathrm{i}\frac{\partial}{\partial \mathrm{x}} + \mathrm{j}\frac{\partial}{\partial \mathrm{y}} + \mathrm{k}\frac{\partial}{\partial \mathrm{z}}$ is the grad operator.

$$\nabla \cdot \vec{u} = \frac{\partial u_x}{\partial x} + \frac{\partial u_y}{\partial y} + \frac{\partial u_z}{\partial z} \tag{8.46}$$

Substituting Equation 7.46 into 7.45, hence obtaining the differential form of continuity equation in conservative form

$$\frac{\partial \rho}{\partial t} + \nabla \cdot (\rho \vec{u}) = 0 \tag{8.47}$$

By using the vector identity 7.49, the non-conservative, Lagrangian form of the above Equation 7.47 can be written as

$$\frac{\partial \rho}{\partial t} + (\rho \nabla \cdot \vec{u}) + (\vec{u} \cdot \nabla \rho) = 0$$
$$\frac{\partial \rho}{\partial t} + (\vec{u} \cdot \nabla \rho) + (\rho \nabla \cdot \vec{u}) = 0 \tag{8.48}$$

Vector identity

$$\nabla \cdot (\rho \vec{u}) = (\rho \nabla \cdot \vec{u}) + (\vec{u} \cdot \nabla \rho) \tag{8.49}$$

Employing the comoving derivative

$$\frac{D}{Dt} = \frac{\partial}{\partial t} + (\vec{u} \cdot \nabla) \tag{8.50}$$

Hence the non-conservative form of the continuity equation is

$$\frac{D\rho}{Dt} = \rho \nabla \cdot \vec{u} = 0 \tag{8.51}$$

A model of an infinitesimal fluid element is chosen to be moving with the flow, therefore obtaining a non-conservative form of the equation.

8.3.2 Conservation of momentum

Following the same logic and applying Newton's 2nd law for infinitesimally small cubic volume yields the momentum equation in conservation form. Starting with the mass of the cubic volume,

$$m = (\rho) dx dy dz \tag{8.52}$$

The acceleration in x direction with the change in time given by the substantial derivative, thus

$$a_x = \frac{Du_x}{Dt} \tag{8.53}$$

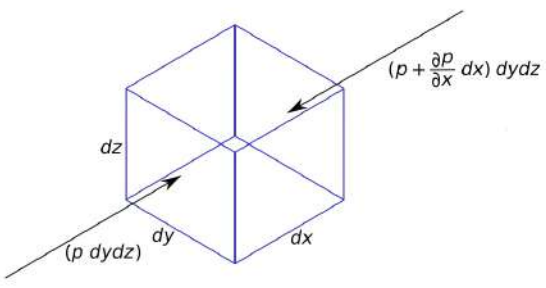

Combining the above two equations gives the expression for the force acting on the infinitesimally small volume in x direction

$$F_x = \rho \frac{Du_x}{Dt} dxdydz \tag{8.54}$$

From now on we are using two assumptions, the forces of gravity are ignored, and the flow is inviscid, meaning there are no viscous forces inducing strain and stress on the fluid. The evaluated parameter is the induced pressure, acting on the faces of the cube in three dimensions. As seen from the diagram, pressure p acting along the dydz and pressure $(\mathrm{p} + \frac{\partial \mathrm{p}}{\partial \mathrm{x}})$ acting along the right hand of dydz. The pressure difference between the two faces is

$$\begin{aligned} \left(p - \left(p + \left(\frac{\partial p}{\partial x} dx\right)\right)\right) dydz = 0 \\ -\frac{\partial p}{\partial x} dxdydz = 0 \end{aligned} \tag{8.55}$$

Equating Equations 7.54 & 7.55 and including the terms with y and z directions yields

$$\rho \left(\frac{Du_x}{Dt} + \frac{Du_y}{Dt} + \frac{Du_z}{Dt}\right) dxdydz = -\left(\frac{\partial \rho}{\partial x} + \frac{\partial \rho}{\partial y} + \frac{\partial \rho}{\partial z}\right) dxdydz \tag{8.56}$$

The volume components cancel on both sides, substituting the ∇ operator for simplicity, we obtain a non conservative form of momentum equation,

$$\rho \frac{D\vec{u}}{Dt} = -\nabla \rho \tag{8.57}$$

The vector identity and the derivative can be used for continuity and momentum equations to change their nature from conservative to non-conservative form.

Substituting the derivative, alters the left side of the momentum relation

$$\rho \frac{D\vec{u}}{Dt} = \rho \frac{\partial \vec{u}}{\partial t} + \rho \vec{u} \cdot \nabla \vec{u} \tag{8.58}$$

The partial derivative term of Equation 7.58 can be expressed alternatively

$$\begin{aligned} \frac{\partial (\rho \vec{u})}{\partial t} &= \rho \frac{\partial \vec{u}}{\partial t} + \vec{u} \frac{\partial \rho}{\partial t} \\ \rho \frac{\partial \vec{u}}{\partial t} &= \frac{\partial (\rho \vec{u})}{\partial t} - \vec{u} \frac{\partial \rho}{\partial t} \end{aligned} \tag{8.59}$$

Using partial derivative relations to expand the second term on the right of Equation 7.58 yields

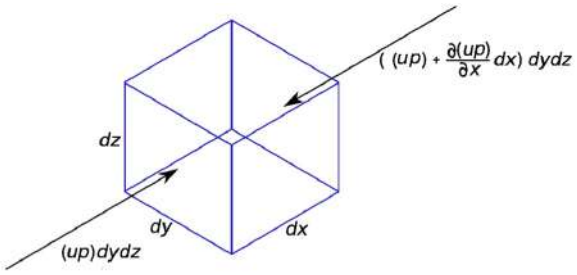

the product of a scalar times a vector

$$\nabla \cdot (\rho u \vec{u}) = u\nabla \cdot (\rho \vec{u}) + (\rho \vec{u}) \cdot \nabla u$$
$$\rho \vec{u} \cdot \nabla u = \nabla \cdot (\rho u \vec{u}) - u\nabla \cdot (\rho \vec{u}) \tag{8.60}$$

Substituting Equations 7.59 & 7.60 into the right side of Equation 7.58

$$\rho \frac{Du}{Dt} = \rho \frac{\partial (\rho u)}{\partial t} - u\frac{\partial \rho}{\partial t} + \nabla \cdot (\rho u \vec{u}) - \vec{u}\nabla \cdot (\rho \vec{u})$$
$$\frac{\partial (\rho u)}{\partial t} - u\left[\frac{\partial \rho}{\partial t} + \nabla \cdot (\rho \vec{u})\right] + \nabla \cdot (\rho u \vec{u}) \tag{8.61}$$

The bracketed term on the right side of the Equation 7.61, is the continuity Equation 7.47 and is equal to zero. Thus, the final conservation form of momentum equation is

$$\rho \frac{Du}{Dt} = \frac{\partial (\rho u)}{\partial t} + \nabla \cdot (\rho u \vec{u}) \tag{8.62}$$

8.3.3 Conservation of energy

The first law of thermodynamics is applied to the moving fluid of a cubic volume. The resultant motion of molecules and atoms within the fluid element is a macroscopic quantity e, representing the internal energy. The rate of change of internal energy inside a volume is expressed in terms of the substantial derivative.

$$\frac{D}{Dt}(e),\ \rho dxdydz \tag{8.63}$$

ZEUS-3D considers the work done by external pressures acting on the surfaces of the cube. Splitting the work done into three spatial components, and starting with x direction displayed by the energy figure above

$$\left(up - \left(up + \frac{\partial (up)}{\partial x}dx\right)\right) dydz = 0 \tag{8.64}$$

$$\frac{\partial(up)}{\partial x}dxdydz = 0 \tag{8.65}$$

Including x and y components

$$-\left(\frac{\partial(u_x p)}{\partial x} + \frac{\partial(u_y p)}{\partial y} + \frac{\partial(u_x p)}{\partial z}\right) dxdydz \tag{8.66}$$

Including the vector operator simplifies the above expression to

$$-p\nabla \cdot udxdydz \tag{8.67}$$

The rate work done on the element due to body and surface forces is equal to the change in internal energy, thus equating equations, we obtain the expression for the internal energy in non-conservative form,

$$\rho\frac{D}{Dt}e = -p\nabla \cdot u \tag{8.68}$$

The conservative form is obtained by the same method as in the momentum equation. Rearranging the above equation in terms of the substantial derivative yields

$$\rho\frac{De}{Dt} = \rho\frac{\partial e}{\partial t} + \rho\vec{u} \cdot \nabla e \tag{8.69}$$

Expanding the partial derivative

$$\rho\frac{\partial e}{\partial t} = \frac{\partial(\rho e)}{\partial t} - e\frac{\partial \rho}{\partial t} \tag{8.70}$$

The second term on the right of Equation 7.69 is modified via the following vector identity

$$\nabla \cdot (\rho e\vec{u}) = e\nabla \cdot (\rho\vec{u}) + \rho\vec{u} \cdot \nabla e, \tag{8.71}$$

rearranging the above expression yields,

$$\rho\vec{u} \cdot \nabla e = \nabla \cdot (\rho e\vec{u}) - e\nabla \cdot (\rho\vec{u}) \tag{8.72}$$

Substituting the altered terms 7.72 back into Equation 7.69

$$\begin{aligned}
\rho\frac{De}{Dt} &= \frac{\partial e}{\partial t} - e\nabla \cdot (\rho\vec{u}) + \nabla \cdot (\rho e\vec{u}) \\
\rho\frac{De}{Dt} &= \frac{\partial(\rho e)}{\partial t} - e\left[\frac{\partial \rho}{\partial t} + \nabla \cdot (\rho\vec{u})\right] + \nabla \cdot (\rho e\vec{u}) \\
\rho\frac{De}{Dt} &= \frac{\partial(\rho e)}{\partial t} + \nabla \cdot (\rho e\vec{u})
\end{aligned} \tag{8.73}$$

The term in brackets represent the contuinuity equation and is set to zero. Substituting the above Equation 7.73 into Equation 7.69, hence obtaining the conservative form of the energy equation

$$\frac{\partial(\rho e)}{\partial t} + \nabla \cdot (\rho e \vec{u}) = -\rho \nabla \cdot \vec{u} \tag{8.74}$$

This forms the complete set of equation s of hydrodynamics in both conservative and non-conservative forms (Anderson 1995).

Appendix D

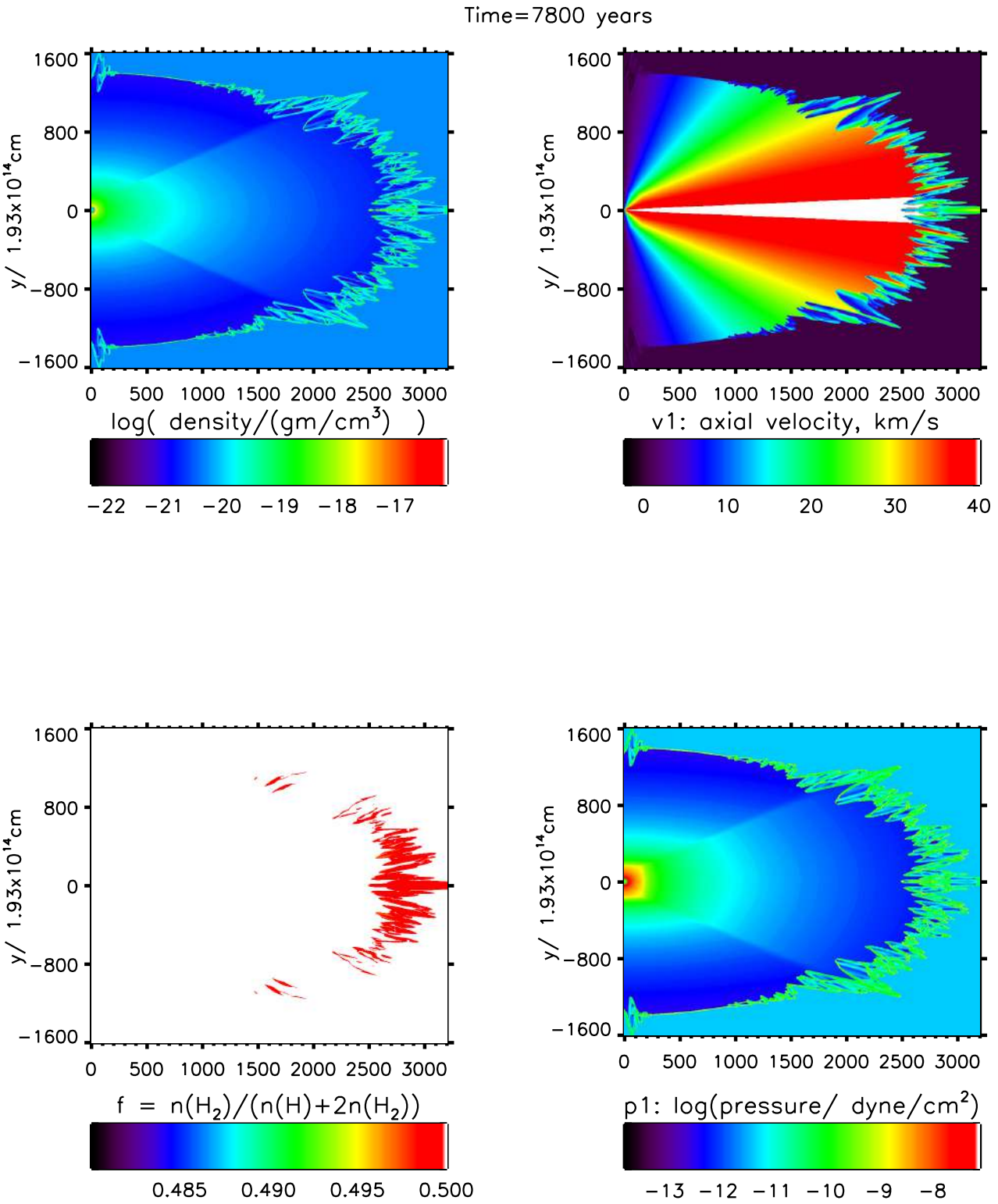

Figure 8.1: Cross-sectional distributions of density, axial velocity, molecular fraction and the pressure generated by a 40 km s^{-1} M1 molecular wind.

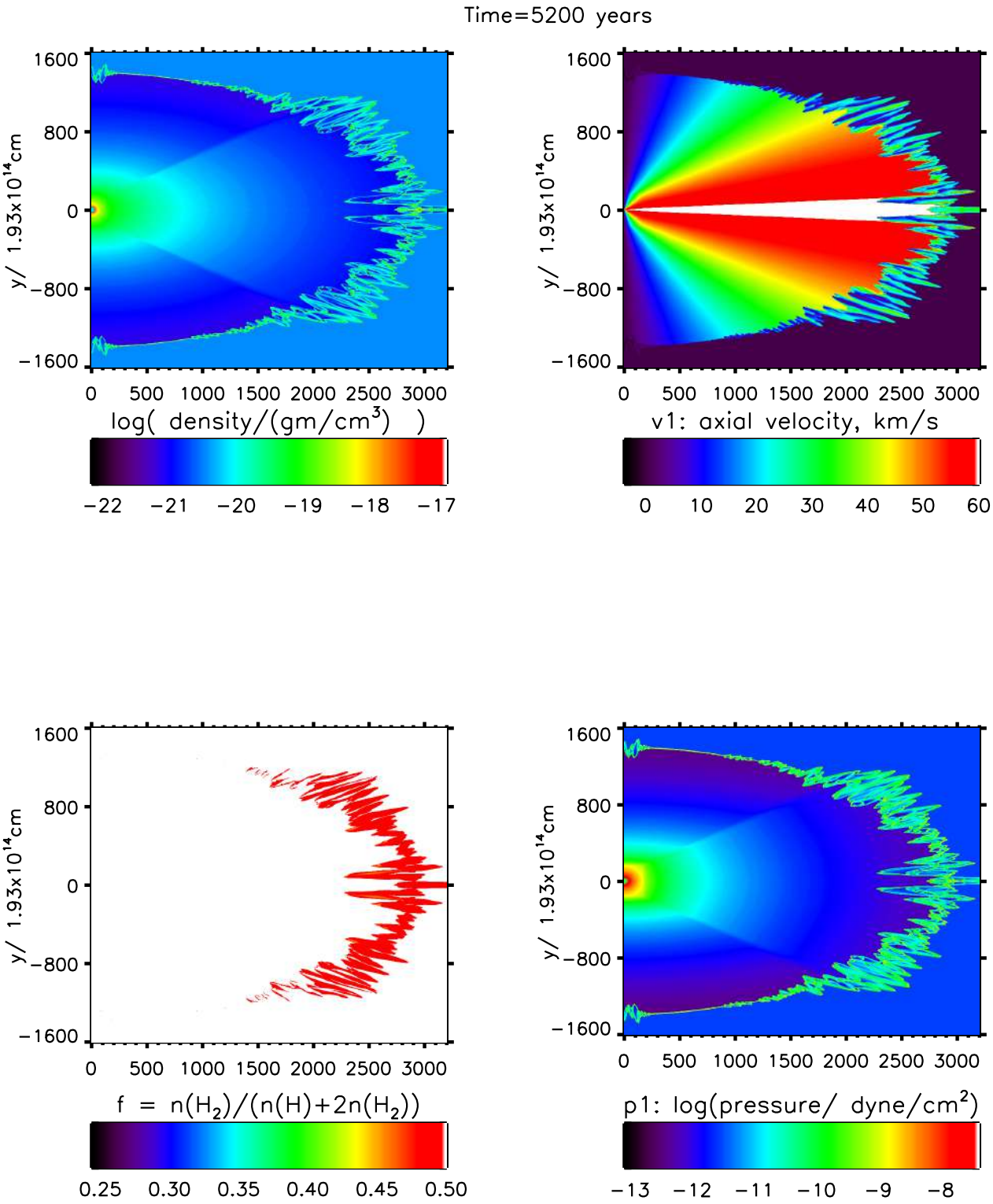

Figure 8.2: Cross-sectional distributions of density, axial velocity, molecular fraction and the pressure generated by a 60 km s^{-1} M1 molecular wind.

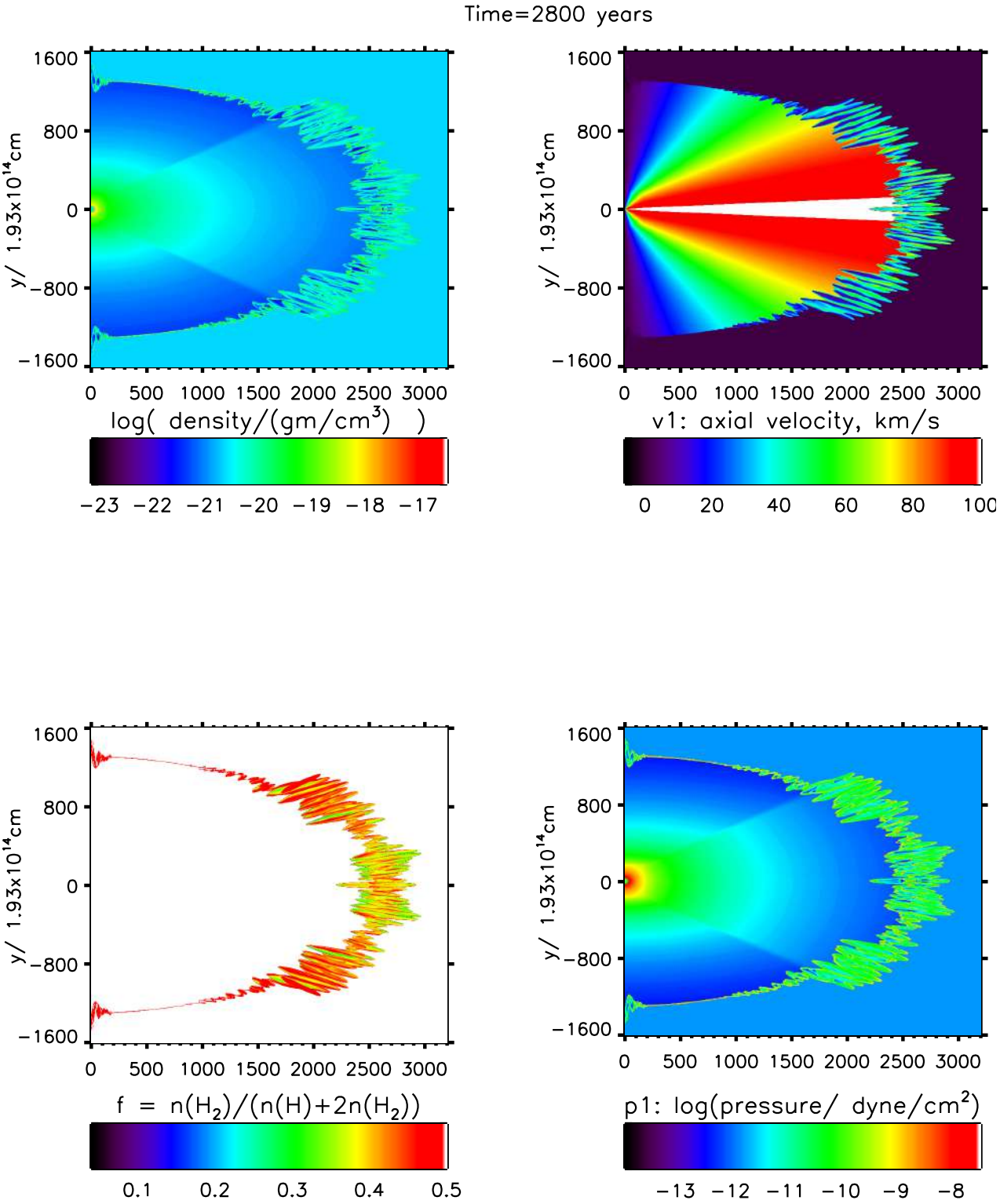

Figure 8.3: Cross-sectional distributions of density, axial velocity, molecular fraction and the pressure generated by a 100 km s^{-1} M1 molecular wind.

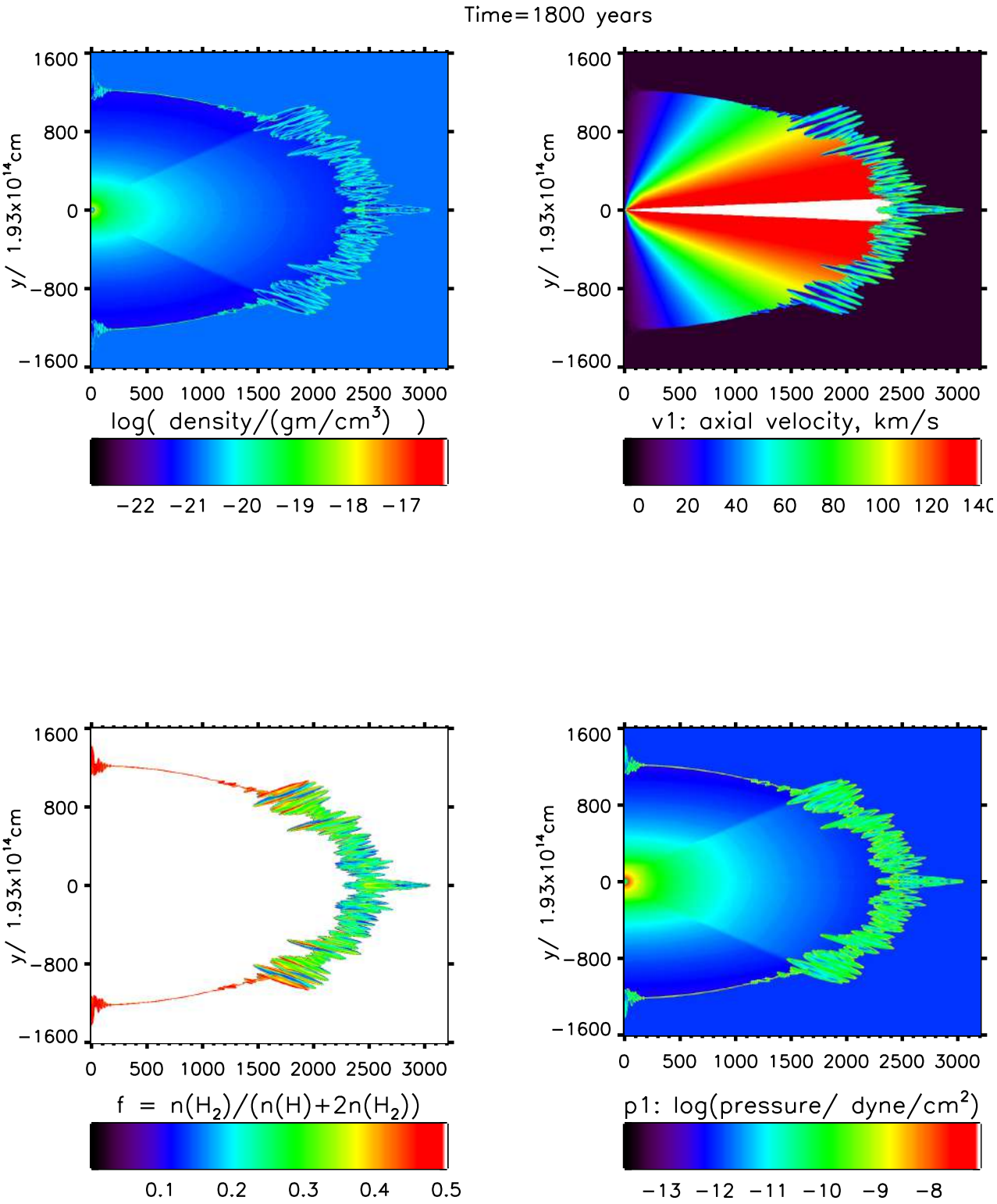

Figure 8.4: Cross-sectional distributions of density, axial velocity, molecular fraction and the pressure generated by a 140 km s^{-1} M1 molecular wind.

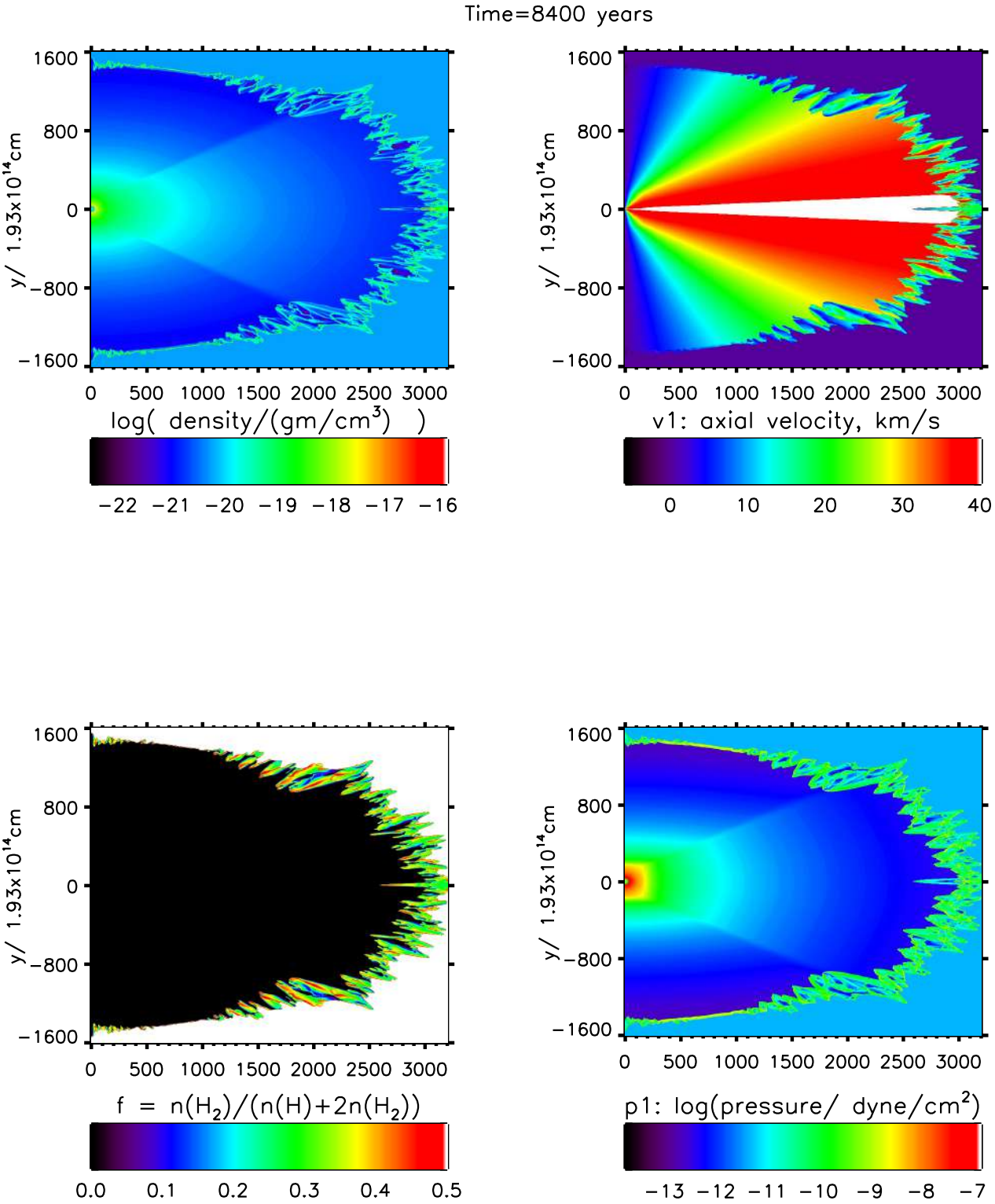

Figure 8.5: Cross-sectional distributions of density, axial velocity, molecular fraction and the pressure generated by a 40 km s^{-1} M3 atomic wind.

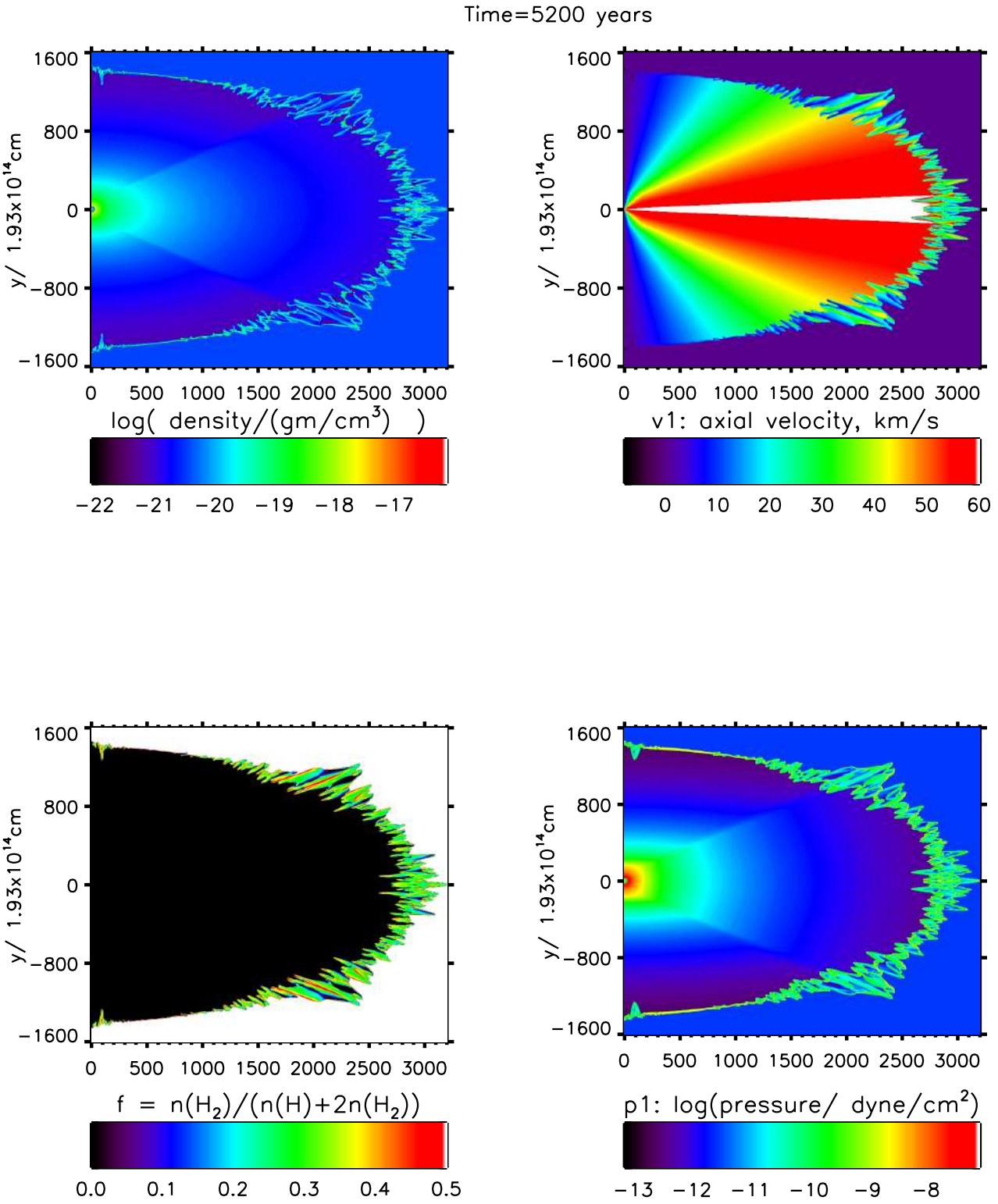

Figure 8.6: Cross-sectional distributions of density, axial velocity, molecular fraction and the pressure generated by a 60 km s^{-1} M3 atomic wind.

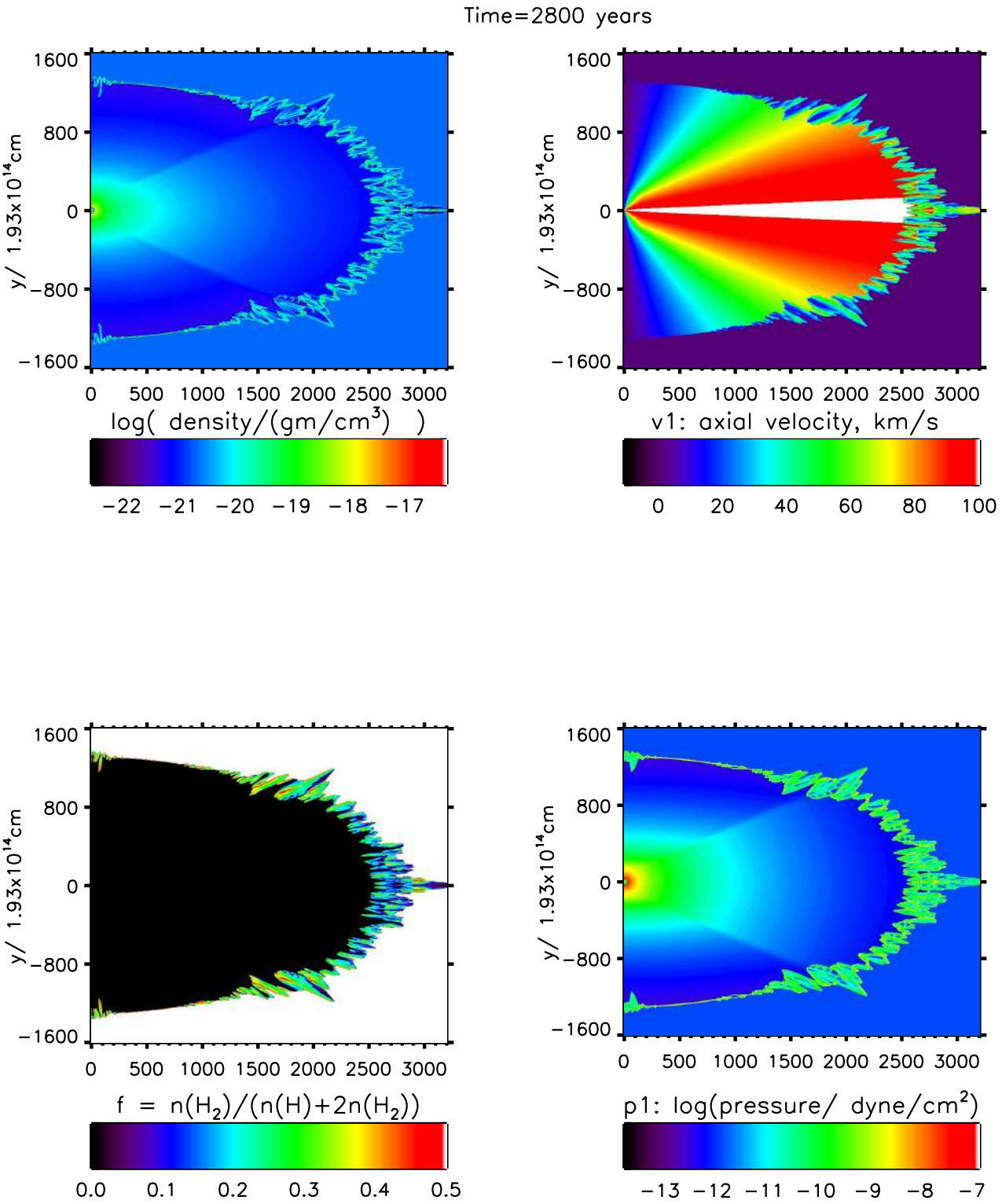

Figure 8.7: Cross-sectional distributions of density, axial velocity, molecular fraction and the pressure generated by a 100 km s^{-1} M3 atomic wind.

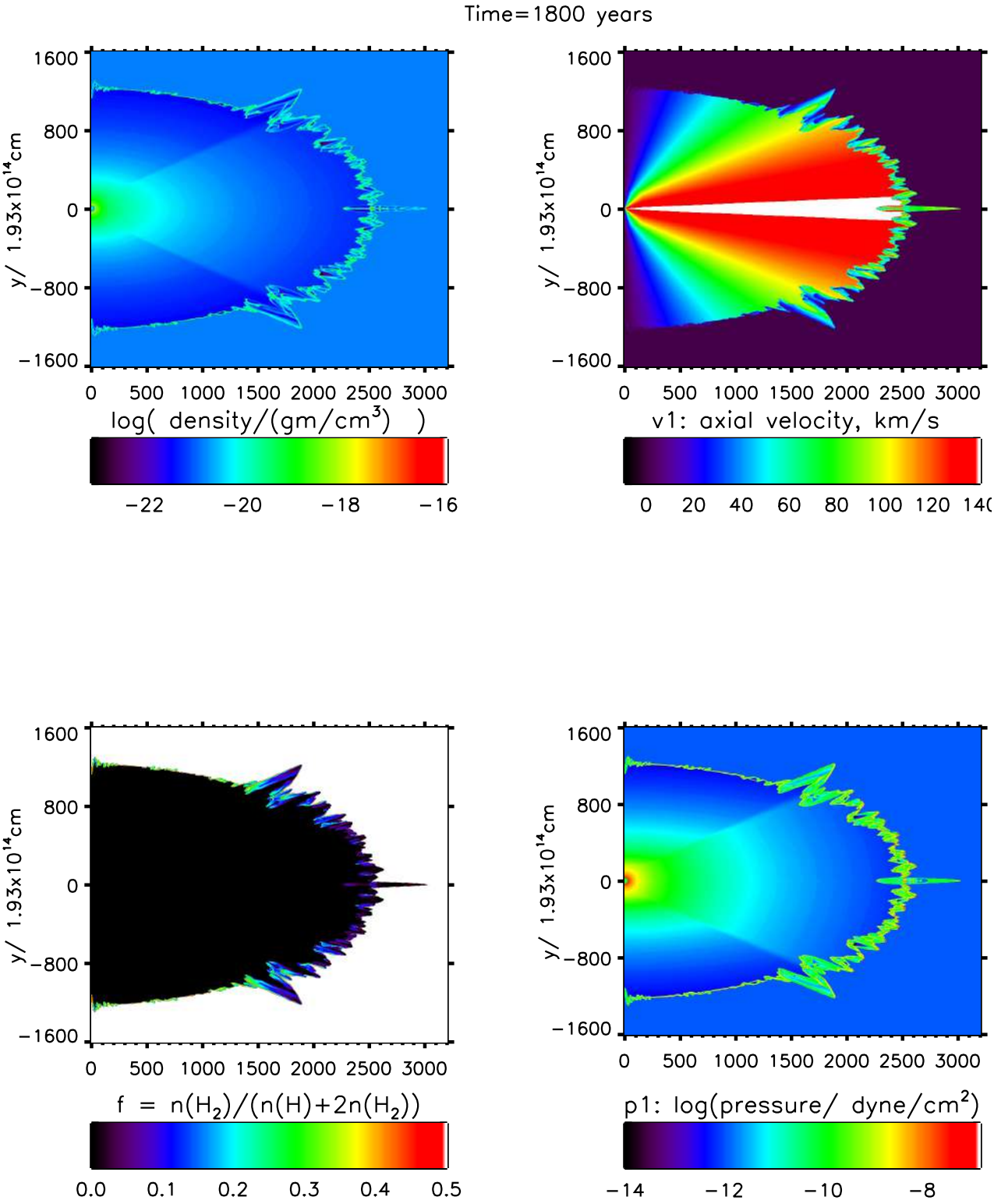

Figure 8.8: Cross-sectional distributions of density, axial velocity, molecular fraction and the pressure generated by a140 km s^{-1} M3 atomic wind.

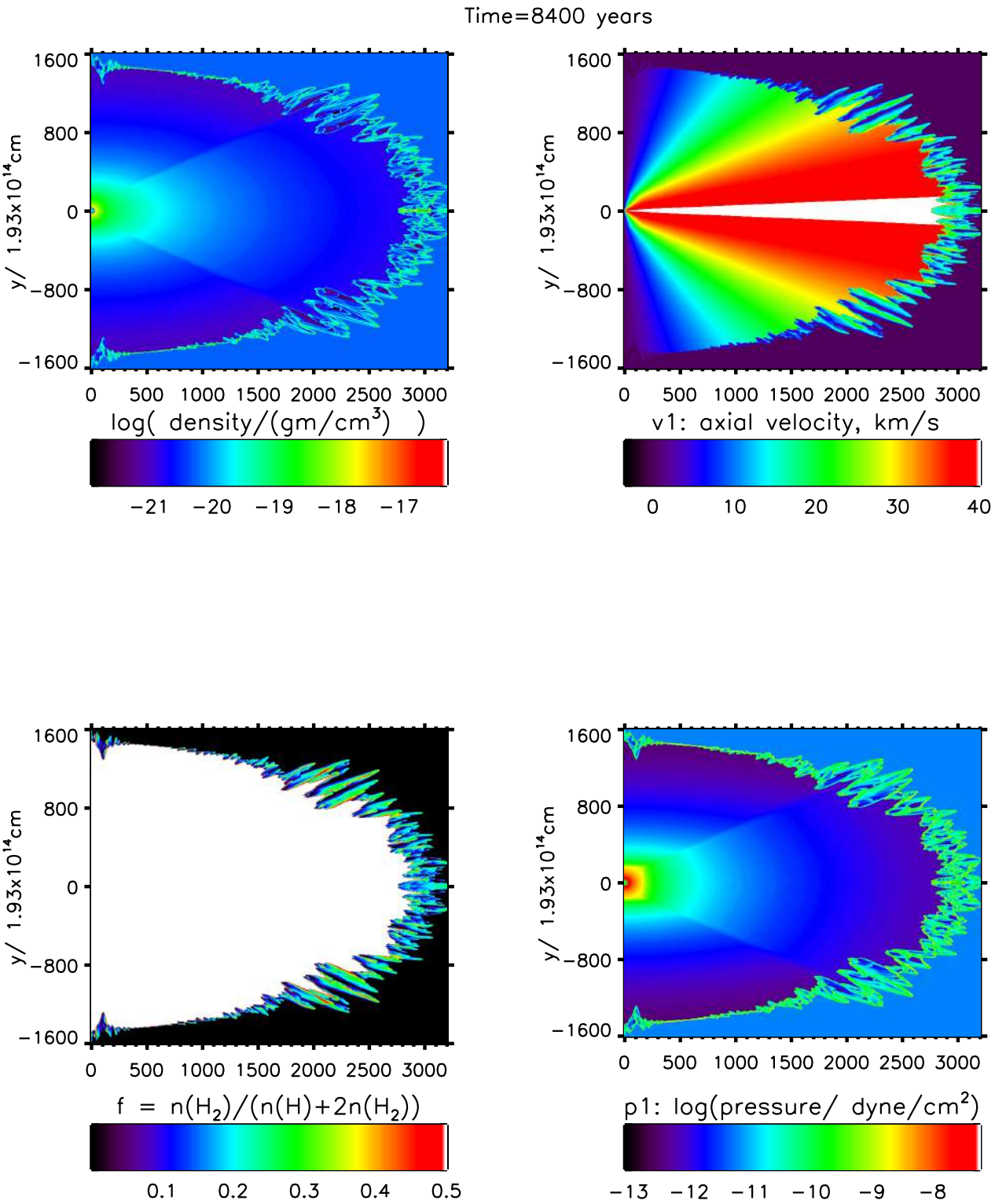

Figure 8.9: Cross-sectional distributions of density, axial velocity, molecular fraction and the pressure generated by a 40 km s^{-1} M2 molecular wind.

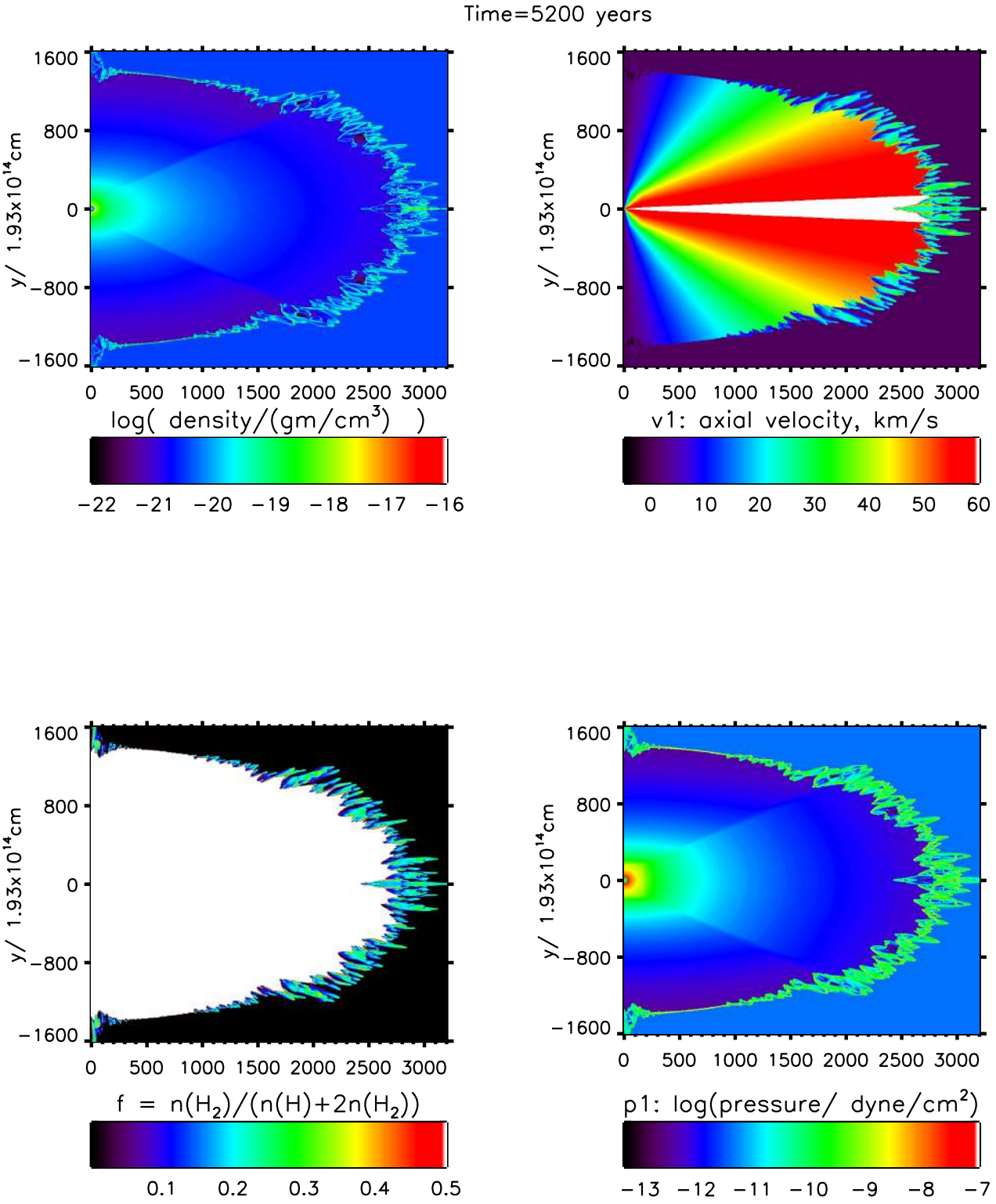

Figure 8.10: Cross-sectional distributions of density, axial velocity, molecular fraction and the pressure generated by a 60 km s^{-1} M2 molecular wind.

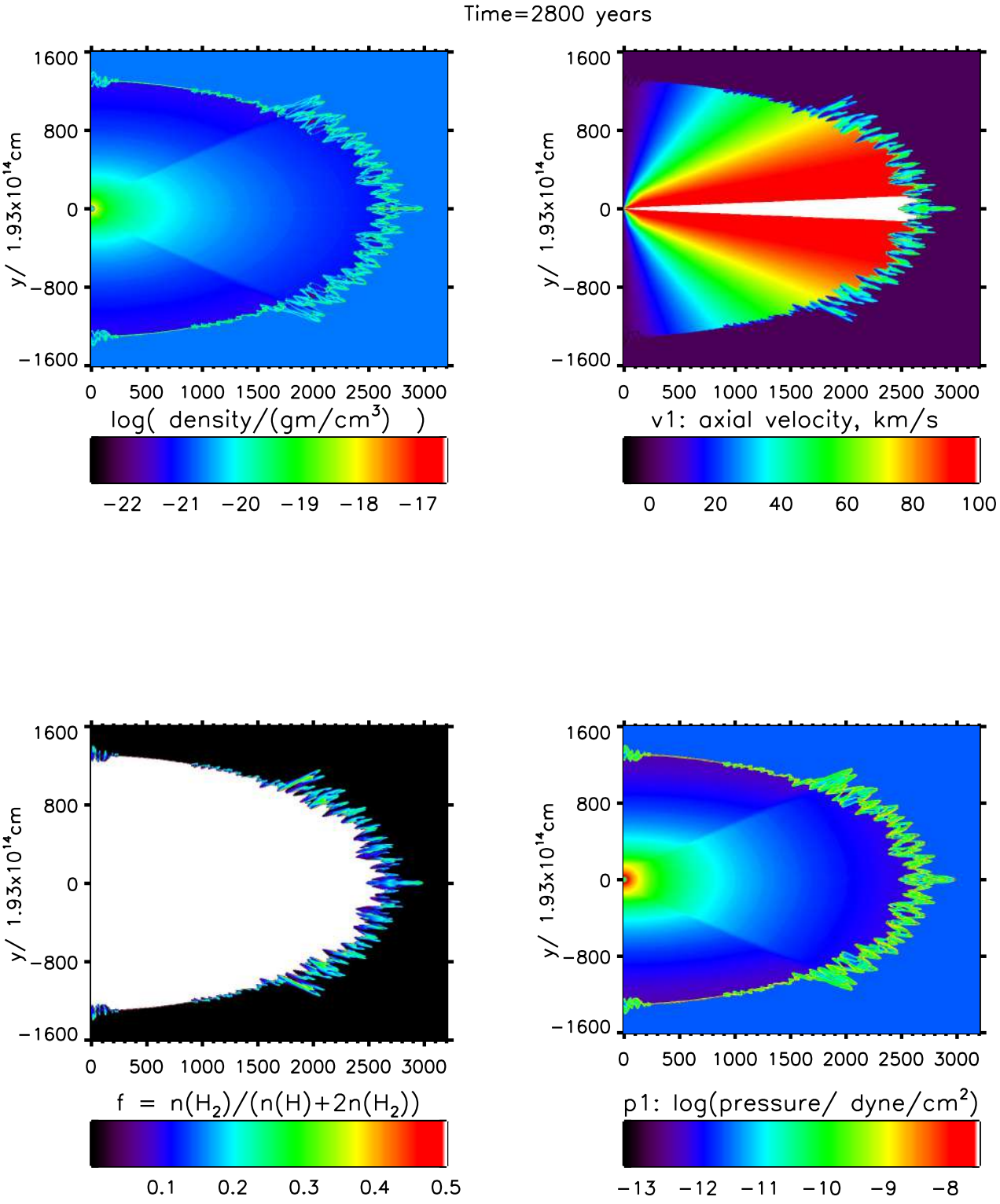

Figure 8.11: Cross-sectional distributions of density, axial velocity, molecular fraction and the pressure generated by a 100 km s^{-1} M2 molecular wind.

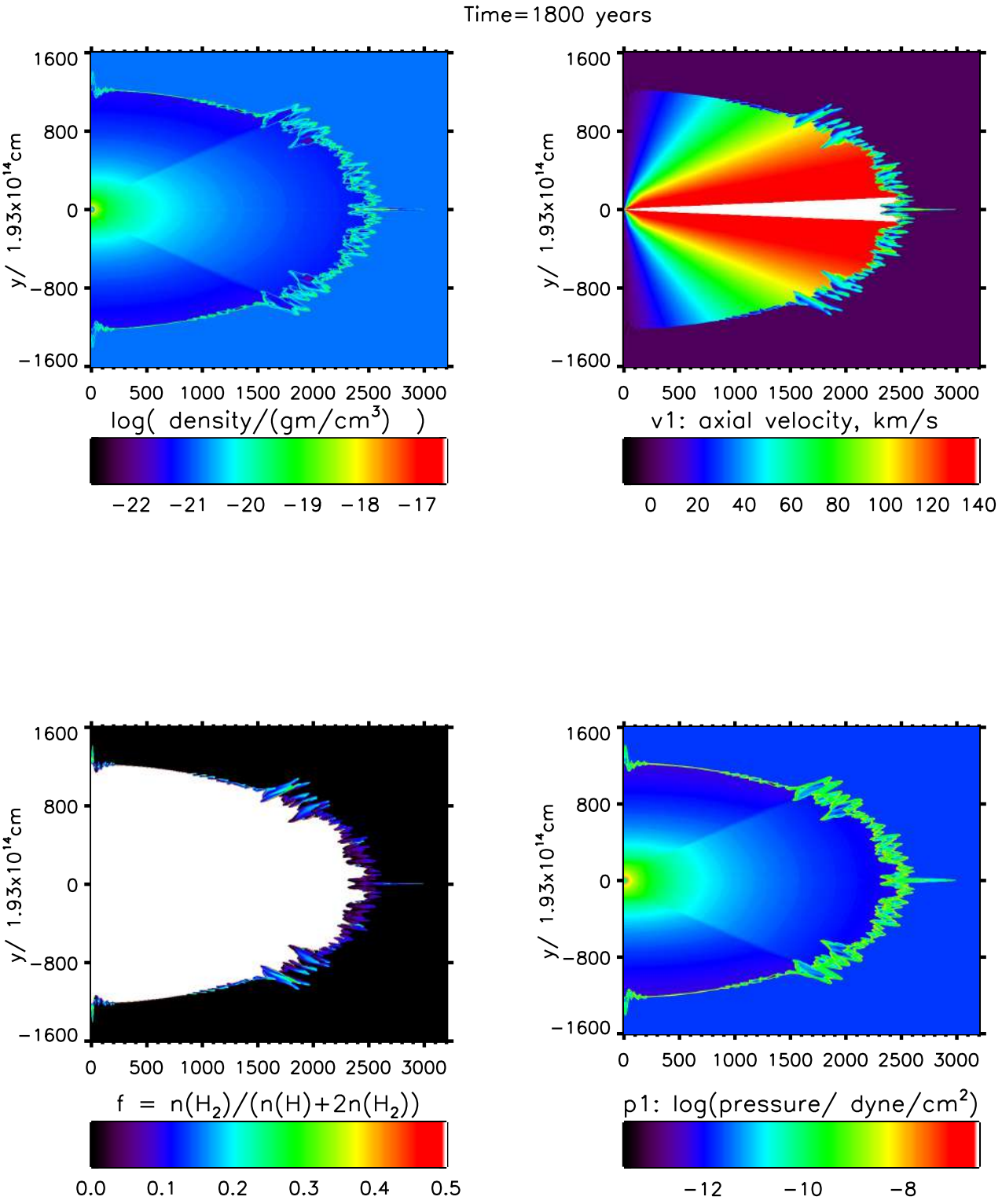

Figure 8.12: Cross-sectional distributions of density, axial velocity, molecular fraction and the pressure generated by a 140 km s^{-1} M2 molecular wind.

Bibliography

Akras S., Gonçalves D. R., Ramos-Larios G., 2017, MNRAS, 465, 1289

Aleman I., Zijlstra A. A., Matsuura M., Gruenwald R., Kimura R. K., 2011, MNRAS, 416, 790

Anderson J. D., 1995, Computational Fluid Dynamics. McGraw Hill International Editions.

Andersson B.-G., Piirola V., De Buizer J., Clemens D. P., Uomoto A., Charcos-Llorens M., Geballe T. R., Lazarian A., Hoang T., Vornanen T., 2013, apj, 775, 84

Arnaud M., Rothenflug R., 1985, A&AS, 60, 425

Balick B., 1987, AJ, 94, 671

Bally J., Lane A. P., 1991, in Elston R., ed., Astronomical Society of the Pacific Conference Series Vol. 14 of Astronomical Society of the Pacific Conference Series, Shocked molecular hydrogen associated with Herbig-Haro objects and molecular outflows: the Cepheus-A flow.. pp 273–278

Black J. H., Dalgarno A., 1976, ApJ, 203, 132

Blake G. M., 1972, MNRAS, 156, 67

Blandford R. D., Payne D. G., 1982, MNRAS, 199, 883

Bloecker T., 1995, aap, 299, 755

Brebbia W. ., 1991, Computational Modelling of Free and Moving Boundary Problems. Walter de Grueter.

Bressan A., Marigo P., Girardi L., Salasnich B., Dal Cero C., Rubele S., Nanni A., 2012, MNRAS, 427, 127

Brown T. M., Bowers C. W., Kimble R. A., Sweigart A. V., Ferguson H. C., 2000, ApJ, 532, 308

Bujarrabal V., Alcolea J., Neri R., 1998, ApJ, 504, 915

Bujarrabal V., Castro-Carrizo A., Alcolea J., Sánchez Contreras C., 2001, aap, 377, 868

Bujarrabal V., Pardo J. R., 2007, Baltic Astronomy, 16, 126

Castro-Carrizo A., Quintana-Lacaci G., Neri R., Bujarrabal V., Schöier F. L., Winters J. M., Olofsson H., Lindqvist M., Alcolea J., Lucas R., Grewing M., 2010, A&A, 523, A59

Cernicharo J., Guelin M., Penalver J., Martin-Pintado J., Mauersberger R., 1989, aap, 222, L1

Chevalier R. A., Imamura J. N., 1983, apj, 270, 554

Clarke D. A., 2010, ApJS, 187, 119

Courant R., Friedrichs K. O., 1948, Supersonic Flow and Shock Waves. Interscience Publishers, inc

Davis C. J., Smith M. D., Gledhill T. M., Varricatt W. P., 2005, MNRAS, 360, 104

Davis C. J., Smith M. D., Stern L., Kerr T. H., Chiar J. E., 2003, MNRAS, 344, 262

Deacon R. M., Green A. J., Chapman J. M., 2004, in Dupree A. K., Benz A. O., eds, Stars as Suns : Activity, Evolution and Planets Vol. 219 of IAU Symposium, Radio Observations of Masers in Post-AGB Stars. p. 853

Deutsch A. J., 1956, ApJ, 123, 210

Dong R., Draine B. T., 2011, ApJ, 727, 35

Dupree A. K., Reimers D., 1987, Mass Loss from Cool Stars. p. 321

Dwarkadas V. V., Balick B., 1998, ApJ, 497, 267

Fang X., Zhang Y., Kwok S., Hsia C.-H., Chau W., Ramos-Larios G., Guerrero M. A., 2018, ApJ, 859, 92

Forde K., 2013, PhD thesis

Frank A., Chen Z., Reichardt T., De Marco O., Blackman E., Nordhaus J., 2018, Galaxies, 6, 113

Frew D. J., Parker Q. A., 2010, , 27, 129

Froebrich D., Makin S. V., Davis C. J., Gledhill T. M., Kim Y., Koo B.-C., Rowles J., Eislöffel J., Nicholas J., Lee J. J., Williamson J., Buckner A. S. M., 2015, MNRAS, 454, 2586

Fryxell B., Arnett D., Mueller E., 1991, ApJ, 367, 619

García-Hernández D. A., Manchado A., 2016, in Journal of Physics Conference Series Vol. 728 of Journal of Physics Conference Series, On the formation of molecules and solid-state compounds from the AGB to the PN phases. p. 032009

García-Segura G., Langer N., Różyczka M., Franco J., 1999, ApJ, 517, 767

García-Segura G., López J. A., Steffen W., Meaburn J., Manchado A., 2006, ApJ, 646, L61

Geballe T. R., Kim Y. H., Knacke R. F., Noll K. S., 1988, apjl, 326, L65

Gledhill T. M., 2005, Monthly Notices of the Royal Astronomical Society, 356, 883

Gledhill T. M., Forde K. P., 2012, mnras, 421, 346

Gledhill T. M., Forde K. P., 2015, MNRAS, 447, 1080

Gledhill T. M., Forde K. P., Lowe K. T. E., Smith M. D., 2011, MNRAS, 411, 1453

Gledhill T. M., Yates J. A., 2003, MNRAS, 343, 880

Guerrero M. A., Villaver E., Manchado A., Garcia-Lario P., Prada F., 2000, ApJS, 127, 125

Habing H. J., 1996, A&A Rev., 7, 97

Hartquist T. W., Williams D. A., 1998, The molecular astrophysics of stars and galaxies, 4

Herwig F., 2005, ARAA Annual Review of Astronomy and Astrophysics, 43, 435

Höfner S., Gautschy-Loidl R., Aringer B., Jørgensen U. G., 2003, A&A, 399, 589

Höfner S., Olofsson H., 2018, A&A Rev., 26, 1

Hollenbach D., McKee C. F., 1979, apjs, 41, 555

Hollenbach D., McKee C. F., 1989, apj, 342, 306

Hollenbach D., Natta A., 1995, ApJ, 455, 133

Hollenbach D., Salpeter E. E., 1971, apj, 163, 155

Hora J. L., Latter W. B., Deutsch L. K., 1999, ApJS, 124, 195

Howe D. A., Hartquist T. W., Williams D. A., 1994, MNRAS, 271, 811

Hrivnak B. J., Kwok S., Su K. Y. L., 2000, Optical Imaging of Proto-planetary Nebulae. p. 155

Hrivnak B. J., Kwok S., Volk K. M., 1989, ApJ, 346, 265

Hrivnak B. J., Smith N., Su K. Y. L., Sahai R., 2008, apj, 688, 327

Huarte-Espinosa M., Frank A., Balick B., Blackman E. G., De Marco O., Kastner J. H., Sahai R., 2012, MNRAS, 424, 2055

Iben Jr. I., Renzini A., 1983, ARA&A, 21, 271

Jaminet P. A., Danchi W. C., Sutton E. C., Bieging J. H., Wilner D., Russell A. P. G., Sandell G., 1991, apj, 380, 461

Johnstone C. P., Güdel M., Lüftinger T., Toth G., Brott I., 2015, A&A, 577, A27

Kane J., Arnett D., Remington B. A., Glendinning S. G., Bazán G., Müller E., Fryxell B. A., Teyssier R., 2000, ApJ, 528, 989

Karakas A. I., 2010, Astrophysics and Space Science Proceedings, 16, 107

Kastner J. H., 2005, in American Astronomical Society Meeting Abstracts #206 Vol. 37 of Bulletin of the American Astronomical Society, Near-death Transformation: Mass Ejection in Planetary Nebulae and Protoplanetary Nebulae. p. 469

Kastner J. H., Weintraub D. A., Gatley I., Merrill K. M., Probst R. G., 1996, ApJ, 462, 777

Kato Y., 2007, Ap&SS, 307, 11

Kelly D. M., Hrivnak B. J., 2003, in Kwok S., Dopita M., Sutherland R., eds, Planetary Nebulae: Their Evolution and Role in the Universe Vol. 209 of IAU Symposium, Near-Infrared Spectroscopy of H_2 in Proto-Planetary Nebulae. p. 269

Kim H., Wyrowski F., Menten K. M., Decin L., 2010, A&A, 516, A68

Kwok S., 1982, ApJ, 258, 280

Kwok S., 1993, araa, 31, 63

Kwok S., 2004, Nature, 430, 985

Kwok S., 2007, The Origin and Evolution of Planetary Nebulae. Cambridge University Press, 2007

Kwok S., 2008, in Deng L., Chan K. L., eds, The Art of Modeling Stars in the 21st Century Vol. 252 of IAU Symposium, Stellar Evolution from AGB to Planetary Nebulae. pp 197–203

Kwok S., Purton C. R., Fitzgerald P. M., 1978, ApJ, 219, L125

Lagadec E., Mékarnia D., de Freitas Pacheco J. A., Dougados C., 2005, A&A, 433, 553

Lagadec E., Verhoelst T., Mékarnia D., Suáeez O., Zijlstra A. A., Bendjoya P., Szczerba R., Chesneau O., van Winckel H., Barlow M. J., Matsuura M., Bowey J. E., Lorenz-Martins S., Gledhill T., 2011, mnras, 417, 32

Lamers H. J. G. L. M., Cassinelli J. P., 1999, Introduction to Stellar Winds

Landau L. D., Lifshitz E. M., 1959, Fluid Mechanics, volume 6 edn. Pergamon Press

Le Bertre T., 1997, in De Greve J. P., Blomme R., Hensberge H., eds, Stellar Atmospheres: Theory and Observations Vol. 497 of Lecture Notes in Physics, Berlin Springer Verlag, Cool Stars Winds and Mass Loss: Observations. p. 133

Lee C.-F., Hsu M.-C., Sahai R., 2009, apj, 696, 1630

Lee C.-F., Sahai R., 2003, ApJ, 586, 319

Lepp S., McCray R., 1983, apj, 269, 560

Lepp S., Shull J. M., 1983, ApJ, 270, 578

Loup C., Forveille T., Omont A., Nyman L. A., 1990, aap, 227, L29

Lykou F., Zijlstra A., Kluska J., Lagadec E., Tuthill P., Avison A., Norris B., Parker Q., 2018, Galaxies, 6, 108

Lynden-Bell D., 1996, MNRAS, 279, 389

Mamon G. A., Glassgold A. E., Huggins P. J., 1988, apj, 328, 797

Manchado A., Stanghellini L., Villaver E., García-Segura G., Shaw R. A., García-Hernández D. A., 2015, ApJ, 808, 115

Marquez-Lugo R. A., Ramos-Larios G., Guerrero M. A., Vázquez R., 2013, MNRAS, 429, 973

Matsuura M., Speck A. K., McHunu B. M., Tanaka I., Wright N. J., Smith M. D., Zijlstra A. A., Viti S., Wesson R., 2009, ApJ, 700, 1067

McDonald I., Zijlstra A. A., 2015, MNRAS, 448, 502

McKee C. F., Storey J. W. V., Watson D. M., Green S., 1982, apj, 259, 647

Meixner M., 2000, Properties of Proto-Planetary Nebulae. p. 135

Messenger S., 2000, Nature, 404, 968

Mishra A., Li A., Jiang B. W., 2016, ApJ, 825, 68

Miszalski B., Acker A., Moffat A. F. J., Parker Q. A., Udalski A., 2009, A&A, 496, 813

Monteiro H., Morisset C., Gruenwald R., Viegas S. M., 2000, ApJ, 537, 853

Moraghan A., 2008, PhD thesis

Nakashima J.-i., Fong D., Hasegawa T., Hirano N., Koning N., Kwok S., Lim J., Dinh-Van-Trung Young K., 2007, AJ, 134, 2035

Neufeld D. A., Kaufman M. J., 1993, apj, 418, 263

Ney E. P., Merrill K. M., Becklin E. E., Neugebauer G., Wynn-Williams C. G., 1975, ApJ, 198, L129

Norman M. L., Winkler K.-H. A., 1985, Supersonic jets. Los Alamos: Los Alamos National Laboratory, 1985

Novikov I., Smith M., 2019, MNRAS, 489, 3710

Novikov I. D., Smith M. D., 2018, MNRAS, 480, 75

Olofsson H., Nyman L.-Å., 1999, aap, 347, 194

Paczyński B., 1971, , 21, 417

Parker E. N., 1961, apj, 133, 1014

Parker Q. A., Acker A., Frew D. J., Hartley M., Peyaud A. E. J., Ochsenbein F., Phillipps S., Russeil D., Beaulieu S. F., Cohen M., Köppen J., Miszalski B., Morgan D. H., Morris R. A. H., Pierce M. J., Vaughan A. E., 2006, MNRAS, 373, 79

Perinotto M., Schönberner D., Steffen M., Calonaci C., 2004, A&A, 414, 993

Piovan L., Tantalo R., Chiosi C., 2003, A&A, 408, 559

Prialnik D., 2000, An Introduction to the Theory of Stellar Structure and Evolution

Raga A. C., Castellanos-Ramírez A., Esquivel A., Rodríguez-González A., Velázquez P. F., 2015, , 51, 231

Ramos-Larios G., Guerrero M. A., Sabin L., Santamaría E., 2017, MNRAS, 470, 3707

Ramos-Larios G., Guerrero M. A., Vázquez R., Phillips J. P., 2012, MNRAS, 420, 1977

Reimers D., 1975, Memoires of the Societe Royale des Sciences de Liege, 8, 369

Renzini A., 1981, in Iben Jr. I., Renzini A., eds, Physical Processes in Red Giants Vol. 88 of Astrophysics and Space Science Library, Red giants as precursors of planetary nebulae. pp 431–446

Reynolds R. J., 1989, ApJ, 345, 811

Riera A., García-Lario P., Manchado A., Suárez O., García-Hernández D. A., Guerrero M. A., 2003, in Arthur J., Henney W. J., eds, Revista Mexicana de Astronomia y Astrofisica Conference Series Vol. 15 of Revista Mexicana de Astronomia y Astrofisica Conference Series, Observations of the Jet-Like Structure Associated with the Binary Planetary Nebula GLMP 621. pp 82–82

Riera A., Velázquez P. F., Raga A. C., Estalella R., Castrillón A., 2014, A&A, 561, A145

Rosen A., Smith M. D., 2004a, MNRAS, 347, 1097

Rosen A., Smith M. D., 2004b, A&A, 413, 593

Rosenfield P., Johnson L. C., Girardi L., Dalcanton 2012, ApJ, 755, 131

Ryden B., 2016, Dynamics. Ohio State Graduate Astrophysics Series, Office of Distance Ed & eLearning at OSU

Sabbadin F., Benetti S., Cappellaro E., Turatto M., 2000, A&A, 361, 1112

Sahai R., Hines D. C., Kastner J. H., Weintraub D. A., Trauger J. T., Rieke M. J., Thompson R. I., Schneider G., 1998, ApJ, 492, L163

Sahai R., Morris M., Sánchez Contreras C., Claussen M., 2007, AJ, 134, 2200

Sahai R., Morris M. R., Contreras C. S., Claussen M. J., 2012, in IAU Symposium Vol. 283 of IAU Symposium, Understanding the immediate progenitors of planetary nebulae. pp 180–183

Sahai R., Morris M. R., Villar G. G., 2011, AJ, 141, 134

Sahai R., Trauger J. T., 1998, AJ, 116, 1357

Sahai R., Trauger J. T., Watson A. M., Stapelfeldt K. R., Hester J. J., Burrows C. J., Ballister G. E., Clarke J. T., Crisp D., Evans R. W., Gallagher III J. S., Griffiths R. E., Hoessel J. G., Holtzman J. A., Mould J. R., Scowen P. A., Westphal J. A., 1998, ApJ, 493, 301

Salaris M., Weiss A., Cassarà L. P., Piovan L., Chiosi C., 2014, A&A, 565, A9

Sánchez Contreras C., Bujarrabal V., Castro-Carrizo A., Alcolea J., Sargent A., 2004, ApJ, 617, 1142

Sánchez Contreras C., Sahai R., Gil de Paz A., 2002, ApJ, 578, 269

Sandin C., Höfner S., 2003, A&A, 404, 789

Santander-García M., Bujarrabal V., Koning N., Steffen W., 2015, A&A, 573, A56

Saraph H. E., 1973, Journal of Physics B Atomic Molecular Physics, 6, L243

Schirrmacher V., Woitke P., Sedlmayr E., 2003, A&A, 404, 267

Schoenberner D., 1979, A&A, 79, 108

Schönberg M., Chandrasekhar S., 1942, ApJ, 96, 161

Schönberner D., Jacob R., Steffen M., Perinotto M., Corradi R. L. M., Acker A., 2005, A&A, 431, 963

Shapiro P. R., Kang H., 1987, apj, 318, 32

Shull J. M., Beckwith S., 1982, ARA&A, 20, 163

Shull J. M., Hollenbach D. J., 1978, ApJ, 220, 525

Smith M. D., 1986, MNRAS, 223, 57

Smith M. D., 1994a, mnras, 266, 238

Smith M. D., 1994b, A&A, 289, 256

Smith M. D., 2004, The origin of stars. Imperial College Press, ISBN 1-86094-501-5, 2004, XIII + 248 pp.

Smith M. D., Davis C. J., Rowles J. H., Knight M., 2014, MNRAS, 443, 2612

Smith M. D., Khanzadyan T., Davis C. J., 2003, MNRAS, 339, 524

Smith M. D., Rosen A., 2003, mnras, 339, 133

Smith M. D., Rosen A., 2005, MNRAS, 357, 579

Smith M. D., Rosen A., 2007, MNRAS, 378, 691

Smith M. D., Smarr L., Norman M. L., Wilson J. R. ., 1981, Nature, 293, 277

Smith N., 2013, MNRAS, 429, 2366

Smith N., Balick B., Gehrz R. D., 2005, AJ, 130, 853

Steffen W., Koning N., Esquivel A., García-Segura G., García-Díaz M. T., López J. A., Magnor M., 2013, MNRAS, 436, 470

Stone J. M., Norman M. L., 1992, apjs, 80, 753

Stone J. M., Xu J., Mundy L. G., 1995, Nature, 377, 315

Strickland R., Blondin J. M., 1995, ApJ, 449, 727

Sutherland R. S., Dopita M. A., 1993, apjs, 88, 253

Suttner G., Smith M. D., Yorke H. W., Zinnecker H., 1997, aap, 318, 595

Szczerba R., Siódmiak N., Stasińska G., Borkowski J., 2007, aap, 469, 799

Taylor K. N. R., Storey J. W. V., Sandell G., Williams P. M., Zealey W. J., 1984, Nature, 311, 236

Tielens A., 2005, The Physics and Chemistry of the Interstellar Medium. Cambridge University Press

Toalá J. A., Arthur S. J., 2014, MNRAS, 443, 3486

Turner J., Kirby-Docken K., Dalgarno A., 1977, ApJS, 35, 281

Ueta T., Meixner M., Bobrowsky M., 2000a, apj, 528, 861

Ueta T., Meixner M., Bobrowsky M., 2000b, in Kastner J. H., Soker N., Rappaport S., eds, Asymmetrical Planetary Nebulae II: From Origins to Microstructures Vol. 199 of Astronomical Society of the Pacific Conference Series, Dual Axisymmetry in Proto-planetary Nebula Reflection Nebulosities: Results from an HST Snapshot Survey of PPN Candidates. p. 195

Ueta T., Murakawa K., Meixner M., 2005, aj, 129, 1625

van de Steene G. C., Ueta T., van Hoof P. A. M., Reyniers M., Ginsburg A. G., 2008, A&A, 480, 775

van de Steene G. C., Wood P. R., van Hoof P. A. M., 2000, in Kastner J. H., Soker N., Rappaport S., eds, Asymmetrical Planetary Nebulae II: From Origins to Microstructures Vol. 199 of Astronomical Society of the Pacific Conference Series, Hα Emission Line Profiles of Selected Post-AGB Stars. p. 191

van der Veen W. E. C. J., Habing H. J., Geballe T. R., 1989, A&A, 226, 108

van Marle A. J., Keppens R., 2012, A&A, 547, A3

Vassiliadis E., Wood P. R., 1994, ApJS, 92, 125

Velázquez P. F., Riera A., Raga A. C., 2004, A&A, 419, 991

Velázquez P. F., Riera A., Raga A. C., Toledo-Roy J. C., 2014, ApJ, 794, 128

Vishniac E. T., 1994, ApJ, 428, 186

Wakelam V., Bron E., Cazaux S., Dulieu F., Gry C., Guillard P., Habart E., Hornekær L., Morisset S., Nyman G., Pirronello V., Price S. D., Valdivia V., Vidali G., Watanabe N., 2017, Molecular Astrophysics, 9, 1

Wallerstein G., Knapp G. R., 1998, ARA&A, 36, 369

Whitworth A. P., Clarke C. J., 1997, mnras, 291, 578

Winters J. M., Le Bertre T., Jeong K. S., Helling C., Sedlmayr E., 2000, A&A, 361, 641

Wood P. R., Faulkner D. J., 1986, ApJ, 307, 659

Wood P. R., Olivier E. A., Kawaler S. D., 2004, ApJ, 604, 800

Zhu X., Wang H., Fan Y., Du Z., He H., 2012, Science China Physics, Mechanics, and Astronomy, 55, 1720